

p-ISSN 1811-1165

e-ISSN 2413-2179

VOLUME 15, No. 2(30), 2018

EURASIAN
PHYSICAL
TECHNICAL

JOURNAL

KARAGANDA STATE UNIVERSITY NAMED AFTER E.A. BUKETOV

KARAGANDA, THE REPUBLIC OF KAZAKHSTAN

EURASIAN PHYSICAL TECHNICAL JOURNAL

p - ISSN 1811-1165
e - ISSN 2413-2179

Volume 15, No. 2(30), 2018

1st issue – March, 2004

Journal Founder:

**KARAGANDA STATE UNIVERSITY
NAMED AFTER E.A. BUKETOV**

**Е.А.БӨКЕТОВ АТЫНДАҒЫ ҚАРАҒАНДЫ
МЕМЛЕКЕТТІК УНИВЕРСИТЕТІ**

**КАРАГАНДИНСКИЙ ГОСУДАРСТВЕННЫЙ
УНИВЕРСИТЕТ ИМ. Е.А.БУКЕТОВА**

Contact information:

Editorial board of EPhTJ (Build. 2, room 221)
Karaganda State University
named after E.A. Buketov
Universitetskaya Str.28, Karaganda,
Kazakhstan, 100028
Subscription index: 75240
Tel: +7(7212)77-04-03
Fax: +7(7212)77-03-84
E-mail: ephjt@mail.ru

Signed to print on **27.12.2018**
Format 60x84 1/8. Offset paper.
Volume 19.0 p.sh. Circulation 300 copies.
Agreed price. Order No. 136.

Басуға **27.12.2018** қол қойылды.
Пішімі 60x84 1/8. Офсеттік қағазы.
Көлемі 19.0 ес.-б.т. Таралымы 300 дана.
Бағасы келісім бойынша. Тапсырыс № 136.

Подписано к печати **27.12.2018**
Формат 60 × 84 1/8. Офсетная бумага.
Объем 19.0 печ.л. Тираж 300 экз.
Цена договорная. Заказ № 136.

Printed in the Publishing House
of the KarSU named after academician E.A.Buketov

академик Е.А. Бөкетов атындағы ҚарМУ
баспасының баспаханасында басылып шықты

Отпечатано в Издательстве
КарГУ имени академика Е.А.Букетова

PROJECT MANAGER, RECTOR

Kubeev E.K., Karaganda State University named after E.A.Buketov,
Karaganda, Kazakhstan

Chief EDITOR

Sakipova S.E., Karaganda State University named after E.A.Buketov,
Karaganda, Kazakhstan

EDITORIAL BOARD

Aringazin A.K., Institute for Basic Research, L.N. Gumilev Eurasian
National University, Astana, Kazakhstan

Dueck J., Erlangen-Nuernberg University, Erlangen, Germany

Dzhumanov S., National University of Uzbekistan named after
M. Ulugbek, Tashkent, Uzbekistan

Epik E.Ya., Institute of Engineering Thermophysics, National Sciences
Academy of Ukraine, Kiev, Ukraine

Ibrayev N.Kh., Institute of Molecular Nanophotonics, Karaganda State
University named after E.A.Buketov, Karaganda, Kazakhstan

Jakovics A., Faculty of Physics and Mathematics, University of Latvia,
Riga, Latvia

Kidibaev M.M., Issyk-kul State University named after K.Tynystanov,
Karakol, Kyrgyzstan

Kumekov S.E., Kazakh State National Technical University named
after K.Satbaev, Almaty, Kazakhstan

Kuritnyk I.P., Department of Electronics and Automation,
High school in Oswiecim, Poland

Miau J.J., Department of Aeronautics and Astronautics, National
Cheng Kung University, Tainan, Taiwan

Pedrini C., University Claude Bernard Lyon I, France

Potapov A.A., V.A.Kotelnikov Institute of Radio Engineering and
Electronics of RAS, Moscow, Russia

Pribaturin N.A., Institute of Thermal Physics, SB RAS, Novosibirsk,
Russia

Rahimov F.K., Tajik State National University, Dushanbe, Tajikistan

Saulebekov A.O Kazakhstan Branch of Lomonosov Moscow State
University, Astana, Kazakhstan

Shragr E.R., National Research Tomsk State University, Tomsk,
Russia

Stoev M., South-West University «Neofit Rilski», Blagoevgrad,
Bulgaria

Trubitsyn A.A., Ryazan State Radio Engineering University, Russia

Zhanabaev Z.Zh., Al-Farabi Kazakh National State University, Almaty,
Kazakhstan

CONSULTANT OF TRANSLATION

Yakhina S.B., Karaganda State University named after E.A. Buketov,
Karaganda, Kazakhstan

TECHNICAL EDITORS

Akhmerova K.E., Kambarova Zh.T. Karaganda State University
named after E.A.Buketov, Karaganda, Kazakhstan

© Karaganda State University, 2018

© Қарағанды мемлекеттік университеті, 2018

Registered by the Ministry of Culture, Information and Public Adjustment of the Republic of Kazakhstan.
Қазақстан Республикасы мәдениет, ақпарат және қоғамдық келісім министрлігімен тіркелді
Registration Certificate No. 4382-Zh, November 7, 2003.

CONTENTS

| | |
|--|----|
| PREFACE | 4 |
| NONLINEAR PHYSICS. MODELING OF THE NONLINEAR PHYSICAL AND TECHNICAL PROCESSES. | |
| Potapov A.A. ON THE ISSUES OF FRACTAL RADIO ELECTRONICS: Part 1. PROCESSING OF MULTIDIMENSIONAL SIGNALS, RADIOLOCATION, NANOTECHNOLOGY, RADIO ENGINEERING ELEMENTS AND SENSORS..... | 5 |
| Potapov A.A. ON THE ISSUES OF FRACTAL RADIO ELECTRONICS: Part 2. DISTRIBUTION AND SCATTERING OF RADIO WAVES, RADIO HEAT EFFECTS, NEW MODELS, LARGE FRACTAL SYSTEMS..... | 16 |
| Kazhikenova S.Sh. COMPUTER SIMULATION FOR THE FLOW OF HIGH-TEMPERATURE MELTS..... | 24 |
| Saulebekov A.O., Trubitsyn A.A., Kambarova Zh.T., Saulebekova D.A. ELECTROSTATIC ENERGY ANALYZER OF CHARGED PARTICLES ON THE BASIS OF A QUADRUPOLE-CYLINDRICAL FIELD IN THE “RING-AXIS” FOCUSING REGIME..... | 35 |
| Dudin I.V., Narimanov R.K., Narimanova G.N. RESISTANCE MOMENT AT ROTATION OF AN ELLIPSOID IN VISCOUS FLUID.... | 40 |
| MATERIAL SCIENCE. TECHNOLOGIES FOR CREATING NEW MATERIALS. | |
| Kucherenko M.G., Nalbandyan V.M. FORMATION OF THE SPECTRAL CONTOUR WIDTH OF NANOPARTICLES PLASMON RESONANCE BY ELECTRON SCATTERING ON PHONONS AND A BOUNDARY SURFACE..... | 49 |
| Guchenko S.A., Koval N.N., Yurov V.M., Krysin O.V., Zavatskaya O.N. PROPERTIES OF TI/CU MULTILAYER COATINGS..... | 58 |
| Shaikenova A., Beisenov R., Muratov D. CHEMICAL VAPOR DEPOSITION GROWTH OF WS ₂ CRYSTALS..... | 66 |
| Shaikenova A., Beisenov R., Muratov D. STUDYING THE MECHANISM OF GRAPHENE FORMATION BY CHEMICAL VAPOR DEPOSITION SYNTHESIS. | 70 |
| Ibrayev N.Kh., Afanasyev D.A. ELECTRICAL CHARACTERISTICS OF SEMICONDUCTOR POLYMER FILMS DOPED WITH SILVER NANOPARTICLES..... | 76 |

ENERGETICS. THERMOPHYSICS. HYDRODYNAMICS.

| | |
|--|-----|
| Bezrodny M.K., Sakipov K.E., Aytmagambetova M.B., Zhakishev B.A. USING THE SYSTEM OF FINE PURIFICATION OF GASES IN THE DISPOSAL OF INDUSTRIAL AND DOMESTIC WASTE..... | 83 |
| Sakipov K.E., Abirov A.A., Sharifov D.M., Makhmudov B.N. EXPERIMENTAL STUDIES OF THE VORTEX HYDRAULIC ELEVATOR | 89 |
| Perchatkina E.V., Minkov L.L. NUMERICAL SOLUTION OF THE PROBLEM OF SUPERSONIC GAS FLOW IN TWO-DIMENSIONAL CHANNEL WITH THE OSCILLATING UPPER WALL..... | 98 |
| Yershina A.K., Ydyryssova A.A. ELEMENTARY CALCULATION OF SAILING WIND TURBINES..... | 104 |
| Sattinova Z., Ramazanova G., Zhabbasbayev U., Assilbekov B., Mussenova E. INVESTIGATION OF THERMAL CONDITIONS OF THE MOLDING PROCESS OF SLURRY BERYLLIUM OXIDE..... | 110 |
| Shrager E.R., Sakipova S.E., Tanasheva N.K., Akhmerova, K.E., Botpayev N., Kussaiynova A.K. STUDY OF ELECTRO-PHYSICAL PARAMETERS OF WIND TURBINES..... | 117 |
| Shaimerdenova K.M., Stoyev M., Tusypbaeva A.S., Rakhmankyzy A., Sekerbaeva G. ANALYSIS OF THE EFFECT OF ELECTRO-DISCHARGE WATER TREATMENT ON ITS PURIFICATION DEGREE..... | 123 |
| TECHNIQUE, DEVICES AND PHYSICAL METHODS OF EXPERIMENT | |
| Fayzullaev A.R., Astanov S.Kh, Ergasheva N.M. APPLICATION OF SPECTROSCOPY IN THE PROCESS OF OBTAINING DYES FROM ONION PELL..... | 128 |
| Zhunossov Y.T., Zhumadilov K.Sh., Chaizhunusova N.Zh., Sayakenov N.B., Shabdarbaeva D.M., Gnyrya V.S., Azimkhanov A.S., Stepanenko V.F., Fujimoto N., Shichijo K., Hoshi M. APPLICATION OF DOSIMETRY METHODS FOR INTERNAL ORGANS EXPOSURE AND POSSIBLE INFLUENCE TO REMOTE EFFECTS..... | 133 |
| SUMMARIES..... | 139 |
| INFORMATION ABOUT AUTHORS..... | 147 |
| GUIDELINES FOR AUTHORS..... | 150 |

Dear Authors and Readers!
Honourable colleagues!

This issue of the “Eurasian Physical Technical Journal” offers to your attention original research scientific articles devoted to the solution of actual problems of modern physics and technology. These are review articles, presenting the results of more than 20-year thematic research on fractal radio electronics. Interesting scientific papers are dedicated to modeling of complex processes of melting, heat and mass transfer, phenomena in solid state physics and features of elementary particles.

Eurasian Physical Technical Journal provides a platform for researchers and scientists to share their research on the physics of nanotechnology. A number of articles are devoted to the problems of alternative energy. The authors propose methods to improve the ecology of the environment, as well as new technologies for physical research in biophysics.

It is known that scientific conferences are useful place for the international exchange of scientific information.

22-23 November 2019 E.A. Buketov Karaganda State University invites all interested persons to participate in the 11th International scientific conference «CHAOS AND STRUCTURES IN NONLINEAR SYSTEMS. THEORY AND EXPERIMENT», devoted to the 70th anniversary of the professor K. Kussaiynov. We hope that all interested scientists will be able to discuss vital topics of modern physics at this conference.

The Eurasian Physical Technical Journal offers to publish scientific articles of those who are interested in reaching out to the international audience.

We are looking forward to see you amongst the authors of our future publications.

Respectfully,
Chief Editor, Saule E. Sakipova
Karaganda, December, 2018

UDC 537.86 + 621.37 + 621.396.96

**ON THE ISSUES OF FRACTAL RADIO ELECTRONICS:
Part 1. PROCESSING OF MULTIDIMENSIONAL SIGNALS,
RADIOLOCATION, NANOTECHNOLOGY, RADIO ENGINEERING
ELEMENTS AND SENSORS.**

Potapov A.A.

V.A. Kotelnikov Institute of Radio Engineering and Electronics of RAS, Moscow, Russia, potapov@cplire.ru

The paper presents fractal approaches to solving problems of radio electronics at all stages of radio waves radiation and reception with the subsequent processing of incoming information. This part of the article deals with the processing of information flows in radio systems. The basics of circuit design of new types of fractal antennas and fractal sensors are presented, a sketch of the development of fractal nanotechnologies is given. A brief description of the features of electrodynamic modeling of real miniature fractal antennas is given. The rationale for fractal-scaling or scale-invariant radiolocation is given.

Keywords: Radio physics, radio electronics, nanotechnologies, image processing, fractal antennas, fractal generators, texture, fractal, scaling.

Introduction

The creation of broadband and ultra-wideband radio systems has always been one of the main tasks of modern radio electronics. The expansion of the operational frequency bandwidth is due to modern trends in the development of radiolocation, telecommunications, radio engineering in order to increase the speed of information transmission, the level of jamming immunity and the information capacity of radio systems of any range. Along with the increasing complexity of modern radio-electronic equipment and its functions, it is necessary to consider new physical principles for the element base and radiotechnical systems. In this case, the theory of fractals and the theory of deterministic chaos [1–4] become extremely important.

The main directions of design and development of new fractal radio elements, antennas, metamaterials, as well as fundamentally new radio systems for radiolocation and telecommunication problems, i.e. issues that apply to the entire radio electronics. The study is conducted within the framework of the research area “Fractal Radiophysics and Fractal Radioelectronics: Designing Fractal Radio Systems”, proposed and developed by the author based on the theory of fractals and deterministic chaos in IRE of RAS since the late 70s of the XX century [1-4].

1. Fractal processing of information flows in radio systems

When collecting, converting and storing information in modern complex systems for monitoring remote and mobile objects under conditions of intense interference, the latest methods for processing information flows and multidimensional signals become very important. Typically, the features of such complex systems exert at different spatial-temporal scales. The most adequate estimates of the state of the system under study and the dynamics of the change in the state of its subsystems are realized using the theory of fractals and processing multidimensional signals in fractional space with the necessary consideration of scaling effects [1-6]. The following briefly

summarizes selected experimental results of the fractal processing of multidimensional signals from objects of different physical nature (Figures 1-5).

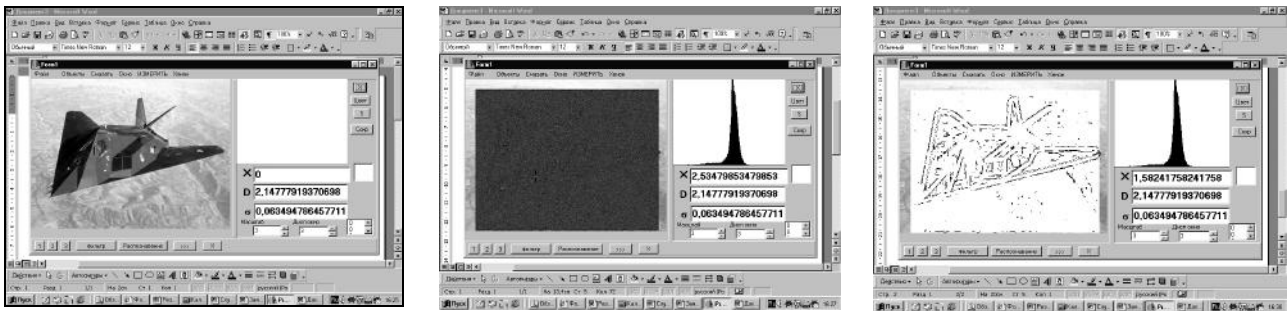


Fig.1. The original image of the aircraft (left), the image of the aircraft under the influence of noise jumbling: signal-to-noise ratio $q_0^2 = -3$ dB (middle), the results of fractal detection (right)

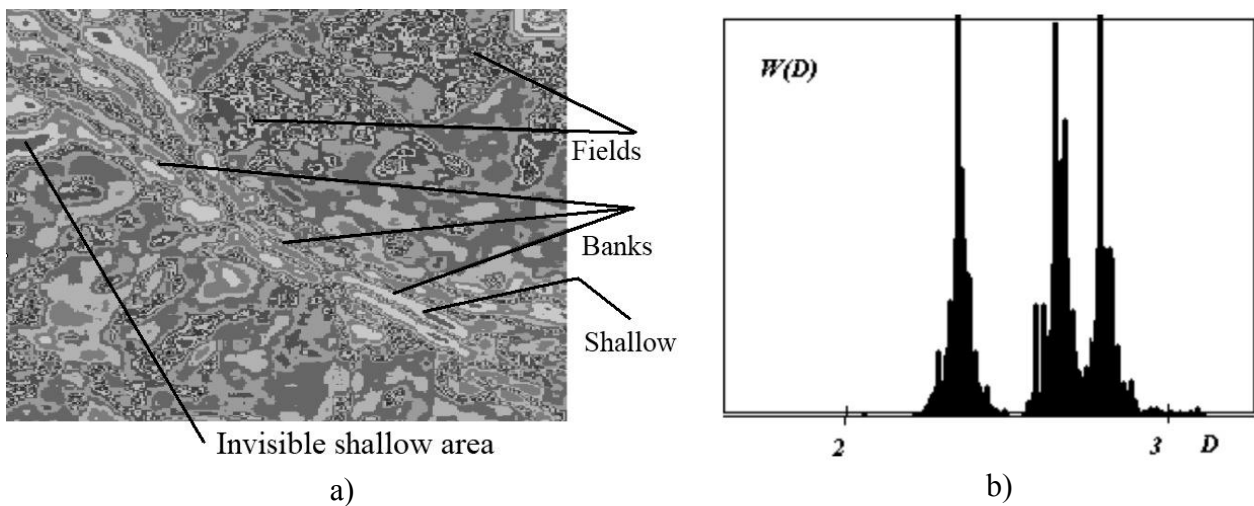


Fig.2. An example of earth surface differentiating by the field of fractal signatures D (a) and the empirical distribution of D when segmenting land cover textures in the radar image

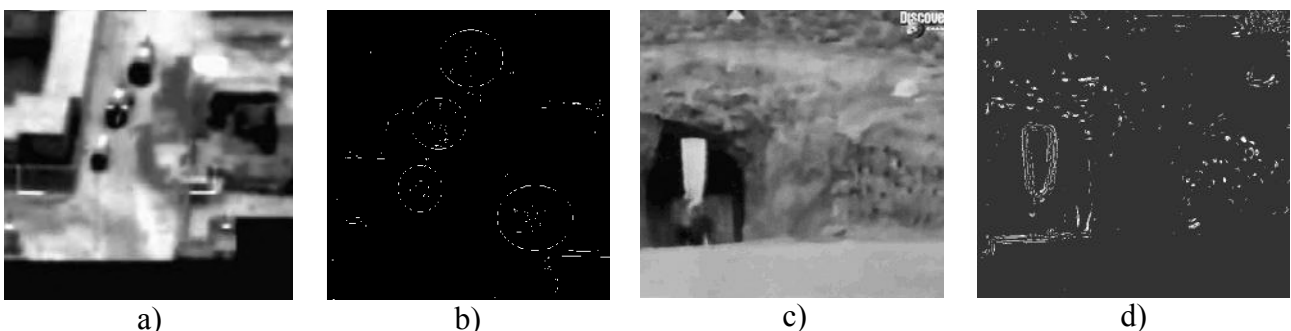


Fig.3. Images of the terrain with moving machines (a) and mountainous terrain with a tunnel (c) with UAVs and filtering results according to estimates of the fractal dimension D (b, d)

The results (UAV, SAR, medicine, etc.) show that fractal processing methods give an increase in the quality and detailing of objects and targets in a passive and active mode approximately by several times. These methods can be successfully applied to information processing from space, aviation complexes, low-profile high-altitude pseudo-satellites (HAPS) or detection of HAPS clusters and UAVs, synthesized clusters of space antennas and space debris.

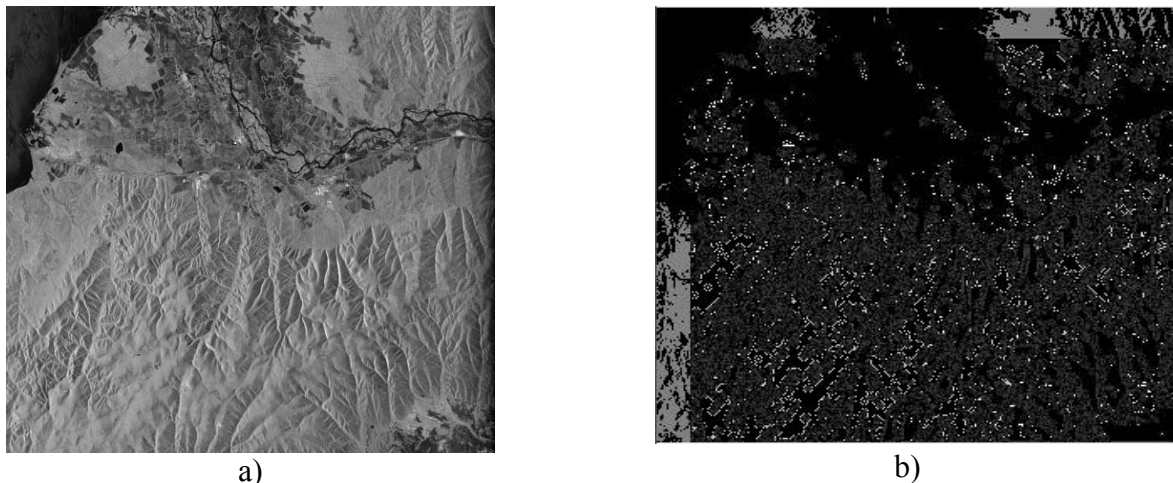


Fig.4. The Selenga river delta in the PALSAR SAR image (a) and the result of fractal processing (b).

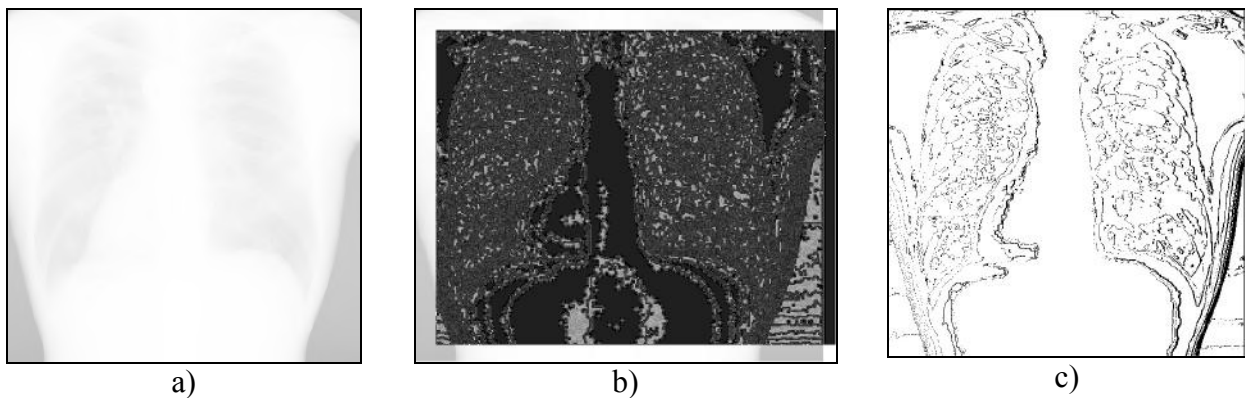


Fig.5. An example of solving the problem of fractal clustering of an X-ray image (a) by the value of estimating the fractal dimension D (b) and the fractal edge detection (c)

2. Fractal labyrinths as miniature fractal antennas

For the past few years, the fractal labyrinth topology has become a fast-growing object of interest for scientists. The software created by the author and his colleagues was called “Fractalizer” [7, 8]. The software (the window shown in Figure 6a) contains the first graphic area of the graph in order to select the shape of the fractal curve generator and the discretization interval. To the right of the generator panel there are graphical tools for determining parameters, such as the iteration number of the main branch, the number of branches, the number of branches iteration, the width and height of lines, the minimum gap between unrelated elements (elementary lines) of the structure, etc. Software can save fractal structures in a universal and well-known drawing size as Autodesk DXF. A DXF file can be imported as fractal antenna geometry into most modern computer developments and software modeling, such as ANSYS, Solid Works, etc. Moreover, the software “Fractalizer” has a setting panel for launching Ansoft HFSS as a software for fractal structure modeling. The process is automated for electrodynamic modeling of real miniature fractal antennas. The information exchange scheme you can see in Figure 6, b.

First, the program builds the main curve based on a user-defined generator, which is the first iteration of the fractal. Then the program calculates the number of break points of the curve (the number of angles) and stores them as points of a possible base of branches. Then, using a random

number generator, the loop program selects the base branch point and builds this branch before the specified user iteration is completed or before the obstacle is reached (another curve).

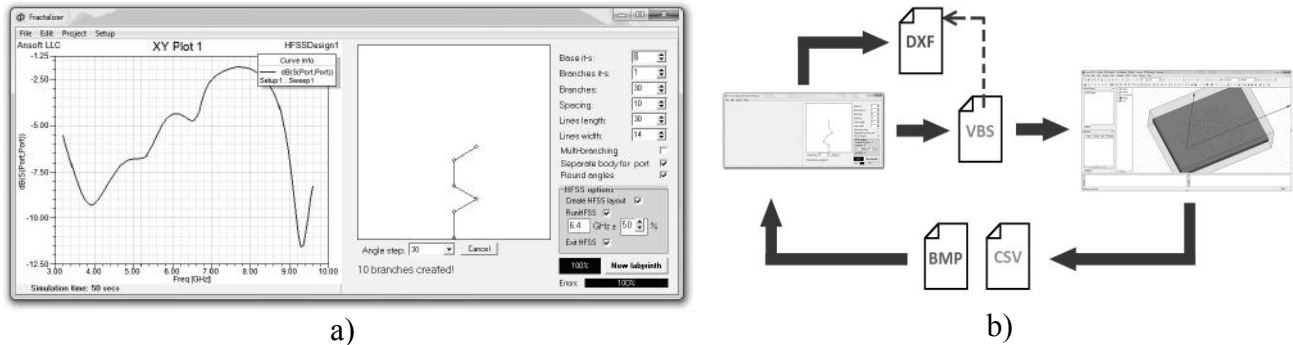


Fig.6. Computer window for design stages software (a) and information exchange (b)

The number of loops must be specified by the user. After the structure is ready, the software reports the number of successfully created branches and saves the structure as a DXF file. Examples of the synthesis of fractal antennas are shown in Fig. 7. The results obtained using the software were automatically imported into the AnsoftHFSS 12 simulation environment based on the finite element method (FEM). The results of modeling a fractal antenna (Figure 7 a) are shown in Figure 7 b. A fractal antenna has two resonances. The first one corresponds to a frequency below 1 GHz, i.e., the antenna is capable of receiving a wave length of 0.32 m.

3. Fractal labyrinths and genetic algorithms in the synthesis of apertures of large robust antenna arrays

Antenna arrays are one of the main components of large modern radio systems. The theory of application of fractals and fractional calculus makes for combining the achievements of classical amplitude and stochastic arrays [3]. The first type of antenna arrays has relatively small side lobes in the directivity pattern, but it is sensitive to element placement errors and excitation current values. The second type of arrays is resistant to element placement errors and their failure, but is characterized by a relatively high level of side lobes in the directivity pattern. The application of the principle of scaling (fractals) for antenna arrays makes it possible to more flexibly control the directivity pattern in the side lobes area.

The author has proposed to synthesize large stochastic robust antenna arrays using the properties of fractal labyrinths. This will make it possible to control the energy of the side lobes. The second step is to unite several fractal labyrinth clusters with different fractal dimension D in the synthesis space of a large antenna array. Therefore, in this natural way we come to adaptive fractal antennas. Here it is necessary to use genetic algorithms [9] to optimize the space-time large and extra-large antenna apertures that conform by specified quality and detection criteria.

5. Fractal generator

Consider an example of mathematical modeling of the basic fractal self-oscillatory system (FSOS) [10]. An oscillator with a small degree of nonlinearity was chosen for research, namely, a generalized oscillator of a sinusoidal signal (Figure 8 a), the action of which in the classical theory is given by the equation of motion:

$$u'' + \lambda(a)u' + \omega^2 u = 0, \quad (1)$$

where ω is the oscillation frequency of the system, a is the amplitude of the signal, $\lambda(a)$ is the equivalent attenuation coefficient, equal to:

$$\lambda(a) = \frac{\omega}{Q} (1 - k(a)R) = \frac{1}{C} \left(\frac{1}{R} - k(a) \right), \quad (2)$$

where Q is the quality factor, R and C are the load resistance and the capacitance of the circuit, respectively.

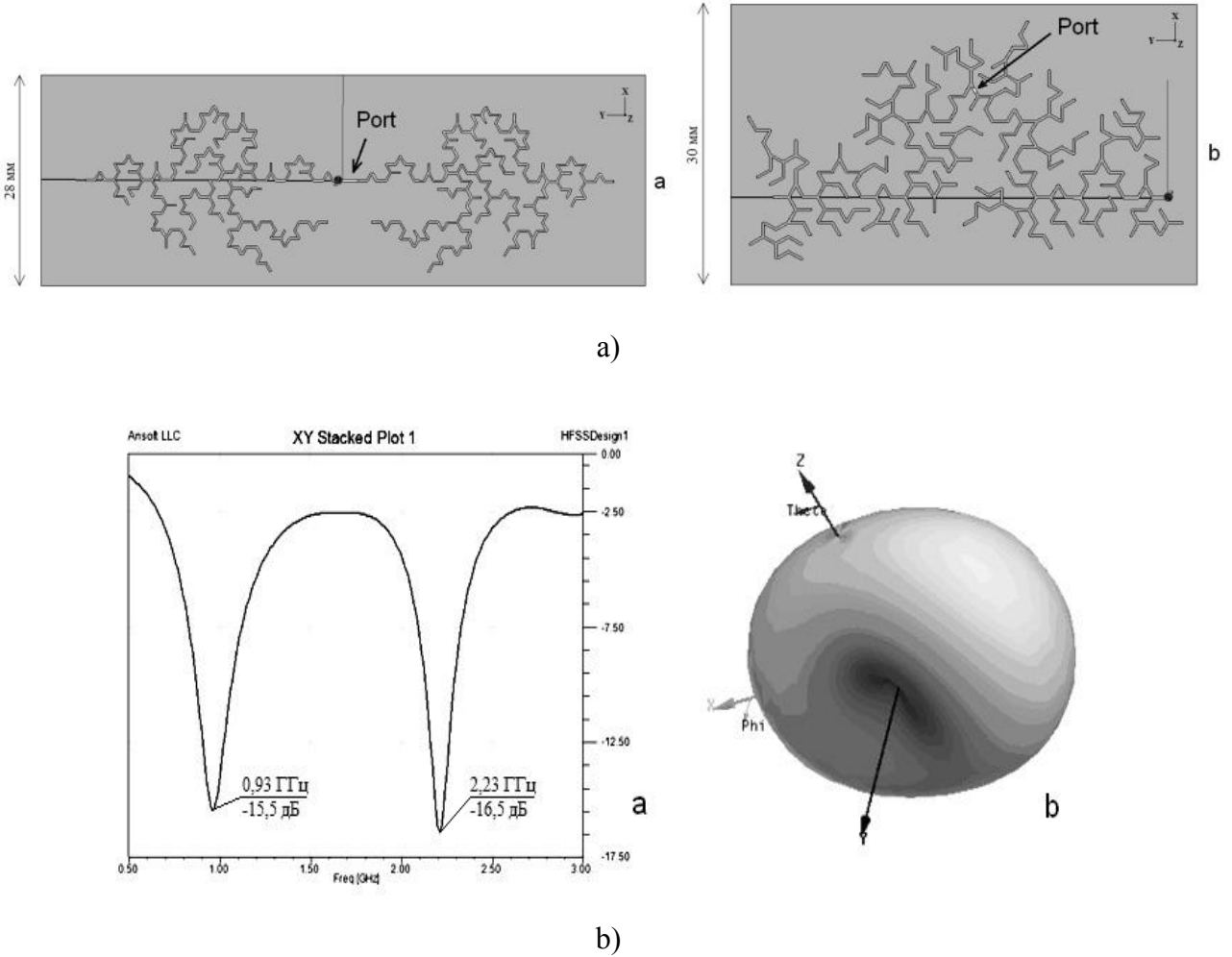


Fig. 7. Created fractal labyrinths for the synthesis of fractal antennas (a), the reflectivity factor in the frequency domain and the three-dimensional directivity pattern of the fractal antenna (b).

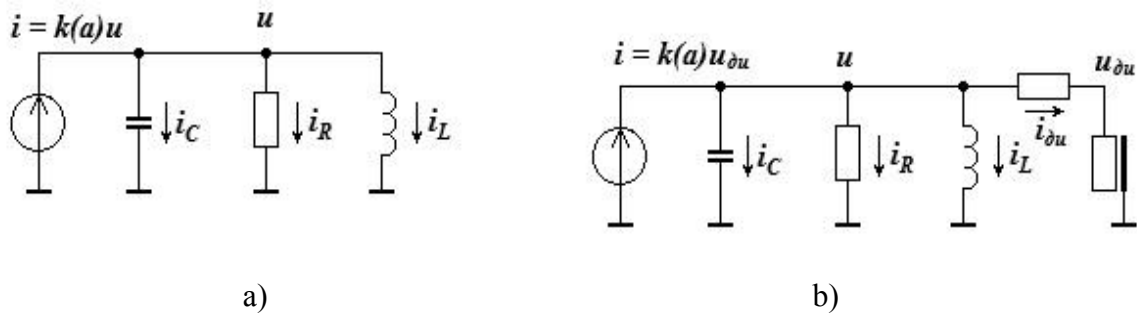


Fig.8. Classical self oscillator (SO) - (a), SO with a fractal chain of positive feedback (b).

Assume that the positive feedback (PFB) loop in the generator circuit is a fractional differentiating circuit based on a long RC line that can be interpreted as a certain distribution of the PFB loop parameters, for example, such as shown in Figure 8 b. In this case, assuming the current by the fractional integrator $i_{\partial u}$ being much smaller than the current iR , the equation of motion becomes:

$$u'' + \frac{1}{RC}u' + \omega^2u = \frac{1}{C}k(a) {}_L D^\alpha(u), \tag{3}$$

where ${}_L D^\alpha$ is a left-side Liouville derivative of α order [3].

Considering that $u \approx a \cos(\omega t)$, we have:

$$\lambda_\alpha(a) = \frac{1}{C} \left(\frac{1}{R} - k(a)k_{\partial u} \sin(\alpha\pi/2) \right). \tag{4}$$

In equation (4), $\alpha = 0 \dots 1$ is the order of the fractional impedance [3, 9] of the PFB loop, and $k_{\partial u}$ is the amplitude coefficient of the fractional chain transmission. The resulting expression (4) indicates a greater oscillation damping of the fractional system in comparison with the classical one at equal L, C, R and $k_{\partial u} = 1$.

The growth of the motion amplitude, in particular, of the signal, as a slow function of time in accordance with the method of equivalent linearization, will be determined by the following expression:

$$a' = \frac{\lambda_\alpha(a)}{2} a = \frac{a}{2C} \left(\frac{1}{R} - gS(a) \sin(\alpha\pi/2) \right), \tag{5}$$

where g is the gain, $S(a)$ is the magnitude of the nonlinearity, $S(a) \leq 1$ and $gS(a) = k(a)$.

The growth of the amplitude at different g is illustrated in Figure 9. From the first to the third graph, the value of g takes on increasing values 0, 166; 0.175 and 0.184.

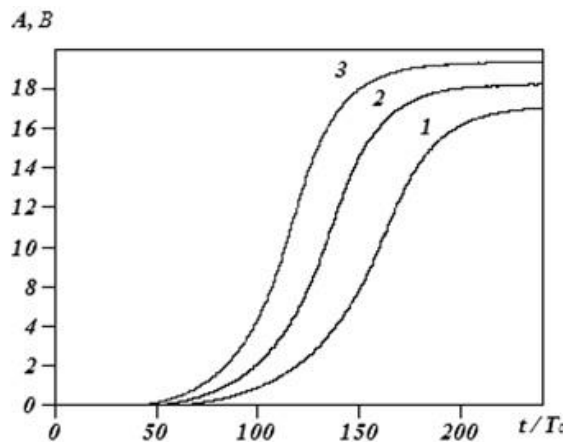


Fig.9. Excitation of a fractal auto-oscillatory system for various g .

Thus, a fractional or fractal PFB is identical to a retarded PFB. Note that the delayed PFB can be only a special case of the fractional one, and can also be a feature of the fractality of a dynamic system.

5. Fractal nanotechnologies and fractal radar absorbing materials

The elementary extension of a Cantor mathematical set, when proceeding to the physical level, makes it possible to come over to the cantor blocks in the plane technology of nanostructures [8,

11]. Percolation synthesis for nanostructured composites proposed by the authors in 2007 is also possible [12]. The use of the recursive procedure makes for a self-similar hierarchical structure up to the formation of separate conductive bands on the chip and in nanostructures. It is necessary to take into account and calculate the mutual and collective influence of electromagnetic fields on all components of the chip: conductive tracks, semiconductor, insulator, etc. The non-linear Cardar-Parisi-Zwang equation (CPZ) is used when spraying a substance on a solid surface. In [13], the CPZ equation for the anisotropic growth of the surface before the onset of a gradient catastrophe is solved in the small-angle approximation.

Modern and promising absorbing materials and surfaces should have a wide spectrum of electromagnetic radiation absorption at arbitrary angles of incidence and polarization of the incident radiation. From this perspective, the use of fractal metamaterials and artificial composites, which can be attributed to “smart” materials, is the most promising way [3, 8, 11]. In addition to direct use, they can have many functions. The inverse problem is solved in estimating the effective coefficients of the dielectric and magnetic permeability of a multilayer fractal medium, which can be tensors in the case of anisotropic materials. The medium can be formed by packets (fractal "sandwiches") of miniature fractal antennas [14]. The associated topological fractal structure makes for modulating the transmittance of electromagnetic waves. The lowest attenuation frequency corresponds to wavelengths, which can significantly exceed the external dimensions of a fractal plate that makes such fractal structures super-wave reflectors. Photonic crystals use Bragg scattering to create bandpass gaps [3, 14]. As a result of the Bragg scattering mechanism, the width and transverse dimensions of the photon crystals should be several wavelengths. Fractal photon and magnon crystals have a number of advantages compared to their classical analogs and are essentially new media to transmit information.

6. Fractal signatures in microrelief evaluation problems

Based on the experiments the researchers carried out, they were among the first to propose evaluating methods for using of fractal characteristics of surface quality of the products and the microrelief properties of modern materials [3, 15]. The intensive development of processing methods using concentrated energy flows leads to significant difficulties in the description and evaluation of roughness compared with the profile method.

In these cases, the shape of the roughness elements and the distribution of the elements are significantly different from the conventional Gaussian concept, which was formed long ago as part of processing materials by chiseling, see Figure 10 [3, 15].

| Title | Type of terrain | Title | Type of terrain |
|-----------------|---|----------------------------------|---|
| Mushroom shaped |  | Hollows |  |
| T - shaped |  | Globules |  |
| Peaks |  | Dispersion (globular-dispersion) |  |
| Splats |  | Cogs |  |
| Botiroid |  | Moire pattern |  |

Fig.10. Types of relief elements of modern micro-surfaces

Problems of forming surface quality, including such important quality characteristics as its roughness, become especially important due to the development of new energy technologies for metalworking. These problems also dominate in the field of nanotechnology, when the formation processes are considered not as a secondary property, but as a “response” of the structure of the surface layer to the influence of a certain physical process, and as a property of the structure itself; the more so the sizes of such layers are comparable with electron free path.

In [15], at the microrelief level of such processed surfaces, the authors demonstrated the existence of fractal clusters with irregularities distributed according to power laws with heavy tails (Figure 11). The presence of fractality in various environments can be controlled, in particular, by changing the skin effect and impedance. It is the spatial / temporal evolution of the current that makes for the electromagnetic fields to “feel” the fractal properties (fractal signatures) of the physical medium under study [3].

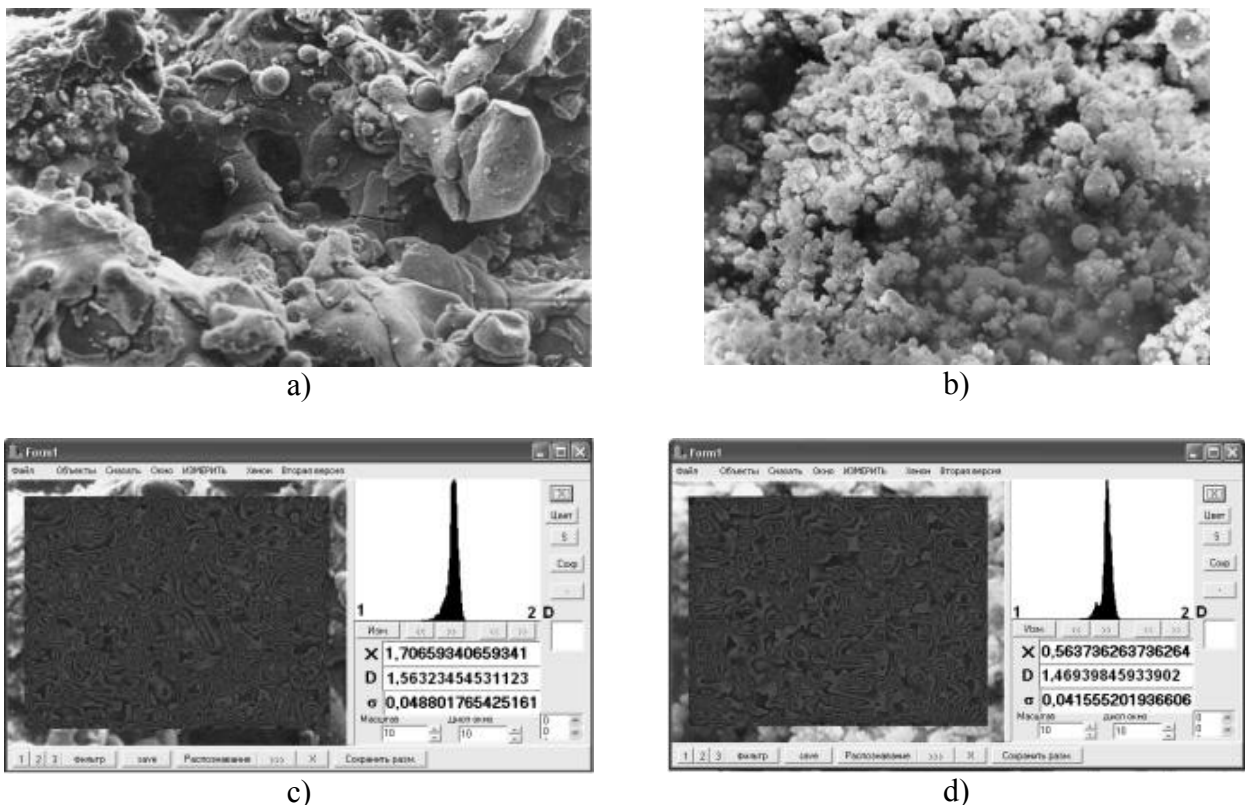


Fig.11. Fractal analysis of samples with plasma spraying: (a, b) – a 2D-image of the surface of the samples; (c, d) - the field and histogram of local D

7. Fractal radio systems

The increasing complexity of radio-electronic equipment and its functions makes it necessary to consider the fractal theory to develop new elementary base and new radio systems. The development of the world's first fractal non-parametric detector of radar signals makes for creating an entire fractal radio system [3, 16]. Fractional memristor on the quantum Hall effect is considered in [17].

Fractal structures and processes open up a new field of applications in radio electronics. Such fractal radio systems are described in detail in [18], in which Figure 3 shows the developed concept of fractal radio systems and fractal radio elements. Fractal radio systems contain fractal antennas, as well as digital fractal detectors, and use fractal methods for data processing; future devices will be able to use fractal methods of modulation and demodulation of radio signals.

8. Fractal-scaling or scale-invariant radio location

Detection of low-contrast objects against the background of natural intense interference inevitably requires the calculation of a fundamentally new characteristic that differs from the functionals related to interference and signal energy, and is determined only by the topology and dimension of the received signal. Introduction of radar concepts of "deterministic chaos", "texture", "fractal" and "fractal dimension D" [1-5] to scientific use allowed us for the first time in the world to propose and then apply new dimensional and topological (and not energy!) features or invariants (Figure 13), which are combined under the generalized concept of "sampling topology" ~ "fractal signature".

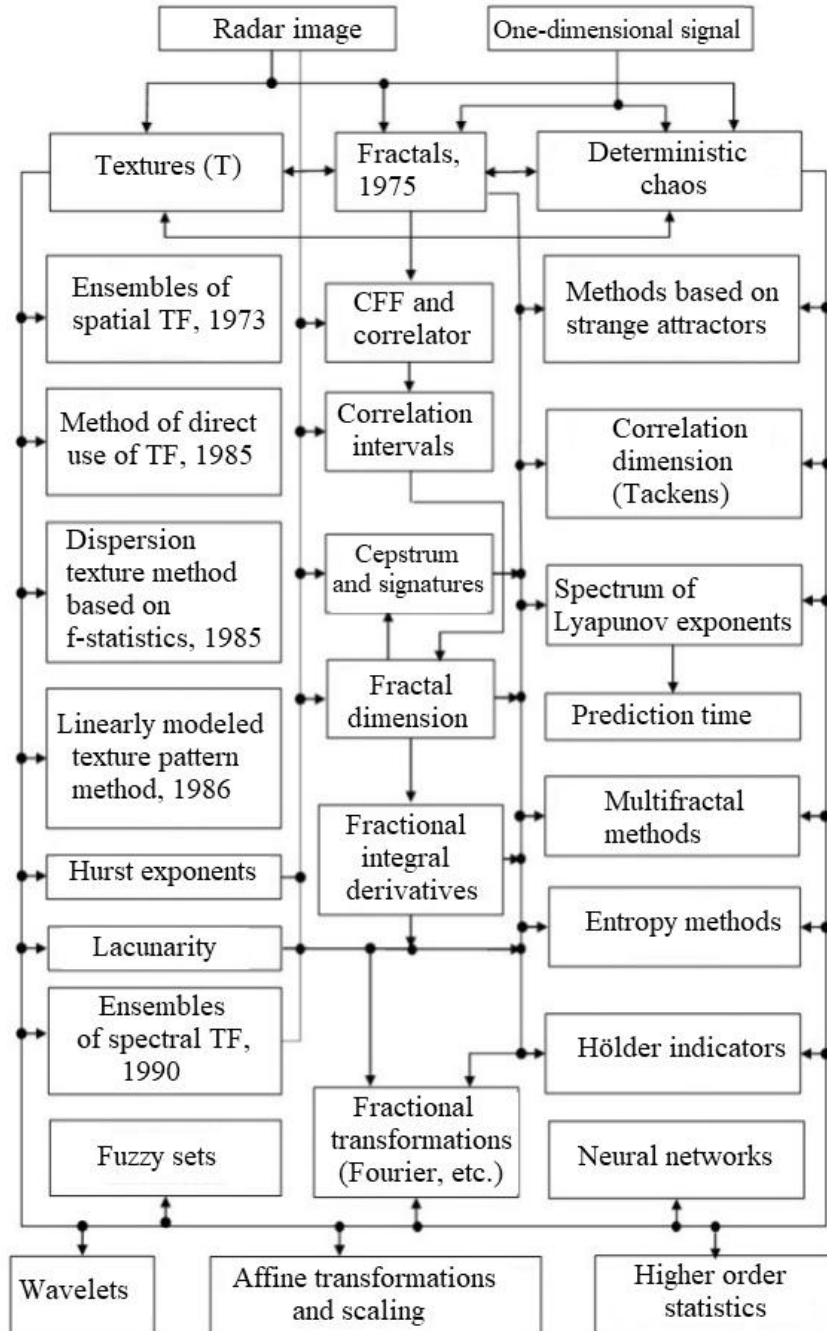


Fig.13. New topological features and methods for detecting low-contrast objects against interference (TF - textural features, CFF - coherence frequency function)

Fractal radiolocation [16, 19] is based on three postulates: 1 – signal / image intelligence, based on the theory of fractional measure and scaling effects to calculate the field of fractal dimensions; 2 – the sample of the received signal in the noise relates to the class of stable non-Gaussian probability distributions of D signal; 3 – topology maximum for minimum energy of the input random signal. These postulates open up new possibilities for stable operation support at small q_0^2 or for increasing radar range. Algorithms for detecting extended objects and targets in optical and radar images using texture processing were created by the authors as early as in the 80s of the 20th century (see the left column in Figure 13).

Classical methods for processing multidimensional signals fundamentally only distinguish the information constituent related to an integer-valued measure. Fractal-scaling methods for processing signals, wave fields and images in a broad sense are based on that part of the information that was not taken into account in the classical methods of radar data processing.

Based on many years of research, new theoretical directions were formulated and developed in the theory of statistical solutions, statistical radio engineering and statistical radiophysics, for example, “Fractal analysis and its application in the theory of statistical solutions and statistical radio engineering” or, briefly, “The statistical theory of fractal radiolocation”, “Statistical Fractal Radio Engineering, Theoretical Foundations of Fractal Radiolocatío”, etc.

Conclusion

For the first time in Russia and in the world, fractal-scaling methods have been created, developed and applied for the tasks of radiolocation, the formation of a fractal element base and fractal radio systems. For the technical implementation of the methods of fractal radioelectronics, it is necessary to have a base of new elements that makes it possible to process signals in a fractional measure space and simulate fractal objects and processes with the dynamics of fractional order differential equations. Promising elements of fractal radio electronics are functional elements with the implementation of their fractal impedances based on the fractal geometry of conductors on the surface (fractal nanostructures) and in space (fractal antennas), the fractal geometry of the surface microrelief of materials, etc. The results (UAV, SAR, medicine, etc.) show that fractal processing methods give an increase in the quality and detailing of objects and targets in passive and active modes approximately by several times. These methods can be successfully applied to processing of data from space, aviation complexes, low-profile high-altitude pseudo-satellites (HAPS) or detection of HAPS and UAV clusters, synthesized clusters of space antennas and space debris.

A new type and method of modern radiolocation has been discovered, proposed and substantiated, namely, fractal-scaling or scale-invariant radiolocation. This results in fundamental changes in the very structure of theoretical radiolocation, as well as in its mathematical apparatus. Fractal radiolocation can adequately describe and explain a much wider class of radar phenomena. Conducted research in the field of theoretical radiolocation can effectively solve problems of detecting signals in conditions of intense interference and develop new fractal MIMO systems.

This study continues the author's series of studies on the rationale to apply the fractal theory, physical scaling and fractional operators in matters of radio physics and radio electronics, first started in the USSR at the Institute of Radio Technologies and Electronics of the USSR Academy of Sciences in the late 1970s. Scrupulous bibliographic studies prove the complete and absolute world priority of the author in all "fractal" areas in radio physics and radio electronics (the list of author and his students' works includes more than 1000 scientific papers, including 35 monographs and chapters in monographs in Russian and English).

Acknowledgments

Supported by the project “Leading Talents of Guangdong Province”, № 00201502 (2016-2020) in the Jinan University (China, Guangzhou).

REFERENCES

- 1 Potapov A.A. *Fractals in radiophysics and radiolocation*. Moscow, Logos. 2002, 664 p.
- 2 Bunkin B.V., Reutov A.P., Potapov A.A. et al. *Issues of advanced radiolocation*. Moscow, Radio Engineering, 2003, 512 p. [in Russian]
- 3 Potapov A.A. *Fractals in radiophysics and radiolocation: Sample Topology*. 2nd revised and enlarged edition. Moscow, University Book, 2005, 848 p. [in Russian]
- 4 Potapov A.A. *Fractals and chaos as a basis for new innovative technologies in modern radio systems. Supplement to the book: Kronover R. Fractals and chaos in dynamic systems*. Moscow, Technosphere, 2006, pp. 374-479.
- 5 Potapov A.A., Gulyaev Yu.V., Nikitov S.A., Pakhomov A.A., Herman V.A. *The latest techniques of image processing*. Moscow: FIZMATLIT, 2008, 496 p. [in Russian]
- 6 Potapov A.A., Rekhviashvili S.Sh. Simulation of Properties of Images with Atomic Resolution in a Scanning Probe Microscope. *Technical Physics*. 2018, Vol. 63, No. 6, pp. 777 – 781.
- 7 Potapov A.A., Slezkin D.V., Potapov V.A. Fractal labyrinths as the basis of the geometry of new types of fractal antennas and fractal antenna arrays. *Radio Engineering*, 2013, No. 8, pp. 31-36. [in Russian]
- 8 Potapov A.A., Potapov Alexey A., Potapov V.A. Fractal Radioelement's, Devices and Fractal Systems for Radar and Telecommunications. *Proc. 14th Sino - Russia Symposium on Advanced Materials and Technologies*. Beijing: Metallurgical Industry Press. 2017, pp. 499 – 506.
- 9 Potapov A.A., Shifrin Ya.S., Kuzeev R.R. Genetic and Self-Similar Approaches for the Fractal Antennas Designing. *Antennas*. 2014, No. 3(202), pp. 25–48.
- 10 Potapov A.A. Oscillator with Fractional Differential Positive Feedback as Model of Fractal Dynamics. *J. Computational Intelligence and Electronic Systems*. 2014, Vol. 3, No. 3, pp. 236–237.
- 11 Potapov A.A., Potapov A.A. (junior), Potapov V.A. Fractal capacitor, fractional operators and fractal impedances. *Nonlinear world*. 2006 Vol. 4, No.4-5, pp. 172 – 187. [in Russian]
- 12 Potapov A.A. Fractal antennas, impedances, and radar absorbing coatings – “smart” materials. *Materials of the First International. scientific conf. "Nanostructured Materials - 2008: (NANO - 2008)"*. Minsk: Belarusian science, 2008, pp. 532. [in Russian]
- 13 Kulikov D.A., Potapov A.A., Rassadin A.E., and Stepanov A.V. Model for growth of fractal solid state surface and possibility of its verification by means of atomic force microscopy // IOP Conf. Ser.: Mater. Sci. Eng. 2017, Vol. 256, No. 012026, 10 p. <https://doi.org/10.1088/1757-899X/256/1/012026>.
- 14 Potapov A.A. Fractal antennas, nanotechnologies, resonances and plasmons. *Advances of modern radio electronics*. 2011, No. 5, pp. 5-12. [in Russian]
- 15 Potapov A.A., Bulavkin V.V., German V.A., Vyacheslavova O.F. Investigation of the microrelief of processed surfaces using fractal signature methods. *Journal of Technical Physics*. 2005 Vol. 75, No. 5, pp. 28-45.
- 16 Potapov A.A. On strategic directions in the synthesis of new types of texture-fractal radar detectors of low-contrast targets with contour extraction and coordinate location against the background of high-intense ground, sea and rainfall clutters. *Proceedings of IV All-Russian «RTI Systems of ASD-2016» STC to mark 100th anniversary of the Scientific and Research Institute for Long-Distance Radio Communications and the 70th anniversary of the Academician A.L. Mints RTI*. Moscow, N.E. Bauman MSTU Publishing House, 2017, pp. 438 – 448.
- 17 Rekhviashvili S.Sh. and Potapov A.A. Memristor and the Integral Quantum Hall Effect // *J. Communications Technology and Electronics*. 2012, Vol. 57, No. 2, pp. 189 – 191.
- 18 Potapov A.A. Analysis and synthesis of topological radar detectors of low-contrast targets against the background of high intensity noise as a new branch of radiolocation and theory of statistical solutions. *Eurasian Physical Technical Journal*, 2016, Vol.13, No.2 (26), pp. 13 – 24.
- 19 Potapov A.A. Textural and fractal-scaling methods for detecting, processing and recognizing weak radar signals and low-contrast images against the background of intense interference. *Bulletin of aerospace defense (PJSC "SPA" Almaz)*. 2018, No.2 (18), pp. 15-26.

UDC 537.86 + 621.37 + 621.396.96

**ON THE ISSUES OF FRACTAL RADIO ELECTRONICS:
Part 2. DISTRIBUTION AND SCATTERING OF RADIO WAVES, RADIO
HEAT EFFECTS, NEW MODELS, LARGE FRACTAL SYSTEMS**

Potapov A.A.

V.A. Kotelnikov Institute of Radio Engineering and Electronics of the RAS, Moscow, Russia, potapov@cplire.ru

The paper presents fractal approaches to solving problems of radio electronics at all stages of radiation and reception of radio waves with the subsequent processing of incoming information. In the second part of the article, fractal effects arising from the propagation and scattering of waves in randomly inhomogeneous media are considered. The radar equation for sounding a fractal object is detailed. Models based on fractals and strange attractors for radio wave scattering by plant cover are proposed.

Keywords: radio physics, radio thermal radiation of the atmosphere, radio wave scattering, fractal, scaling, strange attractors, large fractal systems.

Introduction

In this part of the article the author considered fractal effects arising from the propagation and scattering of waves in randomly inhomogeneous media; detailed the radar equation for sounding a fractal object; proposed models based on fractals and strange attractors for radio wave scattering by plant cover, i.e. issues that relate to the whole radio electronics. The study is conducted within the framework of the research area “Fractal Radiophysics and Fractal Radioelectronics: Designing Fractal Radio Systems”, proposed and developed by the author based on the theory of fractals and deterministic chaos in the IRE of the RAS since the late 70s of the XX century [1-4].

1. Fractal effects during wave propagation in the troposphere

When waves propagate in the atmosphere, it is necessary to take into account turbulence and its multi-scale character. In the modern theory of turbulence, it is assumed that the vortex layers coagulate into complex fractal structures [5]. The author, together with the Almaz Central Design Bureau, previously carried out multiscale experimental work on creating a data bank on the spatial-temporal characteristics of millimeter-wave scattering for the subsequent analysis and synthesis of radar image textures using simple and complex phase-manipulated signals of very large database $\geq 10^6$; the contribution of hydrometeor space-time distribution to image characteristics. A series of experiments was carried out on the express analysis of fractal fluctuations of ultra-wideband and simple signals of MMW and CMW in the turbulent troposphere at distance range gating. The average wind speed during field experiments was 3 ± 0.5 m/s. The processing showed that in summertime (air temperature of $20^0 - 25^0$) on the surface route 150 m long at a height of 10 m and a radiation wavelength of 8.6 mm for amplitude fluctuations, the fractal dimension $D \approx 1.63$. In this case, the Hurst parameter is $H \approx 0.37$. In the case of radar sounding, the fractal dimension increased to $D \approx 1.72$ ($H \approx 0.28$). In case of drizzling rain, the fractal dimension of amplitude fluctuations decreased to values of the order of $D \approx 1.59$ ($H \approx 0.41$). The magnitude of the standard deviation is < 0.02 . In experiments, processes with $D=1.5$ were never detected. Thus, in the course of field experiments, only anti-persistent processes were observed.

2. Fractal properties of the troposphere radiothermal radiation

In the experiments, the researchers measured mainly the vertical absorption at a wavelength of 8.2 mm. A radiometer with a sensitivity of 0.5 K, made according to the modulation scheme with a super heterodyne receiver at the input, provided measurement of the noise signal in the frequency band $\Delta f = 400$ MHz along the principal and image channels at an intermediate frequency of 250 MHz. The modulation of a signal for a frequency of 1000 Hz was carried out using a ferrite switch. A horn with a directional pattern width of $9^0 \times 1^0$ was used as an antenna. Phase portraits for each series were reestablished on the basis of the data obtained and the autocorrelation functions of the studied series were constructed. The analysis of the statistical characteristics of radiothermal radiation was carried out using the Pearson diagram [3, 22]. Further, the fractal dimension and the Hurst index were measured. The numerical estimates of the correlation dimension D_c and the Hurst index H are summarized in the table.

Table 1. Fractal properties of radiothermal radiation in the MMW range

| Series number | Correlation dimension D_c | Hurst index H |
|-----------------------|-----------------------------|-----------------|
| 1 - Clean troposphere | 1.7746 | 0.2254 |
| 2 - Cumulonimbus | 1.6509 | 0.3491 |
| 3 - Stratocumulus | 1.7172 | 0.2828 |
| 4 - Series | 1.5190 | 0.4810 |
| 5 - Series | 1.4943 | 0.5057 |

The Hurst index, depending on its value relative to the value $H = 1/2$, characterizes either persistence ($1/2 < H < 1$) or antipersistence ($0 < H < 1/2$) of the current sample. In the first case, when $1/2 < H < 1$ we observe a process that preserves the tendency to increase or decrease the instantaneous amplitudes in the sample, i.e. process with memory. In the second case, when $0 < H < 1/2$, increase in the amplitudes of the signal envelope in the "past" means decreasing in the "future", and vice versa, i.e. a more changeable process, often is referred to as a "mean reversion." The measured value of the Hurst index H (see the table) indicates a high antipersistence of the process of radiothermal radiation for all series of measurements.

3. Wave scattering on a stochastic fractal surface

In solving a number of relevant physical and practical problems, one has to deal with the processes of wave scattering on a statistically uneven surface. The need to introduce fractal models are due to the following reasons [1, 3, 6, 7]:

1. Numerous experiments [1, 3] have established that the majority of surfaces can be classified as fractal ones in certain space-time scales.
2. The fractal surface comprises irregularities of all scales relative to the length of the scattered wave.
3. Fractal models of wave scattering are natural generalization of the two-scale model used in remote sounding and radiolocation.
4. Taking into account fractality significantly approximates the theoretical and experimental angular dependences of the specific effective scattering areas (ESA) σ_* [1]. This fact is often interpreted as mainly instrumental error, which is incorrect.

5. The possibility of using non-differentiable functions to describe irregularities; it makes for correct introduction of exponential correlation coefficients.

Next, consider the issues of the theory of wave scattering on a stochastic fractal surface as applied to the problems of the formation of radar images (RI) [6, 7]. In the general case, the radar image can be interpreted as a map (matrix) of ESA σ_* or a signature (portrait) of the object being sounded in the case of a high angular resolution. All the results presented below are of priority in Russia and in the world [1, 3, 6, 7].

The mathematical statement of the problem and the initial relations are given in [1, 6, 7]. The fractal wave front, being non-differentiable, does not have a normal. Thus, the concepts “ray tracing” and “geometrical optics effects” are excluded. In this case, the “topothesy” of a fractal chaotic surface is introduced [1]. The scattering surface is modeled by a range-limited continuous fractal function of irregularities

$f(x)$, which is a modified Weierstrass function $W(t)$. Weierstrass’s two-dimensional range-limited function $W(x,y)$ is written as:

$$W(x, y) = c_w \sum_{n=0}^{N-1} q^{(D-3)n} \sum_{m=1}^M \sin \left\{ Kq^n \left[x \cos\left(\frac{2\pi m}{M}\right) + y \sin\left(\frac{2\pi m}{M}\right) \right] + \varphi_{nm} \right\}, \quad (1)$$

where c_w is a constant providing a single normalization; $q > 1$ is the parameter of spatial-frequency scaling; D is the fractal dimension ($2 < D < 3$); φ_{nm} is an arbitrary phase, uniformly distributed in the interval $[-\pi, \pi]$.

Figure 1 shows the calculated implementations of the Weierstrass function $W(x,y)$ for different scales. The implementation with the fractal dimension $D=2.5$ corresponds to the classical two-dimensional Brownian process (Figure 1 b) [1, 3, 6, 7].

The function $W(x,y)$ is anisotropic in two directions, if M and N are not very large. The function $W(x,y)$ has derivatives and at the same time it is self-similar. Such parameters as the averaged correlation interval $\tilde{\rho}$, mean square deviation σ and the spatial autocorrelation coefficient $R(\tau)$ are traditionally used to numerically describe a rough surface.

Figure 2 shows the dependences $\tilde{\rho}$ on the scale factor q and the fractal dimension of the surface D , respectively [6, 7]. Spatial scattering indicatrices of fractal surfaces in the microwave spectrum are currently studied completely insufficiently.

An extensive bank / catalog of typical types of more than 70 fractal scattering surfaces based on Weierstrass functions, as well as three-dimensional scattering indicatrices and their sections calculated for $\lambda = 2,2$ mm, $\lambda = 8,6$ mm and $\lambda = 3,0$ cm wavelengths for different values of dimension D and changing scattering geometry were investigated and presented in [6, 7] for the first time ever. The field of dispersion ψ_p from the final site S is described by the following expression:

$$\psi_p(\mathbf{r}) = -\frac{iL_x L_y k \exp(ikr)}{\pi r} 2F(\theta_1, \theta_2, \theta_3) \times \sum_{u_{1,0}=-\infty}^{+\infty} \dots \sum_{u_{1,N-1}=-\infty}^{+\infty} \dots \sum_{u_{2,0}=-\infty}^{+\infty} \dots \sum_{u_{2,N-1}=-\infty}^{+\infty} \dots \sum_{u_{M,N-1}=-\infty}^{+\infty} \times$$

$$\times \left[\prod_{n=0}^{N-1} \prod_{m=1}^M J_{u_{nm}}(c_j q^{(D-3)n}) \right] \exp\left(i \sum_{n=0}^{N-1} \sum_{m=1}^M u_{nm} \phi_{nm}\right) \times \text{sinc}(\varphi_c L_x) \text{sinc}(\varphi_s L_y) + \psi_k, \quad (2)$$

where all designations are presented in [6, 7].

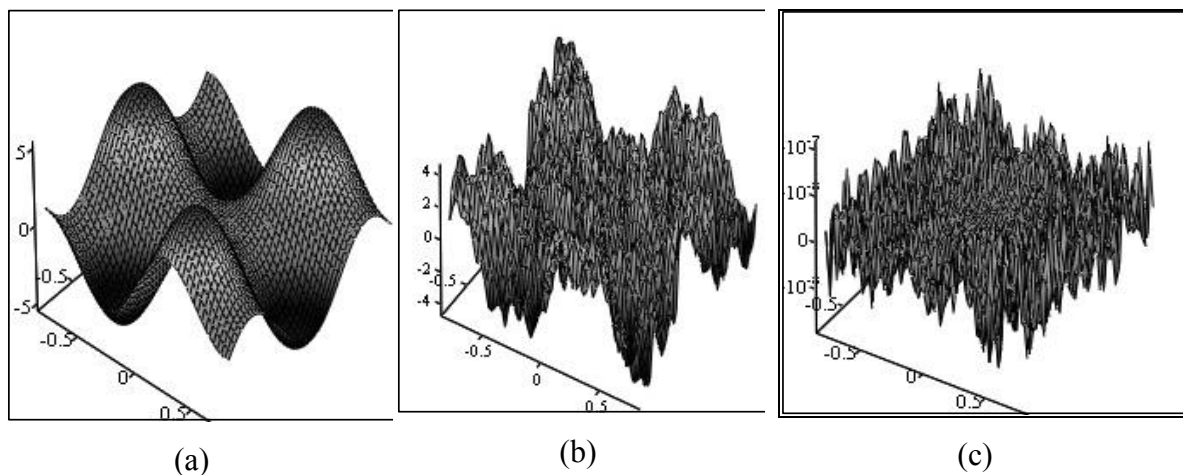


Fig. 1. Examples of Weierstrass function for: a) $N = 2, M = 3, D = 2.01, q = 1.01$; b) $N = 5, M = 5, D = 2.5, q = 3$; c) $N = 10, M = 10, D = 2.99, q = 7$ (c).

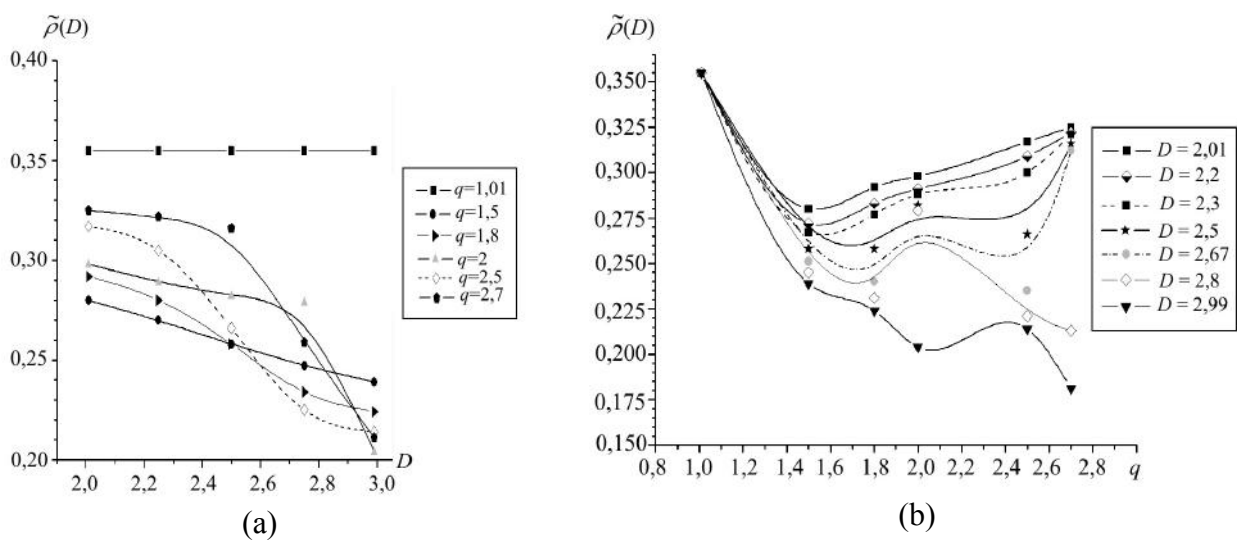
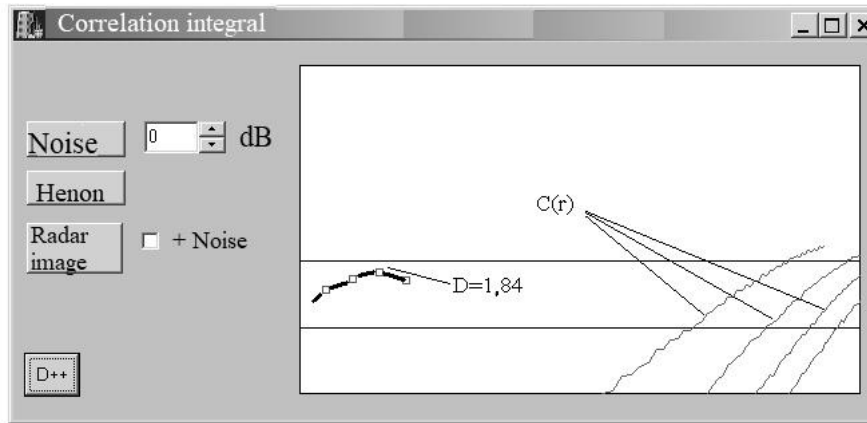


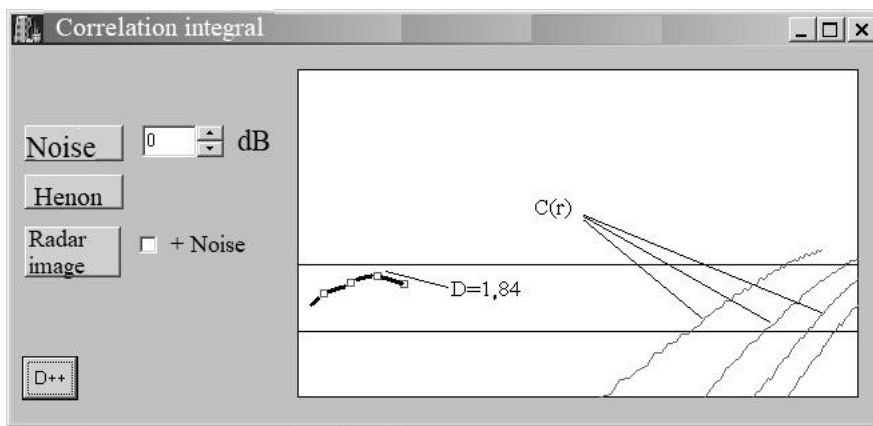
Fig. 2. The averaged correlation interval $\tilde{\rho}$ as a function of D for:
 a) $q = 1.01; q = 1.5; q = 1.8; q = 2; q = 2.5; q = 2.7$ and
 b) as a function of q for $D = 2.01; D = 2.2; D = 2.3; D = 2.5; D = 2.67; D = 2.8; D = 2.99$.

4. Fractals and strange attractors in models of radio wave scattering by plant cover

Processing the enveloping reflected radar signals at a wavelength of 2.2 mm for the first time made it possible to determine the characteristics of a strange attractor controlling millimeter-wave scattering in the phase space [8], see Figure 3a. Radar data were obtained personally by the author at the test site in field experiments as early as in 1979–1980. When reconstructing this attractor from ordered measurements of one variable, it is necessary to construct an embedding space of dimension $m = 2N_0 + 1$ in order to describe all possible topological features of the attractor.



(a)



(b)

Fig.3. Computer screen view with D and $C(r)$ process dependencies:
 (a) – radar reflections from grass (wavelength $\lambda=2.2$ mm); (b) – Gaussian noise.

The value $N_0 \geq \text{int}[D] + 1$ determines the number of differential equations of the 1st order necessary to describe the physical behavior of the dynamical system under study. Here $\text{int}[D]$ is the operation of extracting the integer part of D , and D is the true fractal dimension of the strange attractor. The correlation integral $C(r)$ can also be used as a means of separating deterministic chaos and external white noise. For Gaussian noise (Figure 3b) there is no tendency to saturation. Therefore, the attractor of infinite dimension corresponds to it. This distinction is widely used in processing time realizations of unknown origin.

The following values were obtained (Figure 3a): $D = 1 + 1,84 \approx 2,8$; the embedding dimension $m=7$; Lyapunov index $\lambda_1 \geq 0,6$ bits/c; the prediction time $\tau_{\max} \approx 1.7$ s at correlation time of the reflected signal intensity $\tau \approx 210$ ms and a wind speed of 3 m/s. Therefore, if current conditions are measured with an accuracy up to 1 bit, then all the predictive power in time will be lost in about 1.7 s. At the same time, the prediction interval τ_{\max} of the intensity of the radar signal exceeds the classical correlation time by about 8 times.

The data obtained together with the family of fractal distributions underlie a new dynamic model of radio signals scattered by plant cover. The proposed dynamic model of the electromagnetic wave scattering by earth covers is fundamentally different from the existing classical models. It has a finite number of degrees of freedom, describes the processes of non-

Gaussian scattering and for the first time injects the prediction interval of the intensity of the received radar signal, as well as its fractal characteristics (signatures).

5. "Distributed intelligence" in the team interaction of UAVs

Unmanned aerial vehicles (UAVs) are currently used to solve a wide range of scientific and practical problems and can become the main element in the formation of a common information field [9-11]. The solution of difficult complex tasks is possible only as a result of group use of UAVs. The team is a network of a certain number of similar or different types of UAVs, united by a common target. In practice, it is possible to implement a significant number of types of UAV team flights. The classification of UAV team flights in the process of accomplishing preset tasks is shown in Figure 4. Fractal UAV groupings and fractal flight paths of UAV are also presented there.

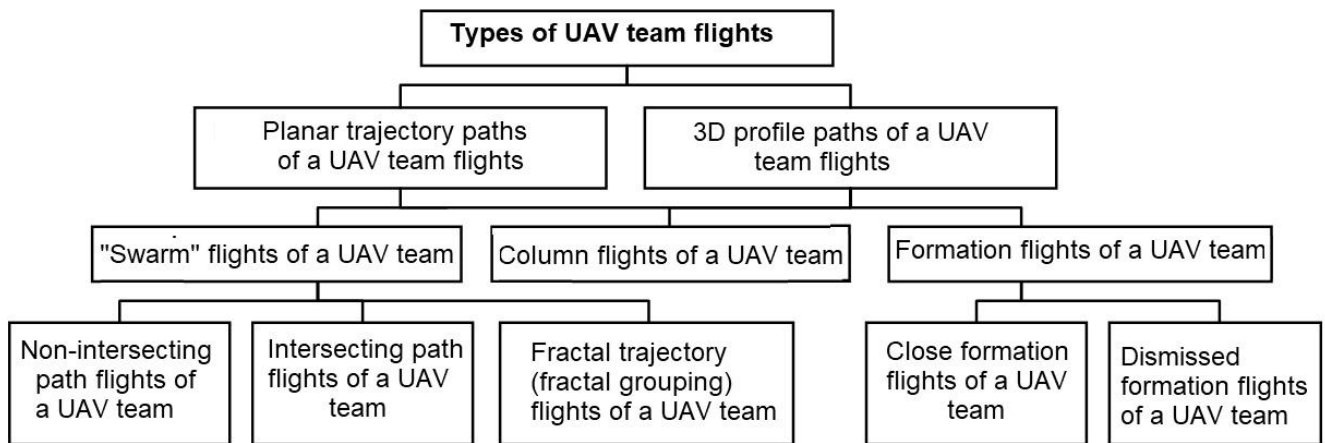


Fig.4 Classification of UAV team flights

In real conditions, UAVs operate in a non-deterministic, unpredictable environment and under counter operation conditions. Each of the UAV performs a series of actions aimed at solving a common task. A parallel should be drawn with biological research that is trying to answer the question of the emergence of cooperative behavior in the process of evolution or the so-called evolutionary strategy [11]. Intellectual or population algorithms (methods) relate to the class of stochastic search optimization algorithms. Population algorithms refer the class of heuristic algorithms for which convergence to a global solution has not been proven, but it has been established experimentally that they provide a fairly good solution.

To teach the UAV to fly like a flock of birds or a swarm of bees is a relevant problem. Then we can control one apparatus, and the rest will be controlled by this technology. And if the leader dies for some reason, the function of the pack leader automatically proceeds to the next vehicle. And so it will be as long as the last instrument operates. For a complex network of multiple micro-(nano-) UAVs, it conducts global monitoring of the territory and objects located on it. The task can be considered within the framework of the concept of a distributed measuring environment, when each point of a certain dynamic environment is capable of performing sensory, measuring and informational functions.

The fractal-graph approach makes it possible to study the growth of complex networks and provides a method for manipulating such networks at the global level, without using a detailed description. At the same time, it turns out that an excessive number of sensors (UAV) does not guarantee their optimal distribution in/along the non-deterministic environment under study. The introduction of the fractal topology of such networks, taking into account the configuration of the study area, will make for monitoring it with the detection of objects, more accurately and using less means (number of UAVs).

6. Waves in disordered large fractal systems

The issues of the general theory of multiple scattering of electromagnetic waves in fractal discrete randomly inhomogeneous media based on modifications of the classical Foldy-Tverskoy theory are considered in detail in [12]. The integral equation for the coherent field and the second moment of the field for the fractal scattering medium respectively are:

$$\begin{aligned} \langle \psi^a \rangle &= \phi_i^a + \int u_s^a \phi_i^s w(\mathbf{r}_s) d\mathbf{r}_s + \iint u_s^a u_t^s \phi_i^t w(\mathbf{r}_s) w(\mathbf{r}_t) d\mathbf{r}_s d\mathbf{r}_t + \iiint u_s^a u_t^s u_m^t \phi_i^m w(\mathbf{r}_s) w(\mathbf{r}_t) w(\mathbf{r}_m) d\mathbf{r}_s d\mathbf{r}_t d\mathbf{r}_m + \dots, \\ \langle \psi^a \psi^b \rangle &= \langle \psi^a \rangle \langle \psi^b \rangle + \int v_s^a v_s^b \langle \psi^s \rangle^2 w(\mathbf{r}_s) d\mathbf{r}_s + \int v_s^a v_s^b \langle \psi^s \rangle \langle \psi^t \rangle^2 w(\mathbf{r}_s) w(\mathbf{r}_t) d\mathbf{r}_s d\mathbf{r}_t + \\ &+ \int v_s^a v_s^b \langle \psi^s \rangle \langle \psi^t \rangle \langle \psi^m \rangle^2 w(\mathbf{r}_s) w(\mathbf{r}_t) w(\mathbf{r}_m) d\mathbf{r}_s d\mathbf{r}_t d\mathbf{r}_m + \dots, \end{aligned} \tag{3}$$

where $v_s^a = u_s^a + \int u_t^a v_t^s w(\mathbf{r}_t) d\mathbf{r}_t$, $w(\mathbf{r}_i) = (\mathbf{r}_i / \mathbf{r}_0)^{E-D}$, other notations are given in [12].

The data of [12] aim to summarize the study of how the problem of multiple scattering of waves on an ensemble of particles is solved and to what extent it is possible to obtain a solution to this problem for the modern theory of multiple scattering of waves in fractal discrete randomly inhomogeneous media when solving problems of modern radiolocation. On the basis of formula (3), the basic concepts of a fractal medium are introduced and the formulation of the mathematics of multiple scattering of electromagnetic waves in a fractal medium is given simultaneously with the physics of the scattering process. The constructed modification of the multiple scattering theory made it possible to include in the consideration the values of the fractal dimension D and the fractal signature $D(r,t)$ of an unordered large fractal system.

7. The radar equation for a fractal target

Calculate the value of the backscattered signal from the fractal medium [12] using the classical radar equation. The received signal power P_s is determined by the radar equation. Here we have two cases:

a) for the far-field region and the two dimensional fractal target (Euclidean dimension $E=2$); then

$$P_s \propto \frac{1}{r^{4-D}}. \tag{4}$$

b) for the far-field region and the three dimensional fractal target (Euclidean dimension $E=3$); then

$$P_s \propto \frac{1}{r^{5-D}}, \tag{5}$$

where r is the distance to the target.

The results (4) and (5) show that the reflected radar signal can be used to estimate the fractal dimension D of the sounded fractal medium or fractal target (such as a

Similarly, on the base of (3)-(5), it is possible to obtain a solution for anisotropic disordered large fractal systems: fractal cascades put one into another, graphs from fractal chains, percolation systems, nanosystems, space debris, clusters of unmanned aerial vehicles or small space vehicles (SSV), of mini- and microclasses as well, dynamic synthesized space antenna groups (cluster apertures), low-observable high-altitude pseudo-satellites (HAPS), space-distributed space systems (clusters) from SSVs for solving problems of emergency situations monitoring, etc.

Conclusion

Fractal effects arising from propagation and scattering of waves in randomly inhomogeneous media are considered. Radar equation for sounding a fractal object is detailed. Models based on fractals and strange attractors for radio wave scattering by plant cover are proposed.

This research continues the cycle of studies in order to establish the application of the fractal theory, physical scaling and fractional operators in issues of radio physics and radio electronics, started by the author for the first time in the USSR at the IRE of the USSR Academy of Sciences in the late 1970s. Careful bibliographic studies prove the author's complete and absolute priority in the world in all "fractal" areas in radio physics and radio electronics. This article, together with [13], provides basic information on the current state in the application of the fractal theory and fractional calculus for innovative technologies.

Acknowledgments

Supported by the project "Leading Talents of Guangdong Province", № 00201502 (2016-2020) in the Jinan University (China, Guangzhou).

REFERENCES

- 1 Potapov A.A. *Fractals in radiophysics and radiolocation*. Moscow, Logos. 2002, 664 p.
- 2 Bunkin B.V., Reutov A.P., Potapov A.A. et al. *Issues of promising radiolocation* (joint monograph). Moscow, Radio Engineering, 2003, 512 p.
- 3 Potapov A.A. *Fractals in radiophysics and radiolocation: Sample Topology*. 2nd, revised and enlarged edition. Moscow, University Book, 2005, 848 p.
- 4 Potapov A.A. *Fractals and chaos as a basis for new innovative technologies in modern radio systems. Supplement to the book: Kronover R. Fractals and chaos in dynamic systems*. Moscow, Technosphere, 2006. pp. 374 – 479.
- 5 Frish U. *Turbulence. Heritage of A.N. Kolmogorov*. Moscow, FASIS, 1998, 346 p.
- 6 Potapov A.A., Laktyunkin A.V. Theory of wave scattering by a fractal anisotropic surface. *Nonlinear world*. 2008, Vol. 6, No.1, pp. 3 – 36.
- 7 Potapov Alexander A. *On the Indicatrixes of Waves Scattering from the Random Fractal Anisotropic Surface. Fractal Analysis - Applications in Physics, Engineering and Technology*. Ed. Fernando Brambila. Rijeka: InTech, 2017, pp. 187 – 248.
- 8 Potapov A.A., German V.A. Effects of Deterministic Chaos and Strange Attractor in the Radar of Dynamic Systems of the Vegetative Cover Type. *Technical Physics Letters*. 2002, Vol. 28, No. 7, pp. 586 – 588.
- 9 Gonzales D., Harting S. *Designing Unmanned Systems with Greater Autonomy: Using a Federated, Partially Open Systems Architecture Approach*. Santa Monica, Calif: RAND, 2014, 96 p.
- 10 Bystrov R.P., Gvozdev A.E., Nemtsov A.V., Potapov A.A., Sheremet I.B. *The current state and prospects of development of unmanned aerial vehicles of the leading states of the world*. Moscow, Central Research Institute of the Ministry of Defense of Russia. 2016, 399 p.
- 11 Potapov A.A. On the Fractal Theory Application in Adaptive Population Methods of Formation of Dynamical Groups of Unmanned Aerial Vehicles and in Processing of Incoming Information in Respect to its Effective Application Theory. *Eurasian Physical Technical Journal*. 2017, Vol. 14, No. 1(27), pp. 6 – 17.
- 12 Potapov A.A. Waves in Large Disordered Fractal Systems: Radar, Nanosystems, and Clusters of Unmanned Aerial Vehicles and Small-Size Spacecrafts. *Journal of Communications Technology and Electronics*. 2018, Vol. 63, No. 9, pp. 980 – 997.
- 13 Potapov A.A. On the issues of fractal radio electronics: Part 1. Processing of multidimensional signals, radiolocation, nanotechnology, radio-engineering elements and sensors. *Eurasian Physical Technical Journal*. 2018, Vol. 15, No. 2(30), pp. 5 – 15.

UDC 532.1+539.19+541.6

COMPUTER SIMULATION FOR THE FLOW OF HIGH-TEMPERATURE MELTS

Kazhikenova S.Sh.

Karaganda State Technical University, Karaganda, Kazakhsnan, sauleshka555@mail.ru

One of the most constructive methods of studying physical properties of melts is computer simulation. This is explained by a large theoretical and applied value of the information obtained with respect to the transfer coefficients, in particular, bulk and shear viscosities. However, for specific calculations there is needed a detailed physical-and-mathematical apparatus. Objective - implementation methods of numerical solution of hydrodynamic equations involving correlation functions viscosity determined using quantum potentials study of the distribution profile of melt flow rate, to obtain the most simple regularization of the original system of hydrodynamic equations containing a physical sense. To implement such a program we will use methods of statistical physics. To the moment of the proposed studies, there were known the ways of solving equations of hydrodynamics for low-temperature liquids without taking into account bulk viscosity. In this paper there is proposed a mathematical model for the flow of high-temperature melts taking into account the nature of the short-range order in them and considering the second viscosity coefficient by the methods of statistical physics. Built distribution of melt flow rate based on the numerical experiments. An algorithm for the numerical integration of the hydrodynamic equations to predict the technological parameters of the filling metal melts.

Keywords: viscosity, potential, computer simulation, melt, the hydrodynamic equations.

Introduction

The method of computer simulation is considered as one of the most constructive methods for studying physical properties of melts. This is explained by a large theoretical and applied value of the information obtained with respect to the transfer coefficients, in particular, bulk and shear viscosities. There has been compiled a program for the numerical solution of equations of hydrodynamics for metal melts. There has been tested a program for solving the Dirichlet problem for the Poisson equation. Based on the theoretical studies carried out there have been calculated parameters determining the relationship between viscosity and interatomic potential. The relationships found permit determine the average values of any physical parameters, in particular, the values of shear and bulk viscosities. Scientific novelty - correlation functions viscosity justified in terms of the quantum-statistical method. The interrelation between the correlation functions with the radial distribution. The numerical scheme, which has good convergence for hydrodynamics equations melts. Built regularization source systems of differential equations by approximating the incompressible melt. Galerkin method is implemented, ensuring the correctness of the study of boundary value problems for an incompressible viscous flow both numerically and analytically.

1. Theoretical part

The methods of quantum statistical physics make it possible to express the coefficients of shear and bulk viscosities by means of correlation functions [1, 2]. This makes it possible to reveal the physical nature of the structure of matter through the operators of the second quantization, so that a powerful apparatus of quantum physics can be connected for the studies. One of the most constructive methods for studying physical properties of melts is computer simulation.

Let us consider one of the variants of splitting hydrodynamic equations with reference to calculation of the melt flow in a flat channel in accordance with Figure 1. Such a melt flow can be described by the following equations of the dimensionless form:

$$\frac{\partial u}{\partial x} + \frac{\partial v}{\partial y} = 0, \quad (1)$$

$$\frac{\partial u}{\partial t} + \frac{\partial u^2}{\partial x} + \frac{\partial uv}{\partial y} + \frac{\partial p}{\partial x} = \frac{1}{\text{Re}} \left(\frac{\partial^2 u}{\partial x^2} + \frac{\partial^2 u}{\partial y^2} \right), \quad (2)$$

$$\frac{\partial v}{\partial t} + \frac{\partial v^2}{\partial y} + \frac{\partial uv}{\partial x} + \frac{\partial p}{\partial y} = \frac{1}{\text{Re}} \left(\frac{\partial^2 v}{\partial x^2} + \frac{\partial^2 v}{\partial y^2} \right), \quad (3)$$

where $\text{Re} = \rho u_0 H / \mu$, H – is the channel width, u_0 – is velocity, ρ – is density, μ – is melt viscosity.

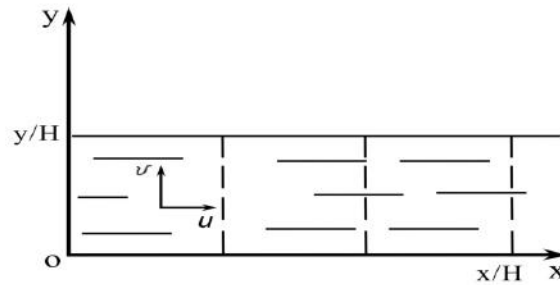


Fig.1. Model of the melt flow in a flat channel

Equations (1) – (3) are integrated at the following initial boundary conditions:

$$\text{at } t = 0, \quad 0 \leq x \leq \frac{\ell}{H}, \quad 0 \leq y \leq 1: \quad u = 1, v = 0, p = p_0,$$

$$\text{at } t > 0, x = 0, 0 \leq y \leq 1: \quad u = 0, v = 0, p = p_0,$$

$$\text{at } t > 0, x = \frac{L}{H}, 0 \leq y \leq 1: \quad \frac{\partial u}{\partial x} = \frac{\partial v}{\partial x} = 0, \frac{\partial p}{\partial x} = -\beta,$$

$$\text{at } t > 0, y = 0, y = 1, 0 \leq x \leq \frac{L}{H}: \quad u = 0, v = 0, \frac{\partial p}{\partial y} = \frac{1}{\text{Re}} \frac{\partial^2 v}{\partial y^2},$$

where β – is the preset pressure gradient, ℓ – is distance from the input to the bench, L – is the channel full length.

Equations (1) - (3) depend on t and can be solved relative to u, v with the help of known numerical methods. But pressure p is given implicitly, since it does not enter the equations in the form of a derivative with respect to t . To exclude this let us write down equation of continuity (1) in the following form:

$$\frac{\partial w}{\partial t} + \frac{\partial u}{\partial x} + \frac{\partial v}{\partial y} = 0,$$

where $w = p + \frac{1}{2}(v^2 + u^2)$ according to the Bernoulli's law.

Then equations (1) – (3) can be reduced to the following two independent systems of equations (4) and (5) that are given below for consideration:

$$\begin{cases} \frac{1}{2} \frac{\partial w_1}{\partial t} + \frac{\partial u}{\partial x} = 0 \\ \frac{1}{2} \frac{\partial u}{\partial t} + \frac{\partial u^2}{\partial x} + \frac{\partial p}{\partial x} = \frac{1}{\text{Re}} \frac{\partial^2 u}{\partial x^2} \\ \frac{1}{2} \frac{\partial v}{\partial t} + \frac{\partial uv}{\partial x} = \frac{1}{\text{Re}} \frac{\partial^2 v}{\partial x^2}, \end{cases} \quad (4)$$

$$\begin{cases} \frac{1}{2} \frac{\partial w_2}{\partial t} + \frac{\partial v}{\partial y} = 0 \\ \frac{1}{2} \frac{\partial v}{\partial t} + \frac{\partial v^2}{\partial y} + \frac{\partial p}{\partial y} = \frac{1}{\text{Re}} \frac{\partial^2 v}{\partial y^2} \\ \frac{1}{2} \frac{\partial u}{\partial t} + \frac{\partial uv}{\partial y} = \frac{1}{\text{Re}} \frac{\partial^2 u}{\partial y^2}, \end{cases} \quad (5)$$

where $w_1 = p + \frac{u^2}{2}$, $w_2 = p + \frac{v^2}{2}$.

Thus, these two systems of equations allow simulating the melt flow in a flat channel. To solve these systems let's proceed as follows: for given initial conditions system of equations (4) is solved at $y = \text{const}$ for a half-time. The data obtained in this case are used as initial conditions for integrating system of equations (5) at $x = \text{const}$ for the next half-time. At the end of the procedure the obtained data are accepted as the final result. It should be noted that here also it is necessary to split the boundary conditions.

We represent the split boundary conditions in our case for system (4):

$$\begin{aligned} \text{at } x=0: & \quad u=1, v=0, p=0, \text{ for } y, \\ \text{at } x=\frac{L}{H}: & \quad \frac{\partial u}{\partial x} = \frac{\partial v}{\partial x} = 0, \frac{\partial p}{\partial x} = -\beta, \text{ for } y, \\ \text{at } x=\frac{\ell}{H}: & \quad u=0, v=0, \frac{\partial p}{\partial x} = \frac{1}{\text{Re}} \frac{\partial^2 u}{\partial x^2}, \text{ for } 0 \leq y \leq \frac{L}{H}. \end{aligned}$$

Then for system (5):

$$\begin{aligned} \text{at } y=\frac{L}{H}, 0 \leq x \leq \frac{\ell}{H}: & \quad u=0, v=0, \frac{\partial p}{\partial y} = \frac{1}{\text{Re}} \frac{\partial^2 v}{\partial y^2}, \\ \text{at } y=0, \frac{\ell}{H} \leq x \leq \frac{L}{H}: & \quad u=0, v=0, \frac{\partial p}{\partial y} = \frac{1}{\text{Re}} \frac{\partial^2 v}{\partial y^2}, \\ \text{at } y=1, 0 \leq x \leq \frac{L}{H}: & \quad u=0, v=0, \frac{\partial p}{\partial y} = \frac{1}{\text{Re}} \frac{\partial^2 v}{\partial y^2}. \end{aligned}$$

2. Modeling of the melt flow in the inclined gutter

Now let's consider the melt flow in the inclined gutter. A general form of the equations is given in [3]. For a particular design they can be treated and written down as follows. Let's direct the Oz axis along the gutter axis assuming that the gutter design is infinitely long and the melt flow is directed along the gutter axis so that only one of the three velocity components u, v, w , remains. Therefore, let the melt flow be isothermal, then the density ρ and the viscosity coefficient $\mu = \text{const}$.

Therefore, the Navier-Stokes equations can be written in the form:

$$-\frac{1}{\rho} \frac{\partial p}{\partial x} = 0, -\frac{1}{\rho} \frac{\partial p}{\partial y} = 0, w \frac{\partial w}{\partial z} = -\frac{1}{\rho} \frac{\partial p}{\partial z} + \gamma \left(\frac{\partial^2 w}{\partial x^2} + \frac{\partial^2 w}{\partial y^2} + \frac{\partial^2 w}{\partial z^2} \right), \frac{\partial w}{\partial z} = 0. \quad (6)$$

Thus, as can be seen from system of equations (6), velocity represents a function only of the x, y , coordinates. In addition, the pressure function p is a function of z . On the basis of (6) we obtain the equation:

$$\frac{dp}{dz} = \mu \left(\frac{\partial^2 w}{\partial x^2} + \frac{\partial^2 w}{\partial y^2} \right). \quad (7)$$

The right part of (7) represents a function of x, y , and the left part is a function of z . From the basic aspects of hydrodynamics it follows:

$$\frac{dp}{dz} = -\frac{\Delta p}{\ell},$$

where Δp – is pressure drop on the arbitrarily selected section, ℓ – is the gutter length.

In addition, due to the presence of the melt free surface in the gutter, pressure is equal to the atmospheric pressure [4]. Since the gutter is inclined to the horizon at some angle α , there appears a volume force which projection on the Oz axis is equal to $F_z = g \sin \alpha = \frac{\Delta p}{\ell}$. Then equation of motion (7) in the Oz direction becomes:

$$\mu \left(\frac{\partial^2 w}{\partial x^2} + \frac{\partial^2 w}{\partial y^2} \right) + \rho g \sin \alpha = 0. \quad (8)$$

To solve this equation we need some boundary conditions. These conditions will be determined by the adhesion of the melt to the bottom of the gutter and the absence of friction on the melt free surface. We denote the depth of the flow as h_1 , the width of the gutter as h_2 . Then the boundary conditions of the problem are written as follows:

$$w = 0 \text{ at } y = 0, \quad \frac{\partial w}{\partial y} = 0 \text{ at } y = h_1, \quad \frac{\partial w}{\partial x} = 0 \text{ at } x = h_2. \quad (9)$$

Thus, equation (8) with boundary conditions (9) will describe the process of the melt flow in concrete gutter type structures. This model is made for the smelting equipment of the SCR – 2000 line which diagram is presented in accordance with Figure 2.

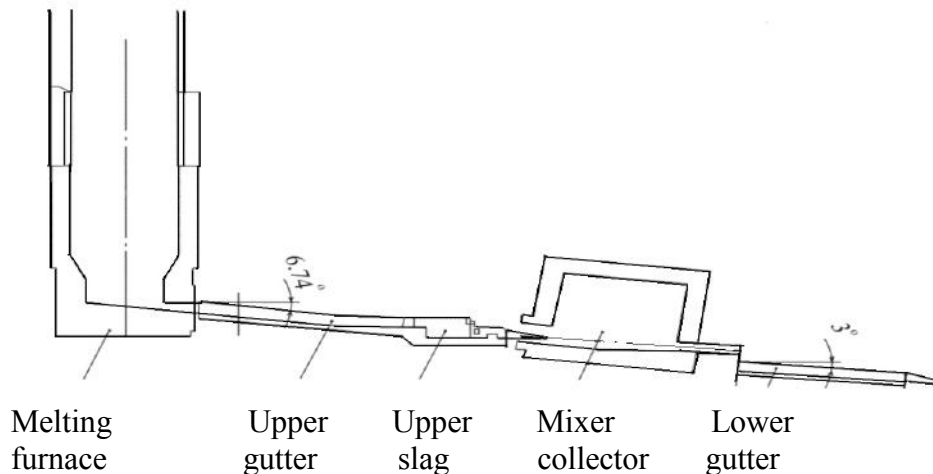


Fig.2. Diagram of the SCR – 2000 line melting equipment arrangement

The calculations have been performed for a lower gutter with the inclination angle of 3° . The section of the lower gutter is presented in accordance with Figure 3 and shows the level of the melt.

Numerical parameters have been determined according to the following calculations: the segment area is $S = \frac{[lr - a(r - h)]}{2}$ where l – is the arc length, a – is bisecant, h – is the segment sagitta:

$$a = 83\text{mm}, h = 18\text{mm}, l \approx \sqrt{a^2 + (16h^2/3)} = \sqrt{83^2 + (16 \cdot 18^2/3)} = 92,8\text{mm}.$$

It follows that:

$$S = \frac{\left[92,8 \cdot \frac{115}{2} - 83 \left(\frac{115}{2} - 18 \right) \right]}{2} = 1029\text{mm}^2.$$

Then, the second flow rate of the melt is: $Q = 3.61 \frac{\text{kg}}{\text{s}}$. Taking this into account, it is possible to determine the average melt flow velocity that is equal to $v_{cp} = 0.45 \frac{\text{m}}{\text{s}}$.

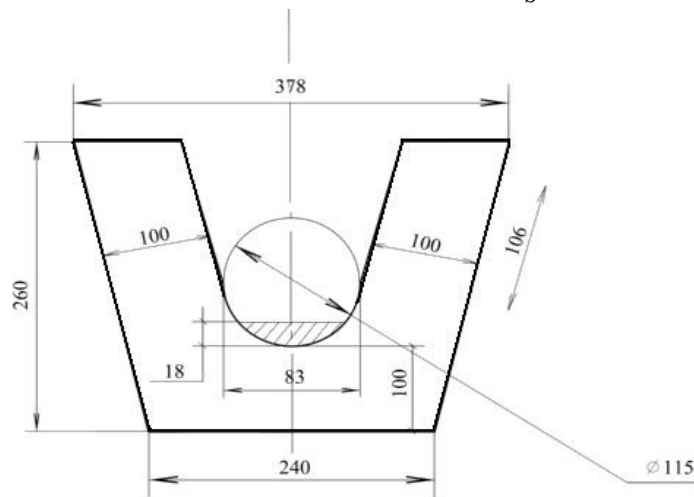


Fig.3. Lower gutter section

The constant steps $\Delta x = \Delta y = 0,02$. were used in the calculations. The time step in the calculations was selected to be equal to $\Delta t = 0,001$. The established results for velocity profiles v and u of the melt flow in a flat channel are shown in Figure 4.

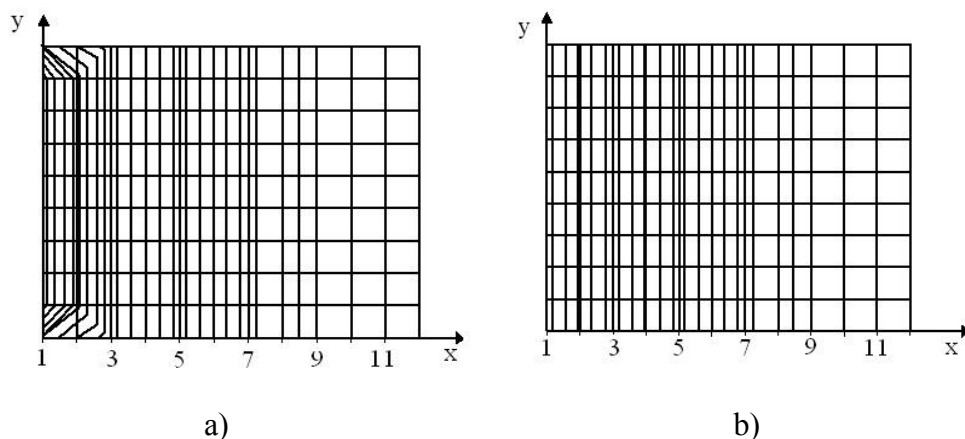


Fig.4. Profiles of: a) – transverse v and b) – longitudinal u velocities

Achieving the steady flow required 3000 steps. The analysis of the results shows the following facts regarding the accuracy of the numerical calculations used. Firstly, when calculating the flow in the input grid cell, the computational error leads to the mass loss of 8-9%. As soon as we reduce the cell size by 10 times, the mass loss is reduced to 4-6%. When calculating with great accuracy, taking into account the features of the boundary conditions, a special numerical scheme was required.

Secondly, the maximum velocity in the central current line is equal to $0.63 \frac{m}{s}$.

This value is approximately 15% higher than the experimental value. The obtained results show that the proposed computational scheme is quite economical and can be used without special problems to calculate the flow for sufficiently small Reynolds numbers. The analysis of the data obtained shows that replacing the continuity condition with an equation for Poisson type pressure, as done in [3], leads to a numerical scheme free from a complicated computational procedure. As it is shown in [5], molten metals can be represented as two-component liquids that consist of ionic and electronic components. This statement permits to apply the virial theorem, thereby assessing the part of the pressure associated with the dynamics and interaction of the ion subsystem, i.e.:

$$p_u = \frac{1}{3\Omega} \left\{ 2K - \sum_{i<j} R_{ij} \frac{\partial V}{\partial R_{ij}} + R_S \frac{\partial V(R_{ij})}{\partial R_S} \right\},$$

where K is kinetic energy.

At this full pressure is determined by the sum of the ion gas pressure p_u and the electronic gas pressure p_{eg} , i.e.: $p = p_u + p_{eg}$.

The ways of their calculation are shown in [5]. The ion gas pressure p_u will be written down in an integral form taking into account the radial distribution function of the atoms $R(r)$. Then for p_u we obtain:

$$p_u = \frac{1}{6\Omega} \int_0^\infty R(r) \left[R \frac{\partial V}{\partial R} + R_S \frac{\partial V}{\partial R_S} \right] dR + \frac{KT}{\Omega}.$$

In this case, it is necessary to pay special attention to the $\frac{\partial V}{\partial R_S}$ behavior because $V(R, R_S)$ is a function of the distance, as well as the $\Omega = \Omega(R_S)$ function that results from the dielectric constant. It is known that the dielectric constant characterizes indirect interaction of ions from the screening electronic subsystem. Thus, the equilibrium state must be considered simultaneously for both subsystems, ionic and electronic.

On the basis of the "sum of compressibility rules" there can be determined how much the model of the molten system is self-consistent. If the value of the volume modulus is determined correctly, the reciprocal value is equal to compressibility. Compressibility is important when considering physical and chemical properties of molten metals. On the basis of [5] it can be asserted that in a crystalline substance the bulk modulus of elasticity is equal to the energy derivative by volume. The static modulus must be coordinated with the dynamic modulus. The dynamic modulus is calculated from the phonon dispersion relation in the long-wave approximation. Consequently, it is closely related to the interatomic interaction. This assertion is the essence of the compressibility rule and is well verified for crystalline metals [5]. Further studies have shown that the sum rule is not completely satisfied for the model of metals constructed by perturbation theory in the second order in terms of empirical potentials. Then the terms of the third and fourth orders appearing in the dynamic matrix give the second-order contribution. The discrepancy results from inclusion of these contributions only when calculating static module and neglecting them when calculating dynamic module.

As it is shown in [6], the inclusion of the higher terms of expansion in the construction of the dynamic matrix approximates the experimental data to theoretical data. This is logical, since the

higher terms of expansion correspond to dispersion interaction. In addition, it can be established that neglecting the dependence of the pair potentials on density results in the dynamic volume modulus β_{din} being the one calculated in the computer model. Taking into account self-consistency, the static modulus can be equal to the dynamic modulus. Calculations carried out for tin have shown that for experimental reconciling the calculated static modulus β_{st} it is necessary to vary experimentally the Hartree energy. But with such a variation the dynamic modulus β_{din} that is well coordinated with the experiment turns out to be too high. A possible explanation for this is that the terms of the third and fourth orders become more important in the dynamic matrix in the region for small q . In this case, in order to maintain the agreement with the experiment, it is necessary to modify the pseudopotential in the indicated region. In this case, the variation of the Hartree energy will correspond to the modified pseudopotential. This is evidenced by the fact that the values obtained for tin turned out to be equal to $3.5 \cdot 10^{-11} \frac{m^2}{N}$.

The data are in good agreement with the experimental data within 10%. These assumptions make it possible to estimate the relaxation time of structural viscosity (that is, bulk viscosity). According to Ya.I. Frenkel, the time of the settled life of an atom is $t = 10^{-11} s$. This value agrees well with the relaxation time of bulk viscosity found. According to the hole theory, it can be assumed that volume deformation of the melt is composed of two types of deformation. The first is instantaneous and delayed. The second is associated with the changing number of holes during the melt motion. The delayed part of the compressibility can be calculated from the formula:

$$\beta_{del} = \frac{\Delta V^2}{VRT} e^{-\Delta H/RT},$$

where ΔV – is a change of the hole volume, ΔH – is the enthalpy increment due to the hole formation.

Then, if the delayed part of compressibility is known, then by the formula given in [7], it is possible to determine bulk viscosity:

$$\mu_V = \frac{t}{\beta_0},$$

where β_0 is equilibrium compressibility, t is the delay time.

3. Results and discussion

Thus, knowing the β_0 value, it is possible to determine the value of bulk viscosity, the nature of the copper melt flow is completely determined by the presence of the melt viscosity, the theoretical and experimental [8] values of which are presented in accordance with Figure 5. Taking into account shear and bulk viscosities of the copper melt, the distribution of flow velocities in the lower gutter at temperatures of 1358 K, 1398 K, 1438 K, 1478 K, 1518 K, 1558 K, 1598 K, 1638 K in projections onto the XOY plane, as well as in the XYZ space are presented in accordance with Figures 6-13 and Appendix B. It can be seen that the lines of constant velocity, isovels, vary from $0.64 \frac{m}{s}$ up to $0.01 \frac{m}{s}$.

$$\mu_{sh} = \rho_0 k_B T \left[1 + \frac{4}{15} I_1 + \frac{1}{15} I_2 \right] \tau, \mu_V = \rho_0 k_B T \left[\frac{3}{5} - \frac{2}{9} I_1 + \frac{1}{9} I_2 \right] \tau - k_0 \tau, \quad (10)$$

Moreover, the maximum flow velocity is reached at the surface itself, and at the bottom of the gutter it is practically zero, that is completely consistent with the conditions of equations (6), (7).

The average value of the isovelocity contour is approximately equal to the average melt flow rate

$$v \approx 0,40 \frac{m}{s}.$$

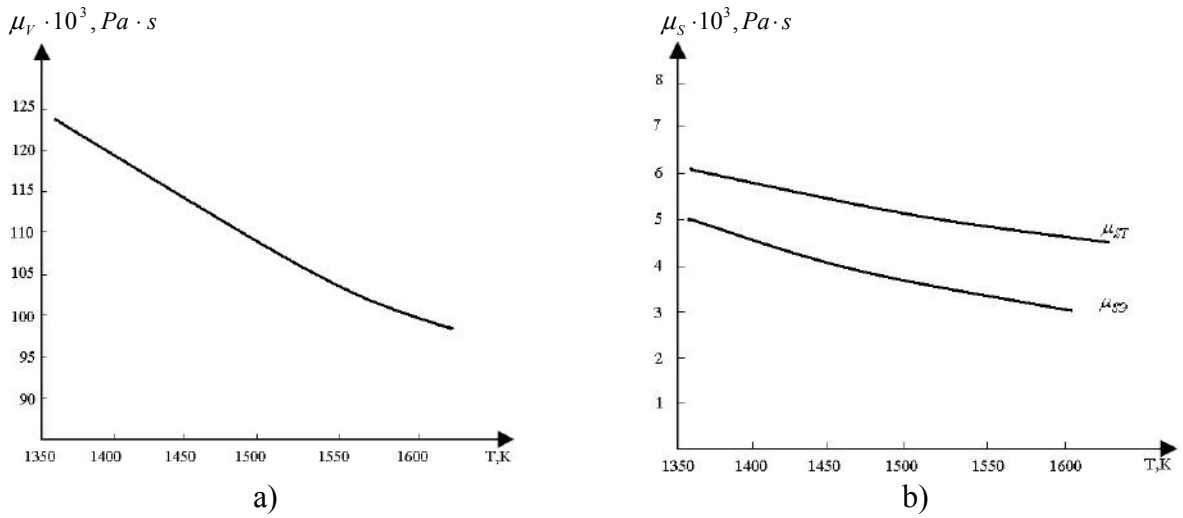


Fig.5. a) Theoretical value of bulk viscosity; b) experimental $\mu_{S\ominus}$ [8] and theoretical values of shear viscosity according to formulas (10).

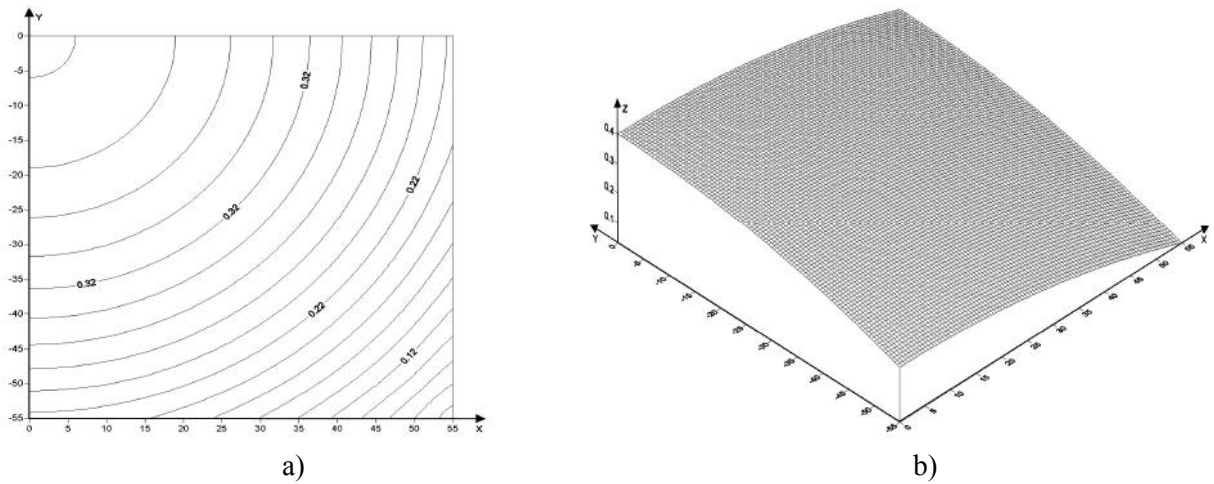


Fig.6. Velocity contour: a) and surface; b) at 1358 K

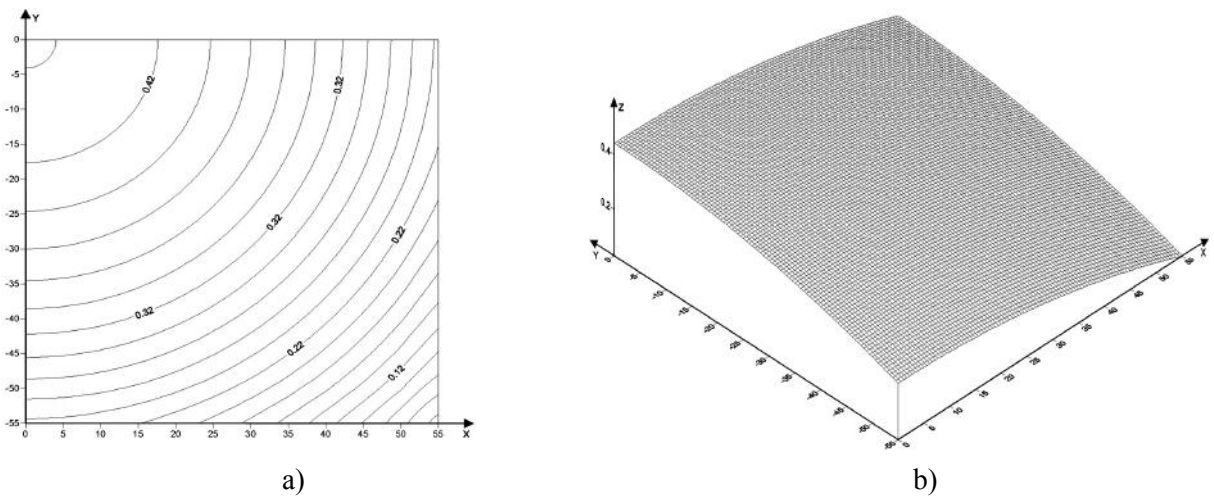


Fig.7. Velocity contour: a) and surface; b) at 1398K

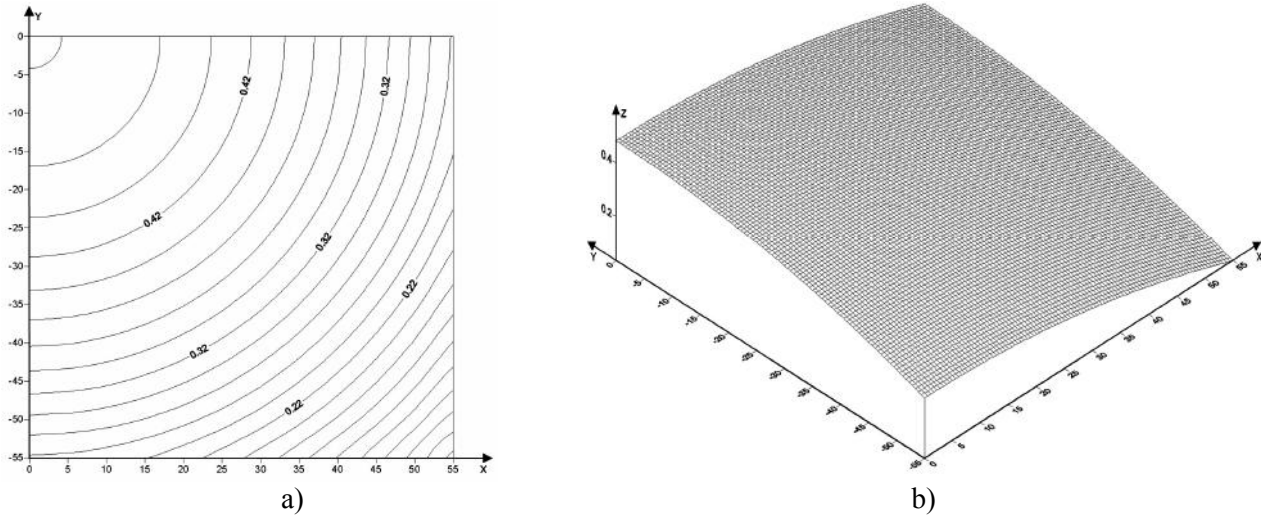


Fig.8. Velocity contour: a) and surface; b) at 1438K

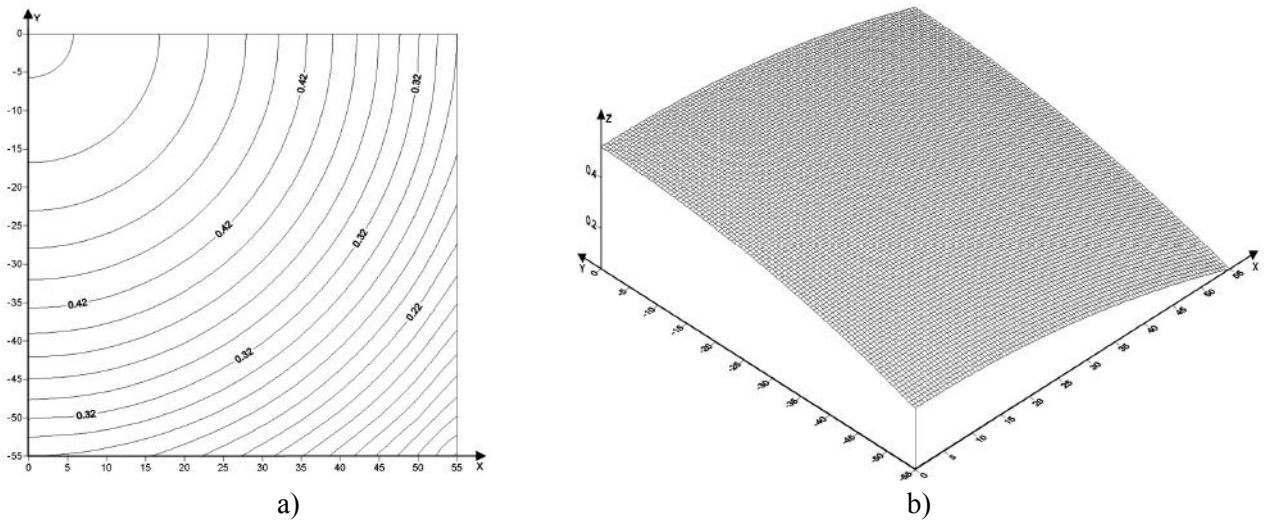


Fig.9. Velocity contour: a) and surface; b) at 1478K

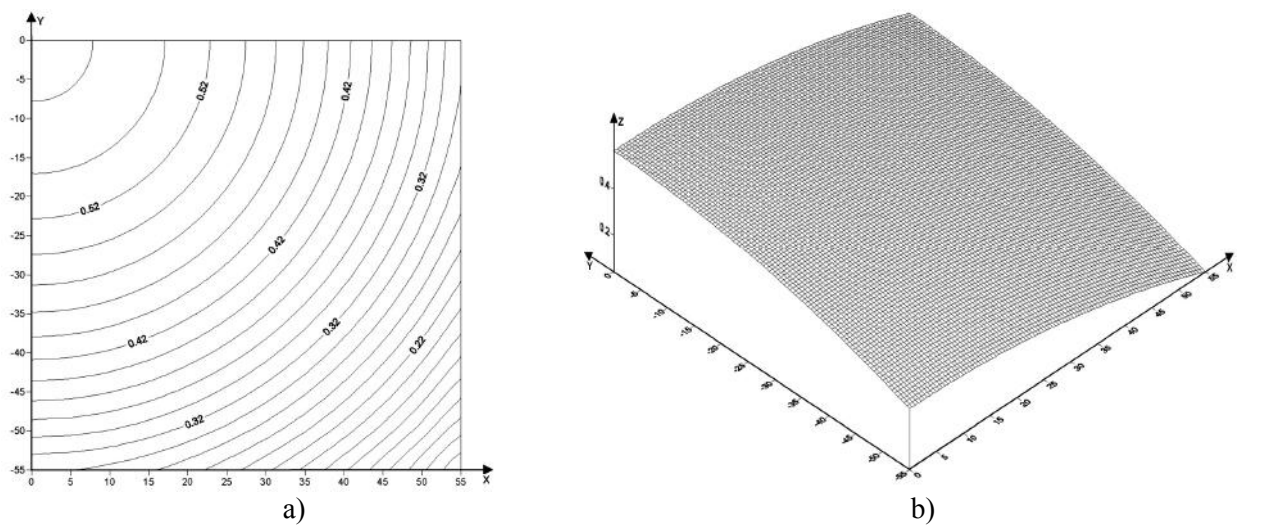


Fig.10. Velocity contour: a) and surface; b) at 1518K

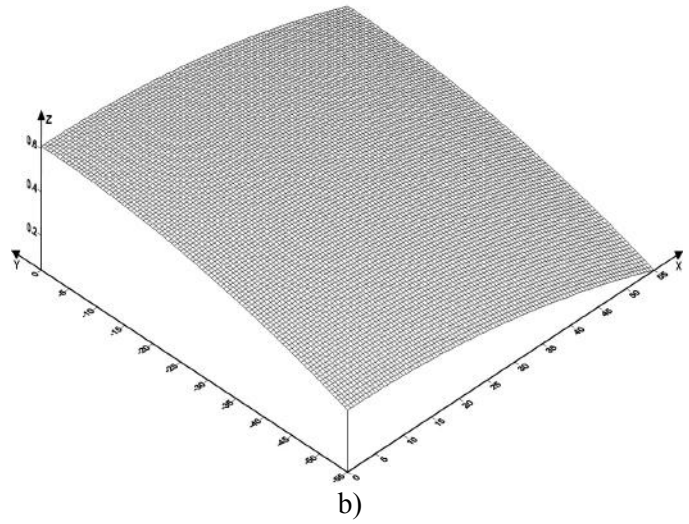
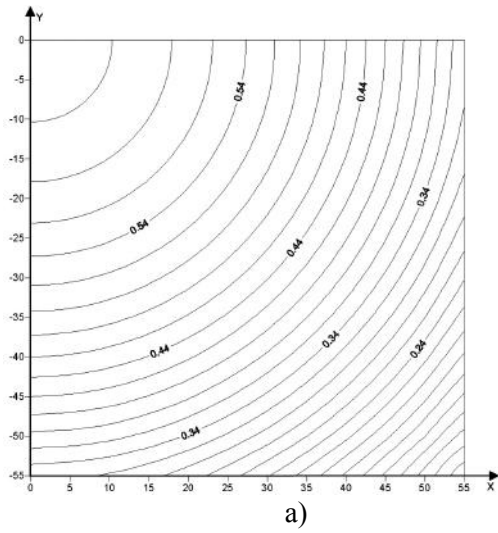


Fig.11. Velocity contour: a) and surface; b) at 1558K

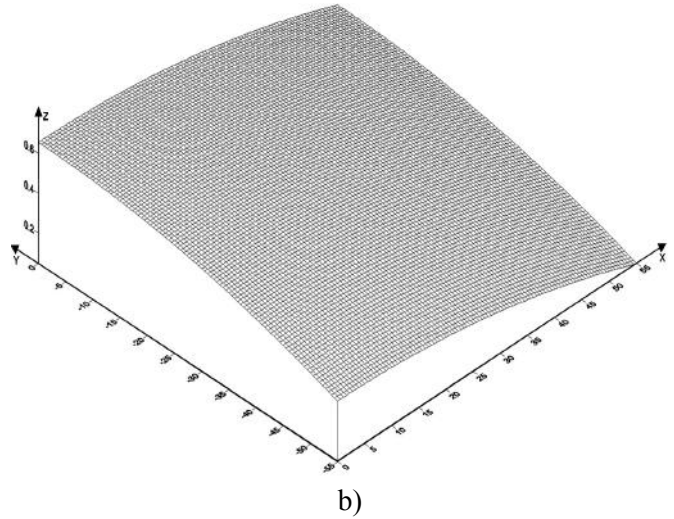
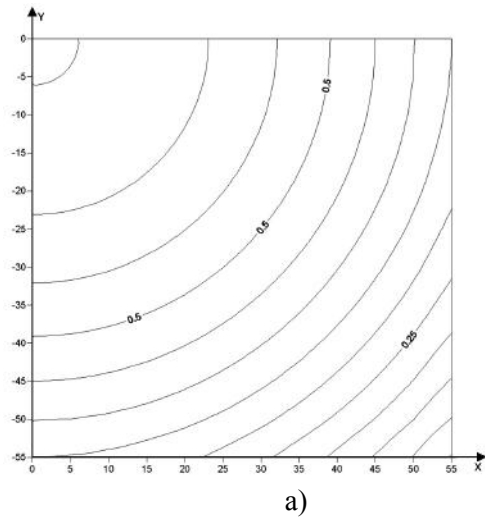


Fig.12. Velocity contour – a) and surface – b) at 1598K

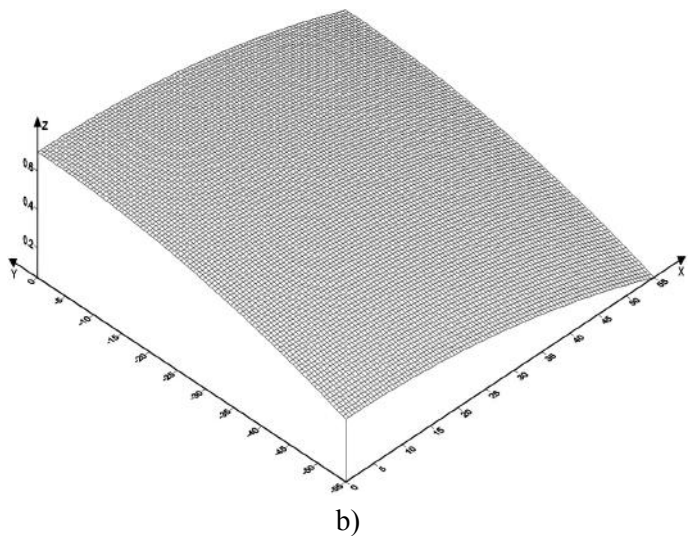
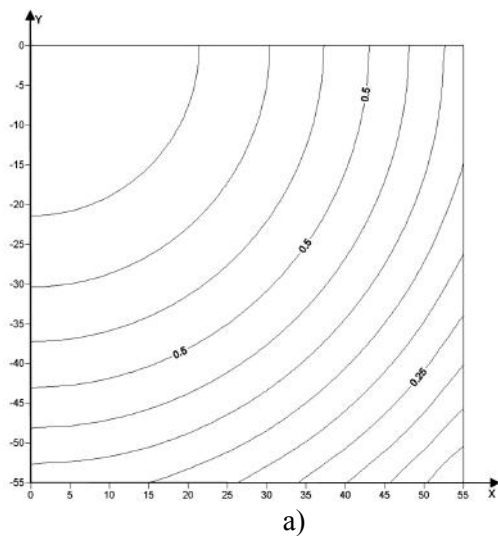


Fig.13. Velocity contour: a) and surface; b) at 1638K

The calculation step for all temperatures remained constant. According to the logic of constructing isovelocity contours, the number of them must remain constant. But in this case the situation is different. The number of contours at the corresponding temperatures is as follows:

| | | | | | | | | |
|------------------------|------|------|------|------|------|------|------|------|
| T, K | 1358 | 1398 | 1438 | 1478 | 1518 | 1558 | 1598 | 1638 |
| n – number of contours | 19 | 21 | 23 | 24 | 26 | 28 | 12 | 12 |

These data show that the number of contours passes through the maximum at the temperature of 1558 K. At lower temperatures, for example at 1358 K, as well as at high temperatures, for example at 1598 K, the velocity distribution is not so dense. This may be due to the fact that the melt near the melting point is not homogeneous due to the existence of formation clusters in it. Heterogeneity at temperatures of 1598 K and above is associated with the thermal loosening of the molten metal structure and is not technologically expedient, since it leads to forming mechanical defects of finished products.

Conclusion

This method of calculation can be used to calculate the motion of a copper melt during filling from converters, from anode furnaces, as well as in the line of continuous casting and rolling in the production of copper wire rod. It is noteworthy that this temperature is close to the optimum copper pouring temperature at JV Kazkat in Zhezkazgan [9].

Thus, theoretical calculations of the optimum flow temperature (viscosity) in the equilibrium system taking into account the melt velocity are consistent being in the interval of the 1423-1558 K optimum, close to the real melting temperatures in industrial conditions.

REFERENCES

- 1 Regel A.R., Glazov V.M. Physical properties of electron melts. Moscow, 1980, 296 p. [in Russian]
- 2 Akhiezer A.I., Petleminsky S.V. Methods of statistical physics. Moscow, RFM Science, 1977, 368 p.
- 3 Kazhikenova S. Sh. Monitoring of Process Flow Diagrams in the Production of Ferrous Metals. *Refractories and Industrial Ceramics*. Springer Link, 2016. Vol.57, No. 4, pp. 360 – 363. <http://link.springer.com/article/10.1007/s11148-016-9984-8>
- 4 Maksimov Ye.V, Torgovets A.K. Mechanics of liquids, gases and friable medium. Almaty, RIC, 1997, 254 p. [in Russian]
- 5 Suleimenov T. *Quantum chemical nature of short-range order in disordered systems*. Thesis for the degree of Doctor of Chemistry. Karaganda, DGP HMI named after Zh. Abishev, 2004, pp. 191.
- 6 Yan X. Wei L, Lei Yao, Xin Xue, Yanbin Wang, Gang Zhao, Juntao Li, Qingyan Xu. Numerical Simulation of Meso-Micro Structure in Ni-Based Superalloy During Liquid Metal Cooling. *Proceedings of the 4th World Congress on Integrated Computational Materials Engineering (ICME 2017). The Minerals, Metals & Materials Series*. 2017, pp. 249-259 https://doi.org/10.1007/978-3-319-57864-4_23
- 7 Lobodyuk, V.A., Koval', Y.N. & Pushin, V.G. Crystal-structural features of pretransition phenomena and thermoelastic martensitic transformations in alloys of nonferrous metals. *The Physics of Metals Metallography*. 2011, Vol.111, pp. 165 – 189. <https://doi.org/10.1134/S0031918X11010212>.
- 8 Shpilrain E.E., Fomin V.A., Skovorodko S.N., Sokol G.F. *Studying viscosity of liquid metals*. Moscow, Nauka, 1983, 244p. [in Russian]
- 9 Kazhikenova S.Sh., Shaltakov S.N., Issagulov A.Z. *Physical and chemical aspects of theory of metallurgical processes*. Monograph. Karaganda. KSTU Publisher, 2010, 257 p. [in Russian]

ELECTROSTATIC ENERGY ANALYZER OF CHARGED PARTICLES ON THE BASIS OF A QUADRUPOLE-CYLINDRICAL FIELD IN THE “RING-AXIS” FOCUSING REGIME

Saulebekov A.O.¹, Trubitsyn A.A.², Kambarova Zh.T.³, Saulebekova D.A.¹

¹Lomonosov Moscow State University, Kazakhstan branch, Astana, Kazakhstan

²Ryazan State Radio Engineering University, Ryazan, Russia

³Ye.A. Buketov Karaganda State University, Karaganda, Kazakhstan, kambarova@bk.ru

A study of corpuscular-optical parameters of the electrostatic energy analyzer scheme based on the quadrupole-cylindrical field which proposed earlier was conducted. The operation regime of the energy analyzer, in which the charged particles source locates on an inner cylinder and a detector locates on the symmetry axis (“ring-axis” focusing regime), was considered. Focusing properties of a quadrupole-cylindrical mirror were calculated. Instrumental function was received. Relative energy resolution and luminosity of the device were estimated.

Keywords: energy analyzer, electrostatic field, quadrupole-cylindrical mirror, corpuscular-optical parameters, angular focusing.

Introduction

Currently, there are many methods of electron spectroscopy for analyzing the solid surface. To satisfy the technological needs, new methods and devices are constantly being created. For the purpose of energy analysis of charged particle flows, electrostatic devices with the geometry of the following fields and their super positions were most often used: a spherical field, a cylindrical field, a hyperbolic field, a uniform field, etc. An important part of the experimental scheme is the energy analyzer - a device that allows to determine a current density of charged particles with energies in the selected range from E to $E + \Delta E$.

A cylindrical mirror became the most widespread, becoming the basic element in most electron spectrometers. A cylindrical mirror has several advantages, such as high energy resolution, simplicity of design, etc. Operation of a cylindrical mirror is based on the focusing and dispersing action of the field in the space between two coaxial cylindrical electrodes on a charged particles beam. The theory and the possibility of practical application of a cylindrical mirror were studied in detail by a scientists group under the guidance of prof. V. Zashkvara [1].

One of ways to improve the operation of energy analysis tools is a modification the deflecting field by changing the shape of an outer electrode of a cylindrical mirror. A design of a quadrupole-cylindrical mirror, which has higher corpuscular-particle parameters compared with a classical cylindrical mirror, was proposed in [2].

The work [3] is devoted to a study of electrostatic quadrupole-cylindrical fields. Results of the calculation of the structure of electrostatic quadrupole-cylindrical fields were given. Equipotential portraits of quadrupole-cylindrical fields of various types were presented. The options for their use in corpuscular optics were discussed. The “ring-ring” focusing regime was previously investigated [4], when a ring source of charged particles and a ring detector are located near an inner cylindrical electrode. It was shown that the scheme mirror with $A = -0.01$ has the best quality of focusing, the outer electrode of which has an increasing exponential profile with a small angle of inclination relative to a symmetry axis of a mirror.

In the present work, a study of corpuscular-optical parameters of the quadrupole-cylindrical mirror in the “ring-axis” focusing regime was carried out.

1. Numerical modeling of a quadrupole-cylindrical mirror

A quadrupole-cylindrical field is constructed on the basis of a superposition of a cylindrical field $\mu \ln r$ and an axially symmetrical cylindrical quadrupole:

$$U_q(r, z) = U_0(\mu + z) \ln r \quad (1)$$

where μ is a coefficient specifying the weight contribution of a cylindrical field.

A quadrupole-cylindrical field (1) at the value $\mu = 1$ coincides with the well-known Wannberg field [5]. Wannberg proposed an electrostatic energy analyzer with a field close to a cylindrical one; the case of angular focusing of beams of various energies near the surface of an inner cylindrical electrode was considered. The focal surface in such an analyzer for the case of focusing on an inner cylindrical electrode has a shape that is close to cylindrical shape.

The potential of the Wannberg field in the coordinate system r, z is described by the following expression

$$U = \frac{V}{\ln \frac{r_1}{r_0}} (1 + Az) \ln \frac{r}{r_0} \quad (2)$$

where A is a small dimensionless parameter.

The presence of a small dimensionless parameter A gives an additional degree of freedom in choosing the desired distribution of an electrostatic field and expands ability to search for the most optimal analyzer scheme based on a quadrupole-cylindrical field.

A quadrupole-cylindrical mirror consists of two axially symmetrical coaxial electrodes. Inner cylindrical electrode with radius r_0 is grounded. Outer electrode under potential U creates field

heterogeneity and has a curvilinear profile $r = r_0 \exp \left[\frac{\ln (r_1 / r_0)}{(1 + Az)} \right]$. The difference from the

classical cylindrical mirror is that the profile of an outer deflecting electrode is well approximated by a cone, a generator of which has a small angle of inclination relative to a symmetry axis of a mirror, equal to ~ 1.75 degrees.

In fig.1 shows the scheme of the energy analyzer at $A = -0.01$ and trajectories in it for case when a source of charged particles is the ring slit on an inner cylinder and a detector is located on a symmetry axis. According to the scheme, charged particles emitted from a real source input to the field through the entrance ring slit on an inner electrode, and under the action of the potential on the outer electrode are deflected back, and after they are recorded by a detector.

Numerical modeling of the energy analyzer was carried out by using the “Focus” program for modeling of corpuscular optics systems [6].

The relative energy of particles is $E/U = 1.3 E [\text{eV}] / U [\text{V}] = 0.9$. Initial entrance angles are $30^\circ - 45^\circ$. Position of a ring source (entrance ring slit) is $x = 1.5$ and $y = 1.0$. The distance of the ring source from its point image is equal to $d = 6.31$. The radius of an inner cylindrical electrode $r_0 = 1$. All sizes are expressed in arbitrary units. The scheme provides a “ring-axis” type second-order angular focusing regime.

Fig.2 shows differences of trajectories in a classical cylindrical mirror (a) and a quadrupole-cylindrical mirror (b). It can be seen that focusing quality of charged particles in a quadrupole-cylindrical mirror is better than in a cylindrical mirror.

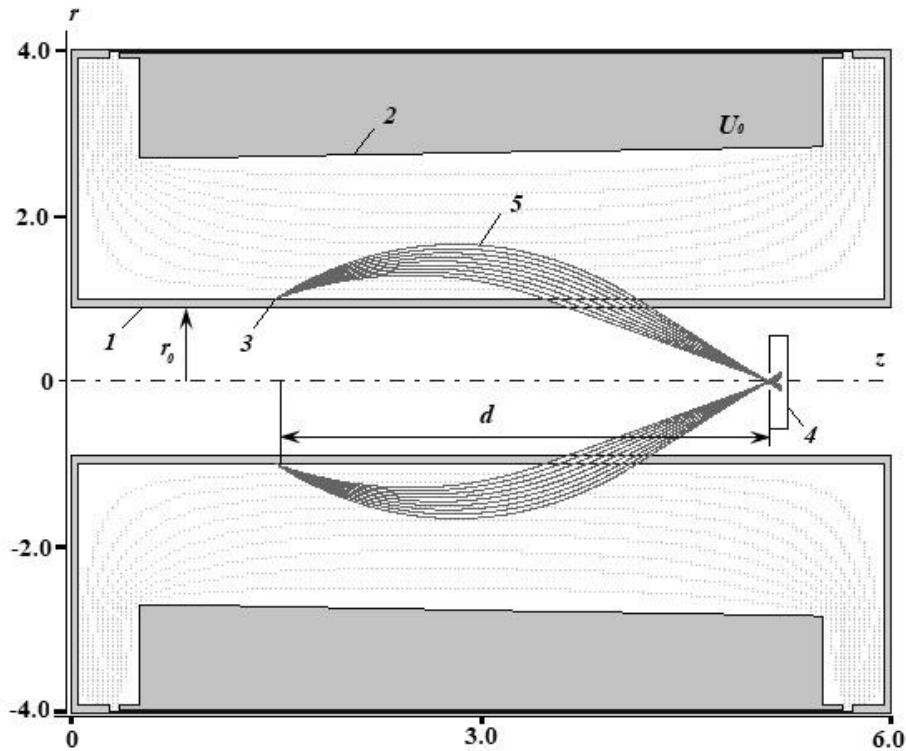


Fig.1. Trajectories of charged particles in the quadrupole-cylindrical mirror: 1 –an inner grounded cylindrical electrode, 2 – an outer deflecting electrode, 3 – a source of charged particles, 4 - a detector, 5 - trajectories of charged particles.

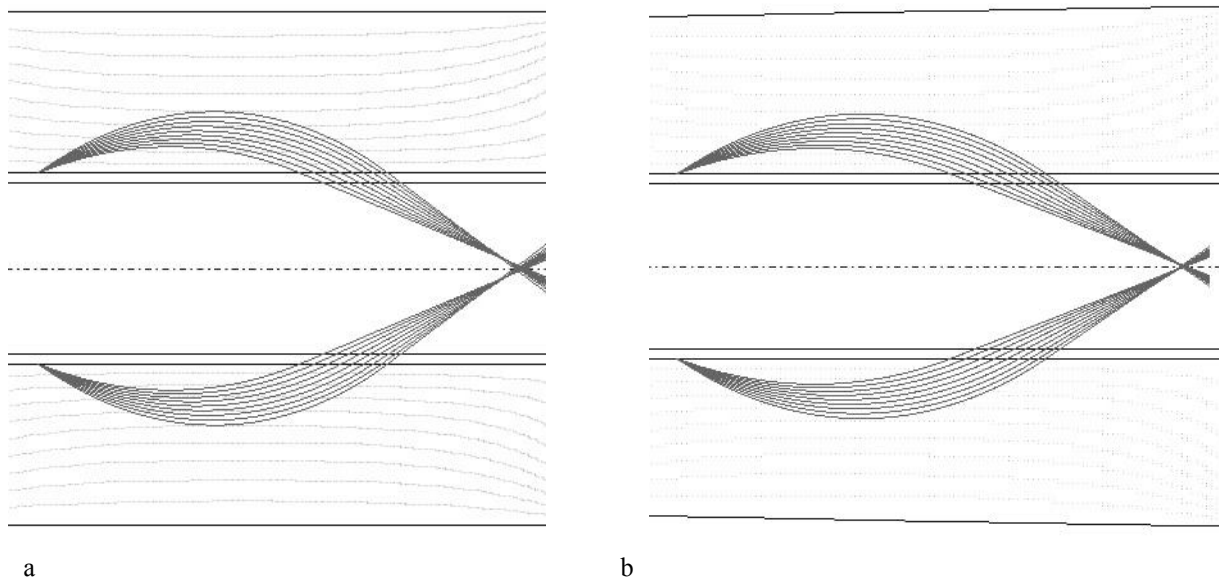


Fig.2. Trajectories of charged particles in a classical cylindrical (a) and a quadrupole-cylindrical mirror (b)

Fig.3 allows to compare the focusing qualities in a cylindrical field and a quadrupole-cylindrical field. It shows the dependence of a intersection point coordinate of a trajectory with symmetry axis z at exit from the analyzer on entrance angle α_0 of particles into the analyzer for second-order angular focusing regime.

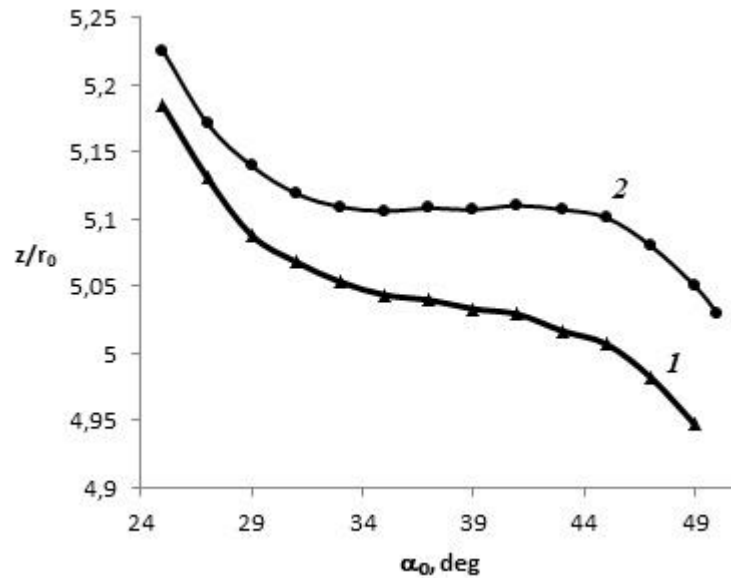


Fig.3. Intersection point coordinate of a charged particles trajectory with symmetry axis z depending on a entrance angle α_0 .

From Fig.3 it is seen that intersection point coordinate of a trajectory with symmetry axis z in the quadrupole-cylindrical mirror in entrance angles range $30^\circ - 45^\circ$ is more constant than in a cylindrical mirror. Thus, a optimal range of entrance angles of particles in a quadrupole-cylindrical field is an initial angles interval $30^\circ - 45^\circ$, which ensures a maximum luminosity $\Omega = 16\%$ and the best focusing of the charged particles beams.

The Table 1 presents calculation results of the corpuscular-optical parameters of the energy analyzer on the basis of the quadrupole-cylindrical field at $A = -0.01$ in the “ring-axis” focusing regime.

Table 1. Corpuscular – optical parameters of the energy analyzer on the basis of the quadrupole-cylindrical field at $A = -0.01$

| Focusing type | «ring-axis» |
|--|-------------|
| Focusing order | 2 |
| Center focusing angle | 36.5^0 |
| X coordinate of focusing | 5.12 |
| Y coordinate of focusing | 0 |
| Total length of the electron-optical scheme, $l = L/r_0$ | 6 |
| Reflection parameter, P | 1 |

Thus, trajectory analysis showed that the design of an energy analyzer based on a quadrupole-cylindrical field has a “ring-axis” type second-order angular focusing of near a central entrance angle of charged particles 36.5° .

To calculate the instrumental function of the quadrupole-cylindrical energy analyzer, particles are launched from a ring source in an initial angles range $30^\circ - 45^\circ$ and initial energies range 0.888-0.912. Fig.4 shows the instrumental function of the energy analyzer based on a quadrupole-cylindrical field at $A = -0.01$ for the “ring-axis” type angular focusing regime.

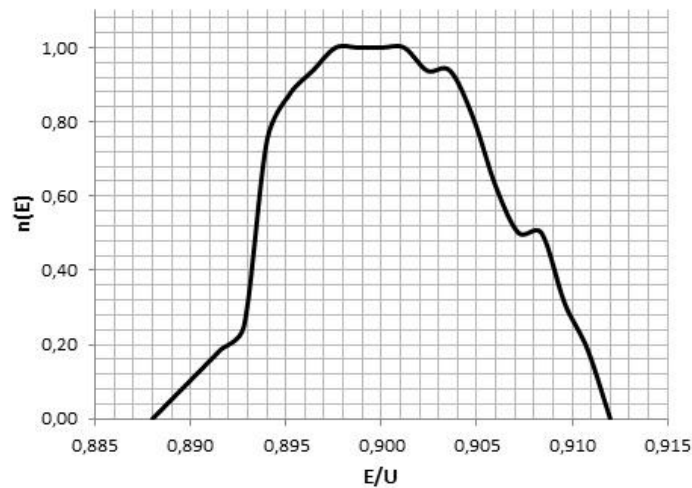


Fig.4. The instrumental function of a quadrupole-cylindrical energy analyzer in the “ring-axis” focusing regime

Relative energy resolution at the half-height of the instrument function of the energy analyzer with an output diaphragm radius of $0.04 r_0$ is 1.5%.

Conclusion

A study of corpuscular-optical parameters of a quadrupole-cylindrical mirror was conducted. Second-order focusing conditions in a quadrupole-cylindrical field were found, when a ring source is imaged at a point on a symmetry axis (“ring-axis” focusing regime). It is shown that the quadrupole-cylindrical mirror provides a higher quality of focusing than a classical cylindrical mirror. The instrumental function of the energy analyzer is calculated. To ensure maximum luminosity, the entrance angles range of particles should be 30° to 45° (wherein luminosity $\Omega = 16\%$).

REFERENCES

- 1 Zashkvara V.V., Korsunskii M.I., Kosmachev O.S. Focusing properties of an electrostatic mirror with a cylindrical field. *Zh. Tekh. Fiz.* 1966, Vol. 36, Issue 4, pp. 132 – 138. [in Russian]
- 2 Kambarova Zh.T., Saulebekov A.O. Development of mirror energy analyzer based on electrostatic quadrupole-cylindrical field. *Eurasian Physical Technical Journal.* 2017, Vol.14, No. 2(28), pp. 42 – 47.
- 3 Kambarova Zh.T., Saulebekov A.O. Calculation of the structure of electrostatic quadrupole-cylindrical fields. *Bulletin of the Karaganda University. «Physics» series.* 2018, No. 1(89), pp. 66 – 71.
- 4 Kambarova Zh.T., Saulebekov A.O. Calculation and modeling of the motion of charged particles in the quadrupole-cylindrical field. *Eurasian Physical Technical Journal.* 2018, Vol. 15, No. 1(29), pp. 55 – 60.
- 5 Wannberg B. An electrostatic mirror spectrometer with coaxial electrodes for multi-detector operation. *Nuclear Instruments and Methods.* 1973, Vol. 107, pp. 549 – 556.
- 6 Trubitsyn A., Grachev E., Gurov V., Bochkov I., Bochkov V. CAE “FOCUS” for modelling and simulating electron optics systems: development and application. *Proceedings of SPIE.* 2017, Vol. 10250, pp. 0V-1 – 0V-7.

UDC 532.58

RESISTANCE MOMENT AT ROTATION OF AN ELLIPSOID IN VISCOUS FLUID

Dudin I.V.¹, Narimanov R.K.¹, Narimanova G.N.²

¹Tomsk State University, Tomsk, Russia, ring_0@mail.ru

²Tomsk State University of Control Systems and Radioelectronics, Tomsk, Russia

The slow rotation of a solid body in a liquid, which is affected by the resistance force, is considered on the example of an ellipsoid. This force is created by both friction forces and pressure forces resulting from the effect of the attached mass. A method of resistance calculation for an arbitrary ellipsoidal body is proposed. Analytical formulas for the resistance forces of an ellipsoid rotating in a viscous fluid are established. The results obtained are applicable for the calculation of multiphase flows in technical devices.

Keywords: ellipsoid, resistance force, rotation, unsteady motion, viscosity

Introduction

The movement of multiphase media in various technological processes is of great interest. These include the task of effluent treatment, sedimentation of dispersed mixtures, the deposition of combustion products emitted from the pipes of industrial enterprises and so on. In nature, we also often observe multiphase currents, in particular, the movement of dust and rain clouds, vortex tornadoes and many other things. Prediction of the evolution of such dispersed two-phase systems should be based on known calculation and experimental data on the strength of the interaction of a single particle of a given shape with a carrier medium taking into account all the properties of the medium and the laws of particle motion.

The solution of the complete problem, taking into account the interaction of each particle with the carrier medium, is an insoluble problem due to a large number of moving particles. As a rule, they are limited by the phenomenological law of the hydrodynamic resistance of a single particle in a carrier medium. The assumption of spherical particle shape is the most common and quite acceptable. In cases, when the shape of the particle differs from the spherical shape, a certain effective radius of a conforming spherical particle is determined, which, when moving under the same conditions, will experience the same resistance of the medium as the original particle.

This approach reasonably led to the fact that most of the efforts to determine the law of resistance were devoted to the study of spherical particles. In many cases, however, a moving particle can more accurately be described as an ellipsoid. And in this regard, studies devoted to the flow around ellipsoids, in particular, ellipsoids of rotation (spheroids) are of interest. In [1, 2], the results of analytical computation on the flow parallel to the main axis of spheroids at small Reynolds numbers are presented. In [3], the results of a numerical calculation of the flow around a uniform stationary stream of spheroids of various shapes with $Re < 100$ in the axially symmetrical formulation are presented, and the values of the integral characteristics are given. In [4–7], the calculated data on the flow around spheroids at Reynolds numbers of about 100 are shown. The values of the drag coefficient depending on the degree of elongation are presented.

The results of numerical and experimental studies make it possible to build correlation dependences used in determining the resistance forces during the motion of particles. Unfortunately, all expressions are approximate and have limits of applicability. From our point of view, attempts to clarify the law of hydrodynamic resistance of a moving body in various conditions will continue for a very long period of time.

The information on the law of resistance of an arbitrary ellipsoid, which makes it possible to more accurately describe the shape of a body moving in a viscous medium, remains relevant. In [8, 9], the problem of slow stationary flow of a viscous flow around a triaxial ellipsoid is solved, a simple calculation formula for its resistance is indicated. In the case of unsteady flows (rotation of the body, acceleration of the flow), the body is affected by the resistance force created by both the friction forces and the pressure forces resulting from the effect of the added mass. Therefore, a more accurate description of the shape of the body becomes more important.

In this paper, the authors consider the actual problem of determining the resistance force during the slow rotation of an ellipsoid in a viscous fluid based on the application of a tension-compression transformation.

1. Determination of the flow fields of a rotating sphere and an ellipsoid.

In exceptional cases, the system of equations of hydromechanics

$$\text{Sh} \frac{\partial \vec{v}}{\partial t} + \nabla \frac{1}{2} \vec{v} \vec{v} - \vec{v} \times \text{rot} \vec{v} = -\text{Eu} \nabla p - \frac{1}{\text{Re}} \text{rot rot} \vec{v}, \quad \text{div} \vec{v} = 0$$

breaks down into a system for velocity

$$\text{div} \vec{v} = 0, \quad \text{rot rot} \vec{v} = 0 \quad (1)$$

and equations for finding the pressure field

$$\text{Sh} \frac{\partial \vec{v}}{\partial t} + \nabla \frac{1}{2} \vec{v} \vec{v} - \vec{v} \times \text{rot} \vec{v} = -\text{Eu} \nabla p, \quad (2)$$

here, equations (1) and (2) use the generally accepted notations for the operators of differentiation, velocity, pressure, and Strouhal, Euler, and Reynolds numbers.

One of these cases is the case of slow rotation of a sphere in a viscous incompressible fluid, when due to sticking the sphere initiates movement in the surrounding unlimited medium, as a result of which a velocity field is established in the fluid [10]

$$\vec{v} = \sigma^{-3} \vec{\omega} \times \vec{\sigma} = \text{rot} \frac{\vec{\omega}}{\sigma}, \quad (\vec{\sigma} = \xi \vec{i} + \eta \vec{j} + \zeta \vec{k}, \quad \vec{\omega} = \omega_1 \vec{i} + \omega_2 \vec{j} + \omega_3 \vec{k}) \quad (3)$$

$$[\vec{v}] = [\vec{\sigma}] = [\vec{\omega}] = 1 \quad \omega_1^2 + \omega_2^2 + \omega_3^2 = 1$$

satisfying the subsystem (1) and the boundary conditions on the sphere itself ($\sigma = 1$)

$$\vec{v}(1) = \vec{\omega} \times \vec{\sigma} \quad (4)$$

and away it (at $\sigma \rightarrow \infty$)

$$\vec{v}(\infty) = 0,$$

where $\vec{\sigma}$ is the radius of the vector, $\vec{\omega}$ is the angular velocity of rotation.

In this case, the friction force resistance moment acts on the rotating sphere

$$\vec{M}(\gamma) = 2 \int \vec{\sigma} \times \gamma \, d\vec{S} = -8\pi \vec{\omega},$$

or in dimensional values [10]

$$\vec{M}(\gamma) = -8\pi \mu R^3 \vec{\omega}, \quad (5)$$

here γ is the strain velocity tensor, μ is the medium viscosity, R is the sphere radius.

As for equation (2), on the basis of which the pressure p is found, and the general formula

$$\vec{M}(p) = \int p \vec{\sigma} \times d\vec{S} \quad (6)$$

for the moment of pressure forces, they can effectively be used for stationary flows. But rotational motions (or their superposition, which is allowed by the system (1)) are by their nature non-stationary. Therefore, to take into account nonstationarity, it is assumed that the moment $\vec{M}(p)$ can be calculated based on the integral theorem on the change of angular momentum

$$\frac{d}{dt} \int \vec{\sigma} \times \vec{v} \, dm = - \int p \vec{\sigma} \times d\vec{S},$$

where dm is the element of mass, $d\vec{S}$ is the element of the surface, on the assumption that the liquid mass rotates like a solid body. Then on the side of liquid the resistance moment will act on the solid.

$$\vec{M}(p) = - \frac{d}{dt} J_g \vec{\omega} = - J_g \frac{\partial \vec{\omega}}{\partial t} - \vec{\omega} \times J_g \vec{\omega},$$

where J_g is the inertia tensor of the solidified body with a uniform density equal to the liquid density. In the case of a sphere, the vector product $\vec{\omega} \times J_g \vec{\omega}$ (it is the one that is obtained by using (6) and the Bernoulli integral for a steady flow) disappears by virtue of central symmetry.

Thus, it can be concluded that when removing active moments supporting the rotation of the sphere near its center of mass, the further (damped) motion of the sphere will be determined by the equation

$$(J_b + J_g) \frac{\partial \vec{\omega}}{\partial t} = - 8\pi\mu R^3 \vec{\omega}, \tag{7}$$

in which, along with the tensor J_g of the hardened liquid sphere, there occurs inertia tensor J_b of the solid sphere or the hollow one itself.

Equation (7) shows that with the active effects being removed, the previous rotation of a solid sphere at a velocity $\vec{\omega}_0$ decreases exponentially

$$\vec{\omega} = \vec{\omega}_0 \exp\left(-\frac{15\mu t}{(\rho_b + \rho_g) R^2}\right). \tag{7'}$$

Consider the flow generated by a rotating solid ellipsoid

$$\left(\frac{x}{a}\right)^2 + \left(\frac{y}{b}\right)^2 + \left(\frac{z}{c}\right)^2 = 1 \tag{8}$$

at an angular velocity

$$\vec{\omega} = \omega_1 \vec{i} + \omega_2 \vec{j} + \omega_3 \vec{k} \tag{9}$$

around some axis passing through its center ($\vec{i}, \vec{j}, \vec{k}$ fixed along the main central axes of the body inertia, and the directions of the semi-axes a, b, c correspond to them).

It is advisable in (8) to replace the ratio of dimensional quantities of x/a type with the relations of dimensionless quantities. This can be done by dividing the numerators and denominators by the same linear scale L used in nondimensionalization of the Navier-Stokes equations. In this case, we obtain the canonical equation of the ellipsoid as follows

$$\left(\frac{x}{\lambda_1}\right)^2 + \left(\frac{y}{\lambda_2}\right)^2 + \left(\frac{z}{\lambda_3}\right)^2 = 1.$$

Then the transformation in vector form

$$\xi \vec{i} + \eta \vec{j} + \zeta \vec{k} = \vec{\sigma} = \left(\frac{x}{\lambda_1}\right) \vec{i} + \left(\frac{y}{\lambda_2}\right) \vec{j} + \left(\frac{z}{\lambda_3}\right) \vec{k}$$

$$\xi^2 + \eta^2 + \zeta^2 = \sigma^2 = \left(\frac{x}{\lambda_1}\right)^2 + \left(\frac{y}{\lambda_2}\right)^2 + \left(\frac{z}{\lambda_3}\right)^2$$

will translate the sphere of unit radius into a preset ellipsoid according to the law of simple tension-and-compression deformation [9]. In this case, the velocity field (3) will also take place in case of a

rotating ellipsoid, and it satisfies in variables \mathbf{x} , \mathbf{y} , \mathbf{z} , both equations (1) and boundary conditions (4), (5). Moreover, each term from (3), i.e. any velocity satisfies the above requirements,

$$\vec{v}_1 = \sigma^{-3} \omega_1 \vec{i} \times \vec{\sigma}, \quad \vec{v}_2 = \sigma^{-3} \omega_2 \vec{j} \times \vec{\sigma}, \quad \vec{v}_3 = \sigma^{-3} \omega_3 \vec{k} \times \vec{\sigma},$$

that is why, the use of expression (9) is quite justifiable, since in fact, it follows the principle of superposition of the simplest flows. But at the same time, the principle of superposition applies to pressure or the squared velocity in the form

$$v^2 = (\vec{v}_1 + \vec{v}_2 + \vec{v}_3)^2 = \sigma^{-6} (\omega_1^2 (\eta^2 + \zeta^2) + \omega_2^2 (\xi^2 + \zeta^2) + \omega_3^2 (\xi^2 + \eta^2) - 2\omega_1\omega_2\xi\eta - 2\omega_2\omega_3\eta\zeta - 2\omega_1\omega_3\xi\zeta)$$

2. Calculation of the projections of the principal moment of resistance from friction forces

First turning attention to calculation of the principal moment generated by friction forces, it is necessary to find the values of the components γ_{ij} of the strain velocity tensor. Since, based on (3), the values of the generalized rates at any point are represented by the equalities

$$\dot{x} = \lambda_1 \sigma^{-3} (\omega_2 \lambda_3^{-1} z - \omega_3 \lambda_2^{-1} y),$$

$$y = \lambda_2 \sigma^{-3} (\omega_3 \lambda_1^{-1} x - \omega_1 \lambda_3^{-1} z),$$

$$\dot{z} = \lambda_3 \sigma^{-3} (\omega_1 \lambda_2^{-1} y - \omega_2 \lambda_1^{-1} x),$$

then using them and the general formula,

$$2\gamma_{ij} = \left(\frac{\partial \vec{\sigma}}{\partial q_i} \middle| \frac{\partial \vec{\sigma}}{\partial q_j} \right)^{-1} \left[\frac{d}{dt} \left(\frac{\partial \vec{\sigma}}{\partial q_i} \frac{\partial \vec{\sigma}}{\partial q_j} \right) + \frac{\partial \vec{\sigma}}{\partial q_k} \left(\frac{\partial \vec{\sigma}}{\partial q_i} \frac{\partial \dot{q}_k}{\partial q_j} + \frac{\partial \vec{\sigma}}{\partial q_j} \frac{\partial \dot{q}_k}{\partial q_i} \right) \right],$$

it can be found that on the surface of the ellipsoid the components of the tensor take the values

$$\gamma_{xx} = -3\xi(\omega_2\zeta - \omega_3\eta), \quad \gamma_{yy} = -3\eta(\omega_3\xi - \omega_1\zeta), \quad \gamma_{zz} = -3\zeta(\omega_1\eta - \omega_2\xi)$$

$$\gamma_{xy} = -\frac{3}{2}(-\omega_1\xi\zeta + \omega_2\eta\zeta + \omega_3(\xi^2 - \eta^2)), \quad \gamma_{yz} = -\frac{3}{2}(\omega_1(\eta^2 - \zeta^2) - \omega_2\xi\eta + \omega_3\xi\zeta)$$

$$\gamma_{xz} = -\frac{3}{2}(\omega_1\xi\eta + \omega_2(\zeta^2 - \xi^2) - \omega_3\zeta\eta).$$

Hereinafter, to abbreviate expressions, the following notations are used

$$\xi = \cos \theta, \quad \eta = \sin \theta \cos \varphi, \quad \zeta = \sin \theta \sin \varphi; \quad 0 \leq \theta \leq \pi, \quad 0 \leq \varphi \leq 2\pi.$$

In these notations, the radius-vector of the current point of the body surface is taken as

$$\vec{\sigma}_s = \vec{i} \lambda_1 \xi + \vec{j} \lambda_2 \eta + \vec{k} \lambda_3 \zeta,$$

so that for a directed element of the ellipsoid surface, the following is correct

$$d\vec{S} = (\vec{i} \lambda_2 \lambda_3 \xi + \vec{j} \lambda_1 \lambda_3 \eta + \vec{k} \lambda_1 \lambda_2 \zeta) \sin \theta d\theta d\varphi. \quad (10)$$

After performing calculations recommended by the formula

$$\vec{M}(\gamma) = 2 \int \vec{\sigma}_s \times \gamma d\vec{S} = 2 \int \vec{\sigma}_s \times (\lambda_2 \lambda_3 \xi \vec{\gamma}_x + \lambda_1 \lambda_3 \eta \vec{\gamma}_y + \lambda_1 \lambda_2 \zeta \vec{\gamma}_z) \sin \theta d\theta d\varphi$$

it turns out that the projections of the principal friction moment on the principal central inertia axes are determined by the equalities

$$M_a(\gamma) = -\frac{4}{5} \pi (\lambda_2 + \lambda_3) (\lambda_2 \lambda_3 + 2\lambda_1 (\lambda_2 + \lambda_3)) \omega_1,$$

$$M_b(\gamma) = -\frac{4}{5} \pi (\lambda_1 + \lambda_3) (\lambda_1 \lambda_3 + 2\lambda_2 (\lambda_1 + \lambda_3)) \omega_2 \quad (11)$$

$$M_c(\gamma) = -\frac{4}{5} \pi (\lambda_1 + \lambda_2) (\lambda_1 \lambda_2 + 2\lambda_3 (\lambda_1 + \lambda_2)) \omega_3$$

Translation of the results (11) into the calculated dimensional form is carried out by multiplying them by the complex

$$\mu \frac{V}{L} L^3 = \mu L^3 T^{-1},$$

then it turns into

$$\begin{aligned} M_a(\gamma) &= -\frac{4}{5} \pi \mu \omega_1 (b+c)(bc+2a(b+c)), \\ M_b(\gamma) &= -\frac{4}{5} \pi \mu \omega_2 (a+c)(ac+2b(a+c)), \end{aligned} \tag{12}$$

$$M_c(\gamma) = -\frac{4}{5} \pi \mu \omega_3 (a+b)(ab+2c(a+b)),$$

that automatically, at $a = b = c = R$, brings to the previously cited result (5) for a sphere. Formulas (12) are convenient because they can be applied to plates (round disks); for needle bodies they lead to a zero result.

3. Calculation of the projections of the principal resistance moment from pressure forces

Starting to determine the resistance moment created by pressure forces, one can first stop on the calculation of the part that arises from the interaction of rotations. In this regard, it is taken into account that

$$\vec{M}(p) = - \int p \vec{\sigma} \times d\vec{S} \approx \frac{1}{2} \int v_s^2 \vec{\sigma}_s \times d\vec{S}$$

where $d\vec{S}$ is defined by (10), and

$$v_s^2 = |\vec{\omega} \times \vec{\sigma}_s|^2, \quad \vec{\sigma}_s = \lambda_1 \xi \vec{i} + \lambda_2 \eta \vec{j} + \lambda_3 \zeta \vec{k}.$$

After performing the calculations, it is found that approximate dimensionless expressions take place for the projections of the moment

$$\begin{aligned} M_a(p) &= -\frac{4}{15} \pi \lambda_1 \lambda_2 \lambda_3 (\lambda_2^2 - \lambda_3^2) \omega_2 \omega_3, \\ M_b(p) &= -\frac{4}{15} \pi \lambda_1 \lambda_2 \lambda_3 (\lambda_3^2 - \lambda_1^2) \omega_1 \omega_3, \\ M_c(p) &= -\frac{4}{15} \pi \lambda_1 \lambda_2 \lambda_3 (\lambda_1^2 - \lambda_2^2) \omega_1 \omega_2, \end{aligned}$$

that after multiplying by the complex

$$\rho V^2 L^3 = \rho T^{-2} L^5$$

take a dimensional form

$$\begin{aligned} M_a(p) &= -\frac{4}{15} \pi \rho a b c (b^2 - c^2) \omega_2 \omega_3, \\ M_b(p) &= -\frac{4}{15} \pi \rho a b c (c^2 - a^2) \omega_1 \omega_3, \\ M_c(p) &= -\frac{4}{15} \pi \rho a b c (a^2 - b^2) \omega_1 \omega_2. \end{aligned} \tag{13}$$

From (13) it can be seen that the resistance moment from pressure forces while ignoring angular acceleration occurs only as a result of the interaction of rotational motions, that is, in those cases when the rotation axis does not coincide with any principal central inertia axes of the ellipsoid itself. Expressions (13) do not apply to any other bodies, as they are only drawn up for an ellipsoid.

In order to be applied to other bodies, it is necessary (13) to represent a more general form by introducing into consideration the inertia tensor of the ellipsoid

$$J = \frac{1}{5} m \begin{pmatrix} b^2 + c^2 & 0 & 0 \\ 0 & a^2 + c^2 & 0 \\ 0 & 0 & a^2 + b^2 \end{pmatrix}, \quad m = \frac{4}{3} \pi abc .$$

In this case (13) take the form

$$\vec{M}(p) = -\vec{\omega} \times J \vec{\omega}$$

and this expression immediately informs that in the general case the resistance moment should be represented as

$$\vec{M}(p) = -\frac{d}{dt} J \vec{\omega} = -J \frac{\partial \vec{\omega}}{\partial t} - \vec{\omega} \times J \vec{\omega}, \quad (14)$$

as stated by the integral theorem on the change in the moment of momentum

$$\frac{d}{dt} \int \vec{\sigma} \times \vec{v} \, dm = - \int \rho \vec{\sigma} \times d\vec{S}.$$

Now the formula (14) makes for obtaining information on the arising resistance moment from pressure forces for other bodies. To do this, it suffices in (14) to choose the inertia tensor J corresponding to the body chosen. For example, for a plate ($a = 0$) you should use

$$J = \frac{1}{4} m \begin{pmatrix} b^2 + c^2 & 0 & 0 \\ 0 & c^2 & 0 \\ 0 & 0 & b^2 \end{pmatrix}.$$

4. Determination of the damped motion of the bodies of some configurations in a viscous medium.

The obtained information for the resistance moments in the form of (13), (14) makes for conclusion that after removing the active effects on maintaining rotation, the subsequent motion of a rigid body near its inertia center in a viscous medium can be described by the equations

1) for a uniform ellipsoid:

$$(m_b + m_g) [(b^2 + c^2) \dot{\omega}_1 + (b^2 - c^2) \omega_2 \omega_3] + 4\pi\mu\omega_1 (b + c)(bc + 2a(b + c)) = 0,$$

$$(m_b + m_g) [(a^2 + c^2) \dot{\omega}_2 + (c^2 - a^2) \omega_1 \omega_3] + 4\pi\mu\omega_2 (a + c)(ac + 2b(a + c)) = 0, \quad (15)$$

$$(m_b + m_g) [(a^2 + b^2) \dot{\omega}_3 + (a^2 - b^2) \omega_1 \omega_2] + 4\pi\mu\omega_3 (a + b)(ab + 2c(a + b)) = 0;$$

2) for a homogeneous plate $a = 0$:

$$(m_b + m_g) [(b^2 + c^2) \dot{\omega}_1 + (b^2 - c^2) \omega_2 \omega_3] + \frac{16}{5} \pi\mu\omega_1 (b + c)bc = 0,$$

$$(m_b + m_g) [\dot{\omega}_2 + \omega_1 \omega_3] + \frac{32}{5} \pi\mu\omega_2 b = 0 \quad (16)$$

$$(m_b + m_g) [\dot{\omega}_3 - \omega_1 \omega_2] + \frac{32}{5} \pi\mu\omega_3 c = 0;$$

The corresponding equations for the motion of a rigid body in vacuum are obtained from those presented for $m_g = 0$ and $\mu = 0$. They conform with the classical ones [11].

For the sphere ($a = b = c$), equations (15) turn into:

$$\dot{\omega}_i + 20\pi \frac{c\mu}{(m_b + m_g)} \omega_i = 0, \quad i = 1, 2, 3$$

the solution is:

$$\omega_i = \omega_{i0} \exp(-k_1 t), \quad i = 1, 2, 3, \quad k_1 = 20\pi \frac{c\mu}{(m_b + m_g)}.$$

For the motion of an ellipsoid with axial symmetry ($\mathbf{b} = \mathbf{c}$), equations (15) become

$$\dot{\omega}_1 + \frac{4\pi(4a + c)\mu\omega_1}{(m_b + m_g)} = 0,$$

$$\dot{\omega}_2 - \frac{a^2 - c^2}{a^2 + c^2} \omega_1 \omega_3 + 4\pi \frac{(a + c)(3a + 2c)}{a^2 + c^2} \frac{c\mu\omega_2}{(m_b + m_g)} = 0,$$

$$\dot{\omega}_3 + \frac{a^2 - c^2}{a^2 + c^2} \omega_1 \omega_2 + 4\pi \frac{(a + c)(3a + 2c)}{a^2 + c^2} \frac{c\mu\omega_3}{(m_b + m_g)} = 0$$

and integrate analytically in elementary functions.

From the first follows

$$\omega_1 = \omega_{10} \exp(-k_2 t), \quad k_2 = 4\pi \frac{(4a + c)\mu}{m_b + m_g},$$

and the second two can be written as equations

$$\omega_2^2 \frac{d}{dt} \frac{\omega_3}{\omega_2} + \frac{a^2 - c^2}{a^2 + c^2} \omega_1 \omega_2^2 \left(1 + \left(\frac{\omega_3}{\omega_2}\right)^2\right) = 0,$$

$$\frac{d}{dt} (\omega_2^2 + \omega_3^2) + 4\pi \frac{(a + c)(3a + 2c)}{a^2 + c^2} \frac{2c\mu}{(m_b + m_g)} (\omega_2^2 + \omega_3^2) = 0.$$

Using them the following are found

$$\frac{\omega_3}{\omega_2} = \text{tg} \left[\text{arctg} \frac{\omega_{30}}{\omega_{20}} - \frac{a^2 - c^2}{a^2 + c^2} \int_0^t \omega_1 dt \right] = \text{tg} \Phi,$$

$$\Phi = \text{arctg} \frac{\omega_{30}}{\omega_{20}} - \frac{a^2 - c^2}{a^2 + c^2} \int_0^t \omega_1 dt,$$

$$\omega_2^2 + \omega_3^2 = (\omega_{20}^2 + \omega_{30}^2) \exp\left(-2 \frac{c(a + c)(3a + 2c)}{(4a + c)(a^2 + c^2)} k_2 t\right).$$

That is

$$\omega_2^2 = (\omega_{20}^2 + \omega_{30}^2) \exp\left(-2 \frac{c(a + c)(3a + 2c)}{(4a + c)(a^2 + c^2)} k_2 t\right) \cos^2 \Phi,$$

$$\omega_3^2 = (\omega_{20}^2 + \omega_{30}^2) \exp\left(-2 \frac{c(a + c)(3a + 2c)}{(4a + c)(a^2 + c^2)} k_2 t\right) \sin^2 \Phi$$

The resulting system of equations for a rotating circular disk $a = 0$, $b = c$ in a resisting medium is integrated in a similar way.

$$\dot{\omega}_1 + \frac{16}{5} \pi \frac{\mu c \omega_1}{m_b + m_g} = 0,$$

$$\dot{\omega}_2 + \omega_1 \omega_3 + \frac{32}{5} \pi \frac{\mu c \omega_2}{m_b + m_g} = 0,$$

$$\dot{\omega}_3 - \omega_1 \omega_2 + \frac{32}{5} \pi \frac{\mu c \omega_3}{m_b + m_g} = 0.$$

From it for rotation rates follow the basic and explaining formulas

$$\omega_1 = \omega_{10} \exp(-k_3 t), \quad \Phi_1 = \arctg \frac{\omega_{20}}{\omega_{30}} - \int_0^t \omega_1 dt, \quad k_3 = 16\pi \frac{c\mu}{(m_b + m_g)}$$

$$\omega_2^2 = (\omega_{20}^2 + \omega_{30}^2) \exp(-2k_3 t) \sin^2 \Phi_1,$$

$$\omega_3^2 = (\omega_{20}^2 + \omega_{30}^2) \exp(-2k_3 t) \cos^2 \Phi_1.$$

The kinetic energy during the rotational motion of a solid body in accordance with the definition can be found by the formula

$$E = \frac{1}{2} (J_{xx} \omega_1^2 + J_{yy} \omega_2^2 + J_{zz} \omega_3^2).$$

The dissipation of energy with time is determined by the ratio, which is equal for the sphere:

$$R1(t) = \frac{E}{E_0} = \exp(-2k_1 t),$$

for a round disk of c radius:

$$R3(t) = \frac{E}{E_0} = \frac{2c^2 \omega_1^2 + c^2 (\omega_2^2 + \omega_3^2)}{2c^2 \omega_{10}^2 + c^2 (\omega_{20}^2 + \omega_{30}^2)} = \exp(-2k_3 t).$$

In the studied motion of the rotation ellipsoid ($b = c$) by inertia in a resisting medium there should be

$$E = \frac{1}{10} (m_b + m_g) (2c^2 \omega_1^2 + (a^2 + c^2) (\omega_2^2 + \omega_3^2))$$

and, therefore, at $R2 = \frac{E}{E_0}$ there will be

$$R2(t) = \frac{2c^2 \omega_{10}^2 \exp(-2k_2 t) + (a^2 + c^2) (\omega_{20}^2 + \omega_{30}^2) \exp(-2 \frac{(a+c)(3a+2c)}{(4a+c)(a^2+c^2)} k_2 t)}{2c^2 \omega_{10}^2 + (a^2 + c^2) (\omega_{20}^2 + \omega_{30}^2)}$$

Figure 1 shows the dependencies of $R2(t)$ in case of different ratios.

$\frac{a}{c} = 1, 5, 10$, $k_2 = 1$ и $\omega_{10} = \omega_{20} = \omega_{30} = \mu/c^2 \rho_b = 1$.

The graphs are illustrative and only qualitatively show the rapid decay of the rotational motion.

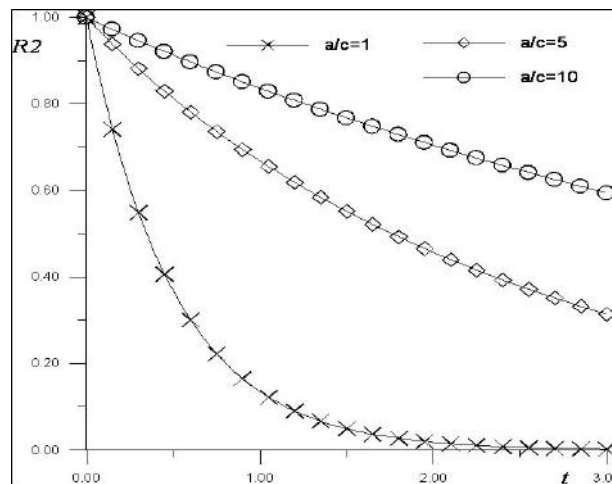


Fig.1. Reduction of the relative kinetic energy of rotation

To determine the rotation law of a solid body in a resisting medium, it is necessary to add the Euler kinematic relations to the equations obtained [11]

$$\dot{\psi} \sin \theta \sin \varphi + \dot{\theta} \cos \varphi = \omega_1,$$

$$\dot{\psi} \sin \theta \cos \varphi - \dot{\theta} \sin \varphi = \omega_2,$$

$$\dot{\psi} \cos \theta + \dot{\varphi} = \omega_3,$$

in which ψ , φ , θ indicate Euler angles, but this question becomes of interest only if there are active forces.

Conclusion

Thus, by the example of an ellipsoid, a slow rotation of a solid body in a liquid is considered, taking into account the fact that it is exerted by the resistance force created by both the friction forces and the pressure forces resulting from the effect of the added mass.

Derived equations of rotation by inertia in a resisting medium near the geometric center for ellipsoid bodies can be applied to plates into which an ellipsoid can degenerate. The obtained expressions can be easily applied in the calculations of multiphase flows in technical devices and in the study of natural phenomena.

REFERENCES

- 1 Lamb G. *Hydrodynamics*. M.: Gostekhizdat, 1947. 928 p. [in Russian]
- 2 Happel D., Brenner G. *Hydrodynamics at low Reynolds numbers*. M.: Mir, 1976. 630 p. [in Russian]
- 3 Zamyshlyaev A.A., Shrager G.R. Fluid flow of spheroids at moderate Reynolds numbers. *Fluid and gas mechanics*. 2004, No.3, pp. 25 - 33. [in Russian]
- 4 Lipanov A.M., Semakin A.N. Non-spherical particles: resistance and some flow parameters in unlimited volume. Scientific notes TsAGI. 2011 Vol. Xlii, no. 6, pp. 15 - 22. [in Russian]
- 5 Holser A., Sommerfeld M. New simple correlation formula for the drag coefficient of non spherical particles. *Powder Technology*. 2008, Vol.184, Issue 3, p. 361-365.
- 6 Loth E. Drag of non-spherical solid particles of regular and irregular shape. *Powder Technology*. 2008, Vol. 182, Issue 3, p. 342 – 353.
- 7 Clift R., Grace J.R., Weber M. *Bubbles, drops, and particles*. New York: Academic press, 1978, 380 p.
- 8 Dudin I.V., Narimanov R.K. *Resistance of a triaxial ellipsoid slowly moving in a viscous fluid*. Preprint №37. TSU publishing house, Tomsk, 2000, 11 p. [in Russian]
- 9 Dudin I.V., Narimanov R.K. Resistance with slow movement of the ellipsoid. *Proceedings of the Tomsk Polytechnic University*, 2004, Vol. 307, No.3, pp. 17-21. [In Russian]
- 10 Landau LD, Lifshits E.M. *Hydrodynamics*, Moscow, Nauka, 1986, 736 p. [in Russian]
- 11 Buchholz N.N. The main course of theoretical mechanics, Part 2, Moscow, 1972, 332 p. [in Russian]

UDC 539.21, 53.096

FORMATION OF THE SPECTRAL CONTOUR WIDTH OF NANOPARTICLES PLASMON RESONANCE BY ELECTRON SCATTERING ON PHONONS AND A BOUNDARY SURFACE

Kucherenko M.G., Nalbandyan V.M.

Orenburg State University, Centre of Laser and Information Biophysics, Orenburg, Russia, rphys@mail.osu.ru

The effectiveness of the method of narrowing plasmon resonances of nanoparticles by reducing the temperature was evaluated. It is shown that for particles with a radius of less than 70 nm, it is necessary to take into account the scattering of electrons by the particle surface. This condition significantly limits the possibilities of temperature control of scattering. The data on the transformation of the exciton and plasmon bands of the absorption spectra of spherical layered nanocomposites with the core-shell structure in an external magnetic field are presented. It is shown that the splitting of the plasmon resonance band in a magnetic field can be observed only at electron scattering frequencies below 10^{12} sec^{-1}

Keywords: plasmon resonance, nanoparticle, scattering of electrons, exciton-plasmon interaction

Introduction

As is known, at room temperature the frequency of electron collisions with phonons in different metals and semiconductors takes the values $\sim 10^{13} - 10^{14} \text{ sec}^{-1}$. However, to observe in the optical frequency range the spectral changes in the polarizabilities of conducting nanoparticles caused by an external magnetic field, it is important that this coefficient does not exceed $10^{11} - 10^{12} \text{ sec}^{-1}$ [1]. Such a low frequency value γ can be obtained, for example, by lowering the temperature of metals to several tens of kelvins. Only by reducing γ to the required values can one observe the optical manifestations of the influence of an external magnetic field on the physical processes that occur with the participation of metallic nano-objects. These include: absorption and scattering of light, mediated intermolecular nonradiative energy transfer and luminescence near conducting bodies, as well as other similar processes [1].

Quite a large number of works are devoted to the study of electron-phonon collisions in metals and the dependence of various physical phenomena determined by such collisions on temperature. Thus, in [2], the authors investigated individual pure single-crystal silver nanowires (AgNWs) with respect to variations in the characteristics of electrical conductivity, thermal conductivity, and Seebeck coefficient depending on the change in metal temperature from 1.4 K to room temperature. In [3] the electron thermal conductivity of graphene was calculated using various methods by taking into account electron – phonon interactions, including both low-energy, acoustic phonons, and high-energy, optical, and zonal boundary phonons. At low temperatures, the electron thermal conductivity substantially depends on the amount of impurities. However, at room temperature, the impurity effects are small. The authors of [4] studied the contribution of electron-phonon scattering to the electrical conductivity of a quantum cylinder in a longitudinal magnetic field.

1. Experimental installations and measurement techniques

Formulas describing the temperature dependence of the resistance of the nanostructure are obtained in an analytical form, both in the case of the isotropic phonon spectrum and taking into account the effects of the dimensional limitation of phonons. In addition, the authors of this work

investigated the temperature dependence of the conductivity of a quantum cylinder in the case of an isotropic phonon spectrum with a linear dispersion law. It is shown that in the limiting case of relatively low temperatures, the resistance of a quantum cylinder is proportional to the third power of the temperature.

The processes of scattering of conduction electrons are the cause of the electrical resistance of metals. The frequency of electron collisions γ can be determined through the resistivity ρ of the material, using the known formula [5-6]:

$$\gamma = \frac{Ne^2}{m} \rho . \quad (1)$$

Here, m and e are the effective mass and electron charge, respectively, N is the effective bulk density of electrons. The resistivity of metals is written as

$$\rho = \frac{m}{Ne^2\tau} = \frac{mv_F}{Ne^2l}, \quad (2)$$

where v_F is the electron velocity on the Fermi surface, l is the average electron mean free path, and τ is the time between two electron collisions ($\tau = 1/\gamma$).

Two main mechanisms of electron scattering are distinguished:

- 1) as a result of their collision with local fixed centers – defects, impurities, etc.;
- 2) as a result of interaction with thermal vibrations of the lattice – phonons.

The effective frequency of collisions consists of two terms – the collision frequencies in the first and second processes, that is, $1/\tau_{eff} = 1/\tau_{prim} + 1/\tau_{phon}$ [5]. This leads to the Matthiessen rule.

$$\rho = \rho_{resid} + \rho_{ideal}(T), \quad (3)$$

where ρ_{resid} is the residual resistance, independent of temperature T , associated with the technology of obtaining this metal sample and the quality of its manufacture; $\rho_{ideal}(T)$ is the resistance of the ideal lattice of a given metal due to scattering by phonons with a strong dependence on temperature.

This dependence is described by the Bloch – Gruneisen formula [6]:

$$\rho_{ideal}(T/\theta_D) = \frac{K_0}{\theta_D} \left(\frac{T}{\theta_D} \right)^5 \int_0^{\theta_D/T} \frac{x^5 dx}{[\exp(x)-1][1-\exp(-x)]} = \frac{K_0}{\theta_D} \left(\frac{T}{\theta_D} \right)^5 J_5 \left(\frac{\theta_D}{T} \right), \quad (4)$$

where K_0 is a certain temperature-independent constant characteristic of a given metal, θ_D is the Debye temperature, which determines the maximum oscillation frequency of the grating ($\hbar\omega \cong k_B\theta_D$).

For high temperatures $T/\theta_D \geq 1$, a linear temperature dependence of resistance $\rho_{ideal}(T) \sim T/\theta_D$ (Fig. 1 b) follows from (4), whereas for low temperatures, $T/\theta_D \ll 1$ a power dependence $\rho_{ideal}(T) \sim (T/\theta_D)^5$ is characteristic (Fig. 1 a).

For metals with a Fermi surface close to spherical, the law $\rho \sim T^5$ has a place already at $T \leq 0.1\theta_D$. For metals with a more complex Fermi surface, this law begins to be satisfied at lower temperatures, when the value of the thermal background pulse becomes smaller than the dimensions of all characteristic Fermi surface features.

Using formula (4) and Table 1, one can obtain the values of the resistivity of the metal and the frequency γ of electron collisions at an arbitrary temperature T . Temperature dependence $\gamma(T)$ can then be represented as

$$\gamma(T) = \gamma(T_0) \left(\frac{T}{T_0} \right)^5 \frac{J_5(\theta_D/T)}{J_5(\theta_D/T_0)}, \quad J_5(\theta_D/T) = \int_0^{\theta_D/T} \frac{x^5 dx}{[\exp(x)-1][1-\exp(-x)]}, \quad (5)$$

where $T_0 = 293$ K.

As can be seen from the graphs of Fig. 1, the frequency of electron-phonon collisions of different metals takes on the value $\gamma \sim 10^{12} \text{ sec}^{-1}$ at the following temperatures: Au - 30 K, Ag - 40 K, Cu - 54 K, Al - 57 K.

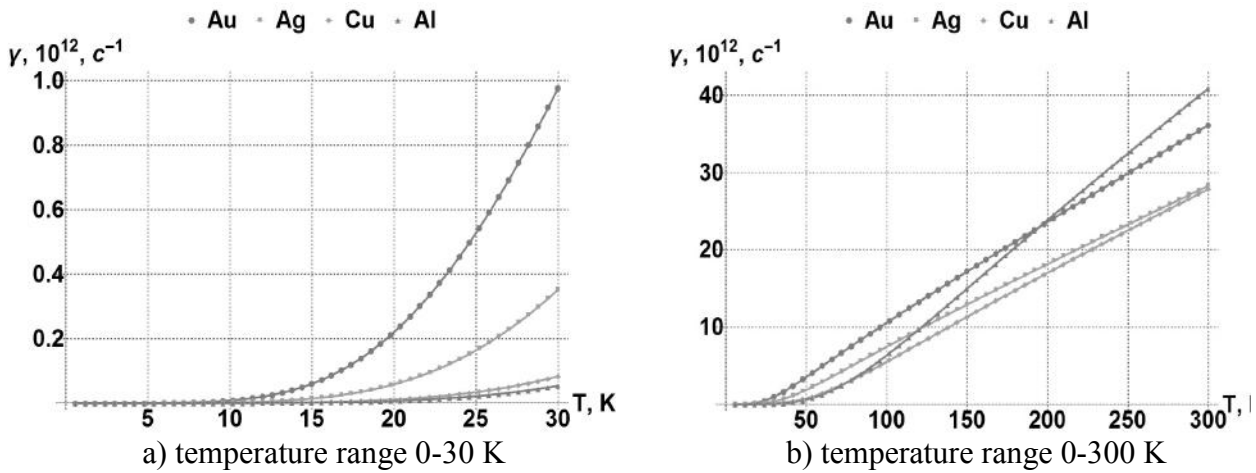


Fig. 1. The dependence of the frequency γ of electron-phonon collisions for various metals (gold, silver, copper, aluminum) on temperature T .

Table 1. Specific resistances and frequencies γ of pure Cu, Ag, Au and Al at 0°C

| Metal | $\rho, 10^{-6}$ Ohm·cm | $\gamma, 10^{13}$ sec $^{-1}$ | $N_e, 10^{22}, \text{cm}^{-3}$ | m/m_e | θ_D, K |
|-------|---------------------------|----------------------------------|--------------------------------|---------|----------------------|
| Cu | 1.55 | 2.5 | 8.5 | 1.49 | 344.5 |
| Ag | 1.49 | 2.56 | 5.86 | 0.96 | 225 |
| Au | 2.06 | 3.28 | 5.6 | 0.99 | 165 |
| Al | 2.5 | 3.64 | 6 | 1.16 | 429 |

In Fig. 2 shows the temperature dependences of the frequency of electron-phonon collisions for various metals in the semi-logarithmic scale in the range of 1–30 K (Fig. 2a) and 1-300 K (Fig. 2b). Already at temperatures above 150 K, the collision frequency γ exceeds the characteristic value $\sim 10^{13} \text{ sec}^{-1}$ for all the metals considered.

In fig. 3a and 3b are shown universal graphs of the temperature dependence of the frequency of electron-phonon collisions, valid for all metals. Relative temperatures T/θ_D are plotted on the horizontal axis, and values for γ are plotted along the vertical axis, without taking into account the characteristic constant related to a particular metal.

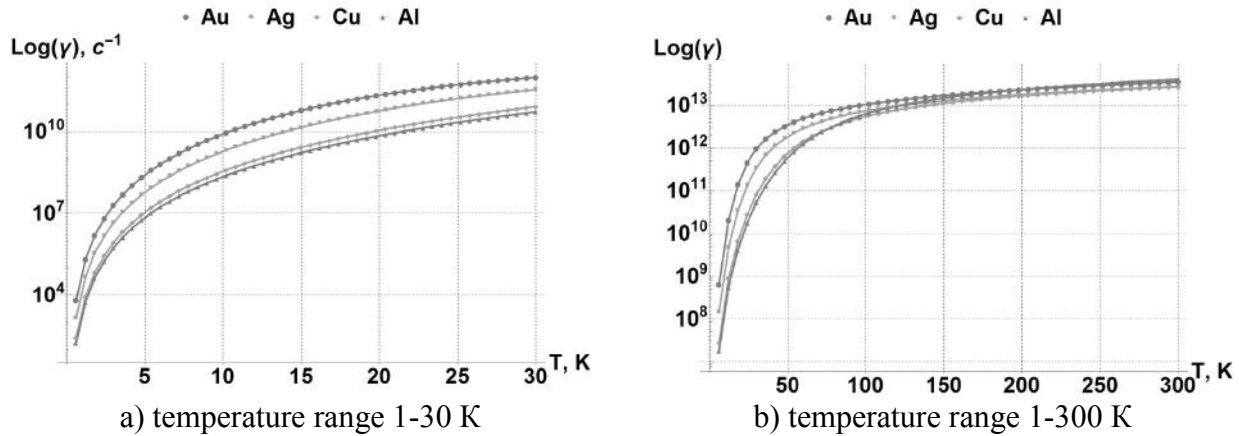


Fig. 2 The dependence of the collision frequency γ of electrons of different metals (gold, silver, copper, aluminum) on the temperature T on a semi-log scale

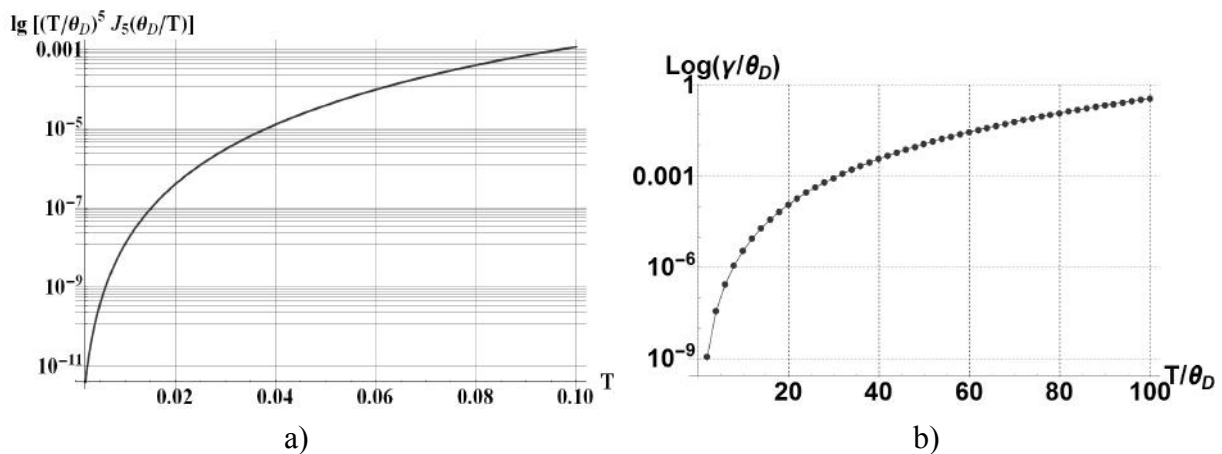


Fig. 3. Universal curve of the temperature dependence of the frequency of electron-phonon collisions in the low- (a) and high-temperature (b) intervals

2. Electron collision frequency taking into account scattering by the surface of a nanoparticle. The effect of dimensional dissipation

In the case of conducting nanobodies, apart from the need to take into account the temperature dependence of the frequency of electron-phonon collisions, it is also important to take into account the dependence γ on particle sizes. The expressions considered above for the electron collision frequency were obtained in the framework of the free electron gas relaxation model, which is valid only for macroscopic objects. In the case when the electron mean free path may turn out to be comparable with the size of the particle itself, the scattering of conduction electrons on its surface will lead to a decrease in the relaxation time, i.e. increase in collision frequency. This effect is especially important for nanoparticles, with their high ratio of surface area to volume.

This increase in frequency γ_{sc} caused by the action of the surface is proportional to the Fermi velocity v_F :

$$\gamma_{sc} = Av_F / R,$$

where R is the effective radius of the nanoparticle, A is a parameter describing the degree of loss of coherence when the electron is scattered from the surface.

The frequency γ of total electron scattering in the case of nanoparticles can be represented by an empirical formula [7, 8], in which γ_{bulk} it is defined by formulas (1) and (5):

$$\gamma = \gamma_{bulk} + \gamma_{sc}. \quad (6)$$

The value of the parameter A for silver and gold lies in the range of $0.1 < A < 0.7$ and $v_F \sim 1,4$ nm/fs [9]. In fig. 4 shows the dependence of the electron collision frequency on the radius R (curve 1) and the temperature T (curve 2) of the metal nanoparticle.

Curve (1) fig. 4 corresponds to the frequency of electron scattering by the surface of particles of different radius R , and curve (2) corresponds to the temperature dependence of the frequency of electron-phonon collisions $A = 0.1, v_F = 1.4$ nm / fs. From the analysis of graphs Fig. 4 it can be concluded that it is impossible to reduce the frequency γ of electron collisions to arbitrary values by lowering the temperature of the metal. When a certain value is reached, the first component in (6) becomes smaller than the second ($\gamma_{bulk} < \gamma_{sc}$), which is responsible for the scattering of electrons on the surface of a particle. Then the main contribution to the scattering will make γ_{sc} . Therefore, a further decrease γ_{bulk} caused by the cooling of the metal no longer contributes to a decrease in the overall frequency γ .

For example, for a gold nanoparticle with a radius of 70 nm (Fig. 4), the collision frequency at which the scattering on the surface becomes more significant than the electron-phonon scattering at a temperature $T = 35$ K is $\gamma \sim 2 \cdot 10^{12} \text{ sec}^{-1}$. A decrease in the frequency γ leads to an increase in the resolution of the lines of the optical absorption spectrum by nanoparticles (Fig. 5).

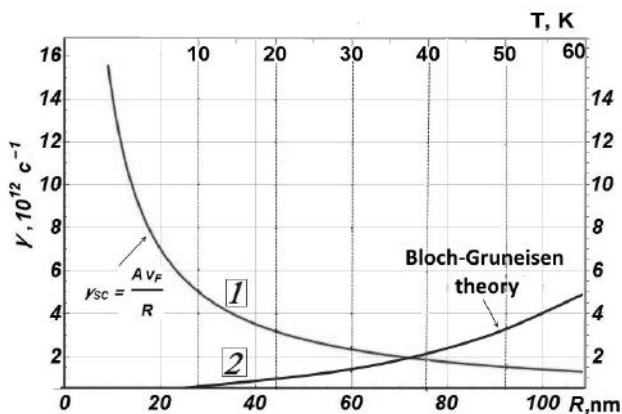


Fig. 4 Dependence of the frequency of electron collisions on the temperature and radius of metal nanoparticles: 1 - dependence of the electron scattering frequency by the particle surface on its radius R ; 2 - temperature dependence of the frequency of electron-phonon collisions in a pure metal.

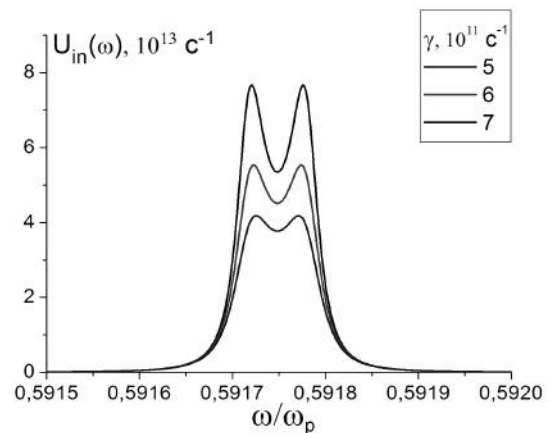


Fig. 5 Splitting of the spectrum of the absorption rate $U_{in}(\omega)$ of the energy of the electromagnetic field in a spherical layered nanocomposite with a magnetized conducting core and excitonogenic shell depending on the magnitude of the plasmon damping coefficient γ .

3. Spectra of nanocomposites with exciton-plasmon interaction

The effect of metallic nanoparticles on various processes sensitive to plasmon resonance has been studied in sufficient detail. In recent years, much attention has been given to the participation of molecular excitons in processes that are developed in metal composite complexes [11–13]. At the next stage of nanotechnology development, it is of interest to study the phenomena that can be caused by the exciton-plasmon interaction. In [14] the effects of plasmon-exciton interaction in the absorption and scattering of light by hybrid nanoparticles consisting of a metal core and a J-aggregate shell of an organic dye were studied. The spectral characteristics of the particles were calculated for two concentric spheres within the framework of the generalized Mie theory in a wide range of wavelengths and geometric parameters of the system for various core materials (Ag, Au, Cu, Al) and the cyanine dye shell (TC, OC and PIC). The eigen frequencies of the hybrid modes of the system and the intensities of the photo absorption peaks are determined. Their dependences on the oscillator strength of the transition in the J-band of the dye, the core radius and the shell thickness are examined. A qualitatively different character of the effect of the interaction of the Frenkel exciton with dipole and multipole plasmons on the optical properties of the composite nanoparticles under study is demonstrated. It is shown that by varying the sizes and optical constants of the materials of the particle, the total number of spectral peaks changes and a significant redistribution of their intensities occur at the maxima. The dominant regions of the processes of absorption and scattering of light in the extinction spectra are found.

The interaction of molecular excitons in organic films with a metal substrate was investigated in [15]. In another paper [16], the authors considered an exciton-plasmon interaction in a three-layer spherical nanocomposite consisting of a metal core (Au) covered by two layers of an organic dye. The first layer of the dye is needed to maintain the connection of plasmons with excitons. The photoluminescence spectrum of the composite obtained in this work contained the narrow-band peak of the J-aggregates, which was amplified locally by plasmons.

In paper [17] dipole polarizabilities and absorption cross sections of two-particle nanoclusters of conductive homogeneous and layered particles with the degenerate electron gas was considered. Frequency dependences of the dipole polarizabilities of clusters consisting of two solid conducting spherical nanoparticles and double-layer metal nanoparticles are investigated versus the geometrical parameters of the system with taking into account the degeneracy of electron gas of its metallic components. It is established that the spectra of the dynamic polarizabilities and absorption cross-sections of clusters have a complex multi resonant structure and strong dependence on the configuration parameters of the cluster, the degree of degeneracy of the metal, and kinetic characteristics of its electron gas. Spectral transformations of the absorption cross-sections of nanoclusters are illustrated under variation of the radii of particles or their nuclei, characteristic lengths of the Thomas-Fermi screening, and frequency of electron collisions. The anisotropic nature of absorption of electromagnetic field energy by a cluster is established: it is shown that the value of the absorption cross section depends on the direction of the electric field strength vector relative to the axis of the cluster.

We investigated the exhibition of the exciton-plasmon interaction in spherical layered nanocomposites with the metal core – crystal-like molecular shell structure. Figure 6 shows the spectra of the absorption rate of the field energy in the exciton-envelope depending on the magnitude of the induction of the external magnetic field at a zero plasmon attenuation coefficient $\gamma = 0$ (Fig. 6a), i.e. without taking into account the energy absorption by the metal core, and the attenuation coefficient of the plasmons $\gamma = 6 \cdot 10^{11} \text{ sec}^{-1}$ (Fig. 6b).

The graphs show that the plasmon resonance in a magnetic field increases in amplitude and splits into two spectral lines, scattering in the region of high and low frequencies with increasing magnetic induction B . At the same time, the effect of the magnetic field on the exciton resonances is small (exciton bands not shown in the figure). When taking into account the field energy absorption

by the metal core of a layered nanocomposite, i.e. when, plasmon resonances broaden and their amplitude decreases by two orders of magnitude. The resonance splitting is observed at the magnetic induction value $B = 10$ T, and an increase in the magnetic induction affects the amplitude of the plasmon resonance, just as with a zero plasmon damping coefficient, i.e. the speed of light absorption in a magnetic field increases, which is reflected in the graphs shown in Figure 6b.

The absorption speed in the volume dV of the excitonogenic layer with coordinates r, θ is determined by the square of the modulus of the local field strength vector $|\mathbf{E}_2(\omega, r, \theta)|^2$ inside the layer and will have the following form [10]

$$dU_{in}(\omega, r, \theta) = \frac{1}{2\pi\hbar} \text{Im}\varepsilon_2(\omega) |\mathbf{E}_2(\omega, r, \theta)|^2 dV, \quad (7)$$

where $\varepsilon_2(\omega)$ is the dielectric constant of the crystal-like excitonogenic layer is determined by the expression [18]

$$\varepsilon(\mathbf{k}, \omega) = \varepsilon_0 - \frac{f^2}{[\omega + i\Gamma(\omega, \mathbf{k})]^2 - \omega_{res}^2(\mathbf{k})}, \quad (8)$$

and ε_0 is the dielectric constant due to all other states of electrons, except for the exciton states; $\Gamma(\omega, \mathbf{k}) \equiv \gamma(\mathbf{k}, \omega) + \eta$ is the relaxation rate due to the interaction of excitons with phonons; factor $f^2 \equiv \Omega_p^2 F$ characterizes the connection of photons with excitons; $\Omega_p^2 \equiv 4\pi e^2 / mv$ is the square of the "plasma frequency"; $F \equiv 2\omega_j m d^2 / \hbar e^2$ is the oscillator strength of a transition; $\omega_{res}(\mathbf{k}) = \omega(\mathbf{k}) + \Delta(\mathbf{k}, \omega)$ is the frequency of excitons renormalized due to interaction with phonons.

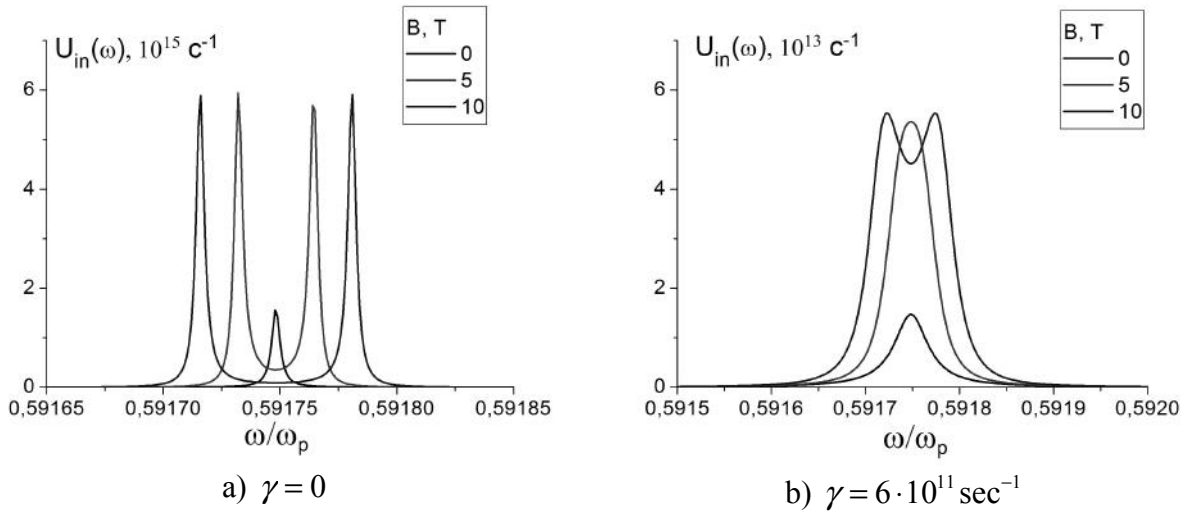


Fig.6. Spectra of the rate of field energy absorption in the excitonogenic shell of a layered on-nanocomposite with a magnetized core, depending on the magnitude of the magnetic induction with a zero-left plasmon attenuation coefficient $\gamma = 0$ (a) and (b) plasmon attenuation coefficient $\gamma = 6 \cdot 10^{11} \text{ sec}^{-1}$.

Thus, the dielectric constant of molecular J-aggregates is a complex function with spatial and frequency dispersion. In this work, only the frequency dispersion for the zero exciton wave vector $\mathbf{k} = 0$ was taken into account. The vector of the electric field strength inside the excitonogenic layer of the shell was represented as

$$\mathbf{E}_2(r, \theta | \omega) = -\vec{\nabla} \left[-\vec{\mathbf{C}}(\vec{\varepsilon}_1, \varepsilon_2, \varepsilon_3) \mathbf{E}_0 \mathbf{r} + \vec{\mathbf{D}}(\vec{\varepsilon}_1, \varepsilon_2, \varepsilon_3) \mathbf{E}_0 \frac{\mathbf{r}}{r^3} \right], \quad (9)$$

where $\vec{\mathbf{C}}, \vec{\mathbf{D}}$ are transformational tensors, expressions for which are given in [10].

Two or three exciton resonances should appear in the spectra, two of which are due to the square of the magnitude vector of the intensity $|\mathbf{E}_2(\omega, r, \theta)|^2$, and the third to the multiplier $\text{Im} \varepsilon_2(\omega)$. However, this resonance did not manifest itself in the calculated spectra, since it merged with one of the two other exciton resonances. In addition, there is a plasmon resonance in the spectrum, even with a zero plasmon damping coefficient $\gamma = 0$, i.e. when the absorption of the field energy by the metal core does not take place. Expression for the rate of field energy absorption by the entire layered spherical nanocomposite

$$U(\omega|B) = \frac{1}{2\hbar} \text{Im}[\mathbf{E}_0^* \vec{\mathbf{A}}(\omega|B) \mathbf{E}_0], \quad (10)$$

where the dipole polarizability tensor of a layered spherical composite with a magnetized core is determined by the expression [10]

$$\begin{aligned} \vec{\mathbf{A}}(\vec{\varepsilon}_1(\omega|\mathbf{B}), \varepsilon_2(\omega), \varepsilon_3) = \\ = [(\vec{\varepsilon}_1(\omega|\mathbf{B}) + 2\varepsilon_2(\omega))(\varepsilon_2(\omega) - \varepsilon_3) + (\vec{\varepsilon}_1(\omega|\mathbf{B}) - \varepsilon_2(\omega))(2\varepsilon_2(\omega) + \varepsilon_3)\xi^3] \times \\ \times [(\vec{\varepsilon}_1(\omega|\mathbf{B}) + 2\varepsilon_2(\omega))(\varepsilon_2(\omega) + 2\varepsilon_3) + 2(\vec{\varepsilon}_1(\omega|\mathbf{B}) - \varepsilon_2(\omega))(\varepsilon_2(\omega) - \varepsilon_3)\xi^3]^{-1} R^3. \end{aligned} \quad (11)$$

An alternative model for the formation of the field energy absorption spectra of the entire layered nanocomposite is based on expression (10). In the spectra calculated on the basis of (10), as before, three resonances manifest themselves - two exciton in the low-frequency region of the spectrum and one plasmon in the high-frequency region.

Conclusion

Thus, the limiting factor for the temperature decrease in the frequency of electron collisions in a metal is the effect of electron scattering by the nanoparticle surface. Thus, a decrease in the nanoparticle radius to $R < 10 \div 15$ nm values leads to a sharp increase in the frequency γ_{sc} by an order of magnitude ($\gamma \sim 10^{13} \text{ sec}^{-1}$), which makes the temperature method of increasing the relaxation time of electrons in small metal bodies of small size ineffective. To perform high-resolution spectral optical measurements for systems containing conducting nanoparticles, joint optimization of geometric and thermodynamic parameters is necessary (Fig. 4). In fact, the critical value of the nanoparticle radius at which electron scattering by the surface makes a contribution comparable to electron to phonon scattering at a temperature $T = 35$ K is a radius of about 70 nm. Although the problem of enhanced resolution of the optical spectra of plasmon nanoparticles was associated with the detection of magnetic effects, in this work we did not consider the possible influence of a magnetic field on the frequency of collisions of electrons with the surface of the nanoparticle. It is expected that in strong fields the frequency of such collisions will decrease due to the curvature of the ballistic electron trajectory. Then, spectral measurements with plasmon nanostructures in a magnetic field can have an improved resolution as the temperature decreases to the subcritical region due to the magnetic suppression of surface scattering. This can contribute to the achievement of the optimal value of the frequency γ of collisions of electrons with phonons of the order 10^{11} sec^{-1} .

Acknowledgements

The work was done by funding the Ministry of Education and Science of the Russian Federation (Minobrnauka) (3.7758.2017/BCh).

REFERENCES

- 1 Kucherenko M.G., Nalbandyan V.M. Absorption and spontaneous emission of light by molecules near metal nanoparticles in external magnetic field. *Physics Procedia*, 2015, Vol. 73, pp. 136 – 142.
- 2 Kojda D. et al. Temperature-dependent thermoelectric properties of individual silver nanowires. Temperature-dependent thermoelectric properties of individual silver nanowires. *Physical Review B*. 2015. Vol. 91, pp. 024302.
- 3 Kim T.Y., Cheol-Hwan Park, Marzar N. The electronic thermal conductivity of grapheme. *Nano. Lett.* 2016, pp. 1 – 15.
- 4 Eminov P.A., Ul'din A A, Sezonov Yu.I. Electron-phonon scattering and conductivity of a quantum cylinder in a magnetic field. *Physics of the Solid State*, 2011, Vol. 53, No. 8, pp. 1707–1713.
- 5 Babichev A.P., Babushkina N.A., Bratkovskii A.M., et al. *Physical values*. Handbook Energoatomizdat. Moskow, Russian, 1991, 1232 p. [in Russian]
- 6 Ziman J.M. *Electrons and Phonons. Theory of Transport Phenomena in Solids*. Oxford: Clarendonpress, 1960, 554 p.
- 7 Genzel L. Dielectric function and infrared absorption of small metal particles. *Zeitschriftfür Physik B Cond. Matter*. 1980, Vol. 37, pp. 93 – 101.
- 8 Kawabata A., Kubo R. Electronic properties of fine metallic particles. II. Plasma resonance absorption. *Jour. Phys. Soc. Japan*. 1966, Vol. 21, pp. 1765 – 1722.
- 9 Persson B.N.J. Polarizability of small spherical metal particles: influence of the matrix environment. *Surface Science*. 1993, Vol. 281, pp. 153 – 162.
- 10 Kucherenko M.G., Nalbandyan V.M. Polarizability spectra of magnetized layered nanocomposites with an anisotropic core or cladding and localized surface plasmons. *Journal of Optical Technology*. 2018, Vol. 85, Issue 9, pp. 524 – 530.
- 11 Saikin S.K., Eisfeld A., Valleau S., Aspuru-Guzik A. Photonics meets excitonics: natural and artificial molecular aggregates. *Nanophotonics*, 2013, Vol. 2, No. 1, pp. 21 – 38.
- 12 Sun Y., Giebink N.C., Kanno H., Ma B., Thompson M.E., Forrest R. Management of singlet and triplet excitons for efficient white organic light-emitting devices. *Nature*. 2006, Vol. 440, No. 7086, pp. 908 – 912.
- 13 Vielma J., Leung P.T. Nonlocal optical effects on the fluorescence and decay rates for admolecules at a metallic nanoparticle. *The Journal of chemical physics*. 2007, Vol. 126, No. 19, pp. 194704.
- 14 Lebedev V.S., Medvedev A.S. Plasmon-exciton coupling effects in light absorption and scattering by metal/J-aggregate bilayer nanoparticles. *Quantum electron*. 2012, No. 42(8), pp. 701 – 713.
- 15 Azarova N., Ferguson A., Jao van de Lagemaat, Rengnath E., Park W., Johnson J.C. Coupling between a Molecular-Transfer Exciton and Surface Plasmons in a Nanostructured Metal Grating. *Journal of Physical Chemistry Letters*. 2013, Vol. 4, No. 16, pp. 2658 – 2663.
- 16 Vasil'ev D.N., Koltsova E.S., Chubin D.A. Effect of the plasmon-exciton interaction on optical properties of core-shell nanoparticle. *Bulletin of the Lebedev Physics Institute*. 2010, Vol. 37, No. 3, pp. 87 – 88.
- 17 Kucherenko M.G., Nalbandyan V.M. Dipole Polarizabilities and Absorption Cross Sections of Two-Particle Nanoclusters of Conductive Homogeneous and Layered Particles with the Degenerate Electron Gas. *Russian Physics Journal*. 2017, Vol. 59, Issue 9, pp. 1425 – 1432.
- 18 Davydov A.S., Mjasnikov E.N. Absorption and dispersion of light by molecular excitons. *Phys. stat. sol.*, 1967, Vol. 20, pp. 153.

UDC 621.9.025.7:669.018.25

PROPERTIES OF TI/CU MULTILAYER COATINGS

Guchenko S.A.¹, Koval N.N.², Yurov V.M.¹, Krysina O.V.², Zavatskaya O.N.¹¹Karaganda State University. E.A. Buketova, Karaganda, Republic of Kazakhstan, exciton@list.ru²Institute of High Current Electronics, Siberian Branch, Russian, koval@hcei.tsc.ru

In this work, we used the cathodes Ti and Cu. Coatings were deposited on steel samples by the ion-plasma method on a vacuum unit while simultaneously spraying the above cathodes. Multilayer coatings were created as follows: Ti was applied for 2 minutes, then Ti+Cu for 2 minutes. A total of 100 layers were applied in an atmosphere of argon and nitrogen. An electron microscopic study was carried out on a MIRA 3 scanning electron microscope of the TESCAN company. The studies were carried out at an accelerating voltage of 20 kV and a working distance of about 15 mm. The optical microstructure was examined on a metallographic microscope Epiquant. The study of the microhardness of the coatings was carried out on a microhardness meter HVS-1000 A. The results of measuring the microhardness of TiN+(Ti+Cu)N in nitrogen show an increase in the hardness of the coating from the standard for titanium nitride TiN values $H = 20$ to $H = 30$ GPa. Electron microscopic studies have shown that TiN+(Ti+Cu)N coatings usually have a columnar structure with filamentous grains 2–5 nm in diameter, elongated in the direction of growth.

When titanium nitride TiN slides over ordinary carbon steel and at room temperature, the coefficient of friction is 0.9, and the coefficient of friction of the TiN+(Ti+Cu)N multilayer coating decreases by a factor of 3 and does not exceed 0.3. An increase in the hardness of the TiN+(Ti+Cu)N coating and a decrease in the friction coefficient by a factor of 3 together leads to a significant increase in wear resistance. This is especially important for cutting tools. If you add up all the advantages of the obtained coatings, including resistance to high-temperature oxidation and their relatively low cost, then you can expect that TiN + (Ti + Cu) N multilayer coatings will find wide application in the metalworking industry, engineering, energy and some other areas.

Keywords: coating, microstructure, microhardness, friction.

Introduction

According to the journal International Manufacturing Technology (Canada), the capacity of the global market for services for applying high-strength wear-resistant coatings is \$ 1.2 billion, with an annual growth of 10-15%, the capacity of the world market for equipment for applying such coatings is \$ 3.9 billion, with an annual growth of 11% . In the segment of equipment for applying protective - decorative coatings on consumer goods, the size of the world market is \$ 100–200 million. In the field of strengthening coatings, the size of the world market is \$ 2-3 billion per year. World leaders in the field of PVD coatings - HAUZER TECHNO COATING (Holland) and INFICON (association of companies BALZERS, LEYBOLD, PFIFFER and US INFICON). The cost of the equipment of such companies is \$ 1.2-1.45 million (German installation of the SS800 is \$ 1.2 million, Japanese UBMS-707 by KOBE STEEL Co. is \$ 1.45 million, and the Dutch HTC-1000 is \$ 1.2 million.), and corrosion-resistant coatings are formed by creating an undercoat by electroplating before applying the PVD coating. The current share of these companies in the EC countries is 38%. According to research by TRYKOR Inc. (USA), for a significant growth in the market for electroplating substitutes, it is necessary to reduce the cost of PVD equipment by 2 times. The price of equipment for applying PVD coatings of the company "Elan-Praktik" (Russia) - \$ 0.6 million. The cost of our software-controlled vacuum unit containing the original plasma generator for cleaning and nitriding parts; original magnetron sputtering system with copper targets; and two arc evaporators with titanium cathodes do not exceed \$ 0.14 million.

Along with the low cost of our installation, we can get cheap coatings due to simultaneous spraying of different cathodes and their multilayer alternation. This is the subject of this work. The

use of the Cu element as an additive in TiN was considered in [1–8]. When used as an additive for Cu, Ag, Ni, etc. in the TiN, ZrN, CrN, AlN, etc. systems, the following trend is observed (Figure 1). An increase in the concentration of the alloying additive leads first to an increase in the hardness of the coating to a certain maximum (Figure 1, b), after which an increase in the content of the additional element leads to a gradual decrease in hardness (Figure 1, a).

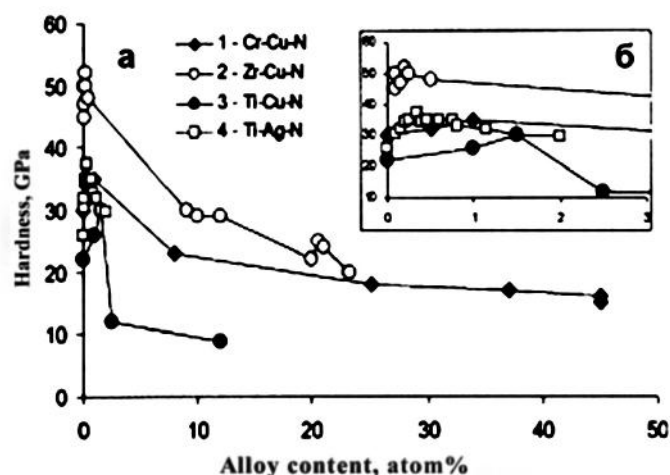


Fig.1 Dependence of the hardness of PM – N films on the content of Cu and Ag dopants [9]. Numbers 1–4 correspond to the data of [1–4].

The vacuum-arc plasma assisted coating deposition method used in [9] is based on the use of a non-independent arc discharge with a combined hot and hollow cathode (a source of gaseous plasma "PINK") and an independent arc discharge with a CP (electric arc evaporator with integral cold cathode), the first stage was carried out in a gas-discharge inert gas plasma generated by the PINK plasma source, with a negative potential (up to 1 kV) applied to metal substrates [10, 11].

To reveal the effect of plasma assisting on the structure, phase and elemental composition, as well as the physicomechanical characteristics of the coatings, thin (3-5 μm) nitride-titanium coatings are formed on substrates made of VK-8 alloy, molybdenum grade MCh and 12X18H10T stainless steel arc deposition with plasma assisted [9]. The ratio of the ion current densities of the gas and metal components (j_p / j_d) to the substrate was changed by spraying nitride coatings by changing the arc current of the original plasma source PINK from 0 to 1.6 at constant pressure of the working gas. A multilayer Ti/TiN coating with a layer thickness of 250 nm was also obtained [12-14]. A typical image of this coating is shown in Fig. 2.

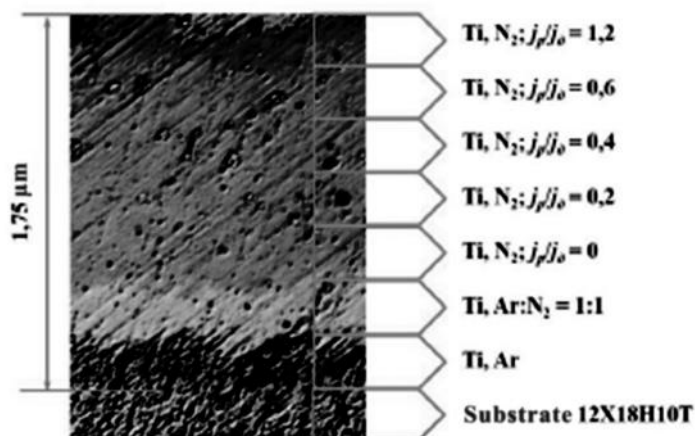


Fig. 2. A typical image of a transverse section of a multilayer Ti/TiN coating deposited on a steel substrate by a vacuum-arc plasma assisted method (optical metallography) [9].

The results of X-ray analysis show that the Ti – Cu – N coating consists mainly of titanium nitride crystallites. The presence of titanium with a hexagonal lattice type is due to the presence in the coating volume of a micro-droplet fraction characteristic of the vacuum-arc deposition method.

The size of coherent scattering regions (CSR) for Ti – Cu – N coatings before and after annealing, determined from the width of x-ray lines, increases from 16 to 20 nm, and to 25 nm, for the initial sample with a Ti – Cu – N coating, and after annealing at temperatures of 600 and 1100 °C. The lattice parameter for the initial Ti – Cu – N coating is slightly lower (0.42298 nm) than the standard value for TiN (0.425 nm).

After annealing at a temperature of 600 °C, the lattice parameter remains almost unchanged; after annealing at 1100 °C, its value increased to 0.42614 nm. In this case, the lattice deformation $\Delta d/d$ decreases by 4 times (from $7.7 \cdot 10^{-3}$ to $1.9 \cdot 10^{-3}$), which may indicate the relaxation of residual stresses [9].

1. Experimental technique

In this work, we used the cathodes Ti and Cu. The coatings were deposited on the steel samples by the ion-plasma method on a HNB-6.6I1 vacuum unit while simultaneously spraying the above cathodes. Multilayer coatings were created as follows: Ti was applied for 2 minutes, then Ti + Cu for 2 minutes. A total of 100 layers were applied in an atmosphere of argon and nitrogen.

An electron microscopic study was carried out on a MIRA 3 scanning electron microscope of the TESCAN company. The studies were carried out at an accelerating voltage of 20 kV and a working distance of about 15 mm. For each sample 4 shots were taken from 4 surface points at different magnifications: 245 times, 1060 times, 4500 times and 14600 times. Energy dispersive analysis was also performed at 4 points on the surface of each sample.

The optical microstructure was studied on an Epiquant metallographic microscope and, on a nanoscale, on an NT-206 atomic force microscope. The study of the microhardness of the coatings was carried out on the microhardness meter HVS-1000A.

2. Experimental results

Figure 3 shows the SEM image of the Ti / Ti + Cu multilayer coating, Figure 4 shows the multilayer EMF map, and Figure 5 shows the XPS spectrum.

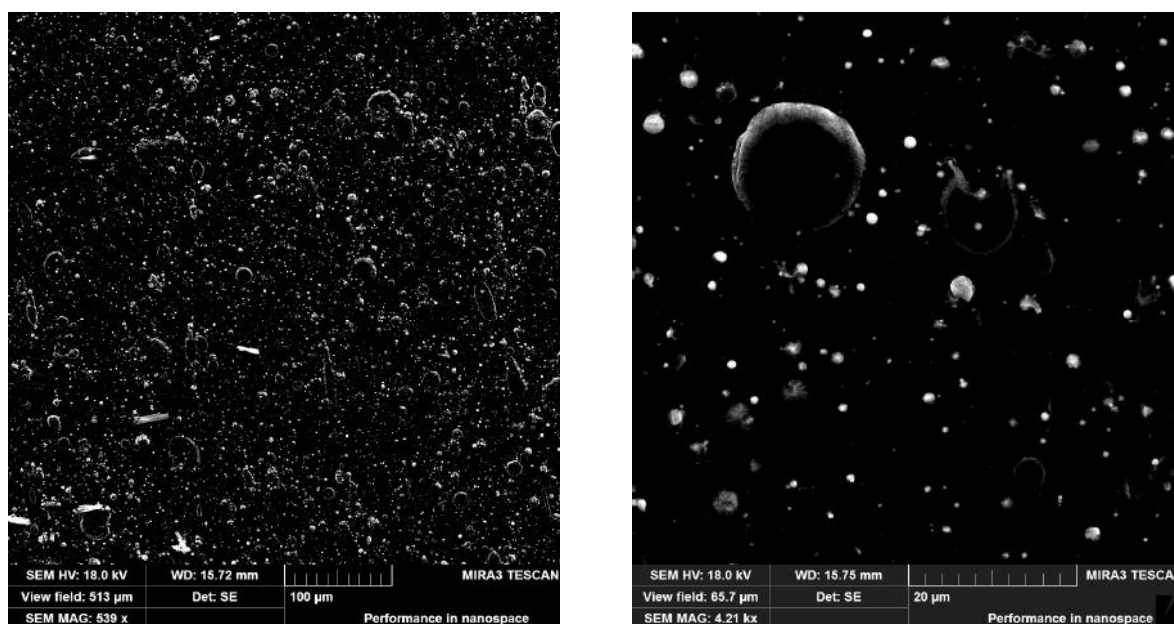


Fig. 3. SEM images of Ti/Ti+Cu at 2 magnifications

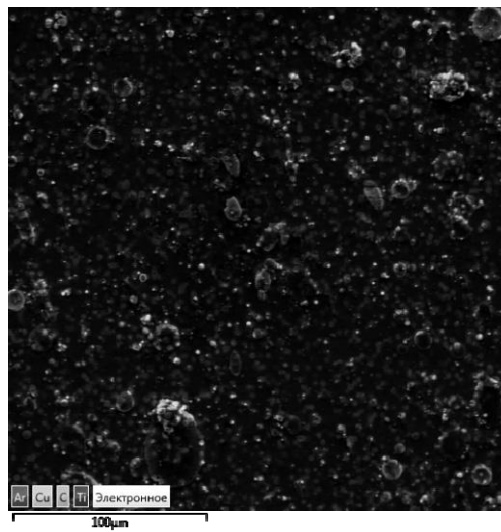


Fig.4. Multilayer EMF map

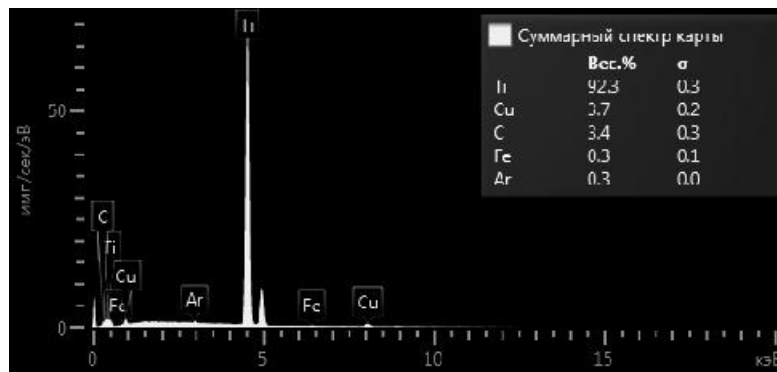


Fig.5. XPS spectrum of Ti / Ti + Cu coating

Figure 6 shows the SEM image of the TiN/(Ti+Cu)N multilayer coating, Figure 7 shows the multilayer EMF map, and Figure 8 shows the XPS spectrum.

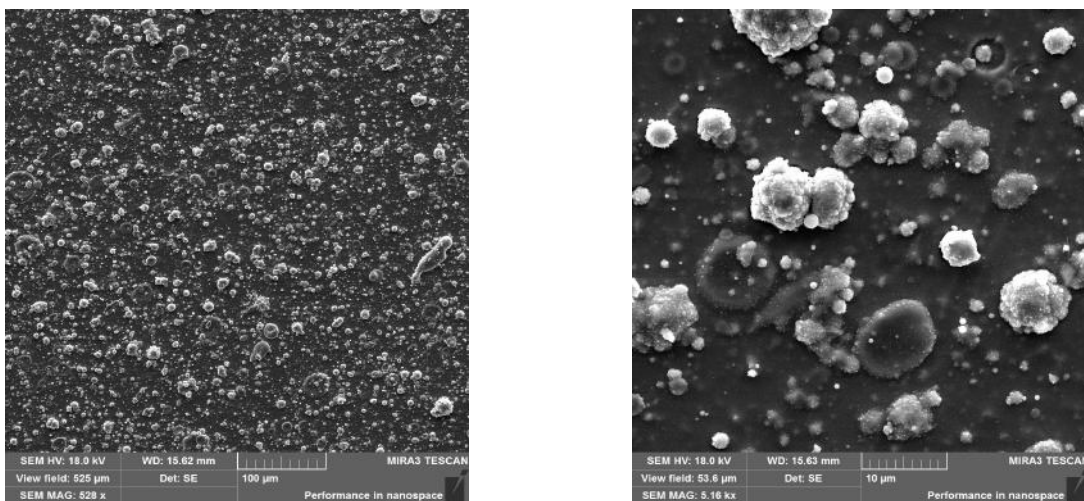


Fig.6. SEM images of TiN/(Ti+Cu) at 2 magnifications

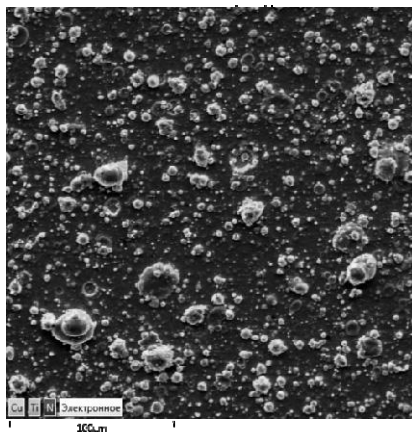


Fig.7. Multilayer EMF map

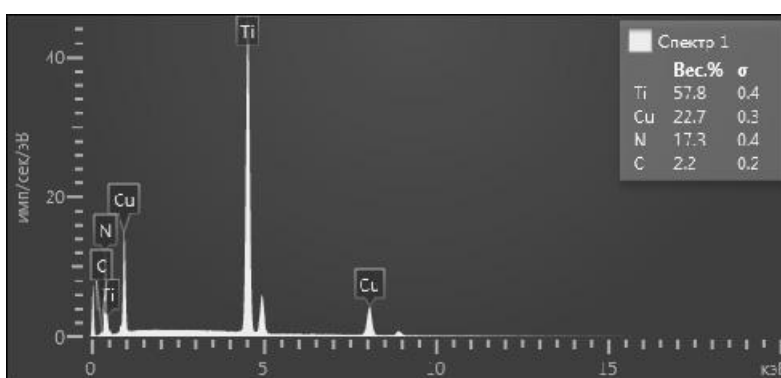


Fig.8. XPS spectrum of TiN/(Ti+Cu)N coating

The results of measuring the microhardness of Ti+(Ti+Cu) in argon and TiN+(Ti+Cu)N in nitrogen are presented in Table 1, and the optical images in Figures 9 and 10.

Table 1 - Microhardness Ti+(Ti+Cu) in argon and TiN+(Ti+Cu)N in nitrogen

| coating | HV0.1 | HV0.025 | HV0.01 |
|--------------|--------|---------|--------|
| Ti+(Ti+Cu) | 499,4 | 539,9 | 559,8 |
| TiN+(Ti+Cu)N | 2288,2 | 2828,5 | - |

The mean value $\mu = 2558$ HV in nitrogen is almost 5 times greater than in argon $\mu = 533$ HV.

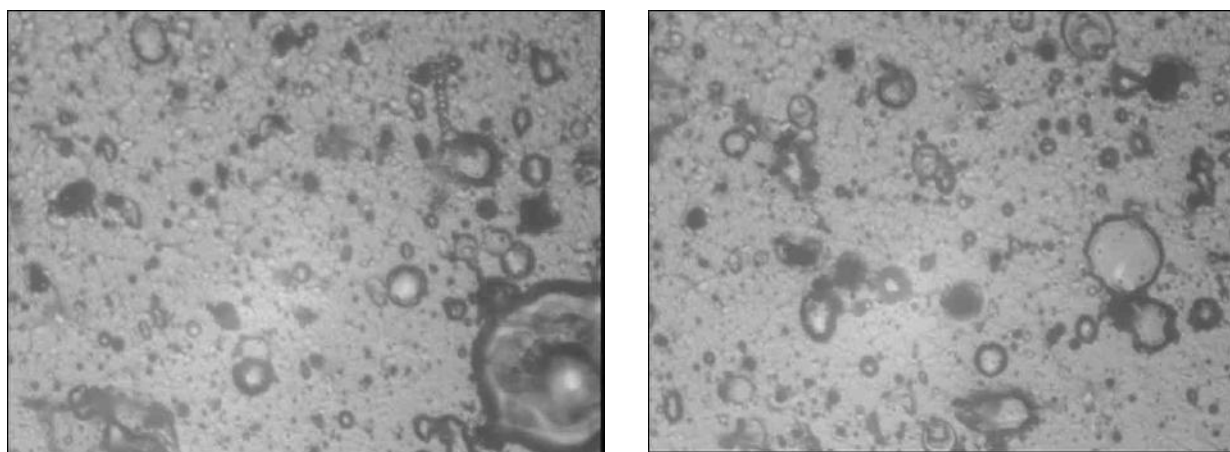


Fig.9. Pictures of the coating Ti+(Ti+Cu) in argon

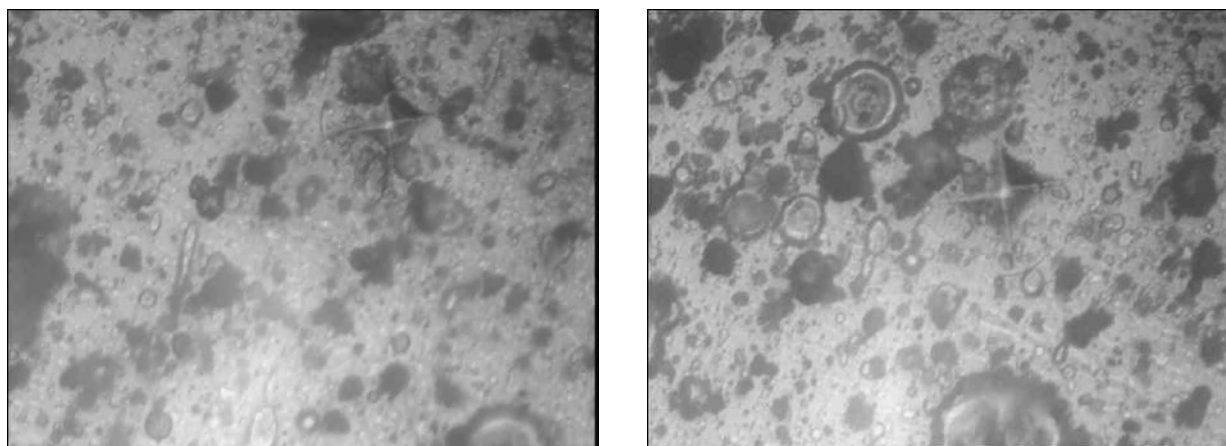


Fig.10. Pictures of TiN+(Ti+Cu)N coating in nitrogen

The results of measuring the friction coefficient of Ti+(Ti+Cu) in argon and TiN+(Ti+Cu)N in nitrogen are presented in Table 2.

Table 2 - Coefficient of friction of Ti+(Ti+Cu) coatings in argon and TiN+(Ti+Cu)N in nitrogen

| coating | μ_1 | μ_2 | μ_{cp} |
|--------------------|---------|---------|------------|
| Uncoated substrate | 0,154 | 0,148 | 0,151 |
| Ti+(Ti+Cu) | 0,247 | 0,220 | 0,234 |
| TiN+(Ti+Cu)N | 0,306 | 0,310 | 0,308 |

3. Discussion of the results of the experiment

From table 1 it follows that the average value $\mu = 2558$ HV in nitrogen is almost 5 times greater than in argon $\mu = 533$ HV. These values are obtained at optimal values of the arc current, the pressure of the reaction gas, the magnitude of the reference voltage and the temperature of the substrate. We have established:

- grinding the grain structure of the coating material with increasing substrate temperature is accompanied by an increase in hardness to some critical average size of nanograin. The decrease in hardness with a further decrease in the average grain size in the coating is due to slippage along grain boundaries (rotational effect). In this case, to further increase the hardness, it is necessary to slow down the process of sliding along grain boundaries. Such inhibition can be achieved due to the formation of an appropriate nanostructure with hardening of grain boundaries. The optimum temperature of the substrate or part is 400 - 450 ° C;

- in most cases, with an increase in the arc current of the evaporator, the microhardness decreases. This is due to the fact that with an increase in the arc current of the evaporator, the coating thickness increases quite quickly, and this leads, in turn, to an increase in the dislocation density in the coating being formed. The optimal value of the arc current $I = 110$ A;

- it was experimentally shown that the samples obtained at nitrogen pressure $P = 0.081\text{--}0.81$ Pa have the most evenly distributed fine dense structure, the minimum content of the droplet phase, pores, influxes, delaminations and the highest microhardness values;

- variation of the reference voltage leads to a significant (more than two times) change in the microhardness of the coatings. Thus, the reference voltage is an important technological regime that determines the strength properties of coatings. It should be noted that the main reason for the reduction of microhardness is the microstructure of the coating, so in the absence of a reference

voltage, the coating is characterized by equiaxial grain size, while at $U = -210$ V there is a columnar structure germinating from the substrate.

Conclusion

The results of measuring the microhardness of TiN+(Ti+Cu)N in nitrogen show an increase in the hardness of the coating from the standard for titanium nitride TiN values $H = 20$ to $H = 30$ GPa. Electron microscopic studies have shown that TiN+(Ti+Cu)N coatings usually have a columnar structure with filamentous grains 2–5 nm in diameter, elongated in the direction of growth.

An increase in the hardness of multilayer coatings with a layer thickness of about 100–150 nm is due to the fact that the generation of dislocations is retarded by the Frank – Read mechanism [15]. If the coating thickness does not exceed 100 - 300 nm, then the film, as a rule, has not a solid, but an “island” structure. A multilayer coating of layers whose thickness does not exceed 300 nm is a special kind of material, the so-called multilayer composite (nanocomposite) [16]. In fact, a multilayer composite combines high-strength, virtually defect-free layers and defects in the form of interfaces between the layers. The essence of the proposed technology for deposition of multilayer nanostructured vacuum ion-plasma coatings of the Ti-Cu-N system is that in a single operating cycle it is provided to combine arc discharges of cathodes made of titanium and copper burning in pairs with a non-self-sustained high-current discharge [9-11].

When titanium nitride TiN slides over ordinary carbon steel and at room temperature, the friction coefficient is 0.9. From table 2 it can be seen that the coefficient of friction of the TiN+(Ti+Cu)N multilayer coating decreases by a factor of 3 and does not exceed 0.3. An increase in the hardness of the TiN+(Ti+Cu)N coating and a decrease in the friction coefficient by a factor of 3 together leads to a significant increase in wear resistance. This is especially important for cutting tools [17].

If you add up all the advantages of the obtained coatings, including resistance to high-temperature oxidation and their relatively low cost, then you can expect that TiN+(Ti+Cu)N multilayer coatings will find wide application in the metalworking industry, engineering, energy and some other areas.

The obtained experimental data show the promise of the developed coatings in many branches of industrial production. In carrying out this work, the fundamental results obtained in the Laboratory of Plasma Emission Electronics (LETEE) of the Institute of Electrical Engineering, Siberian Branch of the Russian Academy of Sciences were taken into account.

Acknowledgements

This work was supported by the Ministry of the Republic of Kazakhstan.
Grants No.0118PK000063 and No. Φ .0780.

REFERENCES

- 1 Andreasen K.P., Jensen T., Petersen J.H., Chevallier J., Bottiger J., Schell N. The structure and the corresponding mechanical properties of magnetron sputtered TiN–Cu nanocomposites. *Surface and Coatings Technology*. 2004, Vol. 182, pp. 268 – 275.
- 2 Li Z.G., Miyake S., Kumagai M., Saito H., Muramatsu Y. Hard nanocomposite Ti–Cu–N films prepared by d.c. reactive magnetron co-sputtering. *Surface and Coatings Technology*. 2004, Vol. 183, pp. 62–68.
- 3 Myung H.S., Han J.G., Boo J.H. A study on the synthesis and formation behavior of nanostructured TiN films by copper doping. *Surface and Coatings Technology*. 2004, Vol. 177–178, pp. 404–408.
- 4 Zhang L., Ma G.J., Lin G.Q., Han K.C., Ma H. Synthesis of Cu doped TiN composite films deposited by pulsed bias arc ion plating. *Nuclear Instruments and Methods in Physics Research: B*. 2014, Vol. 320, pp. 17 – 21.

- 5 Gurskih A.V. *Development of sintered Ti-Cu, Ti-Si cathodes for ion-plasma deposition of nanostructured nitride coatings*. Thesis for the degree of Candidate of Technical Sciences. Tomsk, 2012, 150p.
- 6 Ivanov Yu.F., Koval N.N., Krysina O.V. at el. Superhard nanocrystalline Ti-Cu-N coatings deposited by vacuum arc evaporation of a sintered cathode. *Surface and Coatings Technology*. 2012, Vol.207, pp. 430–434.
- 7 Krysina O.V., Ivanov Yu.F., Koval N.N. Thermal stability of nanocrystalline ternary system coatings based on TiN. *Russian Physics Journal*. 2012, No. 12/2, pp. 179 – 183.
- 8 Ivanov Yu.F., Koval N.N., Krysina O.V. at el. Investigation of the effect of impurities on the synthesis of nanocrystalline layers of titanium nitride from electric arc plasma. *Russian Physics Journal*. 2010, No. 3/2, pp. 119–124.
- 9 Krysina O.V. *Generation of gas-metal plasma in low-pressure arc discharges for the synthesis of multicomponent nanocrystalline protective coatings*. Thesis for the degree of Candidate of Technical Sciences. Tomsk, 2016, 23 p.
- 10 Koval N.N., Ivanov Yu.F., Lopatin I.V. at el. Generation of low-temperature gas-discharge plasma in large vacuum volumes for plasma-chemical processes. *Russian chemical journal*. 2013, Vol. LVII, No. 3-4, pp. 121 – 133.
- 11 Krysina OV, Lopatin IV, Koval N.N. at el. Influence of low-pressure arc discharge modes and the gas-discharge plasma generated by it on etching the surface of materials *Russian Physics Journal*. 2014, No.3/3, pp. 176 – 179.
- 12 Dobrzanski L.A., Adamiak M. Structure and properties of the TiN and Ti(CN) coatings deposited in the PVD process on the high-speed steels. *Journal of Materials Processing Technology*. 2003, Vol. 133, pp. 50 – 62.
- 13 Boxman R.L., Zhitomirsky V.N., Grinberg I. at el. Structure and properties of vacuum arc deposited multi-component nitride coatings of Ti, Zr and Nb. *Surface and Coatings Technology*. 2000, Vol.125, pp. 257 – 260.
- 14 Musil J., Vlcek J., Baroch P. Magnetron discharges for thin films plasma processing / Materials surface processing by directed energy techniques. Edited by Y. Pauleau. London: Elsevier, 2006, pp. 67–110.
- 15 Blagoveshchensky V.V., Panin I.G. Building a dynamic model of the Frank-Reed dislocation source. *Computational technologies*. 2008, Vol.13, No. 5, pp. 5 – 11.
- 16 Gusev A.I. *Nanocrystalline materials: Methods of preparation and properties*. Yekaterinburg: NISO UB RAN, 1998, pp. 205 – 212.
- 17 Tabakov V.P., Chikhranov A.V. *Wear-resistant coating cutting tools operating in continuous cutting*. Ulyanovsk: UISTU, 2007, 255 p.

UDC 548.522

CHEMICAL VAPOR DEPOSITION GROWTH OF WS₂ CRYSTALS

Shaikenova A.^{1, 2*}, Beisenov R.^{1, 2}, Muratov D.^{1, 2}

¹Satbayev University, 22a Satpayev St., Almaty 050013, Kazakhstan

²LLP «Institute of Physics and Technology», 11 Ibragimov St., Almaty 050032, Kazakhstan

*altynay.shaikenova@mail.ru

The synthesis and characterization of WS₂ single crystals grown by chemical vapor deposition (CVD) method thru sulfurization of tungsten oxide thin layer on quartz substrate studied. Synthesis of WS₂ carried out at 800-1000 °C in CVD system. The sulphur vapor transported by argon gas (500 sccm). Obtained WS₂ single crystals characterized by optical microscope, Raman and photoluminescence analysis. Optical microscope analysis demonstrated that triangular WS₂ domains with single-phase crystal structure formed. The thickness of WS₂ is 6 layers, which determined by Raman spectroscopy. Photoluminescence spectroscopy analysis revealed a strong peak between 600-660 nm, typically for a monolayer WS₂ crystal, where the band gap is equal to 1.96 eV.

Keywords: transition metal dichalcogenide, chemical vapor deposition, tungsten oxide.

Introduction

Two-dimensional (2D) materials have significantly different electronic and physical properties than bulk materials, due to electron localization and lack of interlayer interaction, see Figure 1. Optical and physical properties of monolayers of transition metal dichalcogenides (TMDs) have new possibilities for nanoelectronic and optoelectronic devices. Two-dimensional (2D) materials are quite interesting for the manufacture of photosensitive devices, such as photodetectors, multifunction memory devices. In addition, the hybridization of WS₂ layers with other two-dimensional (2D) layered materials intensively studied for fabricating vertical and planar heterostructures. Recently, the synthesis of laminates MoS₂ and WS₂ studied in several approaches, such as mechanical exfoliation, liquid exfoliation and sulfurization of transition metals and oxides of these metals. The CVD method can be more promising for growing a high-quality WS₂ thin sheet [1, 2].

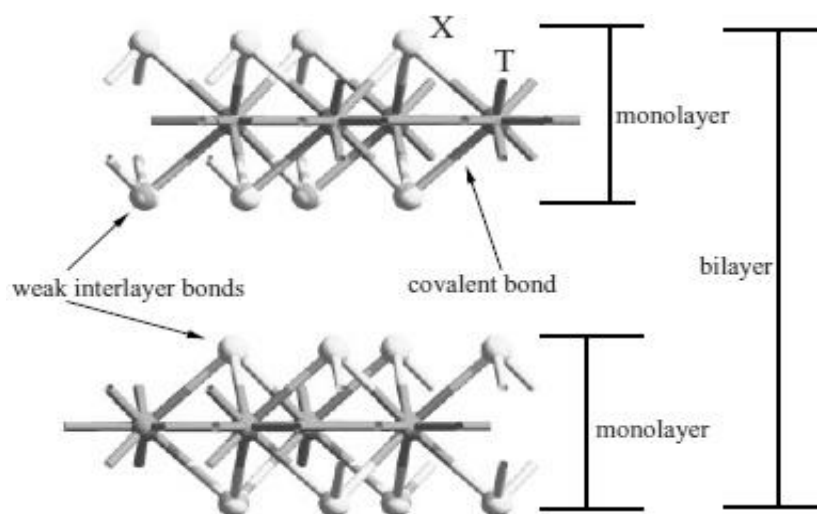


Fig.1. 2D transition metal dichalcogenides.

New 2D optoelectronic devices created by integrating various 2D materials into heterostructures with unique characteristics. However, the synthesis of graphene and related 2D materials and heterostructures remains a problem; therefore, the development of new methods is a quite interesting area of research. Chemical vapor deposition (CVD) recognized as the most effective method for the synthesis of graphene and many other 2D materials.

1. Experimental section

CVD complex setup for the synthesis of two-dimensional materials designed and assembled, see Figure 2, mentioned in previous work [3]. The CVD consist from quartz tube with three heating zones, which operated by thermo controllers. There are gas supply systems controlled by MKS. In addition, there is a pump for reach vacuum. A magnet sample holder used to fix or move out sample in quartz reactor. Therefore, synthesis parameters such as temperature, pressure and gas flow can be managed at the CVD system.



Fig. 2. Main view of the CVD setup

A detailed study of the growth of individual grains of WS_2 carried out in this CVD system. A quartz substrate with a small amount of nanosized WO_3 powder used. The temperature of WO_3 powder is $900\text{ }^\circ\text{C}$ and supplying inert gas flow with the chalcogen vapor through the powder surface, sublimated WS_2 droplets formed on the quartz substrate (Figure 3).

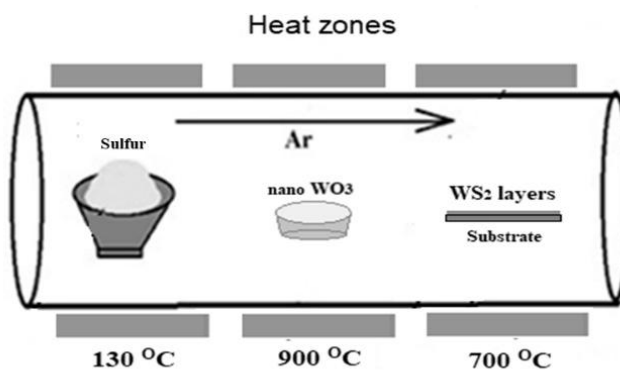


Fig.3. Synthesis of 2-D TMD layers

2. Results and discussion

There is a high-resolution optical microscopy analysis in Figure 4 shows the formation of a two-dimensional layer of a separate domain WS_2 . In the middle of the crystal, a sublimated WS_2 nucleus distinctly observed, which reacts with tungsten and sulphur oxide pairs to form oriented layers of a two-dimensional material.

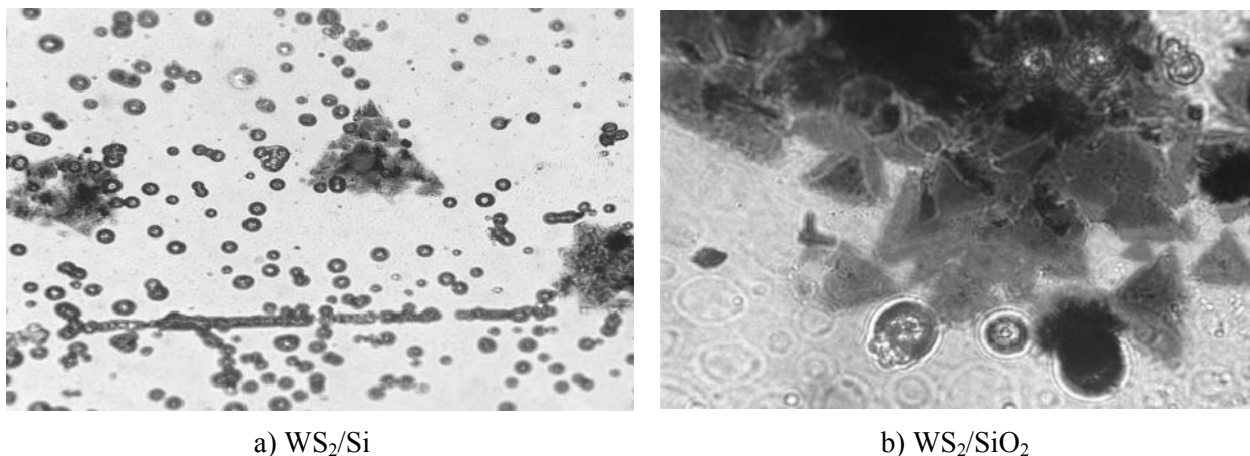


Fig.4. Optical microscope pictures of WS_2 grains: a) onto Si substrate; b) onto SiO_2 substrate

Raman spectroscopy of a grown single crystal of a WS_2 crystal studied using a laser with a wavelength of 514 nm and shows the formation of peaks E_{2g} and A_{1g} modes, which are refer to WS_2 crystals, Fig.5. The intensity of the peaks is almost the same. The choice of the laser length in this wavelength range is due to a more detailed and informative parameter for determining the thickness of the obtained layers compared to other lasers. An analysis of the intensity of the phonon peaks presupposes the formation of a thickness of the region of the contour of the WS_2 crystal in 6 layers.

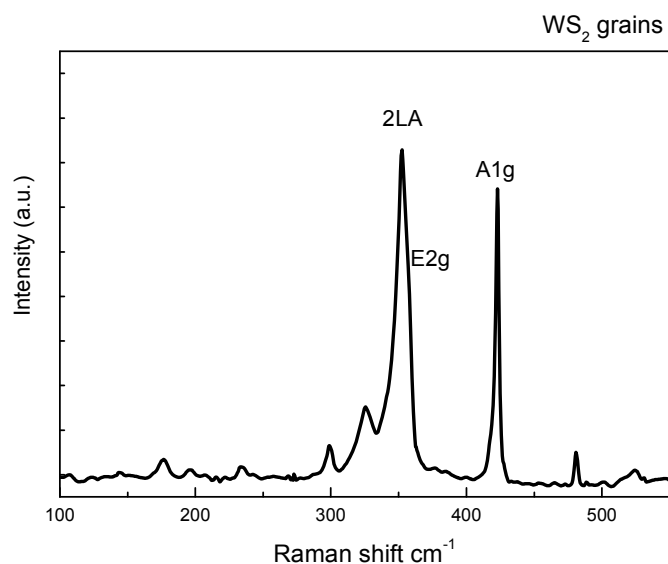


Fig.5. Raman spectroscopy of WS_2 crystal

Figure 6 shows the photoluminescence spectrum of WS_2 grains. The photoluminescence spectrum of a separately synthesized WS_2 crystal showed a band gap value of 1.92 eV in the wave band of 600-660 nm.

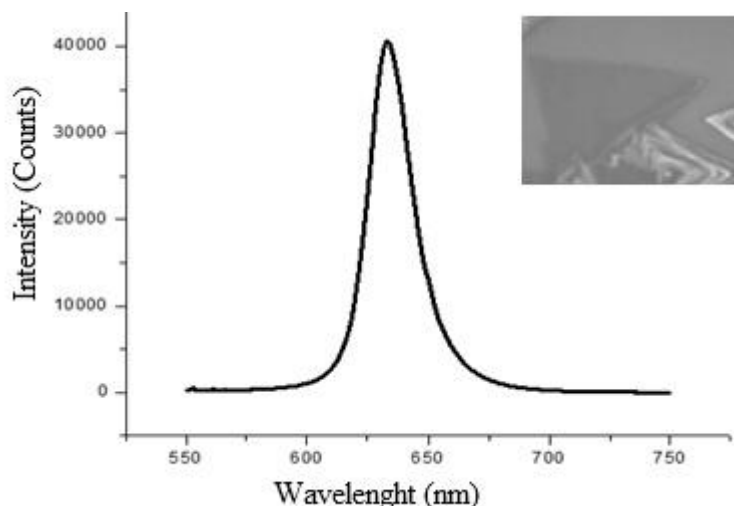


Fig.6. Photoluminescence spectrum for produced WS₂ single crystals

The results suggest that the mechanism of grain growth of 2D TMD single-crystal arrays is possible, with direct control of the nucleation process during the initial growth of 2D TMD films, to minimize the formation of crystallization centres in random places and the formation of inclined and specular grain structures.

Conclusion

Obtained WS₂ single crystals characterized by optical microscope, Raman and photoluminescence analysis. Optical microscope analysis demonstrated that triangular WS₂ domains with single-phase crystal structure formed. The thickness of WS₂ is 6 layers, which determined by Raman spectroscopy. Photoluminescence spectroscopy analysis revealed a strong peak between 600-660 nm, typically for a monolayer WS₂ crystal, where the band gap is equal to 1.96 eV. In the further study hybrid multilayer heterostructures based on graphene will developed, where 2D-TMD layers and nanoparticles will deposit on grown graphene layers by using various techniques for further investigation of their electrical and optical characteristics.

Acknowledgements

This research was funded the program AP05132763 «Development and study of graphene based heterostructures for photocatalytic systems and gas sensors applications» by the Ministry of Education and Science of the Republic of Kazakhstan.

REFERENCES

- 1 Zeng H. L. , Liu G.B., Dai J., Yan Y., Zhu B., He R., Xie L., Xu S., Chen X., Yao W., Cui X. «Optical signature of symmetry variations and spin-valley coupling in atomically thin tungsten dichalcogenides» *Sci. Rep.*, 2013 , Issue 3, pp. 1608.
- 2 Matte H. S. S. R., Gomathi A., Manna A. K., Late D. J., Datta R., Pati S. K., Rao C. N. R., «MoS₂ and WS₂ analogues of graphene», *Angew Chem Int Edit.*, 2010, Issue 49, pp. 4059 .
- 3 Shaikenova A., Beisenov R.Ye., Muratov D.A., «Synthesis of graphene by chemical vapor-phase deposition (CVD) », *Proceeding of the 10th International Scientific Conference «Chaos and Structures in Nonlinear Systems. Theory and Experiment»*, Almaty, June 16-18, 2017, pp. 310 – 314.

UDC 548.522

STUDYING THE MECHANISM OF GRAPHENE FORMATION BY CHEMICAL VAPOR DEPOSITION SYNTHESIS

Shaikenova A.^{1, 2*}, Beisenov R.^{1, 2}, Muratov D.^{1, 2}

¹Satbayev University, 22a Satpayev St., Almaty 050013, Kazakhstan

²LLP «Institute of Physics and Technology», 11 Ibragimov St., Almaty 050032, Kazakhstan

*altynay.shaikenova@mail.ru

Due to their unique properties, 2D materials have a great potential in various applications. It argued that chemical vapor deposition (CVD) method is widely used in the synthesis of graphene. In this paper the experiments results of the synthesis of graphene layers by Chemical Vapor Deposition (CVD) method on the copper (Cu) foil discussed. However, desired quality of graphene layers is not always achievable. Therefore, controllable synthesis in domain size and morphology is required for large-scale applications. Examples of the synthesis parameters of polycrystalline and monocrystalline graphene are given. Mechanism of graphene formation studied during the synthesis process. The sample preparation processes and the main growth mechanisms of multilayer and single-layer graphene by the CVD method discussed. Obtained CVD graphene layers characterized by Raman, AFM and SEM analysis.

Keywords: two-dimensional materials, synthesis, CVD, graphene;

Introduction

Graphene is the first representatives of two-dimensional materials. It is quite interesting material with the thickness of one layer of carbon and has a hexagonal modification. Due to their unique properties, graphene has a potential in the various applications for science and technologies, particular in electronics.

There are a few methods of two-dimensional materials synthesis such as mechanical exfoliation, chemical methods. The mechanical exfoliation is top-down type means splitting of large structures like graphite. The first graphene layers obtained with this method by Gale and Novoselov. The second method is the types of chemical vapor deposition, where the formation of structures comes from the gaseous phase during the decomposition of hydrocarbons.

The CVD synthesis recognized as a reliable method of obtaining high-quality two-dimensional (2D) materials [1]. The production of mono and polycrystalline graphene by the CVD method is two different process, but similar as well. However, there are several key factors, which are distinguishing the single-crystal graphene growth on CVD. One of the main parts for single-crystal graphene growth is preventing the premature crystallization. In addition, the substrates treatment such as elimination of impurities, oxides, defects and other structures contribute to the nucleation and graphene growth. The effect of precursor concentration is also an important factor in the growth of single crystals graphene. One of the main advantages is controlling the synthesis parameters, which allows the synthesis of graphene desired size. Where the synthesis parameters include chamber pressure, temperature heating and cooling, synthesis time, and gas composition and flow rate.

The process shown here is suitable to obtain single-crystal graphene with wafer size. In order to achieve this, deep understanding of graphene growth mechanism and requirements for graphene grain growth needed. According to data, the Cu based graphene growth mechanism (Figure 1a) and reaction conditions are shown where graphene nucleation density is reduced and possibility of growing larger graphene domains by using an extended growth conditions (Figure 1b) [1].

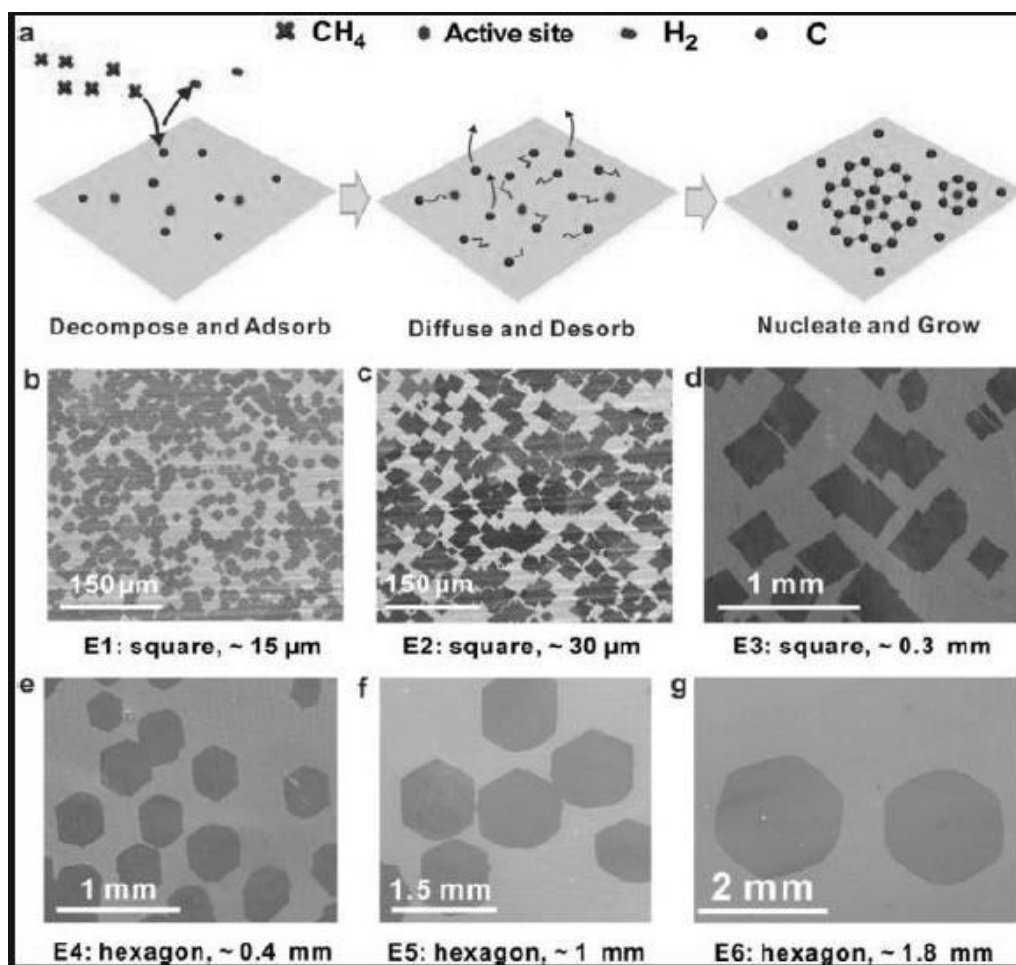


Fig.1. Illustration of the Cu-based graphene growth mechanism and the influence of different parameters on the graphene domain sizes and shapes. (a) Scheme for the Cu-based graphene growth mechanism. Here, red hexagons are used to symbolize the active sites of the Cu surface, and blue spots signify active carbon species $(CH_{x<4})_s$. From the proposed mechanism, the active carbon species from the dissociated CH_4 are apt to agglomerate into thermodynamically stable $(C_nH_y)_s$ species on the active sites of the Cu surface to initialize the graphene growth. (b-g) Typically SEM images of graphene synthesized under different growth conditions: b (E1), c (E2), d (E4), f (E5), and g (E6) [1]

Many studies point to the importance of oxygen in the process of single-crystal graphene growth by the CVD method. Gan et al. showed that soft oxidation of copper substrate before annealing leads to obtain suitable size of copper nanoparticles (Fig. 2a, b) [3]. Copper nanoparticles contributed to nucleation and growth of large single crystals of graphene. In this work, the onset of oxidation identified as the microscopic amount of oxygen in the Ar gas stream or residual oxygen in the CVD chamber. Hao et al. conducted a detailed study of the effect of oxygen at CVD synthesis of graphene process (Fig. 2c) [4]. Different concentrations of oxygen on copper substrate studied by using copper foils with different purity classes, changing the pressure during cleaning process and supplying pure oxygen before graphene growth. Studies have shown that oxygen on the surface of copper substrates reduces the concentration of active centers by surface etching. Thus suppresses early nucleation and promotes the growth of a single-crystal graphene structure.

Magnuson et al. proposed a new view on the role of oxygen in the process of oxidation of copper substrates [5]. Intentionally oxidizing copper substrates formed a layer of copper oxide, which decompose during subsequent annealing and synthesis processes, thereby eliminating residual carbon from the substrate. This behavior called "self-cleaning". There are also other excellent studies of the observation of graphene growth [6].

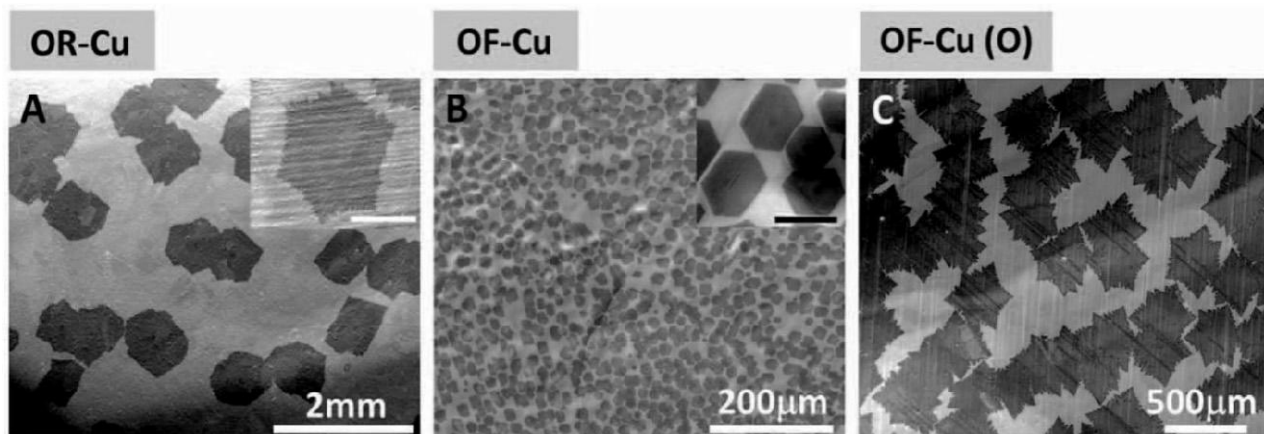


Fig.2. The effect of oxygen on nucleation density and shape of domains on different types of copper substrates: OR-Cu (a) low purity copper substrate; OF-Cu (b) high-quality copper substrate; OF-Cu (O) (c) high-purity copper substrates when exposed to oxygen before the start of graphene deposition [5]

However, a deeper understanding of the influence of oxygen desired in order to understand the full role and mechanism of oxygen atoms while achieving excellent control over the process.

1. Experimental part

CVD setup assembled at the Institute of Physics and Technology (Fig. 3), which includes three zones tube furnace with quartz reactor, and installed gas inlet system. In this system, triple gas supply used: argon, hydrogen and methane.

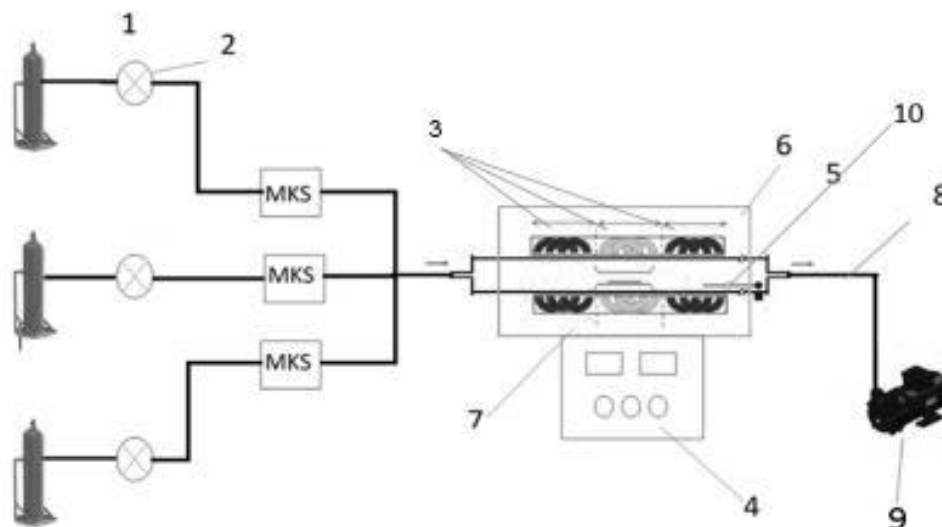


Fig.3. CVD setup for graphene synthesis: 1 - cylinders with gases (Ar, CH₄, H₂); 2 - gearboxes; 3- gas supply controllers; 4 - thermal controller; 5 - quartz tubular reactor; 6 - heating elements; 7- metal substrate; 8- pumping line; 9- mechanical pump; 10-holder; 11-magnet.

Methane plays the role of carbon source for graphene formation. Optimal parameters selected, synthesis of graphene carried at 1050 °C, and the ratio of gases: CH₄: H₂: Ar is 0.25: 0.5: 3. The synthesis time is 20 minutes.

2. Results and discussion

Graphene synthesized on copper substrate, due to its catalytic properties, copper is one of the main materials used in graphene synthesis. In studying the graphene formation on copper substrate was determined that the initial stage is carbon atoms adsorption on the surface. Then, graphene islands formation with same orientation. Subsequently, association of separate graphene islands without defects on the boundaries and high-grade monocrystalline graphene layer (Fig.4).

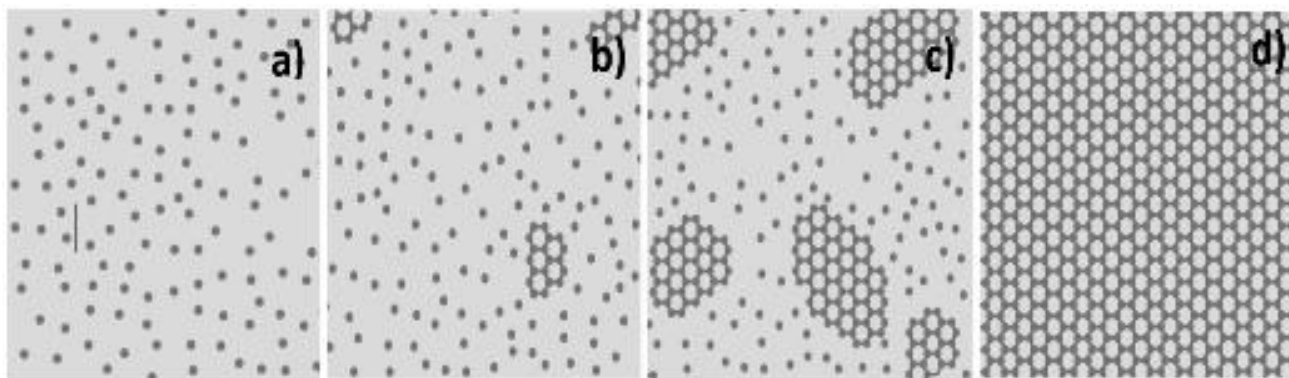


Fig.4. Schematic representation of the mechanism of graphene growth by CVD:

- a) Carbon atoms; b) carbon atoms starting adsorption on the surface; c) growing separated graphene islands with same orientation; d) growing into the whole domain without defects on boundaries;

Ideally, a layer of graphene should formed, but as practice shows, the formation takes place in a semi crystalline order, this indicates individual islands of graphene with different orientations that begin to grow in unite, and then these boundaries form a semi crystalline structure. However, this structure cannot used in electronics due to lack of uniformity (Fig.5).

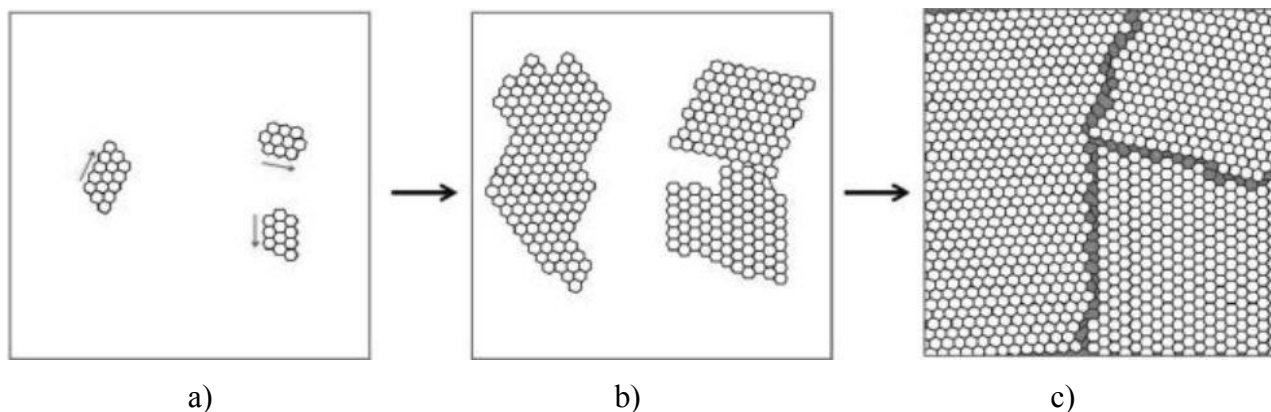


Fig.5. The formation of polycrystalline graphene:

- a) Formation of graphene islands with different orientation; b) graphene islands are spread out; c) growing into the whole domain with defects on boundaries;

In connection with this, a technique for the growth of individual graphene crystals from nucleation was developed. PMMA (polymethyl methacrylate) used for nucleation [7]. At Institute Physics and Technology, the PMMA applied through a pattern mask by photolithography method, and then separate PMMA grains obtained, which then during the high-temperature process residual polymer evaporated and only grains remained during the decomposition of the polymer, that is, definitely oriented carbon points. Next was the process of synthesis. Separate graphene islands obtained in Figure 6.

Figure 6 shows SEM images of synthesized graphene arrays onto PMMA grains with thickness of 2 and 0.4 microns. It is clear seen irregular shaped graphene islands; however, there are some islands close to the hexagonal structure.

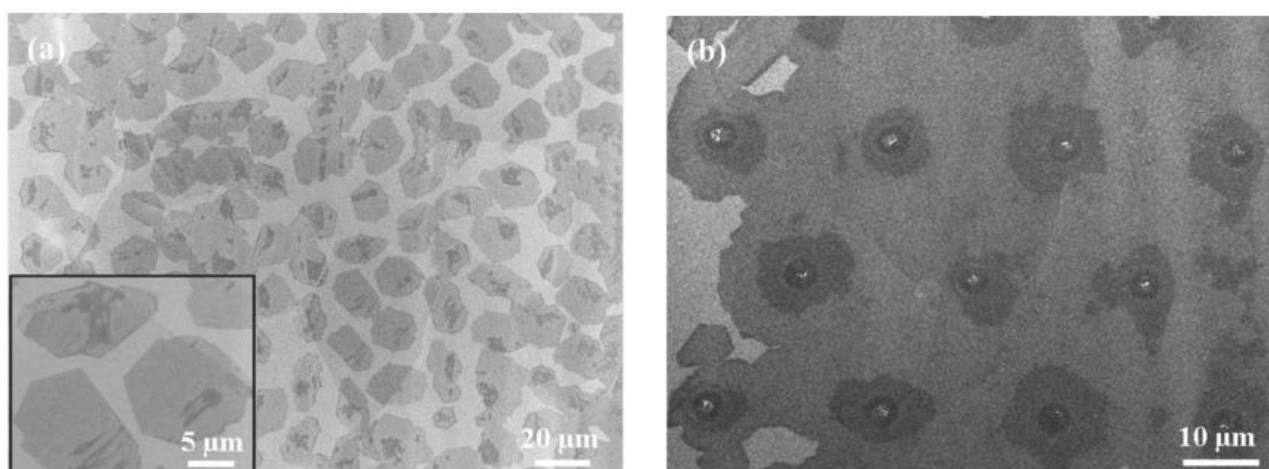


Fig.6. SEM image of graphene grains grown from PMMA grains on a copper substrate:

a) The thickness of PMMA grains are 0.4 microns; b) the thickness of PMMA grains are 2 microns;

Obtained results can be explained that mainly formation of polycrystalline, which consists of several grains. The dark areas on each island indicate several single-layer graphene domains, which formed due to solid carbon precursor (PMMA). As increasing the PMMA grains thickness to 2 microns (Figure 6b) at the same CVD synthesis process, the formation of graphene layer continuously in several layers of domains. Residual PMMA clearly observed on the image as white dots. By controlling the amount of PMMA, growth of graphene films with bi- or more layers become achievable.

Conclusion

New materials based on graphene are promising in photocatalytic systems and gas sensors application. Due to the unique properties of graphene, it is possible to improve the photocatalytic characteristics by introducing it into various semiconductor photocatalysts. Such as adsorption, capacity and electrical conductivity will increase at extended light absorption range [9]. The role of graphene considered as a mediator for electron transfer, which leads to efficient separation of photo generated electron-hole pairs and improving photocatalytic performance. Moreover, it is noted that graphene could also effectively be used as a substitute for noble metals (such as Pt) in the photocatalytic decomposition of water [10].

In further study will develop hybrid multilayer heterostructures based on graphene, 2D-TMD layers, and nanoparticles, which will deposit or grow on graphene layers using various techniques for further investigation of their electrical and optical characteristics. Heterostructures based on graphene has a great opportunity in various applications.

Acknowledgements

This research was funded the program AP05132763 «Development and study of graphene based heterostructures for photocatalytic systems and gas sensors applications» by the Ministry of Education and Science of the Republic of Kazakhstan.

REFERENCES

- 1 Yan Z., Lin J., Peng Z., Sun Z., Zhu Y., Li L., Xiang C., Samuel E. L., Kittrell C. and Tour J. M. Toward the synthesis of wafer-scale single-crystal graphene on copper foils. *ACS Nano*, 2012, Issue 6, pp. 9110 – 9117.
- 2 Mehdipour H. and Ostrikov K., Kinetics of Low-Pressure, Low-Temperature Graphene Growth: Toward Single-Layer, Single-Crystalline Structure. *ACS Nano*, 2012, Issue 6, pp. 10276 – 10286.
- 3 Gan L. and Luo Z. Turning off Hydrogen to Realize Seeded Growth of Subcentimeter Single-Crystal Graphene Grains on Copper. *ACS Nano*, 2013, Issue 7, pp. 9480 – 9488.
- 4 Hao Y., Bharathi M.S., Wang L., Liu Y., Chen H., Nie S., Wang X., Chou H., Tan C., Fal-lahazad B., Ramanarayan H., Magnuson C. W., Tutuc E., Yakobson B. I., McCarty K. F, Zhang Y.-W., Kim P., Hone J., Colombo L. and Ruoff R. S. The Role of Surface Oxygen in the Growth of Large Single-Crystal Graphene on Copper. *Science*, 2013, Issue 342, pp. 720 – 723.
- 5 Magnuson C. W., Kong X., Ji H., Tan C., Li H., Piner R., Ventrice C. A., Ruoff Jr. and Ruoff R. S., Yakobson B. I., McCarty K. F, Zhang Y.-W., Kim P., Hone J., Colombo L. and Ruoff R. S. Copper oxide as a “self-cleaning” substrate for graphene growth. *J. Mater. Res.*, 2014, Issue 9, pp. 403 – 409.
- 6 Wang Z.-J., Weinberg G., Zhang Q., Lunkenbein T., KleinHoffmann A., Kurnatowska M., Plodinec M., Li Q., Chi L., Schloegl R. and Willinger M.-G. Direct Observation of Graphene Growth and Associated Copper Substrate Dynamics by in Situ Scanning Electron Microscopy. *ACS Nano*, 2015, Issue 9, pp. 1506 – 1519.
- 7 Wu W., et al. Growth of Single Crystal Graphene Arrays by Locally Controlling Nucleation on Polycrystalline Cu using Chemical Vapor Deposition. *Advanced Materials*. 2011, Issue 23, pp. 4898 – 4903.
- 8 Stroyuk A, Kryukov A, Kuchmii S, Pokhodenko V. Semiconductor photocatalytic systems for the production of hydrogen by the action of visible light. *Theor Exp Chem*. 2009, No. 45(4), pp. 209 –233.
- 9 Lei Han, Ping Wang and Shaojun Dong. Progress in graphene-based photoactive nanocomposites as a promising class of photocatalyst. *Nanoscale*, 2012, Issue 4, pp. 5814.

UDC 537.9; 621.383.51

ELECTRICAL CHARACTERISTICS OF SEMICONDUCTOR POLYMER FILMS DOPED WITH SILVER NANOPARTICLES

Ibrayev N.Kh.¹, Afanasyev D.A.^{1, 2}

¹Buketov Karaganda State University, Institute of molecular nanophotonics, Karaganda, Kazakhstan

²Institute of Applied Mathematics, Karaganda, Kazakhstan, a_d_afanasyev@mail.ru

The electrical properties of composite films based on polymer PEDOT:PSS with a addition of Ag nanoparticles or Ag-TiO₂ nanostructures have been studied. A current-voltage characteristic is observed for polymer solar cells. A short circuit current increased after adding of Ag nanoparticles or Ag-TiO₂ nanostructures to the PEDOT:PSS polymer. Also, an increase in the recombination rate in cells with silver nanoparticles is observed. An electrical impedance is measured for polymer solar cells. A significant increase in the dielectric constant of a PEDOT:PSS film containing silver nanoparticles was detected.

Keywords: semiconductor polymer, silver nanoparticles, polymer solar cell, core – shell nanostructure

Introduction

Polymer solar cells (PSC) are currently considered as one of the promising areas capable of replacing traditional silicon batteries in a number of practical applications [1]. Industrial production of PSCs is quite low in cost due to the possibility of producing large areas by roll printing methods. Also, the technologies used in the production of polymer cells are less environmentally harmful than the technology of production of silicon cells.

Despite the low cost of manufacturing PSCs they have a number of disadvantages. A low efficiency of PSC is the main drawback. Currently, a number of approaches are used to increase PSCs efficiency. An use of nanoparticles (NPs) of metals in PSCs is one of such approaches [2]. In general, silver or gold NPs with the maximum plasmon effect in the visible region of the spectrum among difference materials can be use [3, 4]. However, there are works suggesting the use of other NPs metals, such as aluminum NPs [5].

A bulk heterojunction is the main element of PSC. The heterojunction consists of materials having donor-acceptor properties in relation to charge transfer. The classical substances used to form heterojunction are polymer poly(3-hexylthiophene-2,5-diyl) (P3HT) and methanofullerene molecules [6,6]phenyl-C61-butane acid methyl ether (PCBM). On the basis of these substances PSCs efficiency reaches ~ 5 % [6]. Other auxiliary elements are the anode, cathode and polymers mixture layer PEDOT:PSS (poly (3,4 – ethylenedioxythiophene): polystyrene sulfonate). The PEDOT:PSS layer lies between the anode and the bulk heterojunction. PEDOT:PSS performs the function of a layer with a p-type conductivity of HOMO (high occupied molecular orbital) whose energy levels are located above the HOMO-levels of the P3HT polymer. This allows charge carriers with P3HT to freely enter the anode of the solar cell. Also, the polymer layer PEDOT:PSS is necessary to obtain a more uniform film of P3HT-PCBM heterojunction on its surface.

The efficiency of PSC depends on conductive properties of the polymer film PEDOT:PSS. Therefore, PEDOT:PSS films with increased conductivity are required to obtain PSC with high efficiency. Increasing the conductivity of PEDOT:PSS films can be achieved by adding Ag or Ag-TiO₂ plasmon nanoparticles to the film [7]. This article presents the results of the study of electrical and photovoltaic properties of PSCs with composite films based on PEDOT: PSS with additives of Ag or Ag-TiO₂ nanoparticles. It is shown that the addition of silver nanoparticles to the PEDOT:PSS film leads to a significant change in the dielectric permeability of the medium (ϵ).

1. Experimental part

As shown in [8, 9], the specific conductivity of PEDOT:PSS films is affected by the rate of application and the annealing temperature of the films, as well as the addition of extra solvents to the PEDOT:PSS solution. The results of studies of the effect of adding dimethylformamide and dimethylsulfoxide (DMSO) and the conditions of production on the value of the resistivity of the composite films PEDOT:PSS are given in [10]. A minimum resistance of the films is observed for solution PEDOT:PSS with the addition of 2% DMSO. These results are consistent with the results obtained in other papers [8, 9]. Study of effects of the speed of centrifuge rotation at making of films and the temperature of annealing of films showed that 5000 rpm. is the optimal speed, and 150 ° C is the optimum annealing temperature.

As shown in [7, 11], the addition of silver and gold NPs reduces the resistance of PEDOT:PSS films. In work [10], the results of studies of the complex effect of silver plasmon NPs and additive of DMSO solvent on the conductive properties of PEDOT:PSS films are presented. Aqueous solutions of silver NPs and nanostructures (NSs) of Ag–TiO₂ with concentration $5 \cdot 10^{-9}$ mol/L was used. The method of synthesis of silver NPs and Ag–TiO₂ NSs described in detail in [12]. An addition of organic solvents and metal NPs, NSs leads to a decrease in the electrical resistance in PEDOT:PSS films. This, in turn, should lead to an increase in the efficiency of PSC with highly conductive composite polymer film based on PEDOT::PSS.

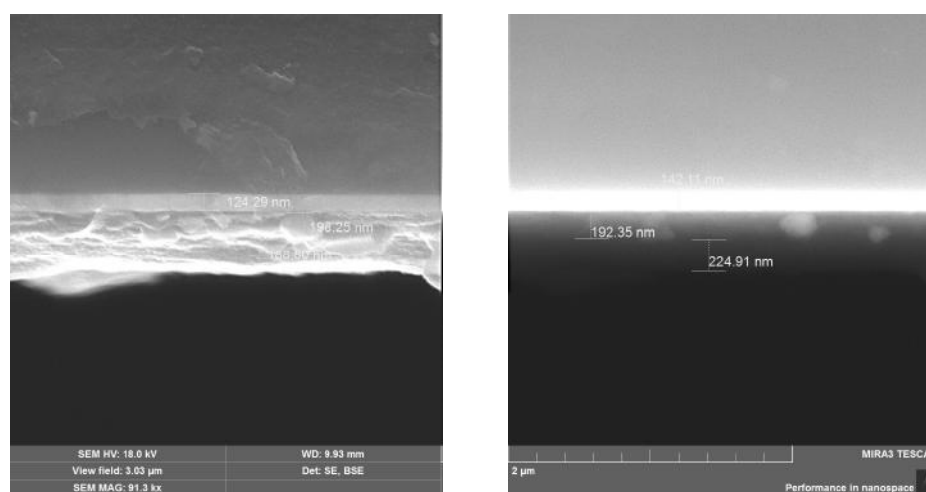
Optimal conditions for the manufacture of composite films with PEDOT:PSS from [10] were used in this work. These optimal fabrication conditions include the concentrations of NPs or NSs, the optimal deposition rate and the annealing temperature of the PEDOT:PSS composite films, used in [10]. The DMSO solution with the concentration of 8% relative to the PEDOT:PSS solution was added to the original solution to improve the electrically conductive properties of the PEDOT:PSS films. The obtained PEDOT:PSS films with the addition of NPs and NSs were used for the manufacture of photovoltaic cells. The size of NPs in colloidal solutions was determined by the method of dynamic light scattering on the analyzer Zetasizer Nano ZS (Malvern). The size of the used NPs or NSs and their absorption spectra are given in [13]. The technique of manufacturing cells is described in detail in [14]. The thickness of polymer films was determined by scanning electron microscope Tescan Mira 3. Glove box SPECS GB 03-2M (Spectroscopic systems) was used for fabrication of P3HT–PCBM layers. Aluminum electrodes was made by thermal evaporation in a vacuum with a pressure not exceeding 10^{-5} Torr. The thickness of the aluminum electrodes was measured using SI–TM106 Subminiature Film Thickness Tester. The thickness of obtained electrodes wasn't less than 100 nm.

Solar simulator with xenon lamp with 100 mW/cm^2 (Photo Emission Tech Inc.) was used for measured of current-voltage characteristics and an efficiency of PSCs. The impedance of the solar cells was measured using the Z500PRO impedance meter in potentiostatic mode with a given constant potential. The method of measurements corresponds to the method used in [14, 15]. The EIS–analyzer program was used to determine the main parameters of the solar cell chain.

2. Results and their discussion

Microscopic data were used to estimate the thickness of different layers. The thickness of the produced films was determined at cross-section cells. An example of a cross-section cells with the structure ITO/PEDOT:PSS/P3HT:PCBM with silver NPs in the layer PEDOT:PSS is shown in Figure 1. These results are shown in Table 1. Layer thickness was estimated from 3 to 5 measurements. At Figure 1, on the cross-section cells in the PEDOT:PSS layer, NPs with sizes corresponding to the size of the PEDOT:PSS layer are observed. However, an amount of large particles in the film is small compared to the average particle size used in the work [13].

For comparison, in Table 1 are shown the results of surface resistance of films obtained by the four-probe method in [10]. It can be seen that the addition of NPs Ag or NSs Ag–TiO₂ in the film leads to a decrease resistance by 3 times.



a) b)

Fig.1. The thickness of the functional layers of the solar cell, when registering the signal from the detector of secondary electrons (a) and reflected electrons (b)

Table 1. A basic geometrical and electrical characteristics of PEDOT:PSS composite layers with additives of Ag NPs or Ag–TiO₂ NSs

| Defined model parameter | Properties of PEDOT:PSS | | |
|---|---------------------------|--------------------------|---------------------------|
| | Without NPs | Ag NPs | Ag–TiO ₂ NSs |
| The thickness of the layer of PEDOT:PSS in the cell (d) | 200 nm | 200 nm | 150 nm |
| The thickness of the active layer of P3HT-PCBM | 180 nm | 170 nm | 140 nm |
| Resistivity (ρ) of PEDOT:PSS films (resistance per square) | $21,3 \cdot 10^3$ Ohm/sq. | $6,7 \cdot 10^3$ Ohm/sq. | $6,5 \cdot 10^3$ Ohm/ sq. |
| ϵ_1 | 2,2 | 10 | 3,7 |

The obtained composite semiconductor films PEDOT:PSS with the addition of NPs or NSs were used for the manufacture of photovoltaic cells. Photovoltaic properties of PSCs were investigated (Figure 2, Table 2). Adding NPs and NSs to PEDOT:PSS leads to an increase in photocurrent. These results are consistent with the results of measuring the electrical characteristics of PEDOT:PSS composite films (Table 1). The highest efficiency is observed for cells with silver NPs. A high value of short-circuit current (J_{sc}) is observed for these cells. The high J_{sc} value indicates good conductive properties of all functional layers in the cell, especially the PEDOT:PSS composite layer. In this case, the value of an open circuit voltage (U_{oc}) is low. The shape of a volt-ampere curves, a low value of fill factor (FF) and value of efficiency indicates the high value of the rate of recombination in PSCs (Figure 2). The increase in the rate of recombination of charge carriers in the cell may be due to two main reasons. The first reason is due to the large thickness of the PEDOT:PSS layer. In our work the thickness of this layer was ~ 150 -200 nm. While, for high-efficiency solar cells, this value is in the range of 50 to 100 nm [2, 3]. The second reason that leads to an increase in the recombination rate may be the presence of large particles in the PEDOT:PSS layer, which lead to a short circuit between the polymer layers or electrodes.

Thus, the addition of NPs to the polymer PEDOT: PSS leads to an improvement in the conductive properties of solar cells. At the same time, there is an increase in the rate of recombination in the cells. Therefore, it is necessary to continue research aimed at reducing the rate of recombination in PSCs.

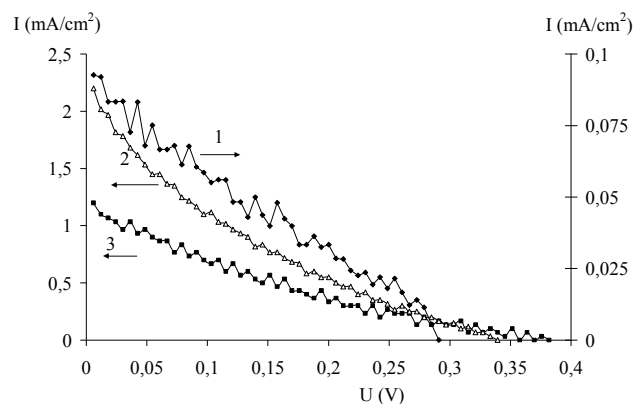


Fig.2. Volt-ampere characteristics of PSC by additives of NPS and NSs Ag or Ag/TiO₂

Table 2. Photovoltaic and electrical properties of cells based on a mixture of polymers P3HT: PCBM

| Layer properties of PEDOT:PSS | Jsc, mA/cm ² | Umax, (V) | Uoc, (V) | η, % | RSER, kOhm/ cm ² | RSH, Ohm/ cm ² |
|-------------------------------|-------------------------|-----------|----------|-------|-----------------------------|---------------------------|
| Without NPS | 0.09 | 0.29 | 0.073 | 0.005 | 151 | 687 |
| Ag NPs | 2.14 | 0.28 | 0.121 | 0.05 | 0.0 | 4·10 ⁻⁵ |
| Ag-TiO ₂ NSs | 1.23 | 0.35 | 0.164 | 0.02 | 3.4 | 579 |

Additional information about processes of transport and recombination of charge carriers in PSCs can be obtained from electrical impedance measurements of cell. The real (Z') and imaginary (Z'') parts of the electrical resistance of solar cells were measured. The method of measurements corresponds to the method used in [14, 16].

The EIS-analyzer program interface is shown in Figure 3. For extract the basic electrical characteristics of solar cell was used electrical model of PSC, which is given in the upper right part of Figure 3, a. It is R1– resistance layer ITO layer; R2 – resistance of a layer of PEDOT:PSS; R3 – resistance of the P3HT-PCBM active layer; R4 – resistance of the interface of P3HT-PCBM and aluminum electrode; C1 – capacitance of a layer of PEDOT:PSS; C2 – capacity of the active layer of P3HT-PCBM; C3 – capacitance of the interface of P3HT-PCBM and aluminum electrode, in this model, in accordance with article [16]. The results of determining the circuit parameters are given in Table 3. Comparison of R2 values for all cells shows that the cells with PEDOT:PSS with silver NPs has the least resistance. The remaining cells have a higher resistance value of the PEDOT:PSS layer.

The capacitance of the C2 layer can be used to estimate the dielectric constant (ϵ) without addition and with addition of NPs and NSs. For this purpose, the formula (1) given in [16]:

$$C = \frac{\epsilon_1 \epsilon_0 A}{d} \quad (1)$$

For calculations it is necessary to know the thickness of PEDOT:PSS films. These values were obtained from the scanning electron microscope measurements of PSCs (Table 1).

The results of determining the dielectric permittivity of PEDOT:PSS films are given in Table 1. As can be seen from the Table 1, the addition of NPs and NSs leads to an increase in the dielectric constant of the film (ϵ_1). Comparison of the value of ϵ_1 for the film PEDOT:PSS with the results given in other works shows their compliance [17]. For example, in [18] for composites based on a dielectric polymer polyvinyl alcohol, a decrease in the dielectric permittivity of the film ϵ_1 was observed. A change in the dielectric characteristics of cells based on PEDOT:PSS and P3HT-PCBM when silver NPs were added to various PSC layers was detected in [19]. An increase in ϵ_1 is observed in this case. However, the increase of ϵ_1 for PEDOT:PSS films with NPs requires additional studies.

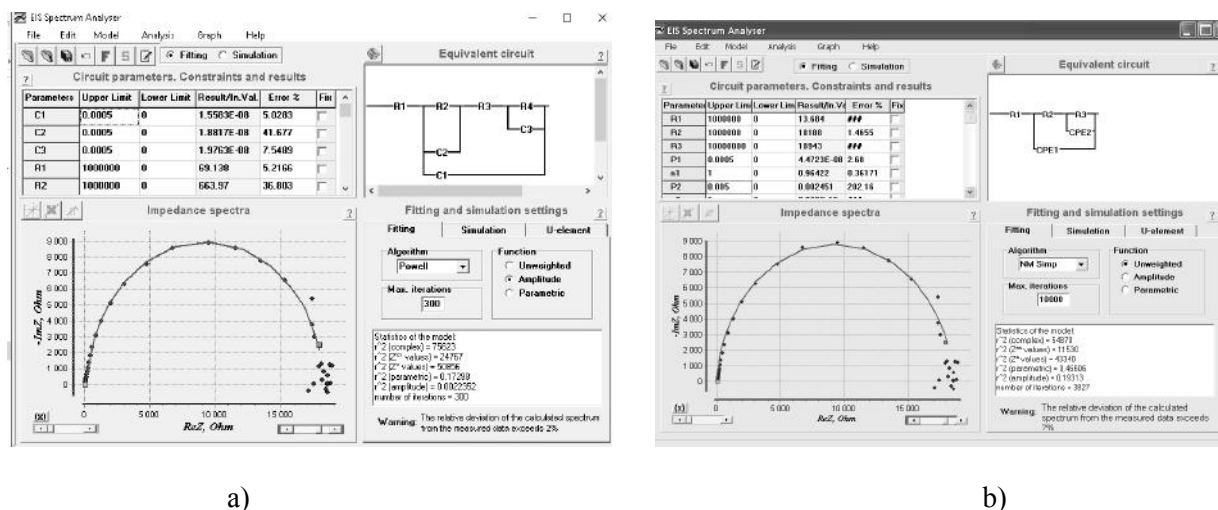


Fig.3. EIS-analyzer program interface with electric models of PSC (upper right corner of the program) within the models given in [16] (a) and [20] (b)

Table 3. Electrical characteristics of PSCs with PEDOT:PSS films with additives of NPs or NSs

| Defined model parameter | Properties of PEDOT:PSS | | |
|-------------------------|-------------------------|---------------------|-------------------------|
| | Without NPS | Ag NPs | Ag-TiO ₂ NSs |
| R1, (Ohm) | 69.0 | 80 | 86 |
| R2, (Ohm) | 664.0 | 231 | 8742 |
| C2, (nF) | 18.8 | 82 | 23 |
| R3, (Ohm) | 197.0 | $1.9 \cdot 10^{-4}$ | 187 |
| C1, (nF) | 15.5 | $1.8 \cdot 10^{-3}$ | 6.97 |
| R4, (Ohm) | $1.7 \cdot 10^4$ | $1.8 \cdot 10^4$ | 181 |
| C3, (nF) | 19.7 | 35 | 94 |

For comparison also the analysis of the impedance of the cells in the model of Biscuit [20]. The electrical diagram of the model is shown in Figure 3, b. The simulation results are given in Table 4. In this model, R1 is the resistance of the electrical contacts and the bulk material; R2 – the resistance to charge transfer in the active region and on the boundary of electrode–active area; R3 – resistance associated with recomenaria electron-hole pairs in the active region; CPE1 is the total capacity of the cell; CPE2 – diffusion capacity.

A comparison of the circuit parameters obtained from results of modeling of electrical circles with used the two models (Tables 3, 4) shows similar values of the circuit characteristics. Effective carrier transfer time (τ_a) and electron mobility (μ) were estimated using the Bisquets model in accordance with the formulas:

$$\tau_d = R3 \cdot C2, \quad \mu = \frac{eL^2}{k_B T \tau_d} \quad (2)$$

where e – electron charge, L – thickness of the active layer, k_B – Boltzmann constant, T – temperature.

Table 4. Electrical characteristics of PSCs with PEDOT:PSS films with additives of NPs and NSs (modeling by the Bisquerts model)

| Defined model parameter | Properties of PEDOT:PSS | | |
|---|-------------------------|---------------------|-------------------------|
| | Without NPS | Ag NPs | Ag–TiO ₂ NSs |
| R1, (Ohm) | 160 | 85 | 71 |
| R2, (Ohm) | 3768 | 224 | 1596 |
| C1, (nF) | 85.0 | 17.2 | 39 |
| n1 | 1 | 0.94 | 0.95 |
| R3, (Ohm) | 5340 | 9342 | 16902 |
| C2, (nF) | 14.0 | 26.0 | 8.7 |
| n2 | 1 | 0.96 | 1 |
| τ_d (μ s) | 75.0 | 243 | 147 |
| μ ($\text{cm}^2 \cdot \text{V}^{-1} \cdot \text{s}^{-1}$) | $1.6 \cdot 10^{-4}$ | $0.5 \cdot 10^{-4}$ | $0.5 \cdot 10^{-4}$ |

The obtained results indicate an increase the time of charge transfer in films with additives of NPs or NSs and a decrease in the mobility of charge carriers in the active layer of these cells. The decrease in the mobility of charge carriers in films with NPs or NSs in the PEDOT:PSS layer contradicts the results obtained by measuring the current-voltage characteristics of the cells (Table 2). In cells with NPs or NSs, a higher current density J_{sc} is observed. It may be necessary to take into account possible changes in the dielectric properties of polymers when metal NPs are added to them when used modeling by the Bisquerts model.

Conclusion

According to the results of the research we can get a number of conclusions:

- the addition of organic solvents and metal NPs leads to a decrease in the electrical resistance of PEDOT:PSS films, which in turn leads to an increase in the efficiency of PSCs;

- the electrical properties of PSCs with composite films based on PEDOT:PSS were investigated. The high conductivity of PEDOT:PSS composite films leads to an improvement in the conductivity of solar cells, which is manifested in an increase in short circuit current. Along with an increase in the short-circuit current, the open-circles voltage decreases, which is associated with an increase in the rate of recombination of charge carriers observed in cells with PEDOT:PSS composite films. A high resistance value is observed for some cells at the interface of the P3HT-PCBM active layer and an aluminum electrode. This result indicates the need to improve the technology of deposition of the aluminum electrode on the P3HT-PCBM layer;

- using the method of impedance spectroscopy, solar cells containing PEDOT:PSS composite films with additions of Ag NPs or Ag–TiO₂ NSs were investigated. A significant increase in the dielectric constant of a PEDOT: PSS film containing Ag NPs has been found. To explain the result obtained, continuation of the research is necessary. A change in the dielectric characteristics of the medium will affect such important properties as the intensity of light absorption by the material, the excitonic transport in the material, and the transport of charge carriers. This, in turn, can significantly change the efficiency of transformation of light energy into electrical energy in PSCs.

Acknowledgements

This work was carried out with the financial support of the Ministry of Education and Science of the Republic of Kazakhstan.

REFERENCES

- 1 Pavlov N. What Barriers Will Overcome Printed Solar Elements. *Vector of High Technologies*. 2013, No.3 (3), pp. 8 – 14. [in Russian]
- 2 Chan K., Wright M., Elumalai N. Uddin A., Pillai S. Plasmonics in Organic and Perovskite Solar Cells: Optical and Electrical Effects *Adv. Optical Mater.* 2017, Vol. 5, No.6. pp. 1600698(1-19).
- 3 Pillai S., Catchpole K.R., Trupke T., Green M. J. Surface plasmon enhanced silicon solar cells *Appl. Phys.* 2007, Vol.101, No.9, pp. 093105(1) - 093105(8).
- 4 Schaadt D.M., Feng B., Yu E.T. Enhanced semiconductor optical absorption via surface plasmon excitation in metal nanoparticles *Appl. Phys. Lett.* 2005, Vol. 86, No.6, pp. 063106(1-3).
- 5 Ikhsanov Sh., Protsenko I.E., Uskov A.V. Increasing the efficiency of organic solar cells using plasmonic nanoparticles *Tech. Phys. Letters*. 2013, Vol.39, No.5, pp. 450 – 453.
- 6 http://www.nrel.gov/ncpv/images/efficiency_chart.jpg
- 7 Kukhta A.V., Pochtenny A.E., Misevich A.V. et. al. Optical and electrophysical properties of nanocomposites based on PEDOT: PSS and gold/silver nanoparticles *Phys. of the Sol. St.* 2014, Vol. 56, No.4, pp. 827 – 834.
- 8 Lee C.S., Kima J.Y., Lee D.E. et. al. Flexible and transparent organic film speaker by using highly conducting PEDOT/PSS as electrode *Synthetic Metals*. 2003, Vol.139, pp. 457–461.
- 9 Wang G.-F., Tao X.-M., Xin J.H., Fei B. Modification of conductive polymer for polymeric anodes of flexible organic light-emitting diodes *Nanoscale Res. Lett.* 2009, No.4, pp. 613 – 617.
- 10 Afanasyev D.A., Ibraev N.Kh. Increasing the conductivity of composite semiconductor polymer films based on Pedot: PSS *Solid State Physics, Functional Materials and New Technologies (FTT-2018): Materials of the XIV International Scientific Conference*. Bishkek- Karaganda, 2018, pp. 11 – 13. [in Kazakh]
- 11 Stratakis E., Kymakis E. Nanoparticle-based plasmonic organic photovoltaic devices. *Materials Today*. 2013, Vol.16, Issue 4, pp. 133 – 146.
- 12 Afanasyev D.A., Ibrayev N.Kh., Serikov T.M., Zeinidenov A.K. Effect of the titanium dioxide shell on the plasmon properties of silver nanoparticles *Russian Journal of Physical Chemistry A*. 2016, Vol. 90, No.4, pp. 833 – 837.
- 13 Afanasyev D.A., Ibraev N.Kh. The Effect of Ag-TiO₂ Nanostructures on Photoprocesses in Poly [3-Hexylthiophene] Polymer *Mat. Res. Scientific-Practical Conference*. Karaganda, 2018, pp. 148–151. [in Kazakh]
- 14 Ibrayev N.Kh., Afanasyev D.A., Zhapabaev K.A. Effect of potassium iodide on luminescent and photovoltaic properties of organic solar cells P3HT-PCBM *IOP Conf. Series: Mat. Sc. and Eng.* 2016, Vol.110, pp. 012067 (1-5).
- 15 Ibrayev N.Kh., Nurmakhanova A., Afanasyev D. Role of spin states in the process of electron energy transformation in P3HT films, doped KI salt *IOP Conf. Series: Materials Science and Engineering*. 2017, Vol.168, pp. 012060.
- 16 Knipper M., Parisi J., Coakley K. et al. Impedance Spectroscopy on Polymer-Fullerene Solar Cells *Zeitschrift für Naturforschung A*. 2007, Vol. 62, No 9, pp. 490 – 494.
- 17 Aleksandrova M., Kolev G.I. et. al. Characterization of Piezoelectric Microgenerator with Nanobranched ZnO Grown on a Polymer Coated Flexible Substrate *Appl. Sc.* 2017, Vol. 7(9), pp. 1 – 11.
- 18 Ghanipourand M., Dorranean D. Effect of Ag-Nanoparticles Doped in Polyvinyl Alcohol on the Structural and Optical Properties of PVA Films *J. of Nanomat.* 2013, Vol. 2. pp. 1 – 10.
- 19 N. Kalfagiannis, P. G. Karagiannidis, et. al. Plasmonic silver nanoparticles for improved organic solar cells *Sol. Energy Mater. Sol. C*. 2012, Vol. 104, pp.165–174.
- 20 G. Garcia-Belmonte, A. Munar, E.M. Barea, J. Bisquert, I. Ugarte, R. Pacios Charge carrier mobility and lifetime of organic bulk heterojunctions analyzed by impedance spectroscopy *Organic Electronics*. 2008, Vol. 9(5), pp. 847 – 851.

USING THE SYSTEM OF FINE PURIFICATION OF GASES IN THE DISPOSAL OF INDUSTRIAL AND DOMESTIC WASTE

Bezrodny M.K.¹, Sakipov K.E.², Aytmagambetova M.B.², Zhakishev B.A.²

¹National Technical University of Ukraine "Igor Sikorsky Kyiv Polytechnic Institute", Kiev, Ukraine, m.bezrodny@kpi.ua

²L.N. Gumilyev Eurasian National University, Astana, Kazakhstan, kafedra_te@enu.kz

The paper solves the problem of the inertial method of sedimentation of dust particles (or liquid droplets), which is based on changing the direction of gas movement with particles suspended in it. Really one of the most serious environmental problems facing humanity is environmental pollution by domestic and industrial waste. These wastes mostly have such undesirable properties as toxicity, carcinogenicity, mutagenicity, corrosion, reactionary ability and fire danger. It is known that the effectiveness of any gas cleaning system is determined by its ability to remove small particles from the gas stream. To obtain a solution to this problem, we considered the possibility of separating heterogeneous gas mixtures by developing the fine purification of gases based on a gradient separator. The system of fine gas cleaning on the basis of a gradient separator is designed to clean gas streams from dispersed particles, separate aerosols, sublimates, and separate heterogeneous gas mixtures into separate components.

Keywords: *gradient separator, domestic and industrial wastes, small particles, separation limit*

Introduction

Currently, strict rules and conditions are being introduced on placement and equipment of landfills for warehousing and disposal of hazardous waste in industrially developed countries. In recent years, the problem of toxic waste disposal has become relevant in the Republic of Belarus, the Russian Federation, the Republic of Kazakhstan and other CIS countries which coincide with the level of its importance worldwide. It is connected with the international strategic trend on comprehensive "greening" of the environment as the factor compensating the degradation of the environment due to industrial development as well as the increasing danger to the population from the accumulation of highly toxic and infected production and consumption waste.

The most common method of processing hazardous organic waste is incineration. For these purposes, industrial thermal devices are widely used, for example, asphalt or cement furnaces, steam boilers, circulating fluidized bed furnaces, rotary kilns. At a temperature of 1000-1200 °C in such furnaces and devices, afterburning of the formed volatile organic compounds is carried out in secondary chambers with additional fuel and oxidizer supply. In some cases, air is enriched with oxygen to increase temperature in burners.

Fire method of waste neutralization and recycling is the most versatile, reliable and effective along with others. In many cases, it is the only possible way to neutralize industrial and domestic waste. This method is used for the disposal of solid waste in any physical condition: liquid, solid, gaseous and pasty. Along with the burning of combustible waste, the fire method is also used for the disposal of non-combustible waste. In this case, waste is exposed to high-temperature (more than 1000 °C) products of combustion.

Incineration is the controlled process of oxidation of solid, liquid or gaseous combustible waste. During combustion, carbon dioxide, water and ashes are formed. Sulfur and nitrogen, contained in wastes, form various oxides during combustion, and chlorine is reduced to HCl. In addition to the gaseous products, solid particles are also formed from the combustion of waste such as metals, glass or slag which require further recycling or disposal.

This method is characterized by high sanitary and hygienic efficiency. The field of the fire method applications and wastes that can be neutralized by this method are constantly expanding. They include waste from organo-chlorine production, basic organic synthesis, production of plastics, rubber and synthetic fibers, oil refining industry, forestry, chemical-pharmaceutical and microbiological industry, mechanical engineering, radio engineering and instrument-making industry, pulp, and paper production and many other industries.

The conducted researches [1-3] demand a critical approach to fire neutralization of toxic waste due to the possibility of the formation of extremely harmful compounds afterwards: dioxins and furans. The disadvantage of fire neutralization is also the use of additional fuel (usually natural gas), which significantly increases the volume of exhaust gases, and therefore significantly increases the load on the gas cleaning system, its size, and material capacity.

In industry, mechanical, electrical and physicochemical methods of gas purification are used [7, 10]. Mechanical and electrical cleanings are used to trap solid and liquid impurities from gases, and gaseous impurities are captured by physical and chemical methods. Mechanical purification of gases is carried out by the sedimentation of impurity particles by gravity or centrifugal force, by filtering through fibrous and porous materials and by washing with water or other liquid. The simplest, but an ineffective and rarely applied method is by the sedimentation of large dust by gravity in so-called dust chambers. The inertial method of sedimentation of dust particles (or liquid drops) is based on the change of direction of gas flow with weighed particles in it. Since the particles density is about 1-3 thousand times more than the gas density, they continue to move by inertia in the previous direction and separate from gas.

1. The gradient separator

The possibility of separation of heterogeneous gaseous mixtures gives opportunities not only to prevent harmful gas emissions, but also to use these components as technological raw materials. It is important to mention that the device separates gaseous mixtures as, for example, oil and water are separated in liquids. The device cannot divide homogeneous gaseous mixtures into components, for example, air into its components (as, for example, it is impossible to separate water and alcohol).

In fact, the efficiency of any gas purification system is determined by its ability to remove small particles from the gas flow, since the problem of removing large particles is basically solved to date. A feature of the gradient gas purification method is the fact that devices have a separation limit which is the zone of large particle sizes. There are reasons to assume that such devices operate at the molecular level in the zone of small particle sizes, i.e. they can remove particles of one molecule size from the flow. The basis for such an assumption is the experiments on laboratory installations while working with various smokes – tobacco smoke is much easier to remove from the flow because it is the thinnest among other smokes. In addition, when working on a pilot plant, sulfur dioxide was derived from the total gas flow, which is possible only if the device works at the molecular level.

Of course, the conducted researches are not enough to make a final conclusion; however, theoretical assumptions indicate that separators, that use a gradient method of gas purification, are capable to extract particles one molecule in size from the gas flow. The system of fine purification of gases on the basis of the gradient separator (figure 1) is intended for cleaning of gas streams from dispersed particles, separation of aerosols, sublimates, a division of heterogeneous gaseous mixtures into separate components.

The dusty gas flow, which is a mixture of gases and weighed particles, moves into the inlet confuser 1, containing 2 equal-profile sites "a" and "b", where the flow is accelerated. On the site "b", the gas flow is provided with an additional impulse of twisting by the guiding device 2.

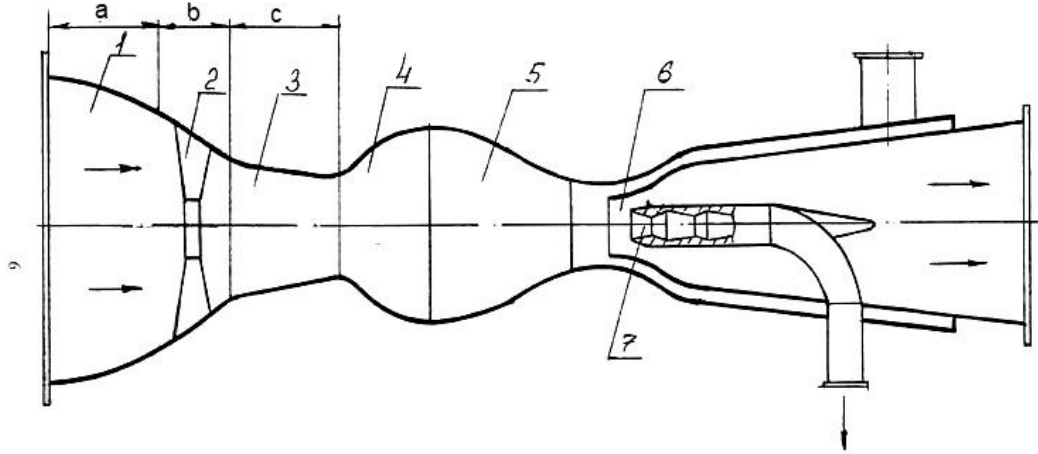


Fig.1. Scheme of the gradient separator

In a confuser 1, gas flow is accelerated, twisted, keeping the laminar structure of a stream. The laminar flow is provided by monotonously increasing the tangential and axial acceleration following these conditions in a confuser 1:

$$\text{On the site «a»: } \frac{dF_i}{dl_i} = \text{const}_1, \quad \text{On the site «b»: } \frac{dF_i}{dl_i} = \text{const}_2,$$

where F – cross-sectional area of the channel; dF – increment along the area; l – site length; dl – increment along the length.

These constants are determined experimentally, depending on the properties of the gas flow (temperature, viscosity, density). Next, the gas flow enters the confuser 3 where the acceleration is continued under the condition $\frac{dF_i}{dl_i} = \text{const}_3$. The third constant is also determined experimentally.

From the confuser 3, the gas flow enters the twisting nozzle 4 where it is provided with a new twisting impulse. The geometry of a nozzle is calculated by the formula:

$$D_i = \sqrt{D_{i-1}^2 + \frac{\Delta l_i \cdot c_0 \cdot D_0^2}{\sqrt{(c_0^2 - 2a_0 l_i - l_i^2 \cdot k)^3}} \cdot (a_0 + k l_i)} \quad (1)$$

where D_i – the diameter of the i -th cross section of a nozzle; Δl_i – the difference between the distances between the i^{th} and the $(i-1)^{\text{th}}$ sections; c_0 – the initial gas velocity at the entrance to the nozzle; a_0 – the acceleration of the flow at the entrance to the nozzle; $k = \frac{a_0}{l}$ – specific increment of acceleration per unit length of the nozzle.

At the exit of the diffuser 4, the gas flow is inhibited due to the geometry of the twisting nozzle. After carrying out the first 3 stages of the flow acceleration, it's twisting with the preservation of the laminar structure, the flow moves into the separation channel of the gradient separator where the flow acceleration is continued in the parabolic confuser 5, then flow is twisted in the nozzle 6.

At the same time, the dusty gas mixture is sucked through the dust-collecting pipe 7 along the channel axis, aligning the velocity and acceleration of the flow along the channel section which prevents turbulence. Gases with high density are removed through the peripheral-radial suction. The condition is, herewith, always fulfilled – the smaller the particle size, the closer to the center its trajectory passes, the easier it is to remove such particles from the gas flow. Therefore, it is

impossible to record the presence of particles at the exit from the gradient separator on highly dispersed two-phase flows.

2. Processes in the gradient separator

The physical phenomenon that resembles the operation of the gradient separator is known to be a tornado. In nature, when a tornado occurs, it is observed in the form of a trunk, which is due to the suction of dust into the discharged core of the rotating gas mass. A similar process takes place in the gradient separator. The presence of a laminar structure of the gas flow, on condition of intensive rotation, allows the removal of components such as sulfur dioxide, fluorine, chlorine (from the periphery of the channel), water vapor, gaseous sublimates (from the center of the channel) from the total flow of industrial gas emissions.

Dimensions of the gradient separator allow it to be installed directly in the bypass flue gas ducts of production lines. The gradient separator is completely erosion-free since the dust is collected in the center of the separation channel and never comes into contact with the construction elements, including the central suction path. Energy consumption for gradient separation is comparable to the energy consumption for the implementation of known methods. The next element in the presented purification system will be an inertial vacuum dust collector, a technological machine for the deposition of dust particles taken from the central section of the gradient separator.

The remaining elements of the gas purification system on the basis of the gradient separator are standard: a condenser, steam jet ejectors, regulating and shut-off valves. Under the action of the smoke exhauster, the flue gases from the steam generator through the bypass flue gas duct are directed to the gradient separator (figure 2). In the separator, dust is concentrated to form a dust cord which is sent to the rough and fine purification bunkers through the central suction where its deposition occurs. Gas is pumped out from the bunkers and the central suction with the help of steam jet ejectors and is then released directly into the atmosphere.

This research work shows the results of the study on the degree of trapping the ashes from coal combustion in an inertial vacuum dust collector. The diagram of this process is presented in figure 3. The principle of operation of the inertial vacuum dust collector is based on a number of effects observed during the gas flow in a so-called negative voltage state ("NV state"). Thus, the particles can enter the channel, but cannot exit. The gas is in this state if the blasting device, that drives it, is located at the exit of the installation. In this case, the gas becomes stretched, and the effects are observed that cannot be explained by the molecular-kinetic theory of gaseous state:

- two jets of gas in the "NV state" do not have any effect on one another (transparent to each other) when crossed at an angle of 90^0 .

- if two jets intersecting at an angle of 90^0 are in the "NV-state" and transport dispersed particles, then after crossing the jets, all particles go to the jet with higher velocity.

- if a high-speed gas jet transports dispersed particles and borders with a stationary gas mass, then that gas mass is a "pump" for particles, i.e. such a mass sucks the particles into itself.

The gas to be purified is sent to the booster nozzle (a). The flow speed of gas particles increases at the exit of the booster nozzle through the inlet pipe because of its constriction, and the gas is stretched and goes into a negative voltage state. The dusty flow passing through section 1 has a velocity greater than the flow in section 2. But the particles in this flow also have high velocity, hence greater kinetic energy, which allows them to overcome section 2 along the tangent and rush in the form of Δ . When the dusty gas flow moves along the rotary chamber, it contacts the sedimentary grid located in the lower part of the rotary chamber, behind which is the stationary gas mass. Particles from the high-speed flow pass into this mass and are deposited in the bunker; however, not all particles are deposited.

Some of them go to the exit of the device and, falling under the influence of the inlet jet, are again sent to the rotary chamber of the system.

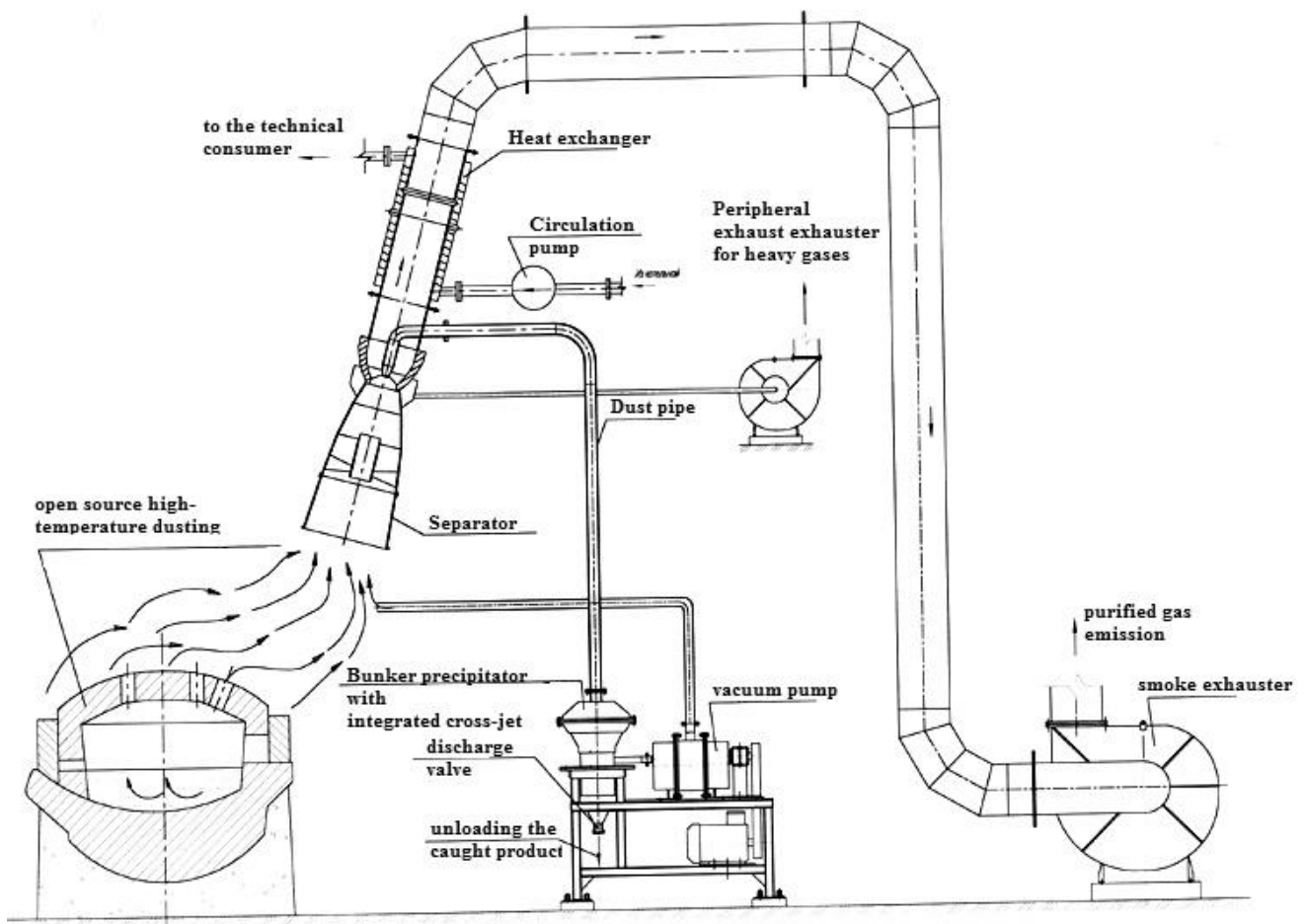


Fig.2. Installation diagram of the gradient separator

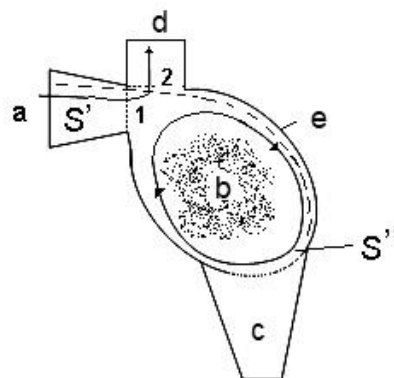


Fig.3. Diagram of the inertial separator dust collector model

There, an aerodynamic trap arises, i.e. particles can get into the rotary chamber of the device but cannot get out of it and are completely deposited in the bunker at the end. For the gas coming out of the rotary chamber, the inlet jet is a filter consisting of gas layers (layers of the filtering material) that is as efficient as cloth filters. The speed of particles decreases as they move, and the pressure gradients in the collecting chamber and the trap are leveled off, making necessary conditions for the particles to fall into the collecting chamber itself. The remaining particles (a small part) fall into the aerodynamic trap, accumulate in it and eventually fall into to the collecting

chamber “c” due to the gravitational force. Herewith, the distance $S' - S'$ determines the place of the particle deposition of a certain size.

Conclusion

The observation of particles falling into the collecting chamber confirms what was described earlier. Only a small fraction (less than 2-3 %) of the particles is attracted to the flow and is carried back into the aerodynamic trap.

The second important aspect of operability of the gas purification device is its erosion safety. In the inertial vacuum dust collector, the current of two-phase flow is formed in such a way that particles cannot overcome an interface and move not touching the walls until the zone of sedimentary grids.

Specific equipment is needed for each type of raw material depending on its characteristics: the temperature of ignition and combustion, burning time and others. Domestic waste is represented by more than 1,700 different components; therefore, selecting necessary equipment and a combustion device is essential. Those purchased abroad are only suitable for sorted, drier (with a moisture content of 7 %) garbage; domestic one has a moisture content of 46-50 %.

Chemical (gas) and physical (ash and slag) under burning constitute 27-29% when traditional technologies are applied to domestic waste. Thus, incomplete combustion products are released into the air. Carbon monoxide is formed during the combustion of the plastic packaging. Carbon monoxide causes various diseases in the presence of chlorine gas and phosgene and emitted dioxins and furans. It is not possible to extract these components from flue gases using standard filters. Ash and slag from single-stage combustion have poisonous concentration. Therefore, the use of the proposed fine gas purification system is quite relevant.

REFERENCES

- 1 Gupta, A. *Problems and progress associated with the disposal of hazardous chlorinated chemical waste*. Manag. Energy Technol., New York, 1987, pp. 75 – 84.
- 2 Dmitriev V.E., et al. Fire disposal of organochlorine wastes. *Industrial Heat Engineering*, 1988, Vol. 10, No. 5, pp. 93 – 97. [in Russian]
- 3 Maltceva A.C., et al. Fire disposal of organochlorine production. *Journal of WMO im.D. I. Mendeleev*. 1982, Vol. 27, No. 1, pp. 67 – 72.
- 4 Aliev G.M.-A. *Technique dust removal and purification of industrial gases*. Moscow, Metallurgy, 1986, 543 p. [in Russian]
- 5 Birger M.I., Waldberg A.Yu., Iagkov B.I., et al. Handbook of dust and ash collection. Edited by Rusanov A.A., Moscow, Energoatomizdat, 1983, 312 p. [in Russian]

UDC 621.311.21:628

EXPERIMENTAL STUDIES OF THE VORTEX HYDRAULIC ELEVATOR**Sakipov K.E.¹, Abirov A.A.², Sharifov D.M.¹, Makhmudov B.N.³**¹L.N. Gumilyev Eurasian National University, Astana, Kazakhstan, kafedra_te@enu.kz²Institute of Scientific, Technical and Economic Studies, Astana, Kazakhstan³S.U. Umarov Physical and Technical Institute, Dushanbe, Republic of Tajikistan

The article presents the results of experimental studies to assess the optimal operation modes of the vortex hydraulic elevator of the autonomous water treatment system. Based on experimental studies, it has been shown that twisting of the working and suction flows significantly increases the ejection capacity of vortex hydraulic elevators. The analysis of the results obtained (the curves of the dependence of the ejection coefficient on the spin parameters) allows us to conclude that there are optimal critical values for the vortex hydraulic elevator and hydraulic elevator with a tangential intake of the intake medium at which the highest value of the ejection coefficient is reached. It was also revealed that the swirling active and passive flows radically affect the mechanism for drawing the intake fluid into the mixing chamber of the hydraulic elevator. An increase in the swirling intensity increases the mixing of the flow, and large pressure gradients occur not only in the axial but also in the radial direction, which leads to an increase in the ejection coefficient. Thus, on the basis of the conducted experimental studies and preliminary technical and economic calculations, it can be concluded that the use of vortex hydraulic elevators for hydro transportation of various mixtures will significantly reduce energy consumption and increase the efficiency of their application.

Keywords: hydraulic elevator, pump, hydraulic mixture, ejection, working nozzle, active stream, passive stream.

Introduction

Hydraulic elevators are used in various industrial sectors: mining, chemical, petroleum, food, gas, gold mining, industrial heat engineering, etc. In the system of agricultural water supply and irrigation of pastures, hydraulic elevators are used to clean mine draw-wells, wells, ponds and other irrigation sources from sediments, and also as water-lifting units for lifting and transporting of water. The widespread use of hydraulic elevators is primarily due to the fact that they are simple in construction, the cost is insignificant, and they are almost trouble-free in operation. Their dimensions are so small that they essentially do not occupy the production area i.e. do not need any premises [1-3].

However, as the practice of using hydraulic elevators shows, their effective operation depends on many factors, including how the working and suction flows are fed into the receiving chamber [4-5]. The swirling flow fundamentally affects the mechanism of fluid flow in the receiving chamber, the work process and hydraulic elevator performance, hydraulic and geometrical parameters, and is characterized by properties that differ from axial flow:

- has axial, rotational and radial velocity components;
- high level of turbulence;
- longitudinal and transverse gradients of static and total pressure;
- the emergence of centrifugal forces and its active influence on the flow, etc. [6-8]

1. Experimental part

The main objective of the research was to determine the ejection coefficient q of the intake medium during tangential flow of active and passive media into the receiving chamber of the hydraulic elevator. These studies were related to the following issues:

- determination of the optimal position of the working nozzle;
- the effect of swirling active and passive streams on the pressure head-rate characteristics of the hydraulic elevator;

Studies of the effect of swirling of active and passive media on the working process of the hydraulic elevator and comparison the obtained results with the results of studies of a direct-flow hydraulic elevator and hydraulic elevator with a tangential intake of the intake medium were carried out on an experimental setup (Fig. 1, 2).

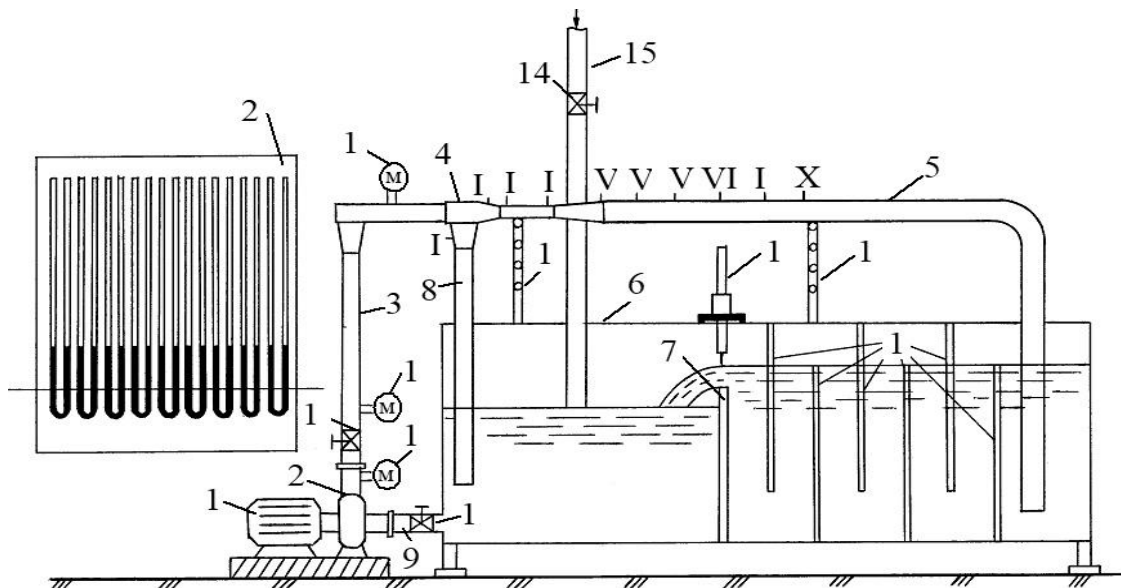


Fig.1. Experimental setup scheme

The experimental setup consists of (fig. 1,2): 1 - electric motor; 2 - centrifugal pump 3K-6; 3 - pump discharge pipe, made of flexible hose; 4 - hydraulic elevator; 5 - hydraulic elevator pressure pipe; 6 - tank with weir 7, at the same time being a reservoir for powering the suction nozzles of hydraulic elevator 8 and the pump 9; 10 - pacifiers; 11 - spitz scale to determine the water level on the weir 7 and the free surface in the tank 6; 12, 13, 14 - valves; 15 - supply pipe; 16, 17, 18 - manometers; 19 - supporting rods with crossbars; 20 - stand with piezometers. Tank 6 with weir 7 is designed to measure the water flow through the pressure pipeline 5, as well as to feed the suction nozzle of hydraulic elevator 8 and pump 9.

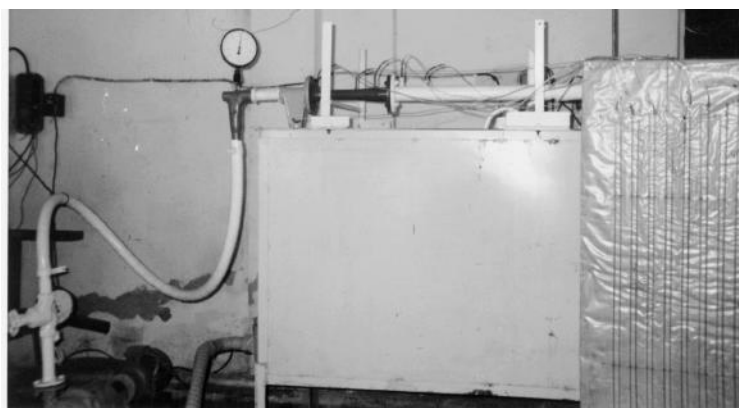


Fig.2. Experimental unit of vortex hydraulic elevator

In order to change the geometric height of the suction, the hydraulic elevator is installed on the crossbars with the possibility of vertical movement along the support pillars 18. By changing the geometric height relative to the free surface of the water, it is possible to study the designs of hydraulic elevators at different vacuum height of suction (from negative to positive). The supply pipe 15 is designed to fill the tank 6 with water and providing a certain level in it. A distinctive feature of the design of hydraulic elevators were methods of supplying of active and passive media to the receiving chamber.

In the first setup (Fig. 3), the active and passive jets are fed directly into the receiving chamber, i.e. as it is used in hydraulic elevator constructions currently used in various industries, industry and technology [1].

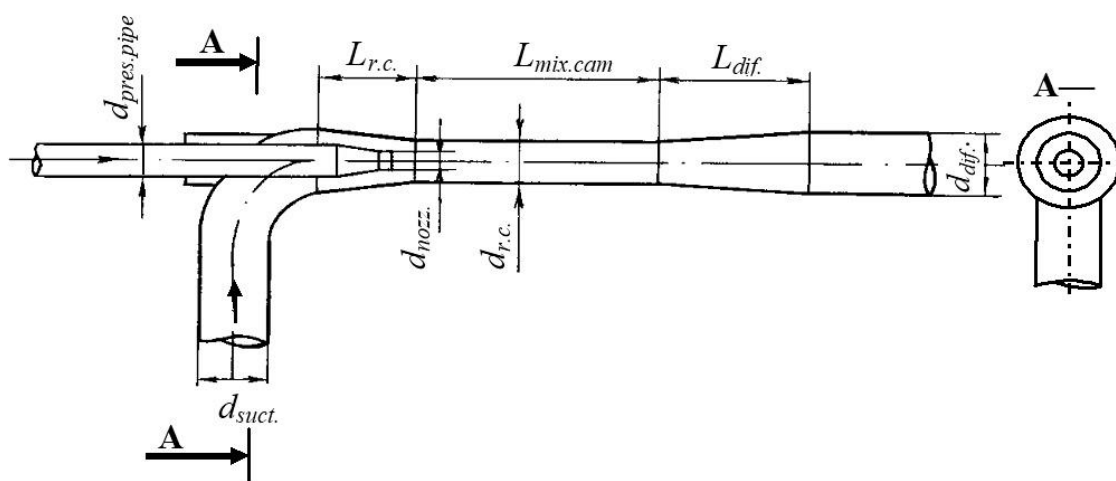


Fig.3. Scheme of direct-flow hydraulic elevator

In the second - the active jet is fed straight into the receiving chamber, passive - with a twist, thanks to a tangential feed (Fig. 4). The third design differs from the previous method of supplying the active jet. The working stream is fed into the hydraulic elevator nozzle through a tangentially cut slit of size $a_0 \times b_0 = 40 \times 17.6$ mm, the area of which is equal to the cross-sectional area of the pump discharge pipeline (Fig. 5).

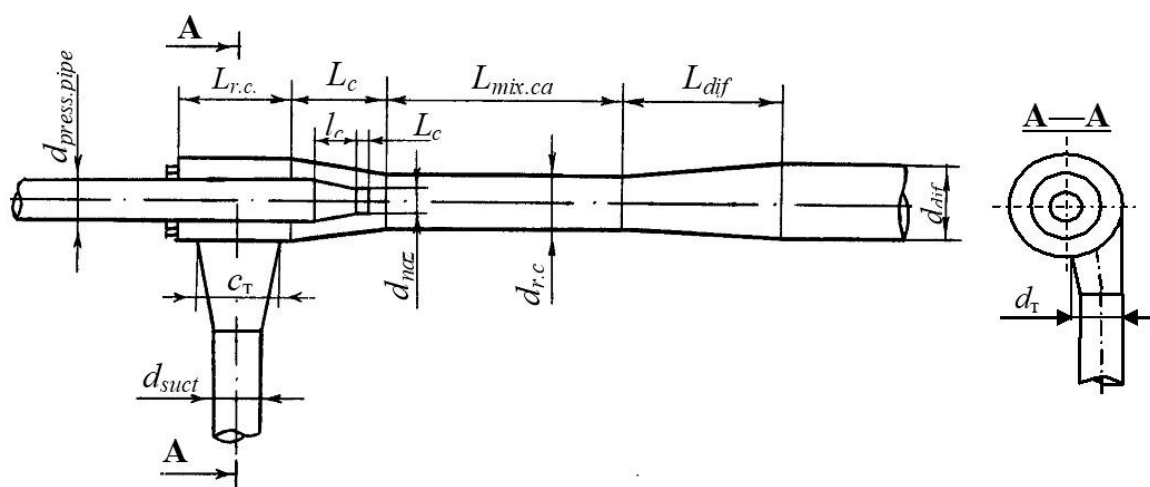


Fig.4. Diagram of a hydraulic elevator with a tangential supply of intake medium

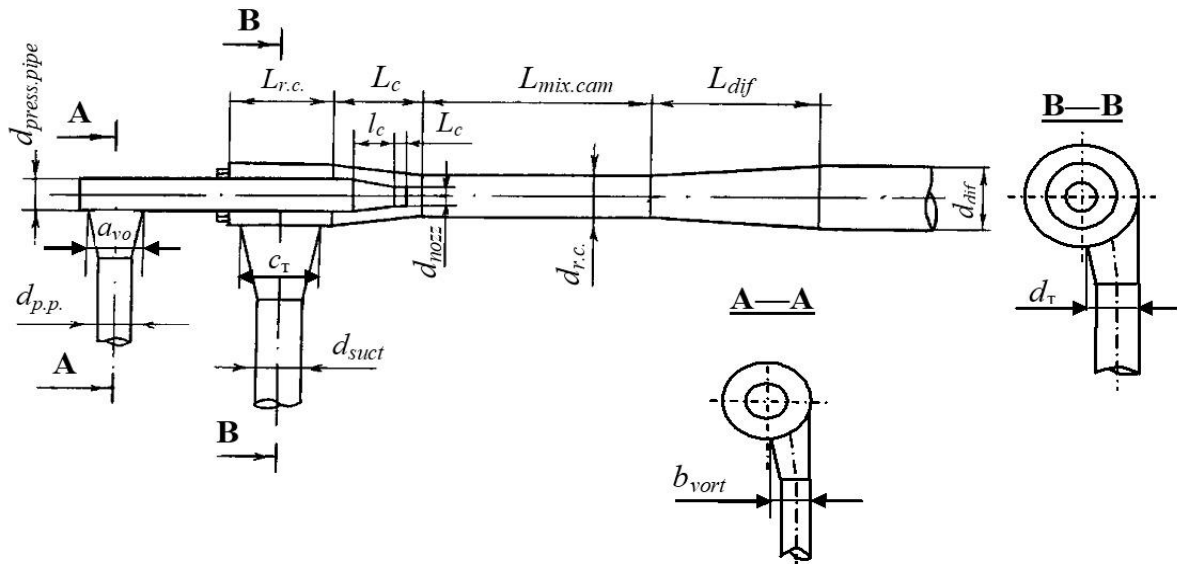


Fig.5. Diagram of the vortex hydraulic elevator

In the design of hydraulic elevators, the condition of coaxiality of structural elements is strictly maintained and made in such a way that the distance from the nozzle to the mixing chamber can be changed, which is achieved due to the fact that the section of the discharge pipe with the nozzle can be moved along the thread. Geometrical dimensions (mm) of the main structural elements of hydraulic elevators are shown in Table 1.

Table 1. Dimensions of the main structural elements of hydraulic elevators

| Type of hydraulic elevators | d_{nozz} | $d_{pres.pipe}$ | $d_{p.p.}$ | $d_{r.c.}$ | d_{suct} | $l_{confus.}$ | $L_{mix.cam}$ | $L_{dif.}$ | L_c | $L_{confus.}$ | $L_{tan r.c.}$ | $L_{vort r.c.}$ | $c_r \times d_r$ | $a_v \times b_v$ |
|---|------------|-----------------|------------|------------|------------|---------------|---------------|------------|-------|---------------|----------------|-----------------|------------------|------------------|
| Direct flow E_{direct} | 15 | 50 | - | 32 | 50 | 60 | 175 | 90 | 15 | 60 | - | - | - | - |
| With tangential fed of intake flow E_{tang} | 15 | 50 | - | 32 | 50 | 60 | 175 | 90 | 15 | 60 | 114 | - | 95x20.7 | - |
| Vortex E_{vor} | 15 | 50 | 30 | 32 | 50 | 60 | 175 | 90 | 15 | 60 | - | 114 | 95x20/7 | 40x17.6 |

The experiments were conducted with the aim of obtaining the coefficient of ejection of hydraulic elevators at different:

- a) pressures of the working fluid;
- b) the distance from the cut of the working nozzle to the beginning of the mixing chamber;
- c) geometric elevation of the hydraulic elevator;
- d) stream spin settings.

To obtain direct or swirling flows, the hydraulic elevator was made of the following separate detachable elements:

- receiving chamber with direct-flow input of the passive medium;
- receiving chamber with tangential passive medium input;
- nozzle with tangential input of the active medium.

2. Research results

Figure 6 presents the forms of jet outflows from the working nozzle: straight-flow and swirling.

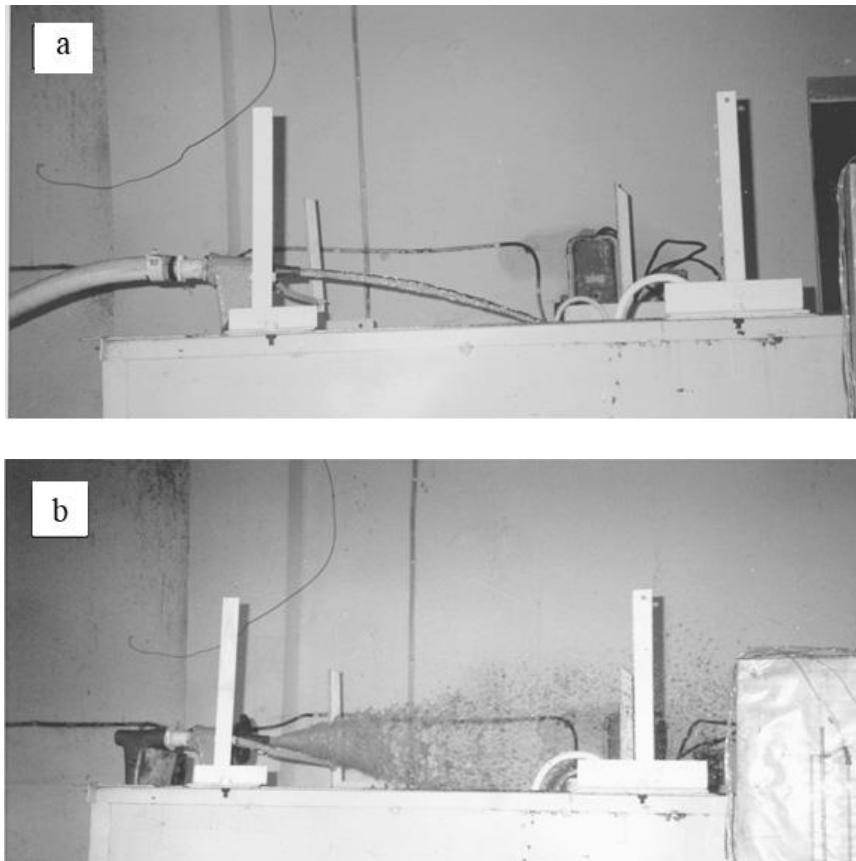


Fig.6. Active jet outflow from a working hydraulic elevator nozzle:
a) a direct flow jet; b) swirling.

In order to study the influence of the position of the working nozzle (Fig. 7) in the receiving chamber on the characteristics of the hydraulic elevator, experiments were conducted at the following distances from the nozzle section to the inlet section of the mixing chamber: $l_c = 0; 10; 20; 30; 40$ mm. During experiments the values of the coefficient of ejection q hydraulic elevators was determined. Figure 8 shows the experimental curves $l_{cr}/d_c = f(q)$.

From the graphical dependences it can be seen that the optimal distance from the nozzle to the mixing chamber is $l_c = 30$ mm, which is equal to $\frac{l_c}{d_c} = 2$ while the diameter of the mixing chamber $d_{\text{mix.cam.}} = 32$ mm and the diameter of the nozzle $d_c = 15$ mm.

According to recommendation [3], when calculating jet devices, the optimal distance from the nozzle to the mixing chamber is based on the condition that with the calculated ejection coefficient q , the area of the final section of the free jet leaving the nozzle is equal to the area of the input

section of the mixing chamber. In this case, it is necessary to calculate the length of the free jet and its diameter at a distance l_{cm} from the working nozzle section.

The value of l_{cm} is determined depending on the value of the ejection coefficient according to the following formulas :

while $q \leq 0.5$

$$l_{cm} = 3.12d_c(\sqrt{0.083 + 0.76q} - 0.29), \tag{1}$$

While $q > 0.5$

$$l_{cm} = 1.43d_c(0.37 + q). \tag{2}$$

Accordingly, the jet diameter $d_{ct.}$ at the entrance to the mixing chamber while $q \leq 0,5$

$$d_{cm} = 3.4d_c\sqrt{0.083 + 0.76q}, \tag{3}$$

while $q > 0.5$

$$d_{cm} = 1.55d_c\sqrt{1 + q}. \tag{4}$$

If, as a result of the calculation, it turns out that the jet diameter d_{cm} is less than the diameter of the mixing chamber $d_{\kappa.cm.}$, then the distance between the nozzle section and the inlet of the mixing chamber is taken to be l_{cm} . At the same time, installation of the nozzle closer than at a distance l_{cm} does not significantly affect the operation of the hydraulic elevator, since the final section of the jet fits perfectly into the mixing chamber.

Recession the nozzle from the mixing chamber can significantly impair the operation of the hydraulic elevator. In this case, the jet does not fit into the inlet section of the mixing chamber. The resulting backflow of the liquid will lead to additional energy loss.

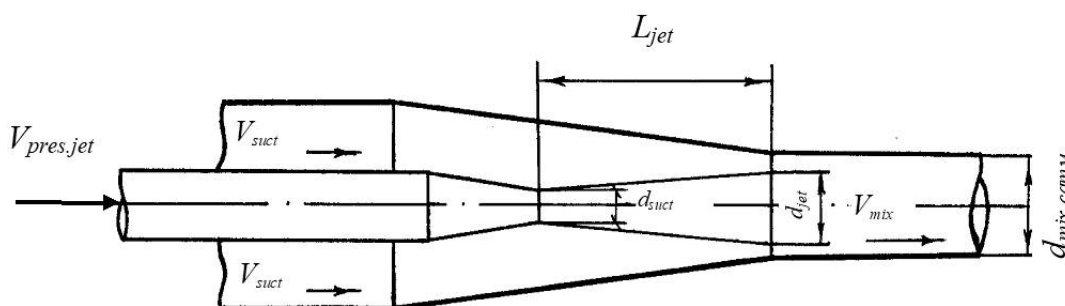


Fig.7. Calculation scheme for determining the optimal nozzle positions

If, as a result of the calculation, it turns out that $d_{jet} > d_{mix.cam}$ then the distance from the nozzle to the mixing chamber is increased by the value of l'_{jet}

$$l'_{jet} = (d_{jet} - d_{mix.cam}) / 2. \tag{5}$$

For the studied design of the vortex hydraulic elevator, the value of l_{jet} can be obtained using the formula

$$l_{cm} = 1.43d_{nozz}(0.079 + q) \tag{6}$$

The twist intensity is characterized by the twist parameter S, which is the dimensionless ratio of the axial component of the moment of flow momentum to the multiplication of the axial

component of the momentum flow and the equivalent nozzle radius [2]. For the vortex hydraulic elevator, the twist parameter is defined as:

$$S_{act} = \frac{\frac{F_{act}}{2}}{1 - \left(\frac{F_{act}}{2}\right)^2}, \quad (7)$$

$$S_{passiv} = \frac{\frac{F_{pass}}{2}}{1 - \left(\frac{F_{pass}}{2}\right)^2}, \quad (8)$$

where $F_{akt} = \frac{V_w^a}{V_o^a}$ и $F_{pass} = \frac{V_w^n}{V_o^n}$ and is the ratio of circumferential and axial velocities of active and passive flows.

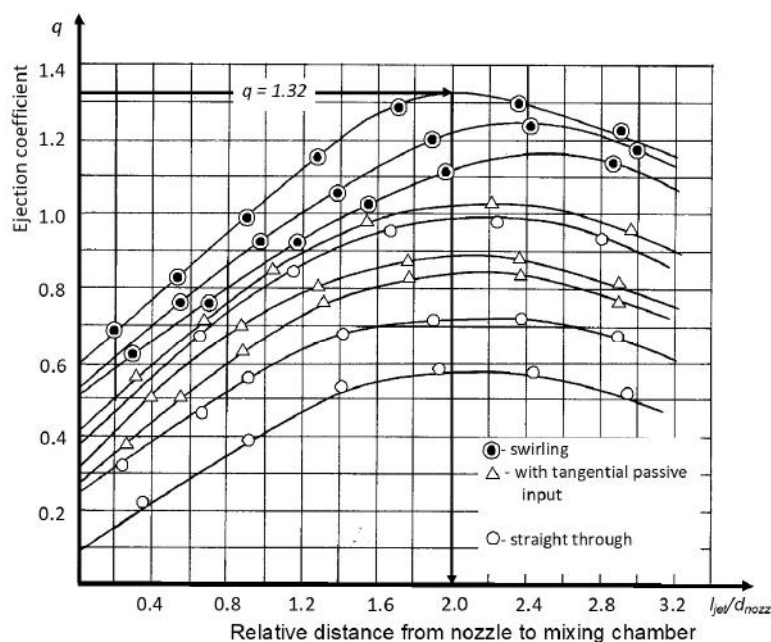


Fig.8. Graph of $l_{jet}/d_c=f(q)$ to determine the optimal distance from the nozzle to the mixing chamber.

Figures 9–11 show the graphs of $q_{suct}=f(S_{act})$, $q_{suct}=f(S_{pass})$, and $q_{suct}=f(S_{act}/S_{pass})$ at various distances from the nozzle section to the throat of the mixing chamber for a vortex hydraulic elevator.

In Figure 12, the dependence curve $q_m=f(S)$ for a hydraulic elevator with tangential entry of a passive medium. As can be seen from the graphs, for the vortex hydraulic elevator the optimal distance from the nozzle to the throat is 30 mm, and the ejection coefficient is $q_{suct}=1.32$. For a hydraulic elevator with a tangential entry of a passive medium, the optimal distance is 20 mm, with $q = 1.01$.

The analysis of the curves of dependences $q_{suct}=f(S_{act})$, $q_{suct}=f(S_{pass})$, $q_{suct}=f(S_{act}/S_{pass})$ and $q_m=f(S)$ allows us to conclude that there are critical values, $S_{kp}^{akt} = 0.11$, $S_{kp}^{nac} = 0.225$, $S_{kp}^{akt}/S_{kp}^{nac} = 0.48$, for the vortex hydraulic elevator.

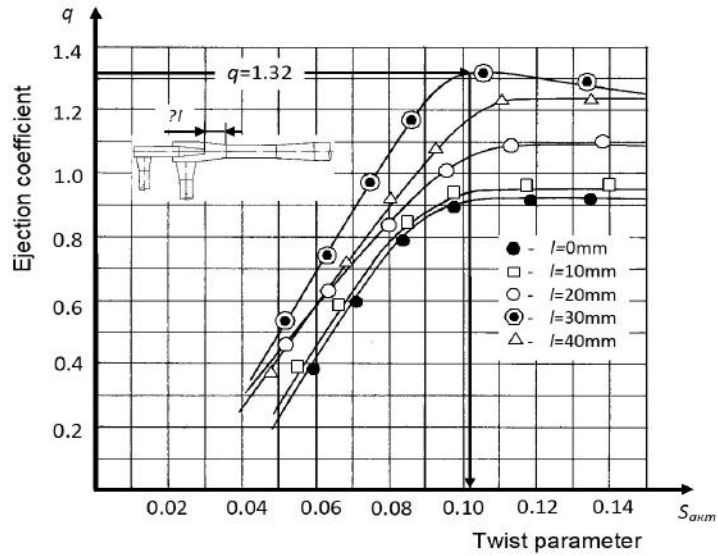


Fig. 9. The dependence of the ejection coefficient on the parameter active thread spins

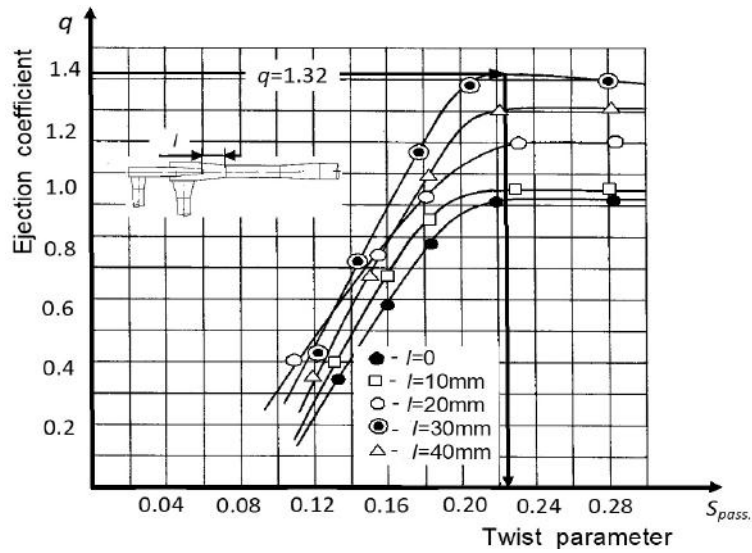


Fig. 10. Connection of the ejection coefficient with the twist parameter of passive stream

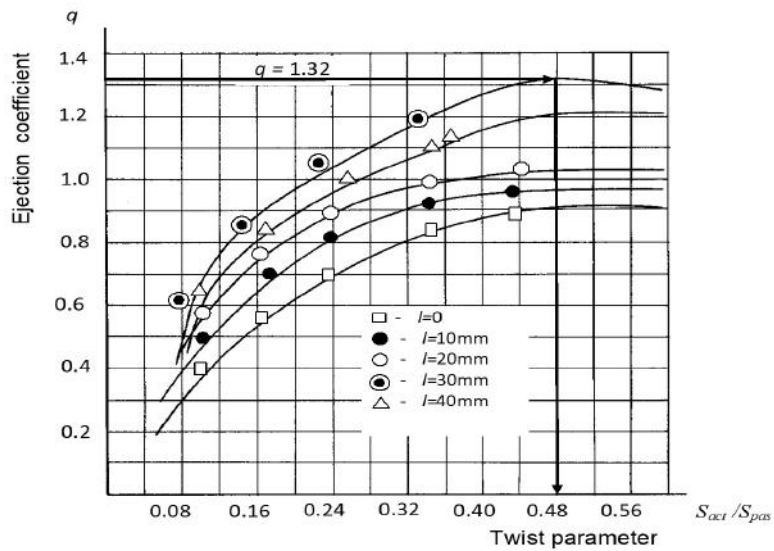


Fig. 11. Graph of $q_{suct} = f(S_{act}/S_{pass})$ dependence.

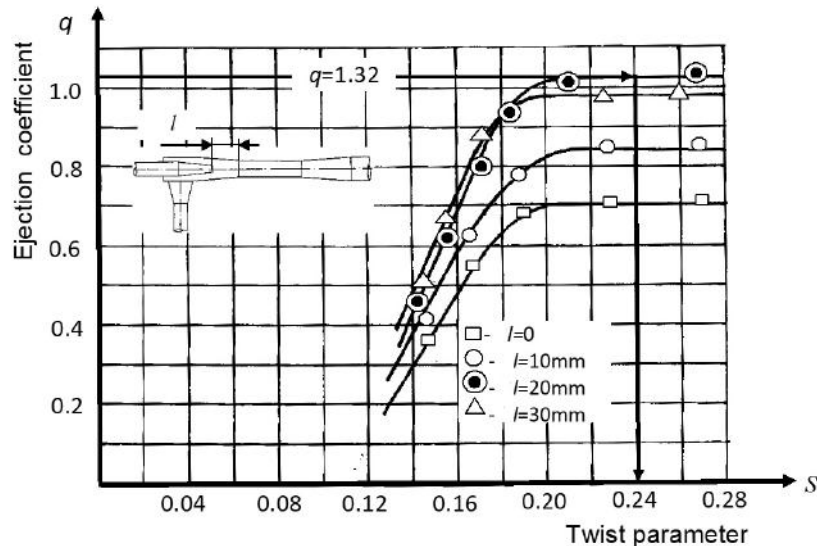


Fig. 12. Dependence of the ejection coefficient on the twist parameter of intake medium

So, $S_{kp}=0.24$ for a hydraulic elevator with a tangential intake of the intake medium at which the highest value of the ejection coefficient is achieved.

Conclusion

Analysis of the research results allows us to conclude that the swirling of active and passive flows radically affect the mechanism for drawing the intake fluid into the mixing chamber of the hydraulic elevator. An increase in the swirling intensity increases the mixing of the flow, during which large pressure gradients occur not only in the axial but also in the radial direction, which leads to an increase in the ejection coefficient.

Due to the involvement of fluid particles in the boundary layer, the spreading in the mixing chamber will be not in the bulk of the stationary fluid, but in the co-drawn suction flow. In the vortex hydraulic elevator in the area between the nozzle section and the mixing chamber, the mutual penetration of active and passive helical flows occurs. The length of the path of interaction between the two-vortex flows will significantly increase compared with the distance from the nozzle exit to the beginning of the mixing chamber, as a result, the amount of the transmitted energy of the active passive flow will increase. Thus, the use of vortex hydraulic elevators in the hydro transportation of various mixtures will significantly reduce energy consumption and increase productivity.

REFERENCES

- 1 Lyamaev B.F. *Hydrojet pumps and installations*. Moscow, 1988, 277 p. [in Russian]
- 2 Gupta A., Lilly D., Seared N. *Swirling flows*. Moscow, Mir, 1987, 589 p. [in Russian]
- 3 Sokolov E.Ya., Zinger N.M. *Inkjet machines*. Moscow, Energy, 1970, 288 p. [in Russian]
- 4 Abduramanov A.A., Abirov A.A., Abduramanov E.A. *Jet pumps. Hydrocyclone pumping units. Pumping stations* (Analytical review). Taraz, 2003, 32 p.
- 5 Lesin A.V., Valeev S.I., Bulkin V.A. Prospects for the development of the separation of suspensions and emulsions in hydrocyclones. *Bulletin of the Technological University*. 2015, Vol. 18, No.10, pp. 55 – 57.
- 6 Basharov M.M., Sergeeva O.A. *Devices and calculation of hydrocyclones*. Kazan, 2012, 92 p.
- 7 Matvienko OV, Evtuyshkin E.V. Theoretical study of the cleaning process of oil-contaminated soil in hydrocyclone devices. *Engineering Physics Journal*. 2007, Vol. 80, No.3, pp.72 – 80.
- 8 Evtuyshkin E.V. *Mathematical modeling of the movement of the dispersed phase and separation in a hydrocyclone*. Thesis of the Ph.D. , Tomsk, 2007, 168 p.

UDC 519.63; 533.697.2; 533.6.011.5

NUMERICAL SOLUTION OF THE PROBLEM OF SUPERSONIC GAS FLOW IN TWO-DIMENSIONAL CHANNEL WITH THE OSCILLATING UPPER WALL

Perchatkina E.V., Minkov L.L.

National Research Tomsk State University, Tomsk, Russia, perchatkinae@mail.ru

In paper we solve the problem of supersonic gas flow in two-dimensional channel with the moving upper wall making oscillations according to the harmonic law. In order to get a numerical solution for gas dynamics equations we have implemented the difference scheme with space and time approximation of the first order using Van Leer's method to compute fluxes. A special form of fluxes in the gas dynamics equations is given, which enables to calculate fluxes on cell faces of difference mesh using Van Leer's method. Depending on a type of harmonic law and initial gas inflow conditions, the peculiarities of angle-shock wave propagation in moving curvilinear domains have been investigated. It has been determined that under a particular oscillation frequency the presence of wall oscillation practically doesn't have an effect on the flow regime inside the domain. While comparing the numerical solution obtained due to our program with the one obtained with Ansys Fluent solver we found that the constructed code operates correctly.

Keywords: oblique shock wave, moving curvilinear coordinate system, Van Leer method.

Introduction

Irregular shape nozzles as the parts of jet engines are wide spread in the various rocket and missile engineering fields nowadays. For instance, variable exit area nozzles optimizing the operation of jet engines under the number of various velocities and nozzle outflow regimes along with the deflectable thrust nozzles with the possibility of changing a thrust vector. During the rocket flight one can observe generation of diverse body and its components vibration: from mechanical vibration caused by rocket-engine starting to the vibration arising due to aerodynamic load while supersonic cruising (flutter).

1. Problem formulation

We consider the domain formed by the upper and lower solid boundaries, Figure 1. Gas inflows to the domain through the left boundary AB with supersonic velocity, which is inclined at an angle α , and drains away through the boundary CD.

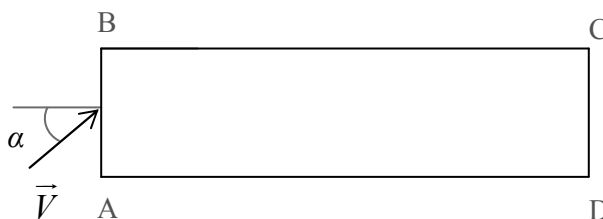


Fig.1. Computational domain

The upper wall BC make oscillations along a vertical axis according to the harmonic law $y = |DC| + A \frac{x}{|AD|} \sin(\omega t)$, wherein point B supposed to be fixed. On initial time we suggest the value of the domain inlet and outlet height is $AB=DC=1$, the domain length is $AD=4$. Gas flow is governed by the system of Euler equations in curvilinear coordinate system (1).

$$\frac{\partial \tilde{U}}{\partial \tau} + \frac{\partial \tilde{F}}{\partial \xi} + \frac{\partial \tilde{G}}{\partial \eta} = 0, \quad (1)$$

where

$$\tilde{\mathbf{U}} = \begin{pmatrix} \rho J \\ \rho Ju \\ \rho Jv \\ \rho JE \end{pmatrix}, \quad \tilde{\mathbf{F}} = \begin{pmatrix} \rho(\alpha - \gamma) \\ \rho u(\alpha - \gamma) + p \cdot y_\eta \\ \rho v(\alpha - \gamma) - p \cdot x_\eta \\ \rho H(\alpha - \gamma) + p \cdot \gamma \end{pmatrix}, \quad \tilde{\mathbf{G}} = \begin{pmatrix} \rho(\beta - \sigma) \\ \rho u(\beta - \sigma) - p \cdot y_\xi \\ \rho v(\beta - \sigma) + p \cdot x_\xi \\ \rho H(\beta - \sigma) + p \cdot \sigma \end{pmatrix}, \quad (2)$$

u, v – components of velocity vector V , directed along x, y axes in Cartesian coordinate system; ρ – density; p – pressure; H – enthalpy, $E + p/\rho$; E – total energy, $\frac{1}{k-1} \cdot \frac{p}{\rho} + \frac{u^2 + v^2}{2}$; k – heat capacity ratio, 1.4; $\alpha = u \cdot y_\eta - v \cdot x_\eta$; $\gamma = x_\tau \cdot y_\eta - y_\tau \cdot x_\eta$; $\beta = v \cdot x_\xi - u \cdot y_\xi$; $\sigma = y_\tau \cdot x_\xi - x_\tau \cdot y_\xi$.

Initial and boundary conditions at the domain inlet are set in the form (3).

$$\rho = 1; u = 2; v = 0.5; P = 1 \quad (3)$$

The boundary conditions at the exit are specified based on the value of the gas flow rate in the last cells. For supersonic flow, $u > c$ (where c is a speed of sound), the boundary conditions at the exit are not specified, otherwise, when the flow is not supersonic, at the right boundary we set the pressure. To obtain a solution to this problem the finite volume method is applied. The determination of flows through the faces of the computational cells was carried out using the Van Lear method. The original equation is a difference scheme with the first order of approximation in spatial and in time variables.

1. Implementation of Van Lear method.

To carry out the splitting procedure in a curvilinear coordinate system, the vector $\tilde{\mathbf{F}}$ (according to [3], [4]) will be represented as:

$$\tilde{\mathbf{F}} = \begin{pmatrix} \rho U_\eta \\ \rho U_\eta^2 + p \\ \rho v_\eta U_\eta \\ \rho H U_\eta \end{pmatrix} + \begin{pmatrix} 0 \\ \rho U_\eta \cdot W_t \\ 0 \\ p \cdot W_t \end{pmatrix},$$

where

$$U_\eta = \frac{y_\eta(u - x_\tau) - x_\eta(v - y_\tau)}{\sqrt{x_\eta^2 + y_\eta^2}}; \quad u_\eta = \frac{u \cdot y_\eta}{\sqrt{x_\eta^2 + y_\eta^2}} - \frac{v \cdot x_\eta}{\sqrt{x_\eta^2 + y_\eta^2}};$$

$$v_\eta = \frac{u \cdot x_\eta}{\sqrt{x_\eta^2 + y_\eta^2}} + \frac{v \cdot y_\eta}{\sqrt{x_\eta^2 + y_\eta^2}}; \quad W_t = \frac{\gamma}{\sqrt{x_\eta^2 + y_\eta^2}}.$$

Vector $\tilde{\mathbf{G}}$ splitting should be carried out in a similar way.

2. The results of the numerical solution

The numerical simulation results of supersonic gas flow in a region with a time-varying geometry have been obtained on a difference mesh 200×50 and are presented using isobars and Mach number isolines. In the considered task, there are two characteristic times of the process - the oscillation period of the domain upper wall and the time of propagation of the sound wave along the region. Firstly, we give the consideration of the first case, when $t_{os} \gg t_{gd}$.

Here $t_{gd} = L/c$ – gasdynamic characteristic time; L – characteristic dimension of the domain;

$t_{os} = 1/\omega$ – characteristic oscillation period; ω – oscillation frequency.

In order to make clear the fact when this condition is fulfilled, the flow pattern mainly does not depend on the presence of oscillations of the domain upper wall, calculations have been made when the gas inflows at an angle $\alpha = 14^\circ$ for the flow in the region with a fixed upper wall (Fig.2) and the flow when the upper wall moves according to the law $y = 1 + 0.17 \frac{x}{4} \sin(0.5t)$, (Fig. 3, 4). Comparison of the position and intensity of oblique shock waves shows that a change in the position of the upper wall with time has virtually no effect on the overall flow pattern.



Fig.2. Pressure and Mach number distributions

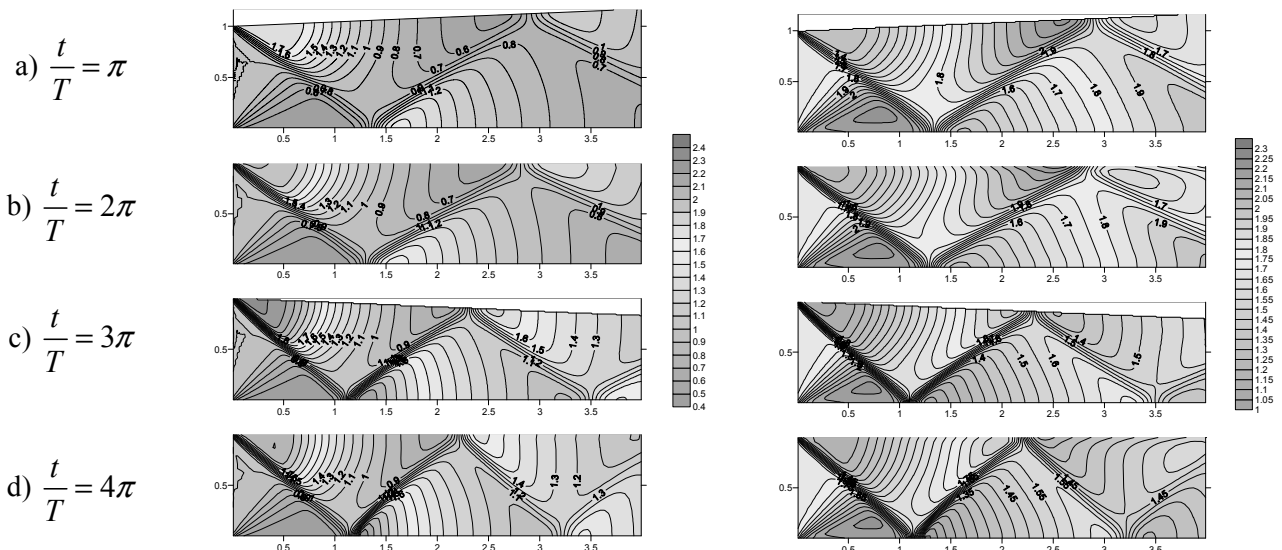


Fig.3. Pressure field

Fig.4. Mach-number distribution

Consider the following case $t_{os} \approx t_{gd}$. This case corresponds to the gas flow in the domain with the upper wall position, changing according to the law $y = 1 + 0.17 \frac{x}{4} \sin(t)$. The calculation results of the pressure fields and the Mach numbers for gas flowing into the region at an angle $\alpha = 0^\circ$ for the one period of time T are presented in Figures 5, 6, respectively. Figure 5 (a) clearly demonstrates that the rise of the upper wall causes the formation of rarefaction wave at the beginning of the region and, on the contrary, when the wall moves down - a compression wave, Figure 5 (c).

In order to establish the dependence of the intensity of shock waves on the law of wall displacement, we carried out a calculation in presence of direct gas inflow (i.e. $\alpha = 0^\circ$) for a region with the upper wall moving according to the law $y = 1 + 0.51 \frac{x}{4} \sin(t)$.

The results of this simulation are presented in Figures 7, 8. A comparison of Figures 5 and 7 allows us to conclude that with an increase in the swing amplitude of the upper wall, the intensity of

generated rarefaction waves (Fig. 5 (a), 7 (a)) and compression waves (Fig. 5 (c), 7 (c)) also increases.

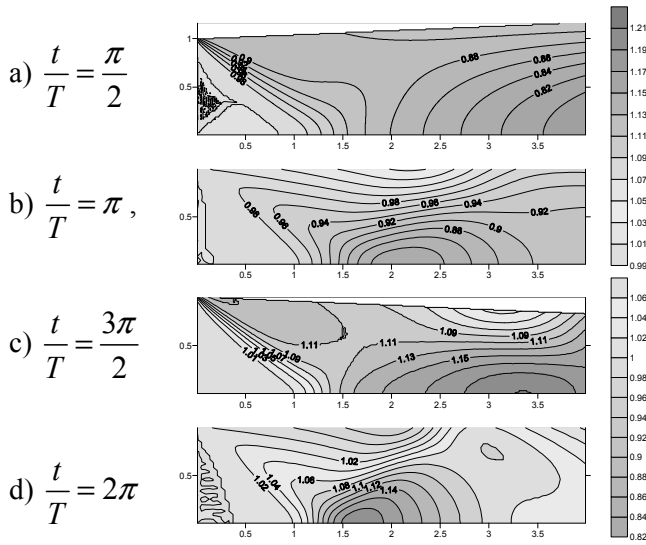


Fig.5. Pressure field

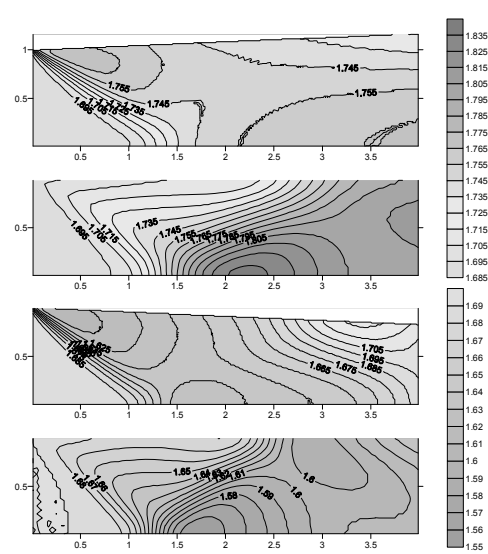


Fig.6. Mach-number distribution

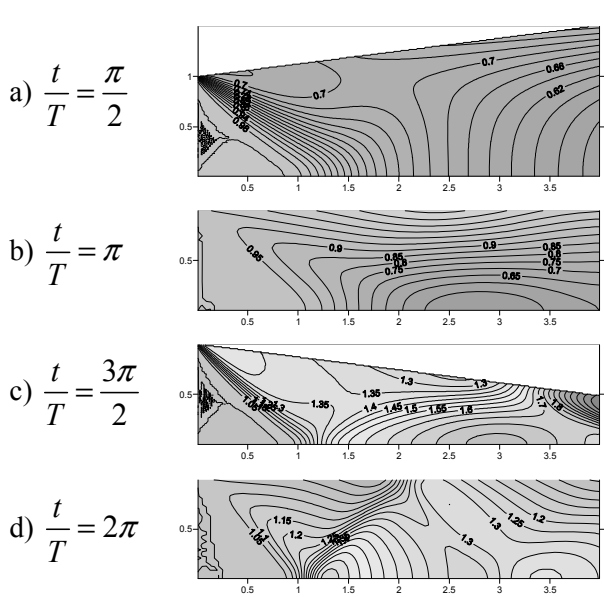


Fig.7. Pressure field

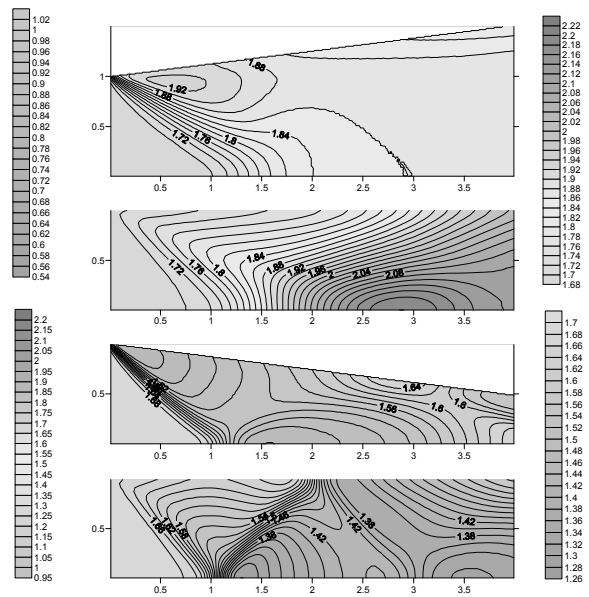


Fig.8. Mach-number distribution

Figures 9, 10 show the calculation results for the case when gas flows into the area at an angle $\alpha=14^\circ$. The movement of the upper wall is described by the law $y=1+0.17\frac{x}{4}\sin(t)$. A comparison of Figure 9 with Figure 3 shows that with an increase in the upper wall oscillation frequency, the intensity of the resulting oblique shock waves weakens. In addition to the above, at the time $\frac{\pi}{2}$, when the upper wall reaches the maximum point (Fig. 9a), the shock waves do not have enough time to propagate along the entire length of the region.

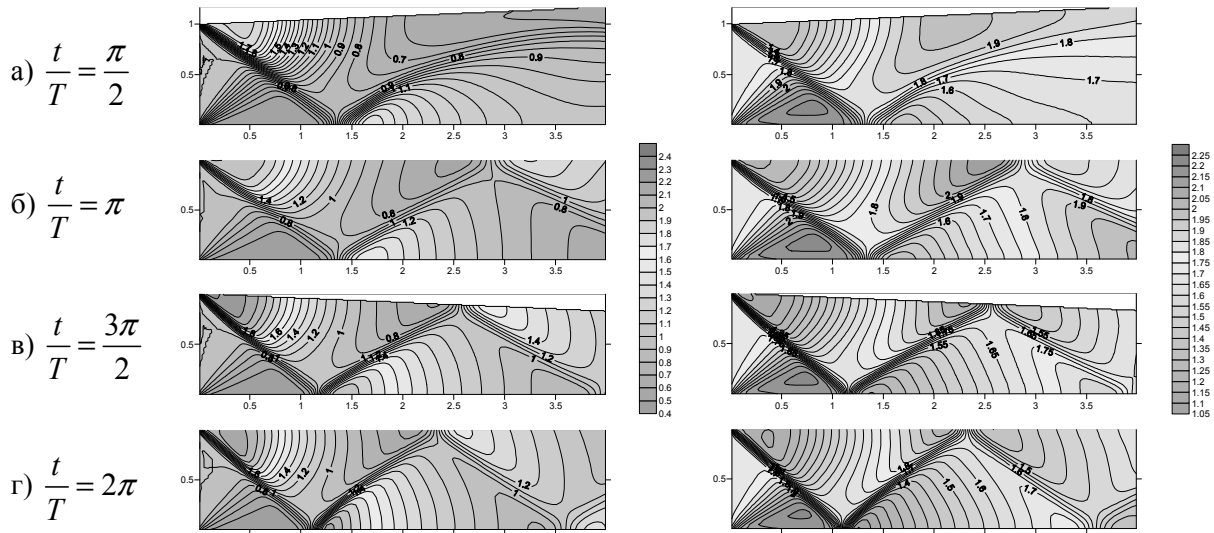


Fig.9. Pressure field

Fig.10. Mach-number distribution

3. The Ansys Fluent results

To verify the simulation results, we calculated the pressure fields and Mach numbers using the Ansys Fluent software. Here are the simulation results for gas flowing into the domain at an angle $\alpha = 14^\circ$, (Fig. 11, 12).

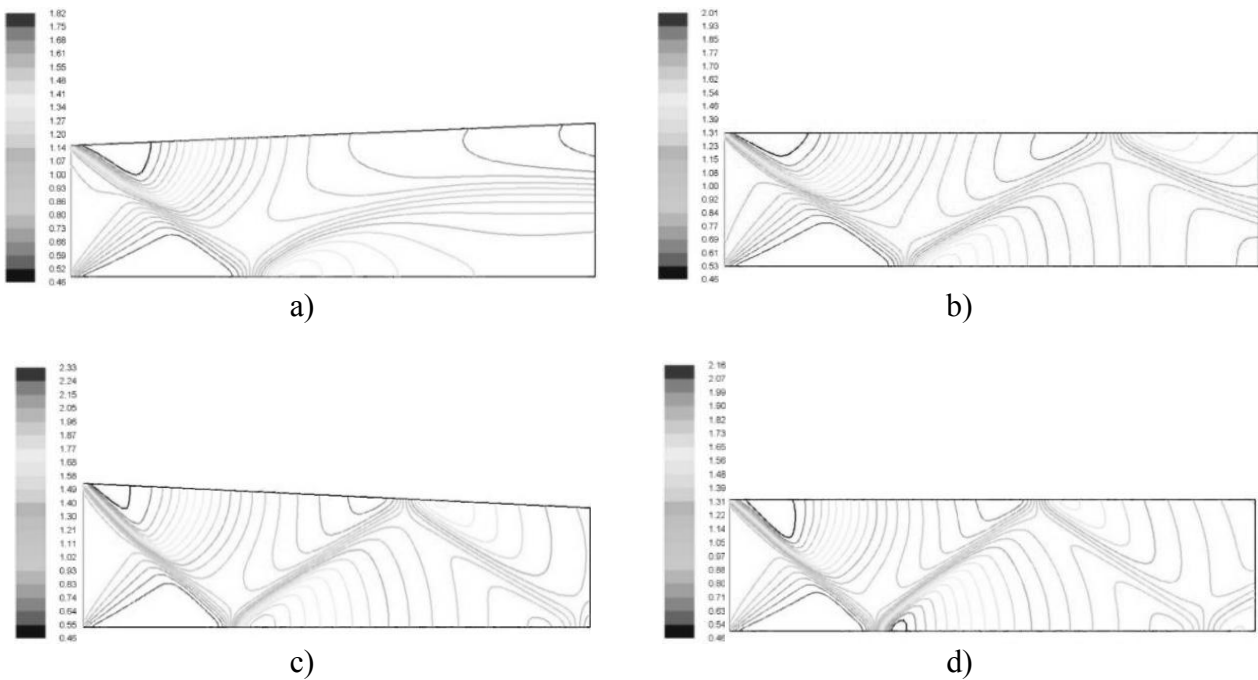


Fig.11. Pressure field as per Ansys Fluent

The law of motion of the upper wall is $y = 1 + 0.17 \frac{x}{4} \sin(t)$. Comparison of the flow pattern, position and intensity of shock waves in Figures 9 and 10, 11 and 12 shows that the created procedure of calculating gas flow in a curvilinear region with moving boundaries allows us to obtain a physically correct numerical solution.

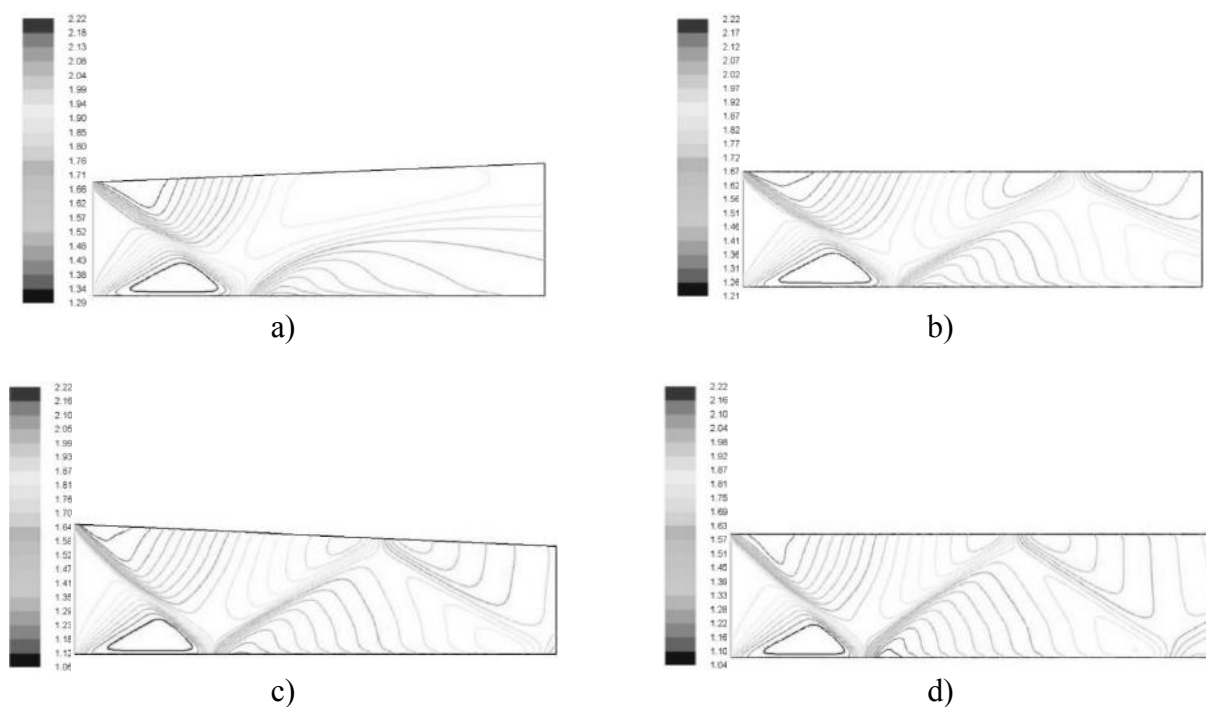


Fig.12. Mach-number distribution as per Ansys Fluent

a) $\frac{t}{T} = \frac{\pi}{2}$, b) $\frac{t}{T} = \pi$, c) $\frac{t}{T} = \frac{3\pi}{2}$, d) $\frac{t}{T} = 2\pi$

Conclusion

We have studied the features of the oblique shock wave propagation in a region in the presence of an oscillation of the upper boundary depending on the type of the harmonic law on which this oscillation is carried out. It was found that at certain amplitude, the oscillation of the wall practically does not affect the nature of the flow in the considered region. A comparison of the numerical solution obtained by the created program with the numerical solution obtained with the Ansys Fluent solver showed the correctness of the created program work.

REFERENCES

- 1 Chorny S.G. *Numerical simulation of currents in turbomachines*. Novosibirsk, Science, 2006, 202p. [in Russian]
- 2 Anderson D., Tannehill J, Pletcher R. *Computational fluid mechanics and heat transfer*. Moscow, Mir, 1990, Vol. 1, 384 p.
- 3 Vinokur M. Conservation equations of gas dynamics in curvilinear coordinate systems. *J. Comput. Phys.* 1974, No. 14, pp. 105 – 125.
- 4 Godunov S.K. *Numerical solution of multidimensional problems of gas dynamics*. Moscow, Nauka, 1976, 400 p. [in Russian]
- 5 Abramovich G. *Applied gas dynamics*. Moscow, Science, 1991, Vol.1, 600 p. [in Russian]
- 6 Toro E. F. *Riemann solvers and numerical methods for fluid dynamics*. London-New York : Springer-Verlag Berlin Heidelberg, 2009, 724 p.
- 7 Kisarova S. Yu. *Mathematical modeling of non-stationary gas-dynamic processes, conjugate heat exchange and ignition of condensed substances in channels of complex shape*. Diss. ... Cand. Phys.-Mat. sciences. Izhevsk, 1995, 160 p. [in Russian]

UDC 621.311.24

DETERMINING THE AERODYNAMIC CHARACTERISTICS OF SAILING WIND TURBINE

Yershina A.K., Ydyryssova A.A.

Kazakh State Women's Teacher Training University, Almaty, Kazakhstan, ainakul82@mail.ru

Wind turbines on the principle of operation can be divided into 3 types: sailing (Savonius), propeller and wing (Darrieus type) wind turbines. In paper the fundamentals of the theory of sailing wind turbines are outlined. The aerodynamic characteristics are determined: lift and drag coefficients, turbine power, use of wind energy, degree of speed, etc. A comparison of the calculation results with experimental data is presented. Satisfactory agreement of the calculation results with known experimental data is shown.

Keywords: Savonius, lift, drag, the degree of rapidity, utilization of wind energy.

Introduction

The general, robust growth of wind power around the world which goes hand in hand with further geographic diversification is very encouraging [1]. New world regions such as Latin America and most recently also Africa are playing an important role in this dynamic development. Obviously many governments have understood that wind power brings great benefits to their societies, as it is emission-free, cheap, domestic and accessible and offers a very attractive pathway to achieving the Paris agreement. However, signs of weakness in particular in Europe are a matter of concern. On Fig.1 shows the total energy consumption of wind energy in the world in 2013-2017.

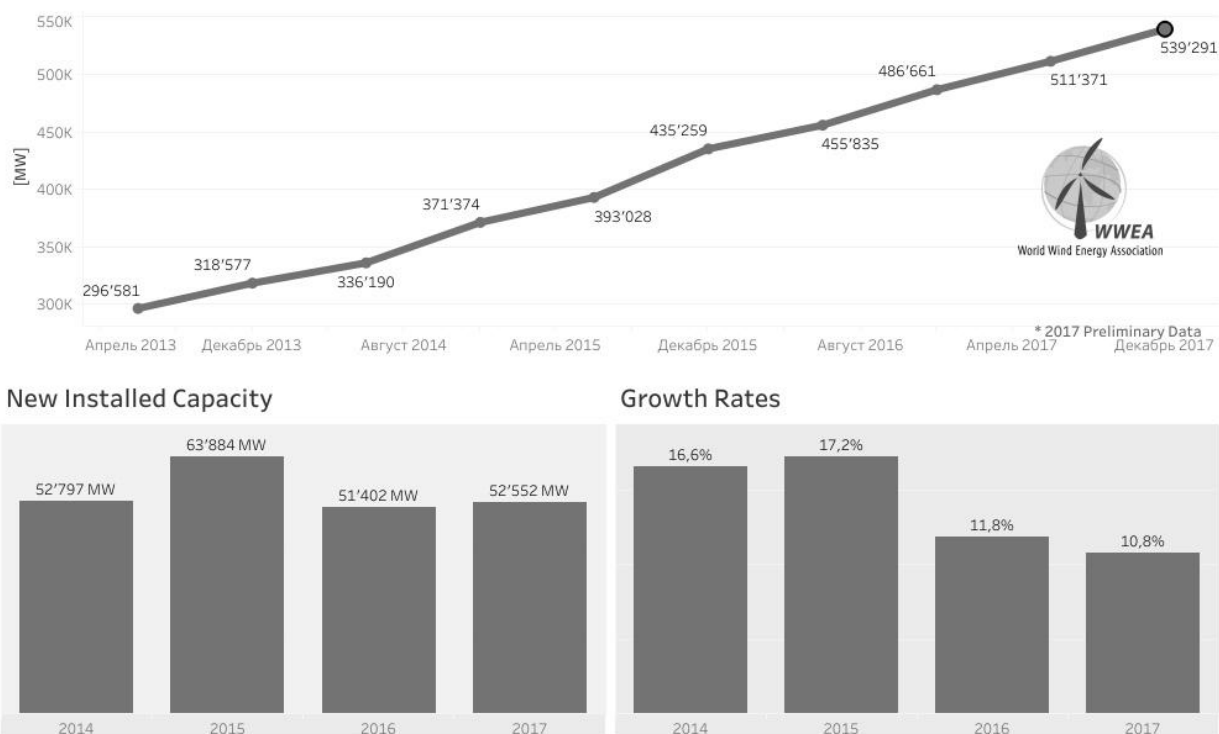


Fig.1. Total installed capacity 2013-2017 (preliminary data), [1]

The European Union and its member states should urgently reinforce their efforts to deploy wind power as part of an overall renewable energy strategy and to work out a roadmap for a 100% renewable energy future [1]. All experts working in the field of renewable energy sources recognize that wind power has a great future in all respects. This explains the interest shown in the development of wind energy in many states.

There is a wide variety of wind turbine designs, but according to the principle of operation, they can be divided into three main types - sailing (Savonius), propeller (wind wheel) and wing (Darrieus type) [2-4]. The basis of our study selected sailing wind turbine. The advantage of our research is that the theoretical approach was correctly chosen to determine the main aerodynamic characteristics of a sailing wind turbine.

1. Construction of a four-blade sail-type turbine

Calculation of a sail - type turbine. As an example, let us consider the operation of a four-blade turbine, the design of which is sketched in Fig. 2a [2]. Each blade perceives the wind pressure to the full extent when rotating from the OA position to the OB position (see Fig. 2b).

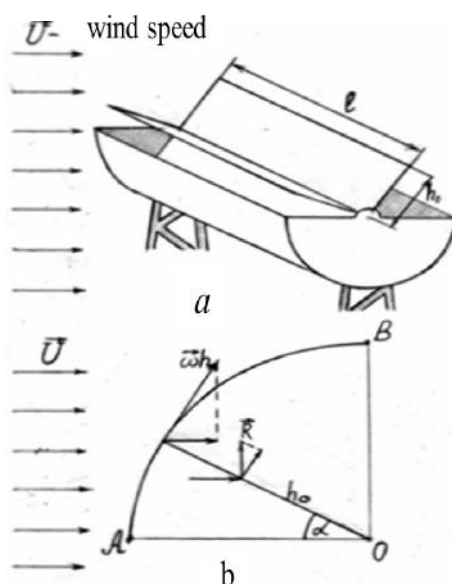


Fig. 2. The scheme of the simplest construction of a four-blade sail-type turbine

Behind the position of the OB , the angle of attack becomes negative and in addition the next blade appears which begins to obscure the previous one. Thus, the rotational moment is transmitted to each blade in the first quarter of the circumscribed circle. Accordingly, in this quadrant, the power transmitted by the wind turbine is registered. It is consumed for the work of lifting force \vec{R}_x and overcoming the force of resistance of the blade \vec{R}_y .

2. Calculation of sailing wind turbines

Let us relate the coordinate system to a rectangular blade rotating in the direction of the wind movement, the area of which $S_0 = l h_0 m^2$.

Then the velocity of flow on the blade will be equal to $|\vec{u}| = |\vec{U}| - |\vec{W}| \sin \alpha$, where $\vec{W} = \vec{\omega} h$ - linear velocity of the blade element at a distance h from the axis of rotation, \vec{U} - wind speed. To

find the resultant force of dynamic pressure, it is necessary to find the resultant vector of the relative velocity of the air flow. With this aim, we integrate the last expression over the surface $S_0 = l h_0$.

$$|\vec{u}_0| = \frac{1}{h_0} \int_0^{h_0} |\vec{u}| dh = |\vec{U}| - \frac{|\vec{W}_0|}{2} \sin \alpha, \text{ where } \vec{W}_0 = \vec{\omega} h_0.$$

Dynamic wind pressure per blade

$$\frac{\rho u_0^2}{2} = \rho \frac{(2|\vec{U}| - |\vec{W}_0| \sin \alpha)^2}{8} \quad (1)$$

The resistance of the blade is determined by the known formula [5]

$$|\vec{D}| = C_x(\alpha) \delta_1 l \rho U_0^2, \quad (2)$$

where $C_x(\alpha)$ - coefficient of resistance of a rectangular plate, is proportional to $\sin^2(\alpha)$ at small angles of attack $0^\circ \leq \alpha \leq 20^\circ$ [6] and $C_x = 1.3$ at $\alpha = 90^\circ$ (see Table 1), δ_1 - the dimensions of the W vortex path behind the plate, the width of which $\delta_1 > h_0$ at $\lambda = \frac{l}{h_0} > 1$.

Heisenberg equating the circulation created per unit time on the edges of a flat plate, located normally to the flow, circulation, carried by vortices, found that $\delta_1/h_0 = 1.54$. In our case, when the breakdown of the vortices occurs only on one side of the plane blade, we assume that $\delta_1/h_0 = 1.27$. The resistance coefficient of the thin symmetrical wing NASA profile 0006 in the range of the angle of attack $0^\circ \leq \alpha \leq 20^\circ$ is well described by the empirical formula:

$$C_x(\alpha_1) = 0.001 + 0.5 \sin^2 \alpha. \quad (3)$$

There are no data for corners of attack « α » more than 20° . At $\alpha \geq 20^\circ$ we can interpolate and write the dependence corresponding to large angles of attack $C_x = 1.3$ at $\alpha \rightarrow \pi/2$

$$C_x(\alpha_2) = 1.5 \sin \alpha - 0.2. \quad (4)$$

Thus, formula (2.5.2) takes the following form

$$|\vec{D}_1| = h_0 l C_x(\alpha_1) \rho \frac{(2|\vec{U}| - |\vec{W}_0| \sin \alpha_1)^2}{8} \quad (2)'$$

at $0 \leq \alpha_1 \leq 20^\circ$.

$$|\vec{D}_2| = 1.27 l h_0 C_x(\alpha_2) \rho \frac{(2|\vec{U}| - |\vec{W}_0| \sin \alpha_2)^2}{8} \quad (5)$$

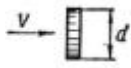
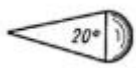
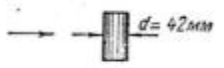
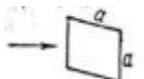
at $\alpha = \alpha_2, 20^\circ \leq \alpha_2 \leq 90^\circ$.

Lifting vector $|\vec{R}| = \frac{C_y}{l h_0} \frac{\rho u_0^2}{2}$ directed towards attack speed \vec{V} at an angle 90° and the force, acting on the lifting of the blade is

$$h_0 l \vec{R} \sin \alpha. \quad (6)$$

Taking into account the fact that, for the plate, the coefficient of lift $C_y = 2\pi \sin \alpha$ in the interval $0 \leq \alpha \leq 20^\circ$ [2, 6] and $R = 0$ at $\alpha_1 > 20^\circ$, to determine the power transmitted to the turbine by the wind.

Table 1. The drag resistance C_x for different bodies

| The name of the body | The form bodies | The ratio of the linear dimensions of the body | The speed of the experiment is v (m / s) | Reynolds number Re | The coefficient C_x |
|-------------------------------|---|--|--|---------------------------------------|-----------------------|
| Round plate |  | – | – | $10.7 \cdot 10^4 \div 227 \cdot 10^4$ | $1.06 \div 1.28$ |
| Cone |  | – | 10 | $2.7 \cdot 10^5$ | 0.34 |
| Cone with spherical base |  | – | 10 | $1.35 \cdot 10^5$ | 0.16 |
| Also |  | – | 10 | $1.35 \cdot 10^5$ | 0.088 |
| Cylinder |  | $\lambda=7$ | $10 \div 30$ | $10^5 \div 3 \cdot 10^5$ | 0.84 |
| Cylinder with spherical bases |  | $\lambda=7$ | $10 \div 30$ | $10^5 \div 3 \cdot 10^5$ | $0.28 \div 0.22$ |
| Ball |  | – | – | $10^5 \div 4 \cdot 10^5$ | $0.44 \div 0.10$ |
| Cylinder |  | 0.2 to 0.8 | 30 | $8.8 \cdot 10^4$ | $0.75 \div 0.65$ |
| Square plate |  | – | – | $10.7 \cdot 10^4$ to $227 \cdot 10^4$ | $1.06 \div 1.28$ |
| Hollow hemisphere |  | – | – | – | 0.33 |
| Hollow hemisphere |  | – | – | – | 1.34 |

To do this, calculate the work done when moving the blade from the OA position to the OB position (see Fig. 2b). In this case, the point A passes the path equal to $\frac{\pi h_0}{2}$ with speed \vec{W}_0 .

Accordingly, the power transmitted to the turbine will be

$$N = N_1 + N_2, \tag{7}$$

where $N_1 = h_0 l \int_0^{\frac{\pi}{9}} (\vec{R} + \vec{D}_1) \vec{W}_0 d\alpha$, $N_2 = h_0 l \int_{\frac{\pi}{2}}^{\frac{\pi}{9}} \vec{D}_2 \vec{W}_0 d\alpha$.

Considering that for a plate at $0^0 \leq \alpha \leq 20^0$, $C_y(\alpha) = 2\pi \sin \alpha$ [2, 6], and, substituting the expressions for $|\vec{R}|, |\vec{D}_1|, |\vec{D}_2|$, taking into account (3) and (4), we obtain

$$N = h_0 l W_0 \int_0^{\frac{\pi}{9}} (2\pi \sin \alpha + 0.001 + 0.5 \sin^2 \alpha) \rho \frac{(2|\vec{U}| - |\vec{W}_0| \sin \alpha)^2}{8} d\alpha +$$

$$+ 1.27 \frac{lh_0}{8} W_0 \int_{\frac{\pi}{2}}^{\frac{\pi}{9}} (1.5 \sin \alpha - 0.2) \rho (2|\vec{U}| - |\vec{W}_0| \sin \alpha)^2 d\alpha \tag{8}$$

Integrals are tabular, easily taken. Performing simple operations, we find:

$$N = 0.027 \rho l h_0 |\vec{W}_0| \left[7.17 U^2 - 6.29 \vec{W}_0 \vec{U} + 0.082 W_0^2 \right]. \tag{9}$$

The coefficients of wind energy is found by dividing the power N transmitted by wind to the turbine by the own power of wind $N_e = l h_0 \rho \frac{U^3}{2}$.

$$\xi = 0.053 \chi [7.17 - 6.30 \chi + 0.082 \chi^2] \tag{10}$$

Where the ratio of the translational velocity of the tip of the turbine blade to the wind speed is called the tip speed ratio (TSR), and is calculated as follows: $\chi = \frac{|\vec{\omega}| h_0}{|\vec{U}|}$ where χ is the TSR, and \vec{U}

is the free wind speed. Equating the first derivative $\frac{d\xi}{d\chi}$ to zero, find the maximum value of the wind power factor ξ_{max} , as well as χ , at which ξ_{max} and $\xi = 0$ are achieved.

So, $\xi = 0$ at $\chi = 0$ and $\chi = 1.16$, and $\xi_{max} = 0.11$ at $\chi = 0.58$.

Wind turbine power is determined by the formula

$$N = \xi \cdot l h_0 \frac{\rho U^3}{2}.$$

where N is power, U - wind speed, ξ is power coefficient, l - height, h_0 - blade width, ρ - air density.

3. Comparison of calculated and experimental data

Fig. 3 presents the experimental data of the P.P. Osipov [7] and calculated curves by the formula (10), as well as the results of calculations on the assumption that the blade does not rotate, but moves translationally with velocity $|\vec{\omega}| h_0$ in the direction of wind movement [6]. As can be seen in Fig. 3, the agreement between the calculated curve (10) and experiment is not more than 10-15%, while the maximum deviation of the dotted curve is much larger.

Light points - the experiments of P.P. Osipov. The solid line is calculated by formula (10). Dotted line - the results of calculation under the assumption that the blade does not rotate, but moves translationally.

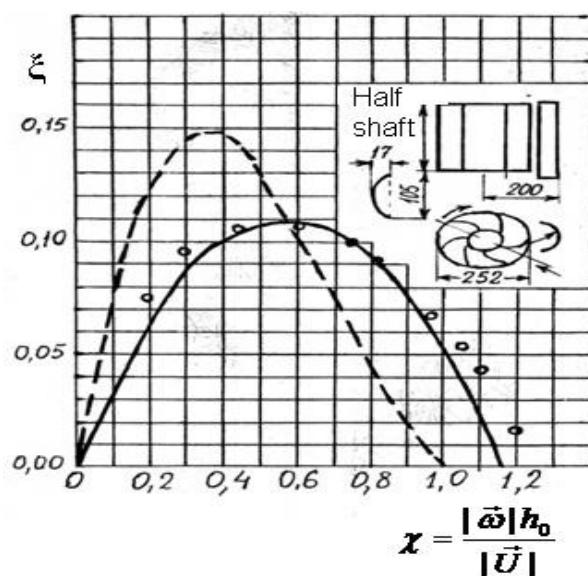


Fig. 3 Rotor power coefficient ξ as function of tip speed ratio χ . Here: $\circ\circ\circ\circ\circ$ – the experiments of P.P. Osipov. — – is calculated by formula (10). --- – the results of calculation under the assumption that the blade does not rotate, but moves translationally.

Conclusion

A theoretical calculation of the main aerodynamic characteristics of a sailing wind turbine has been carried out. Our theoretical results were tested with known experiments [7]. Comparison with experiment showed good agreement. This gave rise to confidence in the correctness of the choice of methods for solving problems.

REFERENCES

- 1 World Wind Energy Association. Statistics. February 12, 2018. Available at: <https://wwindea.org>
- 2 Yershina A.K., Yershin Sh.A., Zhabbasbayev U.K. *Fundamentals of the theory of the wind turbine Darrieus*. Almaty, Kazakh state ISTI. 2001, 104 p. [in Russian].
- 3 A.K. Yershina, Zh.K. Nursadykova, M.A. Borybaeva. *Analysis of developing wind power apparatus in Kazakhstan*. Eurasian phys.tech.j., 2016, Vol. 13, No. 2(26), pp. 99 – 106.
- 4 Yershin Sh., Yershina A.K., Ydyryssova A.A. Vertical-axial two-rotor wind power units Bidarrieus- 1. //Eurasian Physical Technical Journal, 2017, Vol. 13, No. 2(28), pp. 108 – 112.
- 5 Zheng P. *Separated Flows*. Moscow: Mir, 1972. Vol.1, 299 p.
- 6 Loitsyansky L.G. Fluid and gas mechanics: a textbook for universities. - 7th edition corrected - Moscow: Drofa, 2003. - 840 p.
- 7 Poltoratsky V.T. *On the work of a wind turbine with an axis of rotation perpendicular to the flow*: Report of the ENIIN Academy of Sciences of the USSR, 1953,

UDC 638.21.4

INVESTIGATION OF THERMAL CONDITIONS OF THE MOLDING PROCESS OF SLURRY BERYLLIUM OXIDE

Sattinova Z. ¹, Ramazanova G. ², Zhabbasbayev U. ², Assilbekov B. ², Mussenova E. ³

¹L.N. Gumilyev Eurasian National University, 010000, Astana, Kazakhstan, Sattinova_zamira@mail.ru

²Satbayev University, 050026, Almaty, Kazakhstan

³E.A. Buketov Karaganda State University, 100028, Karaganda, Kazakhstan

Results of experiments and calculations of the mathematical model of the motion and heat exchange of the slurry mass in the annular cavity are presented. Temperature distribution, estimated during the experiments, in the form-building cavity of bushing depending on the molding velocity and heat extraction conditions on the walls of form-building of annular cavity lets us determine the transition from liquid (viscous-plastic) state to solid-plastic one. The experiment results were analyzed and generalized using mathematical model of the thermoplastic slurry molding process. The results of calculation are in agreement with the experimental data, and they show physical validity of the proposed mathematical model of the molding process of the beryllium thermoplastic slurry.

Keywords: beryllium ceramics, thermoplastic slurry, suspension, molding process, heat transfer, phase transition, solidification of casting.

Introduction

Technology of slurry molding (extrusion) is very actually nowadays in connection with intensive development of metal injection molding (MIM) technology, where there are the same physical processes. This technology played the important role in the production of functional ceramic for the need of the nuclear, defense and electronic industry.

The development of new areas of science and directions of technology advances increased requirements to the level of properties and to the quality of ceramic fabrications, are increasingly becoming more popular products of complex configuration from new non-metallic materials (high thermal conductivity, oxygen-free, superconducting, etc.). Technology of hot casting under pressure [1, 2] remains the basis for the obtaining long-length, multi-channel, complex shaped ceramic fabrications from non-plastic powders, in spite of the using of isostatic pressing.

However, in spite of the fact that last years a lot of attention has been paid to improving of the technology and creation of the new equipment. Up to now unsolved problem of obtaining without defects products by this method has remained. As a result, in practice it does not often achieve the desired quality of moldings and obtaining of acceptable products, that makes this process low profitability. Obtaining of ceramic fabrications by hot molding from dispersion materials with anomalous physical properties, such as BeO is particularly complicated. In this case, the difficulties of obtaining of quality products were caused firstly by thermal properties of beryllium oxide, in particular, its unique thermal conductivity [2, 4]. Clearly, it is impossible to eliminate taking place technological limitations and problems without the development which they are based on all experience and knowledge of theoretical representations about regularities and mechanisms of regulation of the thermal regime of the casting on the forming process of molding. The results of experimental researches and the generalization by calculations of mathematical model of process molding of the thermoplastic slurry beryllium oxide are presented in this paper.

1. Experimental data of rheological properties of the thermoplastic slurry

The thermoplastic slurry (highly-viscous suspension) represents a two-phase disperse system, where the solid minerals phase - beryllium oxide powder, liquid phase - organic binder [3]. The organic coupler consists of three components: paraffin, beeswax and the oleic acid in the proportion 82%: 15%: 3%. The Shvedov-Bingham rheological model was used to describe the rheological property, the relation between the shear stress τ and shear rate $\frac{\partial u}{\partial r}$ of the thermoplastic slurry:

$$\tau = \tau_0 + \mu \frac{\partial u}{\partial r}, \quad (1)$$

where τ is the shear stress, τ_0 is the yield strength, μ is the plastic viscosity coefficient.

The ultrasonic effect (USE) influences the rheological properties of the slurry. The plastic viscosity coefficient $\mu(Pa \cdot s)$ and the yield strength $\tau_0(Pa)$ of the slurry depend on temperature T , and the experimental data at the relative mass fraction of the binder $\omega = 0.1$ prior the USE are described by the empirical dependencies

$$\begin{aligned} \mu &= 5.5 + 6.2 \exp(-(T - 334)/6), \\ \tau_0 &= 19 + 11.41 \exp(-(T - 340)/5.47) \end{aligned} \quad (2)$$

after the USE:

$$\begin{aligned} \mu &= 2.5 \cdot 10^{14} \exp(-0.09068 T), \\ \tau_0 &= 5.93 \cdot 10^8 \exp(-0.04968 T) \end{aligned} \quad (3)$$

The slurry density is determined by the concentration of the beryllium powder and the binder:

$$\rho = \frac{\rho_{BeO} \cdot \rho_{bin}}{((1-\omega)\rho_{bin} + \omega \cdot \rho_{BeO})} \times 10^3 \quad (4)$$

where ρ_{BeO} is the beryllium density, ρ_{bin} is the coupler density, ω is the relative mass fraction of the coupler in the fractions of unity.

The coupler density is temperature-dependent and is determined by the empirical formula

$$\rho_{bin} = 0.8485 + 0.0755 \cdot \cos(0.0571 \cdot T - 16.736)$$

The beryllium density is $\rho_{BeO} = 3.02 \text{ g/cm}^3$. The coupler density in temperature range from 348 to 318°C varies within the limits $\rho_{bin} = 0.784 - 0.8845 \text{ g/cm}^3$, and at the solidification, the thermoplastic slurry density increases from 2.3498 to 2.4327 g/cm^3 for $\omega = 0.1$.

As the experimental data of [5] show, the USE does practically not affect the slurry thermal conductivity and heat capacity, they depend on temperature in the form

$$\lambda = 7.1 \exp(-0.01T + 2.73), \quad \frac{W}{m \cdot K} \quad (5)$$

$$c_p = 1000 \exp(0.00345T - 0.94), \quad \frac{J}{kg \cdot K} \quad (6)$$

Thus, the rheological properties of the slurry of the beryllium are the functions of temperature, and an aggregative change of the liquid suspension to its solid-plastic state occurs in the molding process.

2. Determination of thermo-physical properties of ceramic products molding process

According to experimental data, the temperature of thermoplastic slurry solidification $T_s = 55^\circ\text{C}$, and the releasing heat of the aggregative change does not affect significantly and scatters rapidly. Determination of the coefficients of heat exchange and heat transfer on the walls of the cavity presents considerable difficulties and it requires a solution of the dual problem. In this

aspect, the solution of the inverse problem with using of experimental data for evaluation of the coefficient of the heat transfer is the simplest.

For simplicity motion of the slurry in the cavity can accept one-dimensional and parameters of the cross section are constant. Heat transfer through the side surface of the filler leads to reduces the temperature of the slurry, and its variation is describing by the equation

$$Gc_p \frac{dt}{dz} = -\pi d_2 k(t - t_w),$$

where G - mass flow rate of the slurry, k - the coefficient of heat transfer through the wall of the cavity, t_w - the temperature of the cooling medium.

Heat capacity of the slurry changes in the transition zone. Increase of the enthalpy during the phase transition can be determined by the apparent heat capacity method [4, 5]. In this method, the latent heat is taken into account by increasing the heat capacity in the phase transition zone. Changing of heat capacity can be represented as [2, 4]:

$$c_p = \begin{cases} c_s, & t < t_s & \text{solid phase} \\ c_{in}, & t_s \leq t \leq t_l & \text{transition zone} \\ c_l, & t > t_l & \text{liquid phase} \end{cases} \quad (7)$$

where $c_{in} = \frac{\int_{t_2}^{t_1} c(t) dt + H_{1 \rightarrow 2}}{t_l - t_s}$, $H_{1 \rightarrow 2}$ - the phase transition specific enthalpy of beryllium slurry is determined by experimental data and is equal to $H_{1 \rightarrow 2} = 7800$ J/kg.

In phase transition function $\alpha(\bar{t})$ is introduced to the transition zone to consider the latent heat, and changing of the slurry heat capacity is expressed by:

$$c_p = c_s \cdot (1 - \alpha(\bar{t})) + c_l \cdot \alpha(\bar{t}) + H_{1 \rightarrow 2} \frac{d\alpha}{dt} \quad (8)$$

where c_s - specific heat of the slurry in the solid state, c_l - specific heat of the slurry in the liquid state, $\alpha(\bar{t}) = 0$ for the pure solid slurry and $\alpha(\bar{t}) = 1$ for the pure liquid slurry, \bar{t} - dimensionless temperature of slurry ($\bar{t} = \frac{t}{t_0}$, t_0 - initial temperature of the slurry at the inlet of the cavity). According to the experimental data of beryllium oxide slurry with binder mass fraction of $\omega = 0,117$ function $\alpha(\bar{t})$ takes a form:

$$\alpha(t) = 5.712 \cdot t - 2.85 \quad (9)$$

The equations (7)-(8) of the method of apparent heat capacity include the latent heat of the phase transition, and are convenient for calculations. For convenience position of the transition zone is not known in advance and is determined as a result of the calculations.

3. Discussion of optimization calculations data

Systematic calculations of the process of forming beryllium ceramics allow to analyze the phenomenon of phase transition at various casting speeds. Numerical calculations take into account the influence of latent heat of crystallization on heat transfer and solidification of the slurry. The process of solidification proceeds as a result of heat release during the phase transition from a liquid to a solid state. The heat of the slurry mass is transferred to the coolant.

The interval of crystallization temperature is an important factor determining the characteristic parameters of the forming process of slurry. The effect of range of the crystallization temperature is to a large extent balanced by the action of thermophysical factors. Depending on the magnitude of this interval and the properties of the slurry, different conditions are created for the formation of the slurry and the flow of the solidification process.

The parameters have changed in the optimization calculations: casting speed, cooling conditions (2 or 3 contour molds) and the design of the cooling circuit. At the inlet of the cylindrical

part of the annular cavity the temperature of the slurry is constant and equal 80°C , which corresponded to the industrial casting conditions.

The release of heat of crystallization during the phase transition of the slurry from the viscous-plastic state to the solid-plastic takes into accounting numerical calculations. The coaxial cavity consists of two concentric cylinders with radii of 6 and 10 mm, respectively, which makes it possible to obtain a ceramic product in the form as a tube. The cooling contour of the cavity is divided into 3 parts (Fig.1). Temperature of the cooling water in the first part is $t_1 = 80^\circ\text{C}$, in the second part is $t_2 = 59^\circ\text{C}$, in the third part is $t_3 = 20^\circ\text{C}$.

The results of calculations of the process of forming beryllium oxide slurry for a three-circuit coaxial annular cavity are considered, which are shown in Figs. 2-4. At the first stage, the process of cooling the hot slip through the walls of the cavity is realized by means of the boundary condition of the first kind.

The total cavity length amounts to $l = 28\text{ mm}$, the lengths of the first, second, and third sections are $l_1 = 9,4$, $l_2 = 9,2$, $l_3 = 9,4$ (fig.2a); $l_1 = 7$, $l_2 = 7$, $l_3 = 14$ (fig.2b); $l_1 = 7$, $l_2 = 14$, $l_3 = 7$ (fig.2c); At the same time changing the casting speed ($U_0 = 10\text{ mm/min}$, 20 mm/min и 50 mm/min) we observe, how to change of the rate of crystallization and the character of the motion of the slurry in the annular cavity.

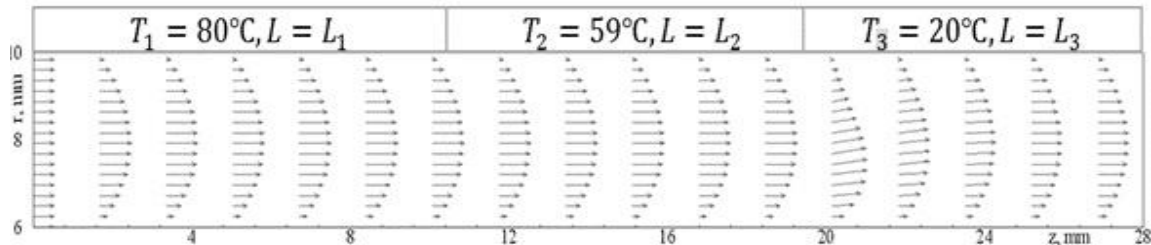


Fig.1. Scheme of flow of thermoplastic slurry in the annular cavity in case of three-circuit cooling.

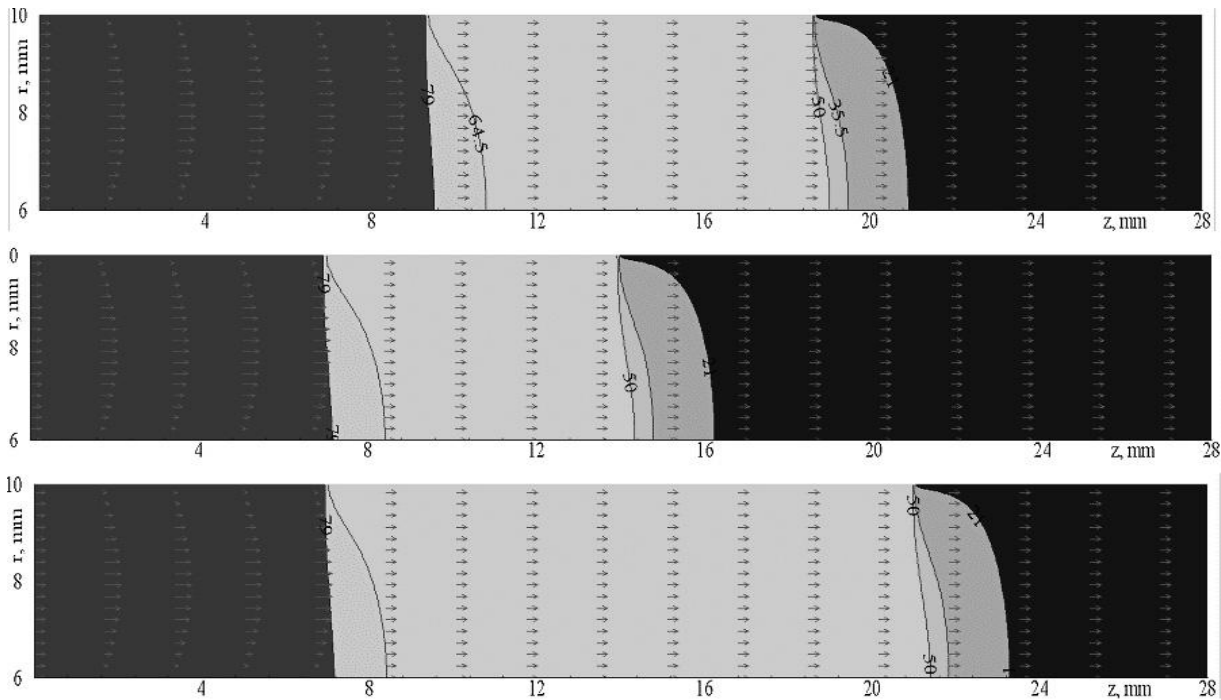


Fig.2. Distributions of the temperature over the annular cavity length at different ratio of the length of the cooling circuits at $U_0 = 10\text{ mm/min}$: a) $L_1=L_3=9,4\text{ mm}$, $L_2=9,2\text{ mm}$; b) $L_1=L_2=7\text{ mm}$, $L_3=14\text{ mm}$; c) $L_1=L_3=7\text{ mm}$, $L_2=14\text{ mm}$.

The temperature of the slurry at the inlet of the channel is constant across the cross-section. The profile of the longitudinal component of the velocity attains the shape of shear flow of the fluid near the inlet section due to high viscosity of the thermoplastic slurry (Fig. 2). Wall temperature in the first cooling contour is $t_1 = 80^\circ\text{C}$ and temperature field changes from $t = 80^\circ\text{C}$ to $t = 64.5^\circ\text{C}$ in this zone (Fig. 2). Temperature isolines (isotherms) show the regions of the constant temperature and internal structure of the slurry mass which is in liquid state.

Wall temperature is $t_2 = 59^\circ\text{C}$ in the second cooling contour. Sharp reduction of the wall temperature generates intensity growth of the slurry cooling, it also leads to the change of the rheological and thermo-physical properties of the slurry. Dynamic viscosity $\mu(t)$, density $\rho(t)$ and yield point $\tau_0(t)$ increase with temperature decrease, and viscous-plastic property of the slurry obviously begins to be evident. The slurry slides along the cavity wall, and sliding velocity ascends down the length of the second contour. It resulted in that profile of the longitudinal component of the velocity down the flow will level with constant center in the near-axial region (Fig. 2).

Heat pick-up growth results in reduction of the temperature field in the second cooling contour (Fig. 2). There is a transition zone in the beginning of the second contour, where temperature field is variable and expresses the transition of the slurry from the liquid state into the viscous-plastic state. The slurry temperature changes from $t = 80^\circ\text{C}$ to $t = 59^\circ\text{C}$ and defines upper boundary of the zone with constant temperature $t_2 = 59^\circ\text{C}$. The slurry mass is viscous-plastic near the wall due to the heat pick-up, while the slurry is liquid in the central part of the cavity. Presence of different structural conditions across the cross-section results in the change of the rheological and thermo-physical properties of the slurry. Isotherms become flat with the motion of the slurry mass. Thermo-physical properties become homogeneous, and all the mass of the slurry turns into viscous-plastic state. Wall temperature in the third cooling contour is $t_3 = 20^\circ\text{C}$, which leads to the further cooling of the slurry mass and temperature reduction from $t = 59^\circ\text{C}$ to $t = 45^\circ\text{C}$ in the transition zone. According to the experimental data, change in aggregate state takes place at temperature $t_f = 55^\circ\text{C}$. In energy equation heat release during aggregate state change occurs due to solidification of the viscous-plastic slurry. Solidification results in density change of the slurry.

Increase of molding velocity $u_0 = 20 \text{ mm/min}$ by twice, while the other parameters stay the same, has an impact on the structural change of the slurry (Fig. 3). Unlike in the previous formation mode, molding velocity leads to the extension of the transition zone of structural changes from one state into another, i.e. from the liquid state into viscous-plastic state and from viscous-plastic state into solid-plastic state (Fig. 3). It is also observed from isotherms distribution, and is explained by the increase of convection component of thermal flow.

Transition zone stretches in the second contour area, and temperature field shows minute rearrangement of the liquid state of the slurry into the viscous-plastic. And the slurry is viscous-plastic near the wall due to the heat pick-up, while in the central part – in a liquid state, i.e. convectional thermal flow exceeds at the expense of molding velocity.

In this area, the slurry temperature changes from 79 to 59°C and defines upper boundary of the zone with constant temperature $t_2 = 59^\circ\text{C}$. Structural change of the slurry from viscous-plastic state into solid-plastic state occurs in the region of the third cooling contour. Broad transition zone is also observed here, where temperature field is defined by convection, heat conductivity and the slurry aggregate state change heat.

At the molding velocity $u_0 = 50 \text{ mm/min}$, the slurry does not solidify in the central part over the entire cavity length, and the main flowing mass is in liquid state (Fig.4). This can lead to shrinkage of the slurry and the formation of shells and voids and a decrease in the strength of the casting.

The molding of the thermoplastic slurry in the annular cavity with three cooling circuits at low molding velocity (10-20 mm / min) shows the hardening of the casting within the mold cavity.

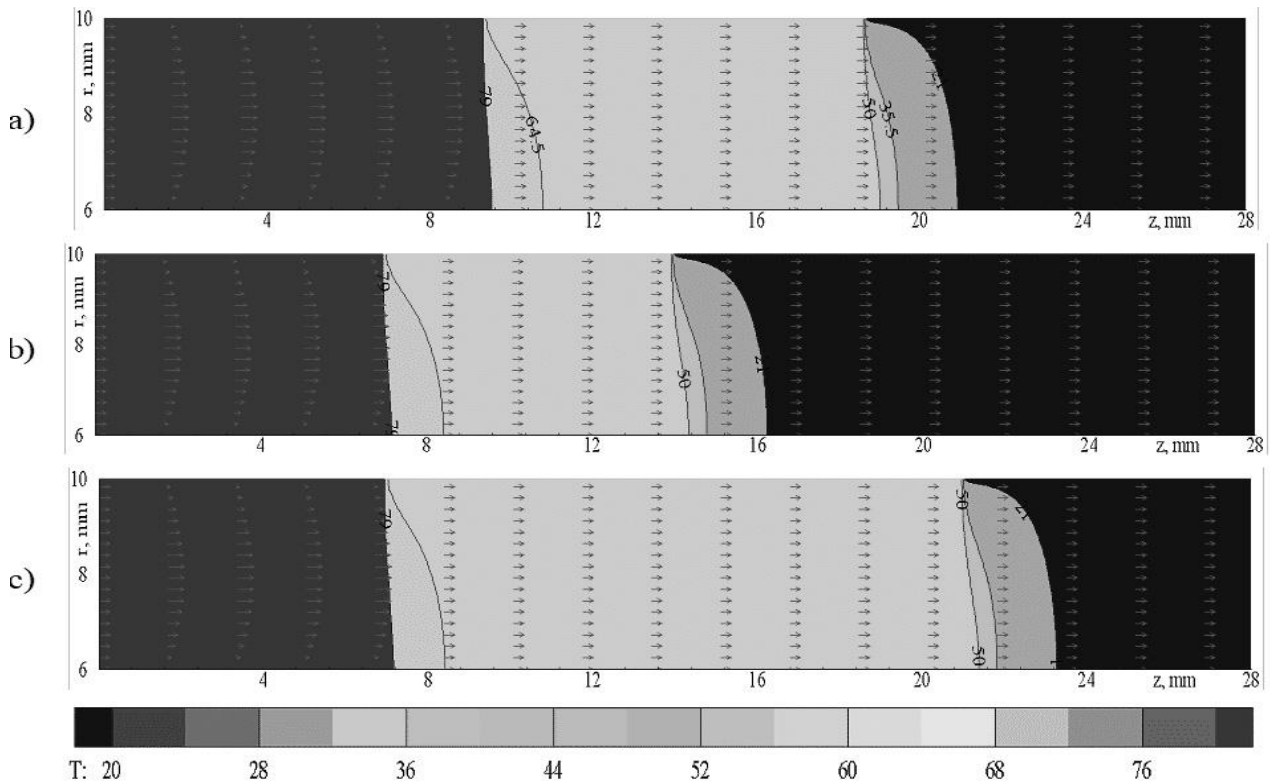


Fig.3. Distributions of the temperature over the annular cavity length at different ratio of the length of the cooling circuits at $u_0 = 20 \text{ mm/min}$: a) $L_1=L_3=9,4 \text{ mm}$, $L_2=9,2 \text{ mm}$; b) $L_1=L_2=7 \text{ mm}$, $L_3=14 \text{ mm}$; c) $L_1=L_3=7 \text{ mm}$, $L_2=14$

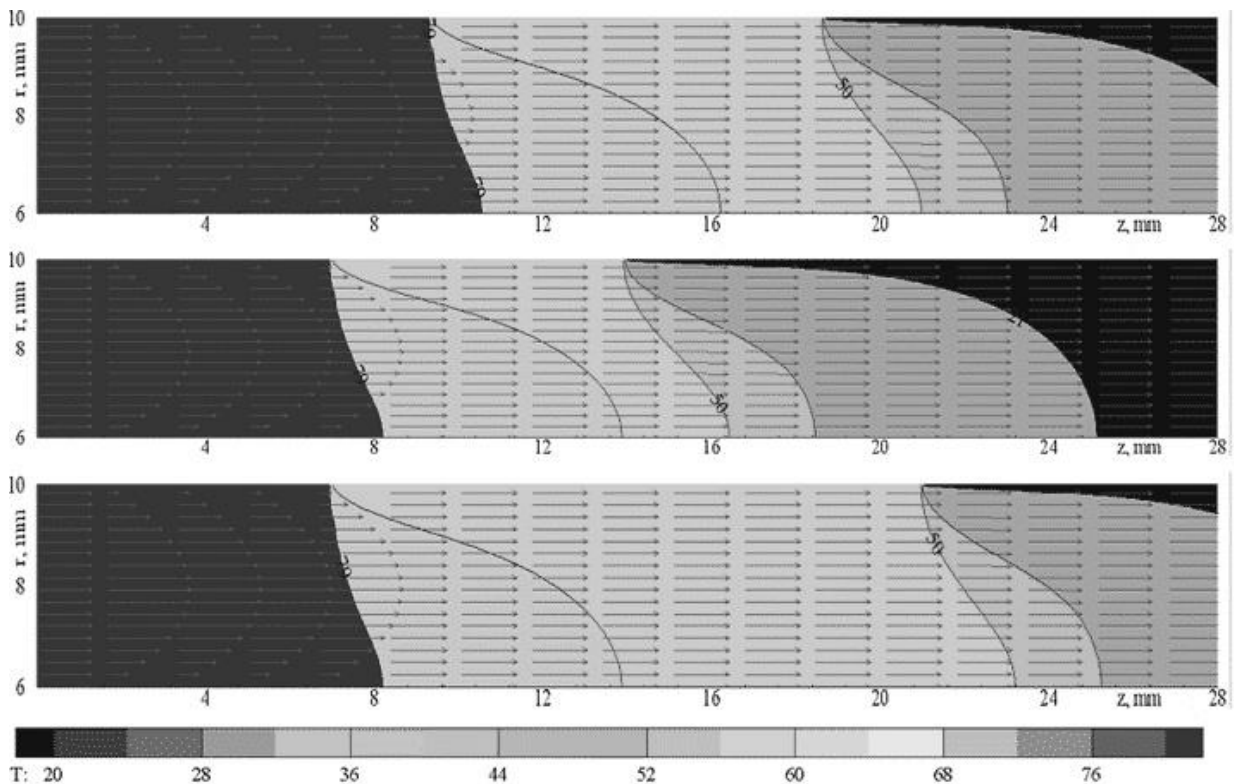


Fig.4. Distributions of the temperature over the annular cavity length at different ratio of the length of the cooling circuits at $u_0 = 50 \text{ mm/min}$: a) $L_1=L_3=9,4 \text{ mm}$, $L_2=9,2 \text{ mm}$; b) $L_1=L_2=7 \text{ mm}$, $L_3=14 \text{ mm}$; c) $L_1=L_3=7 \text{ mm}$, $L_2=14 \text{ mm}$

During the experiments, stated distribution of the temperature in the form-building cavity of filler depending on the molding velocity and conditions of heat extraction on the walls of form-building of annular cavity lets us determine the transition from liquid state to viscous-plastic and from viscous-plastic to solid-plastic state. The results of experiment were analyzed and generalized with using of mathematical model of the process of molding of the thermoplastic slurry. The system of equations of the laws of conservation of mass, momentum and energy of non-Newtonian fluid is considered in common with the rheological Shvedov-Bingham's model.

Rheological and thermo-physical properties of the slurry were found on the basis of experimental data, and they express dependence on the temperature. The coefficients of heat exchange and heat transfer on the walls of the annular cavity were evaluated by solving the inverse problem, and they were refined in the optimization calculations carried out according to the conditions of the experiments.

Obtained coefficients of heat exchange and heat transfer in the calculation let us determine the conditions of heat exchange between the slurry and cooling water, find operational parameters for controlling of heat exchange of molding of the beryllium oxide in the mold cavity.

Conclusion

Investigation of thermo physical properties of the thermoplastic slurry depending on the temperature, the heat at the phase transition is the main problem, in that they largely determine the technological and operational characteristics of beryllium ceramics.

Velocity and temperature fields allowed detecting the peculiarities of motion and heat transfer determining the internal structure of molding process, transformation of the viscous-plastic liquid slurry into solid-plastic state, and establishing the influence of the parameters (velocity, coolant temperature, rheological properties) on solidification process of ceramic slurry mass. One can find in computations the optimal conditions of the ceramics molding process, which allow obtaining the output hardened product with a uniform structure of beryllium.

REFERENCES

1. Dvinskikh Y.V., Popil'skii R.Y., Kostin L.I., Kulagin V.V. Thermo-physical properties of thermoplastic casting slips of some high-refractory oxides. *Ogneupory*, 1979, Vol.65, pp. 37– 40. [in Russian]
2. Shakhov S.A., Bitsoev G.D. *Application of Ultrasound in the Manufacture of High Thermal Conductivity Ceramic Articles*. Ust'-Kamenogorsk. 1999, -P.145. [in Russian]
3. Dobrovolskii A.G. *Slurry Casting*, Metallurgiya, 1977, Moscow, 246 p. [in Russian]
4. Akishin G.P., Turnaev S.K., Vaispapir V.Y., et al. Thermal conductivity of beryllium oxide ceramic. *Refract. Ind. Ceram.*, 2009, Vol. 50, pp. 465–468.
5. Shakhov S.A. and Gagarin A.E. Rheological characteristics of thermoplastic disperse systems treated with ultrasound. *Glass and Ceramics*, 2008, Vol.65, No.3 – 4, pp. 122 – 124. [in Russian]
6. Zhapbasbayev U.K., Ramazanova G.I., Sattinova Z.K., Shabdirova A.D. Modeling of the beryllium ceramics formation process. *J. of the European Ceramic Society*, 2013, Vol. 33, pp. 1403 – 1411.
7. Assilbekov B.K., Zhapbasbayev U.K., Sattinova Z.K., Ramazanova G.I. *Modeling of ceramic products molding process*. Almaty, Kazakhstan, 2017. 145 p. [in Russian]

UDC: 533.682; 533.6.01; 621.548

STUDY OF ELECTRO-PHYSICAL PARAMETERS OF WIND TURBINESShrager E.R.¹, Sakipova S.E.², Tanasheva N.K.^{2,3}, Akhmerova K.E.²,
Botpayev N.³, Kussaiynova A.K.³¹National Research Tomsk State University, Tomsk, Russia² Karaganda State University named after E.A. Buketov, Karaganda, Kazakhstan, sesaule@mail.ru³Institute of Applied Mathematics, MES RK, Karaganda, Kazakhstan

The article discusses the results of research on the effectiveness of wind-driven power plants of small and medium power. The results of tests of two different models of wind turbines combined with a specially designed low-speed electric generator under the conditions of natural wind are discussed. A description of the device and technical parameters of wind turbines is presented. The dependences of electro-physical characteristics on the speed of natural wind during a long time are obtained. It is shown that the power generated by an electric generator with a wind wheel with cylindrical blades is greater than the power of a generator with a sail-type wind wheel.

Keywords: wind turbine, sail blade, rotating cylinder, Magnus effect, electric generator.

Introduction

Wind energy as an environmentally friendly source of energy has great potential in reducing dependence on traditional resources such as oil, gas and coal. One of the most important features of development at the present stage is the increased attention of the world community to the problems of rational and efficient use of energy resources, introduction of energy saving technologies and the search for renewable energy sources (RES).

The growing need of mankind for energy resources leads to the demand for searching and broader use of alternative sources of energy supply. These include primarily wind power engineering. Due to the large territory, the potential of renewable energy sources (hydropower, wind and solar energy) in Kazakhstan is very significant. The development and introduction of wind-driven power plants (WPP) to obtain electrical energy from wind energy is constantly developing, and industrial production of this environmentally friendly energy source can be a new stage of power industry development [1, 2].

In addition to the fact that wind energy does not pollute the environment, it is also capable of producing clean, inexhaustible energy in a local remote area. Moreover, in Kazakhstan there are many remote areas where there is a shortage of electric energy, where it is expensive, and sometimes it is technically impossible and economically impractical to build power lines. The development and production of WPP as an autonomous source of electrical energy for the needs of economic and domestic activities in the field environment, at testing grounds or defense facilities is a very topical issue of modern power industry. Autonomous WPP of small and medium power can provide with electricity a separate building, small farms or military defense facilities, remote from sources of centralized electricity supply. The increased interest in wind-driven power plants (WPP) for the conversion of clean and renewable wind energy necessitates a more thorough analysis of not only their aerodynamic parameters, but their energy characteristics as well. In the framework of project number 0109 PK01319, a special electric generator for small WPP was designed and manufactured. Tests of the developed low-speed electric generator for two types of WPP were carried out at the training and testing ground of the Faculty of Physics and Technology to identify the energy conversion efficiency of low-speed low level wind.

1. Technical characteristics of WPP experimental models

1.1 Experimental model of sail-type WPP

The principle of operation and design of the WPP under study were developed and constructed at the Laboratory of Hydrodynamics and Heat Exchange of the Department of Engineering Thermophysics named after Professor Akylbayev Zh.S. under the guidance of Professor K. Kussaiynov [3,4]. Later various modifications of original models were made, which were installed and successfully function at the testing ground of the Faculty of Physics and Technology.

The first model of the sail-type WPP is a multi-blade wind turbine with a dynamic variable blade shape, made in the form of a triangular "sail". For aerodynamic testing under natural wind conditions, a prototype of a 6-blade sail-type wind turbine with a wind wheel with the diameter of 3 m was constructed, Fig.1. The distinctive novelty of this WPP model is in use of blades made in the form of a triangular flexible sail with a moving end. Sail-type wind turbines have a unique feature - they work equally effectively both at low wind speeds and at high wind speeds. Due to the dynamic changeable shape of the working surface, sail-type wind turbines react quickly to changes in the wind direction [4, 5].

Based on the results of preliminary tests to ensure maximum thrust force of the sail blades, 15 cm elongation of the moving yarn was chosen. The sail-type wind turbine shaft is made of a metal cylinder with a diameter of 30 mm and a length of 1750 mm. The diameter of the metal disk coaxially attached to the shaft is 150 mm, the disk thickness is 10 mm. The pulley has a diameter of 400 mm, and a thickness of 40 mm, intended for a belt drive with a generator. The support rods and frame rods of the wind turbine are 25 mm diameter metal tubes, which are fixed to the disk. The length of each frame rod of the wind turbine is 1570 mm, and the length of the support rods of the wind wheel is 2100 mm. The prototype of the sail-type wind turbine is installed at a height of 5 meters in the prevailing direction of the local wind flow.

1.2 WPP model using the Magnus effect

The second model is that of a WPP with blades in the form of rotating cylinders, as shown in Fig.2.



Fig.1. General view of an experimental sail-type WPP model



Fig.2. General view of an experimental model of WPP with cylindric blades

It is known that when a transverse air stream flows past a rotating cylinder, a lateral force arises due to the Magnus effect [3, 6]. This physical phenomenon is used when designing this model. Cylinders, like propeller blades, rotate the axis of the wind turbine connected to the electric current generator, providing a number of unique properties of the WPP:

- steady work at low and medium wind speeds;
- increased utilization factor of low speed winds;
- the ability to automatically support the constancy of the revolutions of the axis of the wind turbine when the wind speed changes.

A detailed description of WPP with cylindric blades is given in [7]; we just note that in WPP model under study the surface of cylindric blades is smooth. The blades themselves are made of durable material in the form of cylinders with flat ends, Fig.2. The diameter of the cylindric blades is 150 mm, the diameter of the flat end discs is 250 mm, and the height of the supporting tower is 5 m. The main technical parameters of the WPP models under study are shown in table 1.

Table 1. Technical parameters of prototypes of wind turbines.

| WPP type | Sail-type WPP | WPP with cylindric blades |
|---|---------------|---------------------------|
| Wind wheel diameter, m | 3 | 3 |
| Number of blades, pcs. | 6 | 3 |
| Nominal power kW | 1 | 1 |
| Operating wind speed, m/s | 7 | 7 |
| Starting wind speed, m/s | 3 | 3 |
| Operating speed range, m/s | 3-12 | 3-12 |
| Critical wind speed, m/s | 14 | 15 |
| Nominal rotation speed, rpm | 150 | 180 |
| Weight of wind turbine with support, kg | 100 | 80 |

Test and measurement of volt-ampere characteristics were carried out throughout the year under natural wind conditions. Then, according to the test results, the effectiveness of the developed low-speed electric generator for two WPP models was evaluated.

2. Experimental technique

A prototype of an electric generator (EG) was developed for converting wind energy into electrical energy and WPP trial. The most convenient for the constructive combination of the wind-wheel with the electric machine is the EG variant with inductor synchronous generator, assuming a windingless rotor. The specific consumption of materials and the cost of a gearless EG are about the same as the total indicators of a WPP with a high-speed EG increasing gearbox.

A distinctive feature of this EG is that it begins to produce an emf at relatively low speeds of air flow. In addition, the developed version of the EG has a reliable contactless excitation system and starts to generate electricity at frequencies from 50 to 350 revolutions per minute.

The study of the electro-physical characteristics of the low-speed EG depending on the speed of rotation of the generator shaft shows that the changes introduced into the design lead to an increase in the efficiency, which promises the prospect of further improvement. In particular, it was established that the use of two-discs with neodymium magnets as rotors in the design of a low-speed EG makes for noticeable increase in the efficiency of WPP.

To measure the natural wind speed, GEOS #11 anemometer was used, which can be used as a stationary weather station. To measure the angular velocities of the rotating shafts, the AT-8 contact-noncontact digital photo-tachometer was used in the range of 0.1-10,000 rpm. The principle of operation of the AT-8 digital photo tachometer is based on measuring the speed resulting from

the interaction of the rotating magnetic field of a permanent magnet. Rotation from the shaft of the unit, with induction currents induced by this field in a solid metal rotor, provides fast and accurate readings of rotational speed. Measurements of the electro-physical characteristics of WWP on natural wind speed were carried out during the year with seasonal climate changes. The measurement error does not exceed 3-4%.

3. Discussion of the test results

In order to study the electrical and physical parameters of two types of WPP testing models using low-speed electric generator with neodymium magnets as rotors, aerodynamic tests were carried out at the testing ground in natural wind conditions.

Volt-ampere characteristics of WPP testing models were determined at a fixed value of the pulley diameter. 5 and 21 W lamps with powers of were used as a load to determine the current-voltage characteristics. Volt-ampere characteristic of the WPP with rotating cylinders is shown in Fig. 3. The operating point of the generator connected to the load coincides with the maximum power point. Connecting loads can shift the operating point of the system to the area of minimum or even zero power. Therefore, important components of the system are voltage converters capable of matching the wind module with the load.

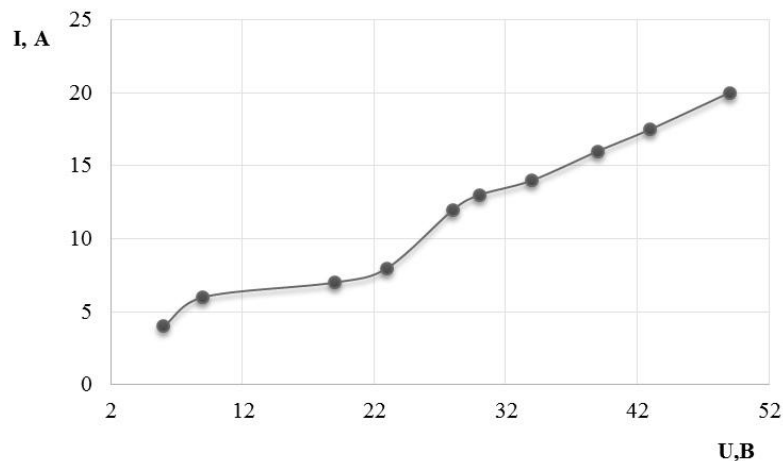


Fig.3. Volt-ampere characteristic of the WPP with rotating cylinders

On the base of the test results, the dependences of the electro-physical characteristics of two prototypes of WPP on shaft rotation speeds at various natural wind speeds were obtained during the year. An increase in wind speed leads to an almost linear increase in the number of revolutions of the wind wheel per minute. This is due to the fact that with increasing wind speed, incident on the wind wheel, almost linearly increases the pressure force acting on the sail blades.

The efficiency of the EG also rises as a result of increasing cross section of the winding wire, which, in turn, determines the amount of generated current. Tests show that when connected to the wind wheel of the WPP with rotating cylindrical blades, EG begins to produce electric current at a lower value of the number of the shaft revolutions. It has been established that for WPP with cylindrical blades the maximum value of the generated electric current I is achieved with a smaller value of the number of revolutions of the wind wheel N , Fig. 4.

The type of dependences of the change in current strength on the rotational speed of the wind wheel for two models of WPP is slightly different from each other. It can be seen that in the whole range of variation of the rotational speed of the wind-wheel, the value of the electric current I is 25-30% higher compared to the current produced by the sail-type WPP. This is probably due to the fact that in the generator the cross section of the winding wire, on which the generated current magnitude directly depends, exceeds the cross section of the wire of the sail-type generator.

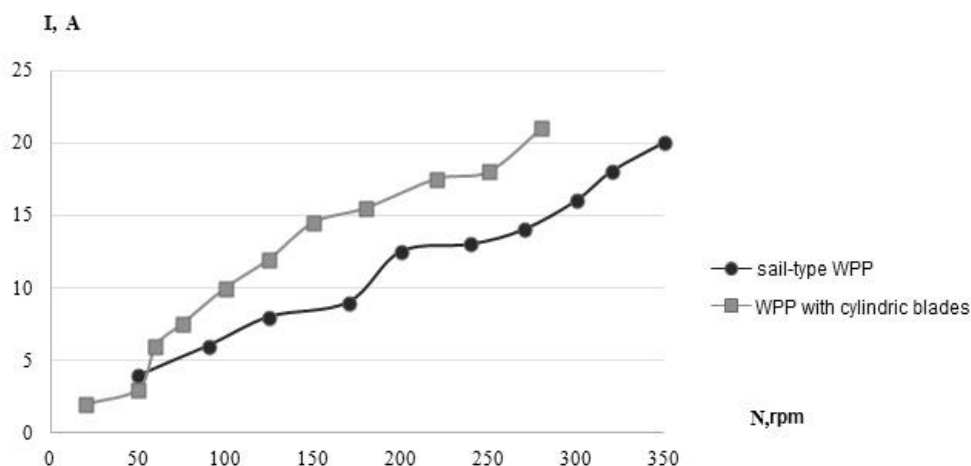


Fig.4. The dependence of the amount of the current produced by generators on the rotational speed of WPP

Analysis of the test results shows that in the entire rotational speed range, the power generated by the electric generator connected to the wind wheel of the WPP with rotating cylinders, exceeds the power generated by the sail-type WPP, Fig.5.

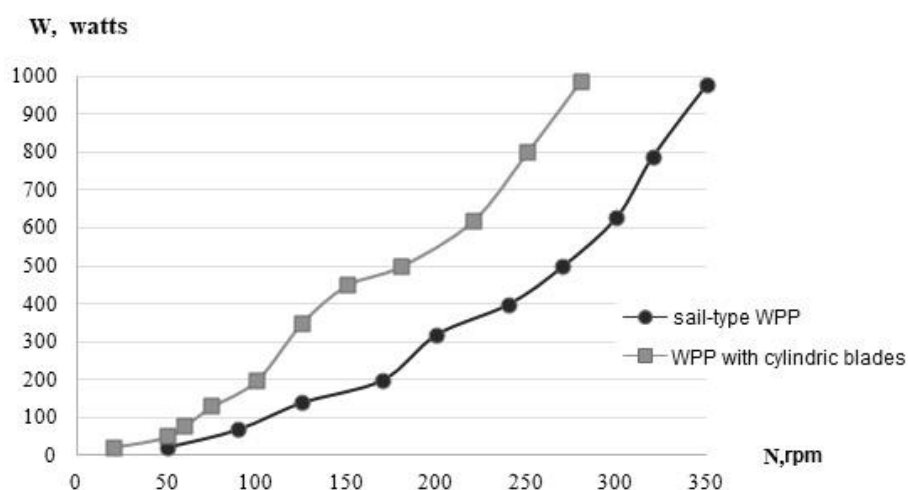


Fig.5. The dependence of the power of electric generators on the rotational speed of the wind wheels.

It can be seen that with an increase in wind speed, the generated power increases almost linearly. At a wind speed of 7 m/s, the wind power plant produces a nominal power of 330 Watts. The maximum generated power at a wind speed of 12 m/s is equal to 970 Watts.

A similar regularity was also obtained for the EMF that occurs on the windings of a generator operating with WPP with "rotating cylindrical blades", at a significantly lower value of the revolutions number of the wind wheel shaft. This is due to the low operating threshold of the generator, and its high efficiency coefficient as well.

Conclusion

The electrophysical characteristics of two models of WPP were studied using the developed low-speed electric generator. As a result of the tests performed for a long time, it was found that the use of gearless wind generators based on arc-type stator electric machines is advisable for low-speed WPP with high torque. This conclusion is due to the lower operating threshold of the

developed EG at a change in wind speed and its higher efficiency coefficient value. Due to its structural connection to the electric generator, it makes for most of the mechanical energy to be converted into electrical energy.

The practical significance of the considered low and medium power WPP also lies in the possibility of their autonomous use for driving various working devices and economic mechanisms at facilities remote from centralized power supply lines.

Acknowledgements

This research was funding by Ministry of Education and Science of the Republic of Kazakhstan of the Program AP051315203 "Development and prototyping wind power plant for alternative power supply using a domestically produced electric generator" for 2018-2020.

REFERENCES

- 1 National program for the development of wind power engineering in the Republic of Kazakhstan until 2015 with a perspective up to 2024. <http://www.windenergy.kz/files/121379>.
- 2 Kussaiynov K., Sakipova S.E., Tanasheva N.K., Kambarova Zh.T. et al. *Wind power plant based on the Magnus effect*. Innovative patent number 30462 of 09/23/2015.
- 3 Kussaiynov K., Sakipova S.E., Kambarova Zh.T., Tanasheva N.K. et al. *Wind turbine for low wind speeds*. Innovative patent number 30829 of 12/29/2015.
- 4 Sakipova S.E., Kambarova Zh.T. A sail type wind turbine for low speed wind. *Eurasian Physical Technical Journal*. 2016, Vol.13, No.1 (25), pp.106 – 116.
- 5 Sakipova S.E., Tanasheva N.K., Kivrin V.I., Kussaiynova A.K. Study of wind turbine model aerodynamic characteristics with a rotating cylinder». *Eurasian Physical Technical Journal*. 2016, Vol.13, No.2 (26), pp.112 – 117.
- 6 Tanasheva N.K., Shrager E.R., Sakipova S.E. et al. Research of aerodynamic characteristics of the wind generator on the basis of Magnus's effect. *Bulletin of the Karaganda University. Physics Series*. 2017, №3(87), pp. 60 – 64.
- 7 Sakipova S.E., Kambarova Zh.T., Tanasheva N.K., Botpayev N., Kussaiynova A.K. Comparative analysis of the electro-physical characteristics of wind turbine models. *Proceeding of the Rep. scientific and practical conf. "Actual problems of thermal power engineering and applied thermal physics"*, Karaganda, 2018, pp. 274 – 278.

Article accepted for publication 10.12.2018

UDC 621.314;537.39

ANALYSIS OF THE EFFECT OF ELECTRO-DISCHARGE WATER TREATMENT ON ITS PURIFICATION DEGREE

Shaimerdenova K.M.¹, Stoev M.², Tusypbaeva A.S.¹, Rakhmankyzy A.¹,
Sekerbaeva G.¹

¹Ye.A. Buketov Karaganda State University, 100028, Karaganda, Kazakhstan, gulzhan.0106@mail.ru

²Neofit Rilа University, South-West, Blagoevgrad, Bulgaria

This article discusses the study of the analysis of the effect of electric discharges on the degree of water purification. A description of the technique for measuring specific electrical conductivity using a conductivity meter is presented. The technical process operation procedure for obtaining purified and decontaminated water during the electro-discharge treatment is given. In the course of the research, the change in the salinity and the specific electrical conductivity of the tap water and natural water samples after the treatment with the electric pulse method was studied. The experiments took into account the processing time and the number of electric pulse discharges.

Keywords: water purification, water quality, electrical conductivity, electric pulse method, pulse discharge.

Introduction

The use of electric hydro-pulse effects is a promising method in the technology of purification, disinfection and activation of water. The electric pulse processing technology based on the unique effect of instantaneous energy release at the moment of electrical discharge in a liquid has huge hidden opportunities and new unexpected broad spheres of useful application due to its versatility [1]. Water quality is an important factor that affects the possibility and practicability of successful cultivation of products and plants. Increasing concentration of salts leads to a decrease in the number of basic macronutrients that can be introduced into the nutrient solution, while maintaining the optimum electrical conductivity of water.

When calculating fertilizers and total electrical conductivity of the treatment solution, it is necessary to take into account the concentration of individual macroelements, as well as sulfates, in order not to exceed the permissible amount of 100 mg/l SO₄. If the water is significantly saline, in order not to reduce the amount of fertilizers applied with the process solution, it is necessary to use ballast-free, readily soluble mineral fertilizers and, if possible, salts with lower electrical conductivity: potash, calcium and magnesium nitrate, monopotassium phosphate [2]

The salt content and electrical conductivity of tap and natural water, treated by electropulse method, were studied as well. In tap water, the salt content usually does not exceed 1000 mg/l, and, as a rule, is in the range of 300-600 mg/l. An electric hydro-pulse plant for water purification and activation has optimal parameters that make it possible to effectively purify, disinfect and activate natural water samples.

This paper presents the results of a study of the effectiveness of using electric pulse discharges for purification and disinfection of water from various natural sources in Central Kazakhstan.

1. Experimental technique

The measurements of the specific electrical conductivity were carried out on a Mark-602 conductivity meter with a conductivity sensor CS-025S and CS-2S. Advantages feature of the brand 602 conductivity meters with a conductivity sensor CS-025 and CS-2S are as follows:

- control of water chemistry treatment at thermal and nuclear power facilities;
- specialized water treatment;
- two channels;
- freely programmable measurement ranges;
- the possibility of independent measurements at two points;
- convenience and accuracy of measurements, minimum maintenance;
- double automatic compensation;
- the possibility of placing the converter unit at a remote distance from the sampling point to 100 meters;
- communication with external devices;
- galvanically isolated current outputs 0-5/4-20/0-20 mA;
- RS-485 port;
- programmable settings with "dry contact" type output;
- aluminum IP65 case;
- the device is reliably protected from dust and moisture;
- illuminated graphic indicator;

Using a conductivity meter, data on the electrical conductivity and salinity of tap and natural water were obtained. Water samples were processed using experimental equipment. During the experiment the plant parameters were as follows: $U=18-40$ kV, $C=0.25, 0.5$ μ F, $l_p=6-8$ mm, the processing impulse $f=2-2.5$ Hz. The experiment was carried out taking into account the different number of electrical discharges and with the subsequent measurement of electrical conductivity and salinity of the water samples under study [3].

2. Process operation procedure for obtaining purified and disinfected water after electrical discharge treatment

To provide a special mode of pulsed water treatment, the test equipment of an electric pulse plant has been developed and constructed [5]. The plant for the implementation of the process operation procedure of purified and disinfected water obtained by electric discharge processing of natural water includes: a cylindrical water tank with the working space of 10 l; working site with a paraboloid reflector and a cylinder-shaped electrode. This site is designed for electric discharge water treatment. To conduct experimental work on obtaining purified and disinfected water in the "Laboratory of Physics of Pulsed Phenomena in Heterogeneous Media" of the Department of Engineering Thermophysics named after Professor Akylbaev Zh.S., a technological scheme for obtaining purified and activated water was assembled. The optimal parameters of the electric discharge technology to provide the process operation procedure for preparation of purified and decontaminated water are shown in Table 1.

The plant works as follows: the untreated water flows into the storage tank with a water level control. Water supply valves open. Reverse feed valves are used depending on the need to rerun treatment. A circulation pump makes for control of the water supply to the decontaminating device. After turning on the EHP plant, the voltage on the capacitor with a capacity C rises to the value U , at which spontaneous breakdown of the air forming gap takes place.

Stored in a capacitor water instantaneously flows through the positive electrode cable into the operating section to the interelectrode space l_p , where in the liquid a pulsed electrical discharge takes place, which is reflected from the paraboloid surface and the negative cylindrical electrode decontaminates the liquid [5].

Table 1. Process operation procedure for the preparation of purified and decontaminated water

| № | Names of indicators | Symbol | Unit of measurement | Numeric value |
|---|-----------------------|--------|---------------------|---------------|
| 1 | Voltage | U | kV | 18-40 |
| 2 | Interelectrode space | l_p | mm | 6-8 |
| 3 | Discharge energy | E | J | 220-400 |
| 4 | Capacitor capacitance | C | μF | 0.25-0.5 |
| 5 | Discharge rate | n | Hz | $2 \div 2.5$ |
| 6 | Plant power | W | kW | 1.5 |
| 7 | Storage tank capacity | v | l | 10 |
| 8 | Pump power | W | W | 60 |
| 9 | Water treatment rate | F | l/min | 80 |

3. Discussion of results

The experiment was conducted on a prototype of the electric hydropulse plant, taking into account the time and number of electrical discharges. The time interval ranged from 1 to 4 minutes, the number of discharges from 25 to 100 discharge blows.

The researchers studied tap water with the following values of salt content $C=401.5 \text{ mg/dm}^3$, SEC $\chi=784.3 \text{ }\mu\text{S/cm}$; water samples from the Fedorovsk reservoir were with the indicators $C=664.9 \text{ mg/dm}^3$, SEC $\chi=1293 \text{ }\mu\text{S/m}$ and the same indicators from the Bukpa River were $C=1018 \text{ mg/dm}^3$, SEC $\chi=1891.2 \text{ }\mu\text{S/cm}$.

Based on the results of the experiment, graphs of the dependence of salt content and electrical conductivity of tap and natural water on the time and number of discharges were obtained (Figures 1-4).

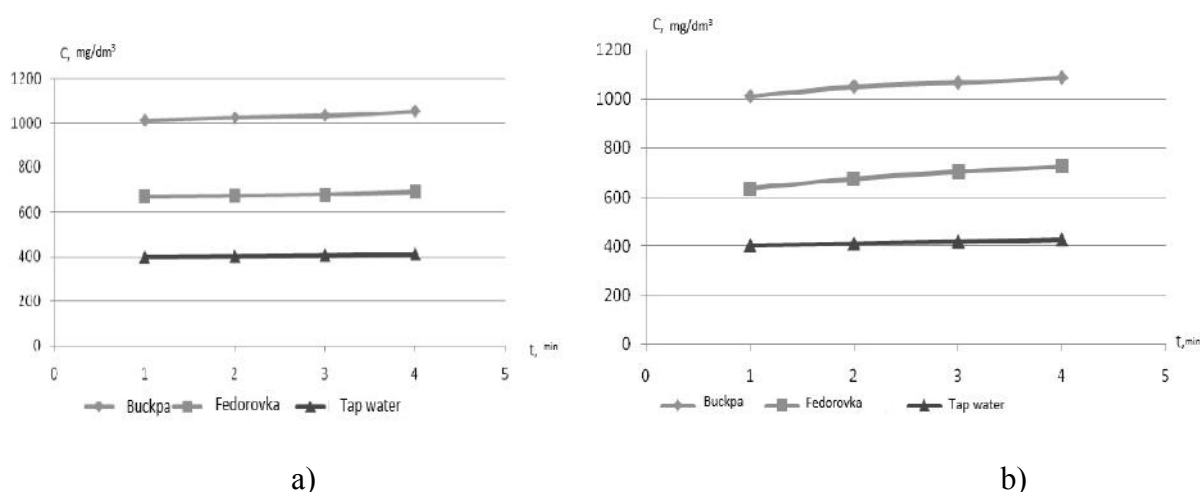


Fig.1. Dependence of the salinity of tap and natural water on time:
a) $C=0.25 \text{ }\mu\text{F}$, $l_p=6 \text{ mm}$; b) $C=0.5 \text{ }\mu\text{F}$, $l_p=7 \text{ mm}$

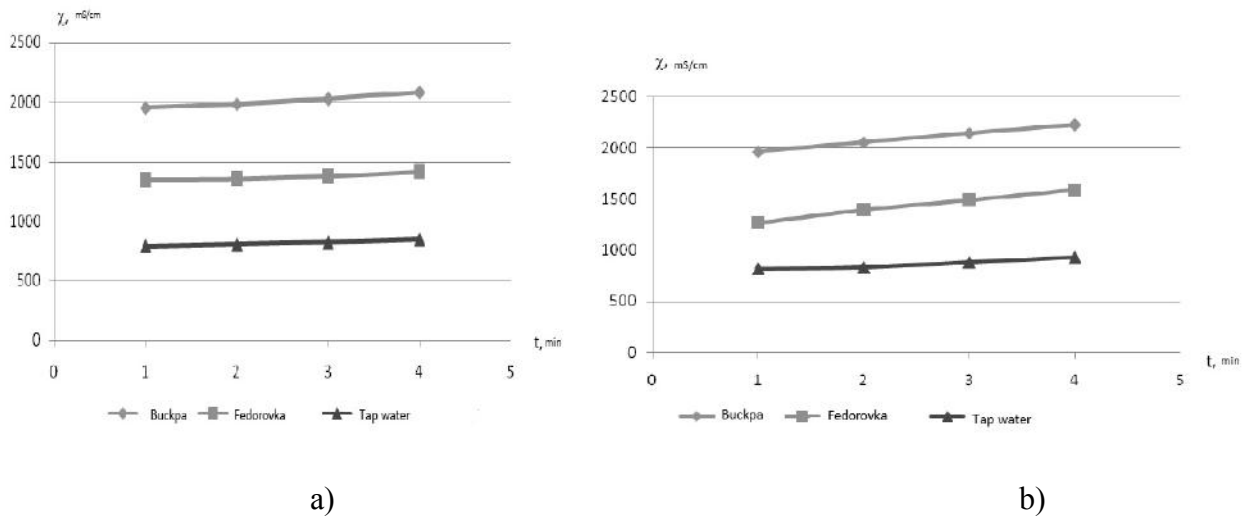


Fig.2. Dependence of electrical conductivity of tap and natural water on time: a) $C=0.25 \mu\text{F}, l_p=6 \text{ mm}$; b) $C=0.5 \mu\text{F}, l_p=7 \text{ mm}$

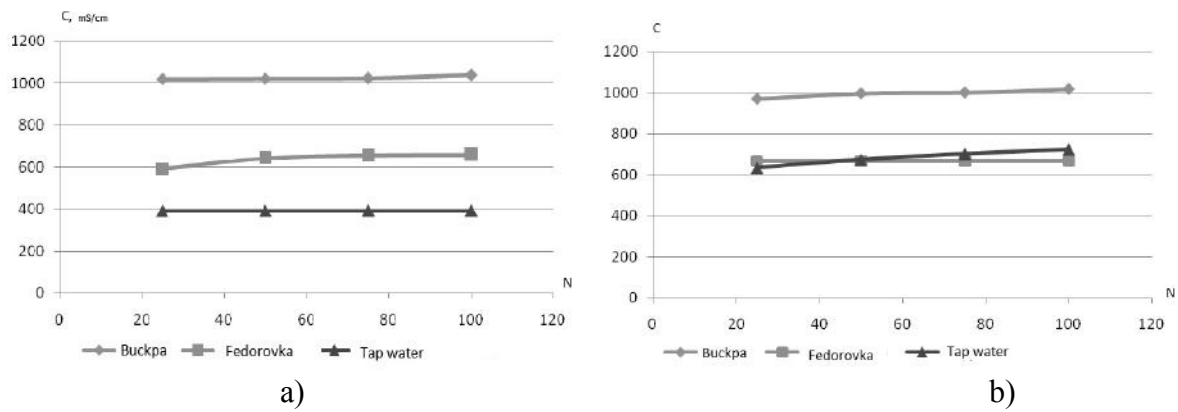


Fig.3. Dependence of the salinity of tap and natural water on the number of discharges: a) $C=0.25 \mu\text{F}, l_p=6 \text{ mm}$; b) $C=0.5 \mu\text{F}, l_p=7 \text{ mm}$

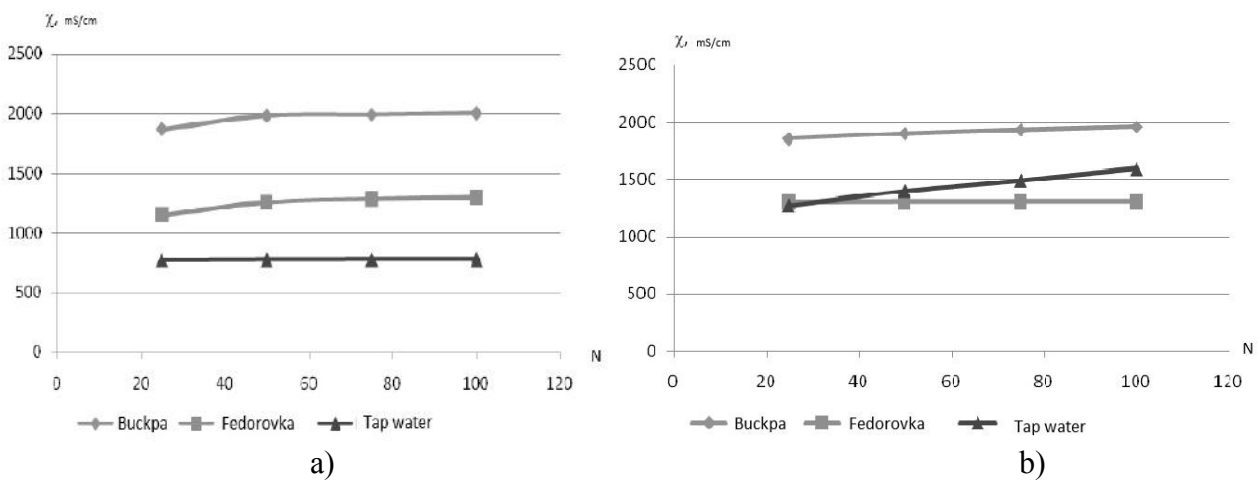


Fig.4. Dependence of electrical conductivity of tap and natural water on the number of discharges: a) $C=0.25 \mu\text{F}, l_p=6 \text{ mm}$; b) $C=0.5 \mu\text{F}, l_p=7 \text{ mm}$

The salinity of the water of the Fedorovsky reservoir and the Bukpa River is characterized by large temporal and spatial variability and represents an extensive area of close interaction between developed agro-industrial complexes and the stream ecosystem [4]. Due to the small size of the water storage basins and their small depths, the main elements of the hydrological and hydrochemical regime of the basins and the state of the ecosystem are subject to significant anthropogenic changes.

Due to the hydraulic effect caused by a pulse discharge in a liquid, an instantaneous release of energy accumulated in the capacitor battery takes place. During discharge, a plasma channel is formed. In the channel with a small cross section, there is an intense local heating of the liquid. When the temperature rises by 1°C, the electrical conductivity increases by approximately 2%. In this connection, when measuring the electric conductivity of the treated by the electric discharge method water, its increase is observed. Electrical conductivity is directly proportional to salt concentration.

Conclusion

The application of the electric-pulse device for water purification makes it possible to solve the issues of protecting water resources from depletion and pollution and their rational use for the needs of the national economy, which is one of the most important problems requiring urgent solutions. Electric hydropulse treatment for water purification makes for:

- reagent-free disinfection of water;
- elimination of all types of microorganisms, including viruses and spores;
- carrying out water treatment regardless of the amount of suspended solids and impurities.

During the study, experimental engineering activities on the development and design of an environmentally-friendly electric pulse water treatment technology were carried out. Thus, these studies demonstrate the advantages of applying a pulsed discharge for decontaminating water with high initial contamination [6].

The obtained results confirm that the application of electric discharge treatment makes it possible not only to carry out water decontamination more efficiently, but also to purify it with a higher initial degree of contamination.

REFERENCES

- 1 Kussaiynov K., Bulkairova G.A., Shaimerdenova K.M., Kutum B.B. et al.; *Patent No. 1794 Republic of Kazakhstan. Installation for electrohydropulse disinfection of running water*. No. 2015/0412.2; publ. 11/15/16, 5 p. [in Kazakh]
- 2 Kussaiynov K., Shaimerdenova K.M., Kutum B.B., Bulkairova G.A., Ranova G., Kivrin V. Effect of electrical discharges on the structure and properties of the electrode system during hydroimpulse treatment of water. *Bulletin of KarSU. Physics series*. 2015, No.3 (79), pp. 49 - 54. [in Russian]
- 3 Vilkov K.V., Grigoriev A.L., Nagel Yu.A., Uvarova I.V. Decontaminating action of a powerful pulsed electric discharge in water. *PZhTF*, 2004, Vol. 30, Issue 7, pp. 48 - 54. [in Russian]
- 4 Program for the development of the agro-industrial complex in the Republic of Kazakhstan for 2013-2020 (Agribusiness 2020), Astana 2012. Available at: <http://www.government.kz/ru/programmy/2246-proekt-razvitiya-eksportnogo-potentsiala-myasa-krupnogo-rogatogo-skota.html> [in Russian]

UDC 535.34+535.37:577.164.12

APPLICATION OF SPECTROSCOPY IN THE PROCESS OF OBTAINING DYES FROM ONION PELL

Fayzullaev A.R, Astanov S.Kh, Ergasheva N.M.

Bukhara Engineering-Technologies Institute, Bukhara, Uzbekistan, s.h.ostonov@rambler.ru

A dye-receiving technology from waste products in the form of onion peel. Spectroscopic methods defined temperature extraction mode pigments. It is shown that bioflavony and extracts from onion peels tend to form complexes with metal ions. It was found that the reaction of complexation with the metal ion of quercetin are characterized by the formation of connection with metal by electron transfer from the metal d orbitals in the π^ orbital of quercetin. The Study of the natural scales dye staffs pommel and cortex of the plants ruyan applicable in textile industry. The Determination main dying pigment of the dye staffs and offers of the methods to stabilizations of the dye staff.*

Keywords: technology, spectroscopy, food coloring, quercetin, rutin, biflavones metal Ionia, electronic orbitals.

Introduction

Natural food colorings (carotenoids, anthocyanins, flavonoids, etc.) are environmentally friendly compounds that do not affect the human body carcinogenically, and are widely used in the food, pharmaceutical and other sectors of the economy [1]. Typically, natural food colors are used in the form of solutions, pastes or powders, where they can be in different molecular forms [1-4]. For effective use of dyes, it is necessary to have information about their spectral-luminescent, optical and other physicochemical characteristics and their changes under the influence of a number of external factors (the nature of the solvent, temperature, concentration, light radiation, etc.) [5,6]. In addition to the use of spectroscopy in the procession, the preparation of natural dyes makes it possible to develop effective methods for obtaining pharmacological preparations and biological active substances [7,8].

1. Objects and technique of research

To the questions of obtaining natural dyes from the onion husks in sufficient quantity there are scientific works. In work [9] the dye from the husk of onions was obtained according to which the plant raw material is extracted, sorbents are sorbed with an inorganic sorbent at a temperature of 70-80°C. Then, desorption is carried out in a continuous stream, an alcoholic solution with citric acid added to it with a mass fraction of 5-10% at a temperature of 80-85° C. In another method for producing a natural dye from an onion husk [10], an aqueous extract of the onion husk is carried out. Before the extraction of the raw material for the preparation of the dye, it is crushed and poured into water in a ratio of 1: 9 or 1:10. Extraction is carried out at 65-90°C and filtration is carried out. After filtration, the extract is evaporated under vacuum at a pressure of 0.3-0.5 MPa or dried to a powdery state. As food acids use citric or acetic acid. In the third, the method for obtaining a natural colorant of the raw material is extracted with water in the presence of a carbonic acid salt, the extraction mixture is heated to 69-79°C and carried out at a pressure of 7.2-10.0 MPa [11].

In the fourth method of obtaining natural dye from the onion husk, the extraction process of the coloring pigments is carried out by extraction, raw materials and before the extraction is added the crushed bark of coniferous trees by a ratio from 3 to 7 to 7 ÷ 3, the mixture is treated with a flow of

carbon dioxide [12]. We used onions for the production of the dye as a raw material. The choice of the object of the study was due to the fact that they contain about 0.4% of the antioxidant in the form of a biflavanoid - quercetin and a rutin with P - vitamin activity. Raw materials are pulverized in a pulverized manner. The resulting semi-finished product was wetted in cold water. Extraction is excreted in the course of ~ 30min. The temperature is 45°C. As an extractant, along with distilled water, ethyl alcohol was used. The chromaticity and concentration of coloring substances was determined by the spectroscopic method. The absorption spectra of the compounds studied were recorded on Specord 50 SA and SF-46 spectrophotometers. To produce them, depending on the concentration of the solution, we used quartz cuvettes with liners, which made it possible to vary the thickness of the measured layer from 0.1 to 50 mm. All measurements were taken at room temperature (297 K). It has been experimentally found that extracts from the onion husks do not have a fluorescent capacity at room temperature.

Therefore, we confined ourselves to considering only the absorption spectra. In order to determine the main coloring pigment of the dye from the onion husks, standard compounds of quercetin and rutin (brands of PTA), often found in the husks of onions, were selected.

2. Results and discussion

Solutions of standard compounds were made in 95% ethyl alcohol with a concentration of 1 mg/ml, which they prepared by accurately attaching the selected flavonoids. In order to select the analytical wavelength of the standard connected, the UV spectrum of the alcoholic solutions of rutin and quercetin and also the extracts of the onion husks were previously obtained. As an example, Figures 1 and 2 show the electronic absorption spectra of the reference extract from the onion husk and quercetin, respectively. The concentration dependence of the absorption spectra of solutions of quercetin, rutin and pigments from onion husks in ethanol in the concentration range 10^{-5} – 10^{-3} M was studied. It was found that the shape of the spectra of the investigated compounds and the intensity of the absorption bands remain practically constant (see Figures 1 and 2 of curve 1-3).

These indicate that the molecules of the derivatives of flavones at given concentration intervals are in monomer states. The absorption spectrum of quercetin in ethanol has three maxima, with $\lambda_{\max} = 258$ nm, $\lambda_{\max} = 301$ nm, $\lambda_{\max} = 377$ nm (Fig. 2).

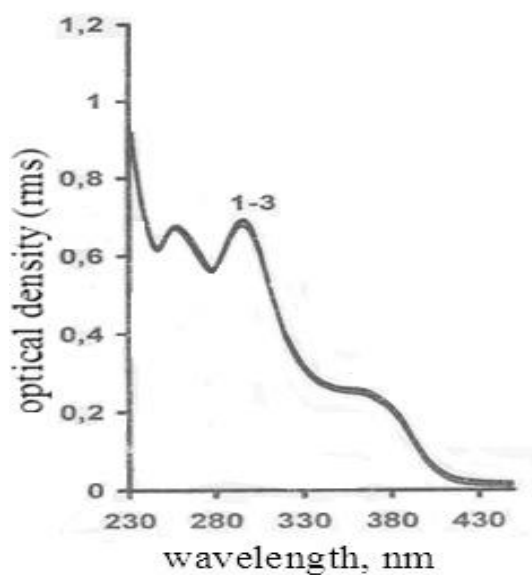


Fig.1. Concentration dependence absorption spectra of the extract from the onion husk:
 $1 \cdot 10^{-5}$, $2 \cdot 10^{-4}$, $3 \cdot 10^{-3}$ M

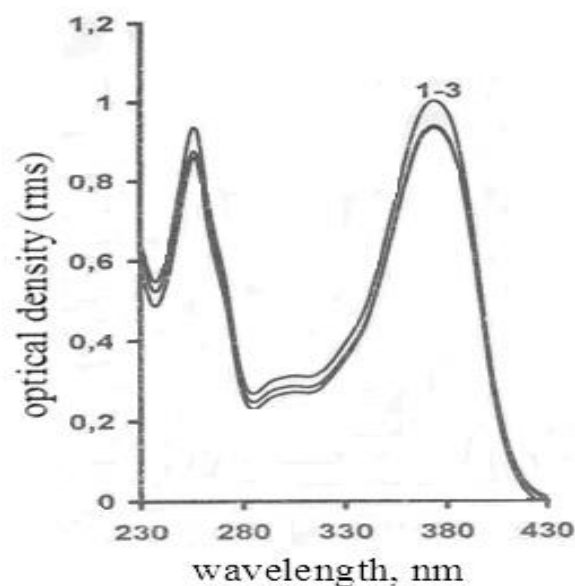


Fig.2. Concentration dependence absorption spectra in ethanol quercetin:
 $1 \cdot 10^{-5}$, $2 \cdot 1.2 \cdot 10^{-4}$, $3 \cdot 5 \cdot 10^{-3}$ M

In these cases, the main absorption bands of rutin are with $\lambda_{\max} = 257$ nm, $\lambda_{\max} = 298$ nm and $\lambda_{\max} = 360$ nm. The results of the experiment showed that the optical density of the alcohol extract of the onion husks outweighs the similar value of the results obtained in the aqueous extract. Taking into account the foregoing, for the preparation of coloring pigments.

The carried out researches have shown that in the case of replacing the extract ant and carrying out this process in ethanol, the optical density of the extract increases ~ 3 times. In this case, the optical density varies from 0.08 to 0.3 units of absorbance. It should be noted that the extraction time and temperature in both extract ants remained the same. Further, a study is conducted to obtain an extract of an alcoholic solvent, depending on the temperature and extraction time. It was found that increasing the extraction temperature from 20°C to 48°C results in a significant increase in the optical density, which varied from 0.3 to 0.9 units of optical density, i.e. in these cases, the color of the extract increased ~ 3 -fold. It was found that the extraction is carried out in alcohol at a temperature of 45 - 48°C and in time of about 2 hours.

In order to determine the proportion of quercetin and rutin in the extracts of onion husks, the method of adding aluminum sulphate, which enters the complication reaction with the selected standard compounds, was used. First of all, we extracted the onion husks in water. Then, a spectroscopic study of the aqueous solution of quercetin and rutin with the addition of aluminum sulfate as an example in Fig. 3 shows the absorption spectrum of the aqueous solution of quercetin as aluminum sulfate $\{\text{Al}_2(\text{SO}_4)_3\}$ is added.

It follows from Fig. 3 that addition of aluminum salts to the aqueous solution of quercetin leads to a simultaneous decrease in the intensity of the band with $\lambda_{\max} = 420$ nm. It should be noted that the introduction of $\text{Al}_2(\text{SO}_4)_3$ ions in an amount from $2 \cdot 10^{-5}$ M to $5 \cdot 10^{-5}$ M deformation of the absorption spectra of the aqueous solution of quercetin is accompanied by the appearance of an isobestic point at $\lambda_{\max} = 405$ nm. Further introduction of aluminum ions from $4 \cdot 10^{-4}$ to $6 \cdot 10^{-2}$ M causes the isobestic point in the absorption spectra to disappear (see curve 4-6 of Fig.3). The appearance of an isobestic point in the absorption spectra indicates that at certain concentrations of the addition of metal ions leads to the formation of complexes.

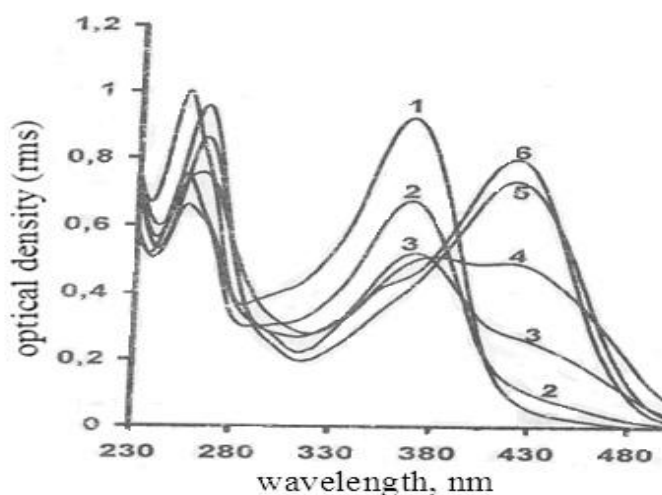


Fig.3. The absorption spectrum of quercetin in water ($c = 10^{-5}$ M) as different amounts of $\text{Al}_2(\text{SO}_4)_3$:
1 – 0; 2 - 10^{-5} ; 3 - $5 \cdot 10^{-5}$; 4 - 10^{-4} ; 5 - $5 \cdot 10^{-4}$; 6 - 10^{-2} M $\text{Al}_2(\text{SO}_4)_3$

In these cases, the solution turns out to be binary molecules of quercetin and complex them with metal ions. The absence of an isobestic point indicates that starting from the added aluminum ions with a concentration of more than $4 \cdot 10^{-4}$ M, complex complexes of biflavone molecules with metal ions are formed in their aqueous solutions. Similar phenomena of spectral changes are observed in the complication of the molecules of rutin with metal ions in aqueous solutions of rutin.

In contrast to quercetin for rutin, a new absorption band is observed and developed at $\lambda_{\max}=427$ nm and the isobestic point occurs at $\lambda_{\max}=410$ nm. Complexation of derivatives of flavonoid with metal ions are discussed in [13].

According to the authors of the complexation of metal ions with derivatives of flavonoids is due to the pronounced electron-donor properties of the latter and their low reduction potential, which for most flavonoids lies in the range of 0.25-0.75. The complication reaction of quercetin with metal ions is characterized by the formation of a ligand-metal bond by transfer of an electron from d-dwelling metal to π^* -orbital quercetin. The structure of the resulting complex compound depends on the nature of the electron density distribution in the ligand. In particular, on the charge on oxygen atoms, where the electron density is maximal. It was found that higher values of the negative charge are located on the oxygen atom of the carbonyl group (-0.312). Charges on other oxygen atoms range from -0.111 to -0.248. Proceeding from the above, it can be assumed that for the quercetin molecule, a complex with metal ions is formed through the oxygen atom of the carbonyl group [13].

On the basis of experimental studies and generalization of the literature data [14], it is established that the derivatives of flavone rutin and quercetin tend to form complexes with metal ions. Based on the results obtained, it is possible to develop spectroscopic techniques for determining the derivatives of flavonoids in aqueous dye extracts from onion husks. For this purpose, the gradient curves for quercetin and rutin were added as aluminum sulfate was added in their aqueous solutions.

In Fig. 4 shows the gradient curve of the aqueous solution of quercetin as the metal ions are added. The obtained dependences of the gradient curve are linear. Using the gradient curve, the proportion of biflavonides in the aqueous extract of the onion husk was determined. Quantitative determination of the content of the sum of flavonoids in onion husks was carried out on the basis of the gradient curves (Fig. 4).

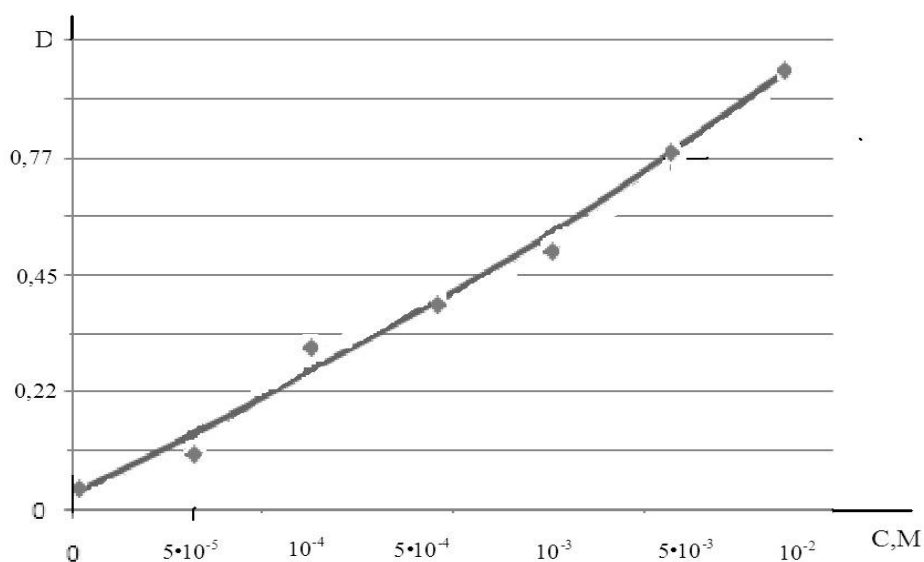


Fig.4. Grading chart for quercetin $\lambda = 440$ nm. Comparative solution: aqueous solution of aluminum sulphate.

Based on the results obtained, a method for the spectrophotometric determination of the total content of flavonoids in terms of their content for rutin or quercetin has been developed. It was found that the content of the sum of flavonoids (in terms of rutin) in the husks of onion -90.3 ± 4.8 $\mu\text{g} / \text{ml}$, (in terms of quartzite) -47.5 ± 2.6 $\mu\text{g}/\text{ml}$.

Conclusion

Thus it is shown that in extracts of onion husks the main coloring pigments are quercetin and rutin. The proportion of biflavonoids is determined in the band of complexes of coloring pigments with metal ions, based on spectroscopic methods of investigation.

Acknowledgment

This work was supported in part by a grant OT-A4-07, Uzbekistan

REFERENCES

- 1 Astanov S.Kh. *Photonics of molecules of food colorings*. Thesis for the degree of Doctor of Phys. and Math. Sciences, Tashkent 2003, 263 p.
- 2 Nizomov N., Kurtaliev E.N., Rahimov Sh.I. Fluorescent aggregates Cyan 40 and Thiazole Orange dyes in solution. *Journal of Molecular Structure*. 2012, Vol. 1029, pp. 142 – 148.
- 3 Kurtaliev E.N., Nizomov N. Photostability of styrylcyanine dye Sbt and its homodimer in solutions". *Proceeding of the 3rd Intern. Symposium "Molecular photonics" dedicated to academician A.N.Terenin*. Repino, St.Petersburg. June 24-29. 2012, pp. 107. [in Russian]
- 4 Fayzullaev A.R., Sharipov M.Z., Shamsiev R.Kh., Rakhmatova M.R., Ostonova N.S., Kudratullaeva Z.Y., Astanov S.Kh. Spectral characteristics of the extract from husks of onion. *Proceeding of the IX Intern. scientific and technical conference "Technology and technology of food production»*, Mogilev, Belarus, 2013, Part1, pp. 87.
- 5 Astanov S.Kh., Fayzullaev A.R., Sharipov M.Sh., Nizamov N., Kurtaliev E.N. Thermodestruction of riboflavin in various aggregate states. *Journal of Applied Spectroscopy*. 2014, Vol. 81, No. 1, pp. 40 – 45.
- 6 Astanov S.Kh., Sharipov M.Sh., Fayzullaev A.R., Kurtaliev E.N., Nizomov N. Spektroskopik study of photo and thermal destruction of riboflavin". *Journal of Molecular Structure* 2014, p. 133 – 138.
- 7 Fayzullaev A.R., Astanov S.Kh., Shamsiev R. Kh. Food colorings. *Toshkent "Fan va technologar"* 2014, 195 p.
- 8 Astanov S.Kh., Fayzullaev A.R. Complex processing of red beet to obtain food coloring of other pathologically active products. Theses reports of the *"Technology and technology of food production»*, Part 1. Mogilev, Belarus, 2014, p. 61.
- 9 Cherenin V.S., Bolotov V.M., Zotov A.P. Method for the production of flavonoid dye from vegetable raw materials. Patent RU№2134280. Published August 10, 1999, [in Russian]
- 10 Novotorov Ye.Yu. *A method for producing a natural colorant from an onion husk*. Patent RU No.2021310, 15.10.1994 [in Russian]
- 11 Kvasenkov O.I. *Method of obtaining the dye from the husks of onions*. Patent RU No.2041899, C1, 1995 [in Russian]
- 12 Kvasenkov O.I. *Method of obtaining the dye from the husks of onions*. Patent RU No.2086587, 27 January 2017 [in Russian]
- 13 Astanov S.Kh., Sharipov M.Sh., Fayzullaev A.R., Nizomov N., Kurtaliev E.N., Hudoynazarov K. Spectral characteristics of some flavonoids by interaction with metal ions". *Proceeding of the III Intern. Conference of Optics and Photonics*, 2013, pp.159 – 162.
- 14 Sorokina O.N., Sumina E.G., Petrakov A.V., Barysheva S.V. Spectrophotometric determination of the total content of flavonoids in herbal medicines. *News of the Saratov University. Chemistry*, Saratov, 2013, Vol. 13, Issue 3, pp. 8 – 11. [in Russian]

APPLICATION OF DOSIMETRY METHODS FOR INTERNAL ORGANS EXPOSURE AND POSSIBLE INFLUENCE TO REMOTE EFFECTS

Zhunossov Y.T.¹, Zhumadilov K.Sh.^{2,7}, Chaizhunosova N.Zh.¹, Sayakenov N.B.¹, Shabdarbaeva D.M.¹, Gnyrya V.S.³, Azimkhanov A.S.³, Stepanenko V.F.⁴, Fujimoto N.⁵, Shichijo K.⁶, Hoshi M.⁵

¹Semey State Medical University, Semey, Abay Str. 103, Kazakhstan

²L.N. Gumilyov Eurasian National University, Astana, Kazakhstan, zhumadilovk@gmail.com

³National Nuclear Center of the Republic of Kazakhstan, Kurchatov, Kazakhstan

⁴A.F. Tsyb Medical Radiological Research Center, Obninsk, Russia

⁵Hiroshima University, 734-8553, Japan

⁶Nagasaki University, 1-12-4, Sakamoto, Nagasaki 852-8523, Japan

⁷National Research Nuclear University "MEPhI", Moscow, Russian Federation

Internal dosimetry study is conducted during rats exposure by dust of ⁵⁶Mn powder during experiment to study exposure effect in Kurchatov reactor complex Baical-1 (Kurchatov city, East-Kazakhstan region). This study was performed by group of scientists from Japan, Kazakhstan, and Russian Federation. It was important to study effect of radiation, due to effect of possible influence to human, and effect of possible internal exposure because of close location to Semipalatinsk Nuclear Test Site and post effect of irradiation due to Hiroshima and Nagasaki atomic bomb, Chernobyl accident and others. It was comparison of data of two scenarios of rat irradiation: a) the experimental box was supplied with air filter only (targeted for animal's breathing); b) the experimental box was supplied with the system of forced ventilation. After exposure to radioactive powder of ⁵⁶Mn radioactivity in organs and tissues of the rats was measured. The result of assessments of internal doses from neutron-activated ⁵⁶Mn in powder, sprayed over experimental animals was compared.

Keywords: internal exposure, Kurchatov, rats, organs, powder of ⁵⁶Mn, samples.

Introduction

The Semipalatinsk Nuclear Test Site (SNTS) is located in Kazakhstan, served for nuclear tests of the USSR in the atmosphere from 1949 to 1962. Radiation doses in this area have been reconstructed in several ways. All the problems of dosimetry at this site were covered in an earlier publication [1-3]. In general, the average doses estimated by biophysical (individual) methods, were lower than the average doses received by physical (environmental) methods. This difference is still the subject of ongoing research [4, 5].

Doses were reconstructed for a cohort of Russian and Ukrainian workers in response to the accident and residents in contaminated Russian territories due to Chernobyl accident. Due to the large number of restored doses, these studies revealed endogenous (with an internal cause or origin) dental Electron Paramagnetic Resonance (EPR) dosimetry problems that appear when the method is applied to large-scale reconstruction of doses [6]. EPR dosimetry is currently used to validate other dosimetry methods that are used in case-control studies to assess the risk of radiogenic cataracts and leukemia [7].

The study of the EPR reconstruction of the dose in survivors of atomic bombing is described in various articles [8, 9]. EPR dosimetry with tooth enamel was used in this case to check doses assessed using cytogenetic dosimetry [6]. EPR doses estimated from 100 tooth samples (69 donors) were compared with doses for the same individuals that were determined cytogenetically from lymphocytes. The agreement between doses evaluated using the two methods confirmed that the

cytogenetic method can be used even several years after acute exposure and that the translocation yield after irradiation in vivo and in vitro were similar. It should be noted that the radiation sensitivity of the tooth enamel to neutrons was not taken into account in this study, as well as in an earlier article [10], which used EPR dosimetry to estimate the dose of external radiation [6].

The applied dose data are based on the tables listed in the DS86 final report such as the free-in-air kermas, the house shielding factors, and organ dose factors for the active bone marrow and the breast. Calculations for the 13 other organs provided in DS86 are possible. To obtain the organ doses for each survivor, it is necessary to obtain information concerning (1) place exposed, (2) whether they were shielded or not, and (3) age. ABS93D body transmission factors for active bone marrow for neutrons and gamma rays agreed with DS86 to within a few percent. Of the survivors studied, 35.123 of them were used for the relative risk estimation of leukemia mortality, adopting the same method as the Radiation Effects Research Foundation (RERF) for comparison. For the observation period from 1968 to 1989, the analyzed relative risks for leukemia mortality at 1 Gy by shielded kerma and by active bone marrow dose are 2.01 and 2.37, respectively, which are consistent with the RERF results [11].

After the atomic bombing of Hiroshima and Nagasaki, Japan, initial radiation directly produced during or shortly after the explosions and residual radiation contributed towards a radiation exposure of the survivors [12]. There are two sources of residual radiation: (1) neutron-activated radioisotopes from materials on the ground and (2) radioactive fallout containing fission products and residual fissile materials from the bombs. Understanding the former is particularly important for evaluating the risks to those people who moved to these cities soon after the detonations and might have inhaled radioactive dust [12-14]. Such individuals were reported to suffer from various syndromes similar to acute radiation effects [15].

1. Materials and methods

a. Animals

Male Wistar rats were delivered from Karaganda State Medical University, Kazakhstan. With purpose to understand the effect of ^{56}Mn radiation, neutron activated $^{56}\text{MnO}_2$ powder was sprayed over rats, and its biological effects were evaluated. The highest doses of internal irradiation were detected in the digestive system, followed by the lungs [16, 17].

They were maintained with free access to basal diet and tap water. In Experiment 1, rats were divided into four groups, with six rats for the ^{56}Mn group and three rats per group for the Mn and control groups. The ^{56}Mn and Mn groups were exposed to $^{56}\text{MnO}_2$ and non-radioactive MnO_2 , respectively. Three rats organs of the ^{56}Mn group were used for dosimetry 3.5–4 h after the exposure. One rat per each group was used on days 3, 14, and 60. In Experiment 2, the exposure was repeated with 12 rats in the ^{56}Mn group and nine rats each in the Mn and control groups. Three rats of the ^{56}Mn group were used for dosimetry 3.5–4 h after the exposure. Then, three rats from each group were killed and examined on days 3, 14, and 60 after the irradiation [18].

b. Irradiation and dosimetry of each organ of rats

Details of irradiation using ^{56}Mn and the corresponding internal dose estimation have been described in previous publications [16, 17]. In brief, $^{56}\text{MnO}_2$ was obtained by neutron activation of 100 mg of MnO_2 powder using the Baikal-1 nuclear reactor at Kurchatov, Kazakhstan. A thermal neutron fluence of $4 \times 10^{14} \text{ n/cm}^2$ was applied to produce $2.74 \times 10^8 \text{ Bq}$ of ^{56}Mn activity.

The activated MnO_2 powder was sprayed into sealed boxes containing six rats per box (one box was used for Experiment 1, and two boxes were used for Experiment 2) [18]. In Experiment 1, the exposure box was equipped with air filters only, while an additional forced ventilation system was installed to improve animal welfare in the boxes in Experiment 2. The same total activity of ^{56}Mn equal to $2.74 \times 10^8 \text{ Bq}$ was used for irradiation in both experiments. The specific activity of

^{56}Mn powder was the same (2.74×10^9 Bq/g) as well. After 1 h, rats were removed from the exposure box(es) into clean (not contaminated) cages, cooled down for 2.5–3 h. Then, three of the animals were killed by intraperitoneal injection of an excessive dose of pentobarbital. A piece of each organ was dissected, weighted and put into a vial. The radioactivity of ^{56}Mn in samples of each organ was measured with a gamma spectrometer. Assessment of internal radiation doses was performed by measuring of ^{56}Mn activity in each organ and calculating the absorbed fractions of internal exposure to photons and electrons. Details of the dosimetry are described in an accompanying paper [16, 19].

2. Results and discussion. Radiation doses due to ^{56}Mn exposure

The radiation dose received from ^{56}Mn varied among different organs (Figure 1). Although the initial activities of neutron-activated MnO_2 powder were similar in Experiments 1 and 2, the radiation doses of each organ received in Experiment 2 were substantially lower than those received in Experiment 1, i.e., the small intestine received 1330 mGy in Experiment 1 while 150 mGy in Experiment 2. However, the distribution of dose values between tissues was similar in the two experiments, being very high in the digestive system, followed by the lungs and skin. Details are given in Stepanenko et al. [16].

In figure 1 shown Specific activity of ^{56}Mn , A_0 , and accumulated doses of internal irradiation, D , in different organs of experimental rats. In Figure 1 we compared two types of results. First is comparison between boxes without ventilation and with ventilation. With same influence of neutron fluencies. In figure 1 (a) is data of activity in different organs and in Figure 1 (b) is data of absorbed dose in organ with two different scenario of irradiation. Numbers of organs are shown in Table 1.

Table 1. Numbers for different organs which were subjected to internal exposure.

| <i>Numbers</i> | <i>Organs</i> |
|----------------|-----------------|
| 1 | Liver |
| 2 | Heart |
| 3 | Kidney |
| 4 | Trachea |
| 5 | Lung |
| 6 | Tongue |
| 7 | Esophagus |
| 8 | Stomach |
| 9 | Small intestine |
| 10 | Large intestine |
| 11 | Eyes |
| 12 | Skin |
| 13 | Whole body |

According to figure 1, the highest value of Activity and dose are detected in organ number 10 (Large intestine) for both experiments, but due to ventilation in Experiment number 2, those data were smaller. And all data are showed the same tendency for decreasing data for experiment number 2 compare to activity and dose in experiment number 1.

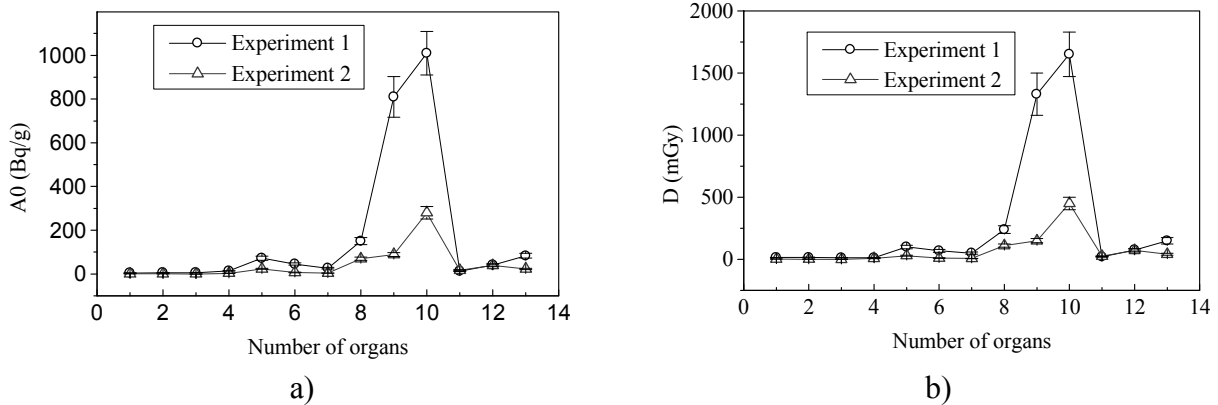


Fig.1. Specific activity of ^{56}Mn , A_0 (a), and accumulated doses of internal irradiation, D (b), in different organs of experimental rats.

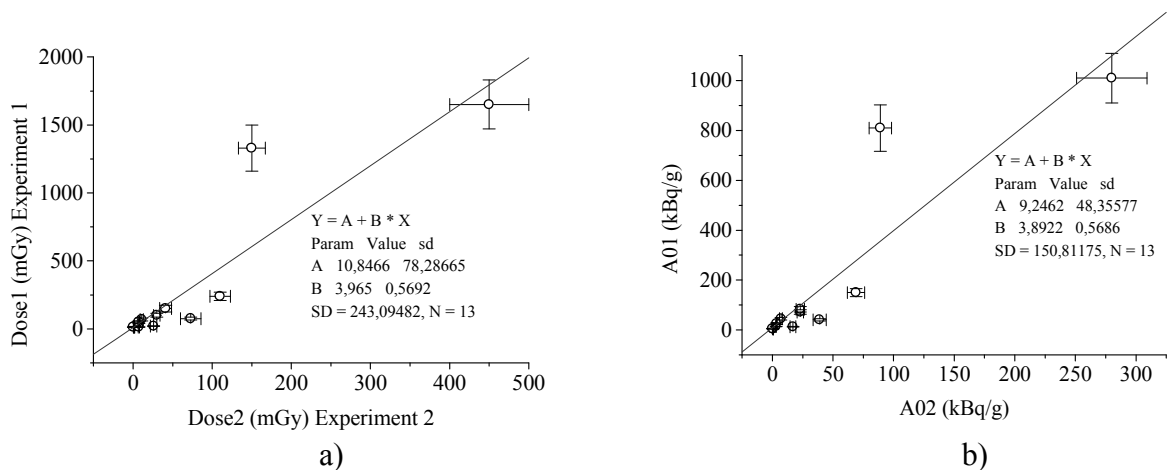


Fig.2. Dependence a) of doses from experiment # 1 versus dose of experiment #2; b) activity from experiment #1 versus activity from experiment #2 in different organs of experimental rats

Correlation between of dose and activity for two scenarios are almost linear, except two values of Dose and Activity for Small intestine and large intestine. The reason for these high doses and activity already explained in [17, 18].

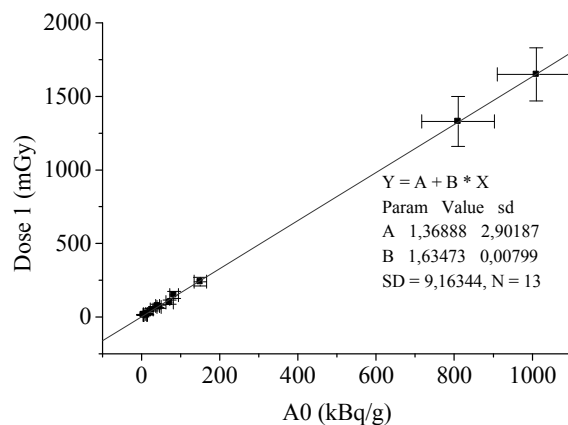


Fig. 3. Dependence of doses from experiment # 1 versus activity of experiment #1 in different organs of experimental rats

Figure 3 is showing the correlation between dose and activity of different organ, which is linear and can confirm correct calculation of internal dose due exposure. Also data of two scenarios compares by statistical t-test with 95% confidence interval of this difference. The two-tailed P value equals 0.1696 and by conventional criteria, this difference is considered to be not statistically significant.

Conclusion

This study investigated the effects of radiation exposure by $^{56}\text{MnO}_2$ powder in male Wistar rats over 60 days and amount of activity and dose calculation in different organs for two scenarios of irradiation. Comparison of this type of irradiation showed significant difference. And it will be recommended to use first scenario of irradiation of rats for better efficiency of irradiation. Although whole body radiation doses from ^{56}Mn were relatively low, higher internal doses were noted in the small intestine and lungs. Increasing of neutron fluencies in future can lead to increasing doses in some other organs like a liver.

Acknowledgment

The study was carried out with the financial support of the Semey State Medical University, Ministry of Health of the Republic of Kazakhstan (research support in the Republic of Kazakhstan). The research of specialists from Japan was supported by JSPS KAKENHI grants No. 26257501 and No. 24310044, Japan

REFERENCES

- 1 Stepanenko V.F., Hoshi M., Bailiff I.K., Ivannikov A.I., Toyoda S., Yamamoto M., Simon S.L., Matsuo M., Kawano N., Zhumadilov Z., Sasaki M.S., Rosenson R.I., Apsalikov K.N. Around Semipalatinsk nuclear test site: Progress of dose estimations relevant to the consequences of nuclear tests. (A summary of 3rd Dosimetry Workshop on the Semipalatinsk nuclear test site area. RIRBM, Hiroshima University, Hiroshima, 9-11 March, 2005). *J. Radiat. Res.* 2006, Vol. 47, Suppl. A, pp. A1– A13.
- 2 Ivannikov A.I., Sanin D., Nalapko M., Skvortsov V.F., Stepanenko V.F., Tsyb A.F., Trompier F., Zhumadilov K. and Hoshi M. Dental Enamel EPR Dosimetry: Comparative Testing of the Spectra Processing Methods for Determination of Radiation-Induced Signal Amplitude. *Health Phys.* 2010, Vol. 98, No. 2, pp. 345 – 351.
- 3 Zhumadilov K., Ivannikov A., Zharlyganova D., Zhumadilov Z., Stepanenko V., Apsalikov K., Rodzi M., Zhumadilova A., Toyoda S., Endo S., Tanaka K., Okamoto T. and M. Hoshi. ESR dosimetry study on population of settlements nearby Ust-Kamenogorsk city, Kazakhstan. *Radiat. Environ. Biophys.* 2009, Vol. 48, Issue 4, pp. 419 – 425.
- 4 Romanyukha A.A., Schauer D.A., Malikov Y.K. Analysis of current assessments and perspectives of ESR tooth dosimetry for radiation dose reconstruction of the population residing near the Semipalatinsk nuclear test site. *J. Radiat. Res.* 2006, Vol. 47, Suppl. A, pp. A55-A60.
- 5 Simon S.L., Baverstock K.F., Lindholm C. A summary of evidence on radiation exposures received near to the Semipalatinsk nuclear weapons test site in Kazakhstan. *Health Phys.* 2003, Vol. 84 (6), pp. 718-725.
- 6 Fattibene P. and Callens F. EPR dosimetry with tooth enamel: A review. *Appl. Radiat. Isot.* 2010, Vol. 68, pp. 2033-2116.
- 7 Bouville A., Chumak V.V., Inskip P.D., Kryuchkov V., Luckyanov N. The Chernobyl accident: Estimation of radiation doses received by the Baltic and Ukrainian cleanup workers. *Radiat. Res.* 2006, Vol.166 (1), pp. 158-167.
- 8 Ikeya M., Ishii H. Atomic bomb and accident dosimetry with ESR natural rocks and human tooth in vivo spectrometer. *Appl. Radiat. Isot.* 1989, Vol. 40 (10-12), pp. 1021-1027.
- 9 Iwasaki M., Miyazawa C., Chida T., Takahashi F., Onai Y. Dental ESR dosimetry of a medical physicist who received occupational radiation exposure for almost 40 y. *Health Phys.* 2002, Vol. 83 (4), pp.534 – 538.

10 Tatsumi-Miyajima J., Okajima S. Physical dosimetry at Nagasaki - Europium-152 of stone embankment and electron spin resonance of teeth from atomic bomb survivors. *J. Radiat. Res.* 1991, Vol. 32 Issue Suppl., pp. 83-98.

11 Hoshi M., Matsuura M., Hayakawa N., Ito C., Kamada N. Estimation of radiation doses for atomic-bomb survivors in the Hiroshima University Registry. *Health Phys.* 1996, May, Vol. 70 (5), pp. 735 – 740.

12 Imanaka T., Endo S., Tanaka K., Shizuma K. Gamma-ray exposure from neutron-induced radionuclides in soil in Hiroshima and Nagasaki based on DS02 calculations. *Radiat. Environ. Bioph.* 2008, Vol. 47, Issue 3, pp. 331–336.

13 Kerr G.D., Egbert S.D., Al-Nabulsi I., Bailiff I.K., Beck H.L., Belukha I.G., Cockayne J.E., Cullings H.M., Eckerman K.F., Granovskaya E., Grant E.J., Hoshi M., Kaul D.C., Kryuchkov V., Mannis D., Ohtaki M., Otani K., Shinkarev S., Simon S.L., Spriggs G.D., Stepanenko V.F., Stricklin D., Weiss J.F., Weitz R.L., Woda C., Worthington P.R., Yamamoto K., Young R.W. Workshop report on atomic bomb dosimetry – review of dose related factors for the evaluation of exposures to residual radiation at Hiroshima and Nagasaki. *Health Phys.* 2015, Vol. 109, No. 6, pp. 582 – 600.

14 Kerr G.D., Stephen D., Egbert S.D., Al-Nabulsi I., Beck H.L., Cullings H.M., Endo S., Hoshi M., Imanaka T., Kaul D.C., Maruyama S., Reeves G.I., Ruehm W., Sakaguchi A., Simon S.L., Spriggs G.D., Stram D.O., Tonda T., Weiss J.F., Weitz R.L., Young R.W. Workshop report on atomic bomb dosimetry – residual radiation exposure: recent research and suggestions for future studies. *Health Phys.* 2013, Vol. 105, No. 2, pp. 140 – 149.

15 Imanaka T., Endo S., Kawano N., Tanaka K. Radiation exposure and disease questionnaires of early entrants after the Hiroshima bombing. *Rad. Prot. Dosim.* 2012, Vol. 149, No. 1, pp. 91 – 96.

16 Stepanenko V., Rakhypbekov T., Otani K., Endo S., Satoh K., Kawano N., Shichijo K., Nakashima M., Takatsuji T., Sakaguchi A., Kato H., Onda Y., Fujimoto N., Toyoda S., Sato H., Dyussupov A., Chaizhunosova N., Sayakenov N., Uzbekov D., Saimova A., Shabdarbaeva D., Skakov M., Vurim A., Gnyrya V., Azimkhanov A., Kolbayenkov A., Zhumadilov K., Kairikhanova Y., Kaprin A., Galkin V., Ivanov S., Kolyzhenkov T., Petukhov A., Yaskova E., Belukha I., Khailov A., Skvortsov V., Ivannikov A., Akhmedova U., Bogacheva V., Hoshi M. Internal exposure to neutron-activated ^{56}Mn dioxide powder in Wistar rats - Part 1. *Dosimetry. Radiat. Environ. Biophys.* 2017, Vol. 56, Issue 1, pp. 47 – 54.

17 Stepanenko V.F., Rakhypbekov T.K., Kaprin A.D., Ivanov S.A., Otani K., Endo S., Satoh K., Kawano N., Takatsuji T., Nakashima M., Shichijo K., Sakaguchi A., Kato H., Onda Y., Fujimoto N., Toyoda S., Sato H., Kolyzhenkov T.V., Petukhov A.D., Dyussupov A.A., Chaizhunosova N.Z., Sayakenov N.B., Uzbekov D.E., Saimova A.Z., Shabdarbaeva D.M., Pivina L.N., Skakov M.K., Vurim A.D., Gnyrya V.S., Azimkhanov A.C., Kolbayenkov A.N., Zhumadilov K.S., Kairkhanova Y.O., Yaskova E.K., Belukha I.G., Skvortsov V.G., Ivannikov A.I., Khailov A.M., Akhmedova U.A., Bogacheva V.V., Anokhin Y.N., Orlenko S.P., Hoshi M. Irradiation of experimental animals by neutron activated dust: development and realization of the method—first results of international multicenter study. *Radiation and Risk*, 2016, Vol. 25, pp. 111–125.

18 Shichijo K., Fujimoto N., Uzbekov D., Kairkhanova Y., Saimova A., Chaizhunosova N., Sayakenov N., Shabdarbaeva D., Aukenov N., Azimkhanov A., Kolbayenkov A., Mussazhanova Z., Niino D., Nakashima M., Zhumadilov K., Stepanenko V., Tomonaga M., Rakhypbekov T., Hoshi M. Internal exposure to neutron-activated ^{56}Mn dioxide powder in Wistar rats – Part 2: pathological effects. *Radiat. Environ. Biophys.* 2017, Vol. 56, Issue 1, pp. 55 – 61.

19 Shichijo K., Fujimoto N., Uzbekov D., Kairkhanova Y., Saimova A., Chaizhunosova N., Sayakenov N., Shabdarbaeva D., Aukenov N., Azimkhanov A., Kolbayenkov A., Mussazhanova Z., Niino D., Nakashima M., Zhumadilov K., Stepanenko V., Tomonaga M., Rakhypbekov T., Hoshi M. Erratum to: Internal exposure to neutron-activated ^{56}Mn dioxide powder in Wistar rats – Part 2: pathological effects. *Radiat. Environ. Biophys.* 2017, Vol. 56, Issue 1, pp. 203 – 204.

| SUMMARIES | ТҮСІНІКТЕМЕЛЕР | АННОТАЦИИ |
|---|----------------|-----------|
| <p>Потанов А.А. Фракталдық радиоэлектрониканың мәселелеріне. 1 бөлім. Көпөлшемді дабылдарды өңдеу, радиолокация, нанотехнологиялар, радиотехникалық элементтер мен датчиктер. Жұмыста радиотолқындардың сәулеленуі және қабылдаудың барлық сатыларына кіретін ақпаратты соңғы өндеумен жүретін радиоэлектрониканың есептерін шешудегі фракталдық әдіс-тәсілдері келтірілген. Мақаланың бұл бөлімінде радиожүйелердегі ақпарат ағындарын өңдеу сұрақтары қарастырылған. Фракталдық антенналар және фракталды датчиктердің жаңа типтерінің сұлбатехниканың негіздері келтірілген, фракталдық нанотехнологияның даму суреті берілген. Шынайы миниатюрлі фракталдық антенналардың электродинамикалық модельдеудің ерекшеліктерінің қысқаша сипаттамасы келтірілген. Фракталды-скейлингтік немесе масштабты-инвариантты радиолокацияның негіздемесі берілген.</p> <p>Потанов А.А. К проблемам фрактальной радиоэлектроники. Часть 1. Обработка многомерных сигналов, радиолокация, нанотехнологии, радиотехнические элементы и датчики. В работе представлены фрактальные подходы к решению задач радиоэлектроники на всех этапах излучения и приема радиоволн с последующей обработкой поступающей информации. В данной части статьи рассмотрены вопросы обработки потоков информации в радиосистемах. Представлены основы схемотехники новых типов фрактальных антенн и фрактальных датчиков, дан эскиз развития фрактальных нанотехнологий. Приведено краткое описание особенностей электродинамического моделирования реальных миниатюрных фрактальных антенн. Дано обоснование фрактально-скейлинговой или масштабно-инвариантной радиолокации.</p> | | |
| <p>Потанов А.А. Фракталдық радиоэлектрониканың мәселелеріне. 2 бөлім. Радиотолқындардың таралуы мен шашырауы, радиожылулық эффектілер, жаңа модельдер, үлкен фракталдық жүйелер. Мақаланың екінші бөлімінде кездейсоқ-біртекті орталардағы толқындардың таралуы мен шашырауы кезінде пайда болатын фракталдық эффектілер қарастырылған. Фракталдық объектіні зондтау кезінде радиолокацияның тендеуі нақтыланған. Өсімдік жабынымен радиотолқындардың шашырау процестері үшін фракталдар мен ғажап аттракторлар негізіндегі модельдер ұсынылған.</p> <p>Потанов А.А. К проблемам фрактальной радиоэлектроники. Часть 2. Распространение и рассеяние радиоволн, радиотепловые эффекты, новые модели, большие фрактальные системы. Во второй части статьи рассмотрены фрактальные эффекты, возникающие при распространении и рассеянии волн в случайно-неоднородных средах. Уточнено уравнение радиолокации при зондировании фрактального объекта. Предложены модели на основе фракталов и странных аттракторов для процессов рассеяния радиоволн растительными покровами.</p> | | |
| <p>Кажикенова С.Ш. Жоғары температурадағы балқымалардың ағынының компьютерлік модельдеуі. Балқымалардың физикалық қасиеттерін зерттеудің ең сындарлы әдістерінің бірі компьютерлік модельдеу болып табылады. Бұл трансферттік коэффициенттерге қатысты алынған ақпараттың үлкен теориялық және қолданбалы құндылығына, атап айтқанда, көлемді және жылжымалы тұтқырлығына байланысты. Алайда нақты есептеулер үшін толық физика-математикалық аппарат қажет. Жұмыстың мақсаты - кванттық потенциалдар көмегімен анықталатын, тұтқырлықтың корреляциялық функцияларын жұмылдыру арқылы гидродинамика тендеулерін сандық шешу әдістемесін жүзеге асыру, балқытпа ағысының жылдамдықтары бейінінің үлестірілуін зерттеу, физикалық мағынасы бар гидродинамика тендеулерінің бастапқы жүйесін аса қарапайым реттендіруді алу. Осындай бағдарламаны жүзеге асыру үшін статистикалық физиканың әдістерін қолданамыз. Ұсынылған зерттеулердің сәтіне сұйықтықтың гидродинамикалық тендеулерін шешу үшін, төменгі температуралық сұйықтықтар үшін тұтқырлығы ескерілмеген. Осы мақалада жоғары температуралық балқымалардың ағыны үшін математикалық модель ұсынылып, олардың қысқа қашықтықты тәртібін ескере отырып, статистикалық физика әдісімен екінші тұтқырлық коэффициентін қарастырады. Сандық эксперименттер негізінде балқытпа ағынының жылдамдықтарын үлестіру салынған. Металл балқытпаларды құюдың технологиялық параметрлерін болжауға мүмкіндік беретін, гидродинамика тендеулерін сандық интегралдау алгоритмі әзірленген.</p> | | |

Кажикенова С.Ш.

Компьютерное моделирование потока высокотемпературных расплавов.

Одним из наиболее конструктивных методов изучения физических свойств расплавов является компьютерное моделирование. Это объясняется большой теоретической и прикладной ценностью информации, полученной в отношении коэффициентов переноса, в частности объемной и сдвиговой вязкости. Однако для конкретных расчетов необходим детальный физико-математический аппарат. Цель работы – реализация методики численного решения уравнений гидродинамики с привлечением корреляционных функций вязкости, определяемых с помощью квантовых потенциалов, исследование распределения профиля скоростей течения расплава, получение наиболее простой регуляризации исходной системы уравнений гидродинамики, содержащей в себе физический смысл. Для реализации такой программы мы будем использовать методы статистической физики. К моменту предлагаемых исследований были известны способы решения уравнений гидродинамики для низкотемпературных жидкостей без учета объемной вязкости. В данной работе предложена математическая модель течения высокотемпературных расплавов, учитывающая природу ближнего порядка в них и учитывающая второй коэффициент вязкости методами статистической физики. Построено распределение скоростей течения расплава на основе численных экспериментов. Разработан алгоритм численного интегрирования уравнений гидродинамики, позволяющий прогнозировать технологические параметры розлива металлических расплавов.

Саулебеков А.О., Трубицын А.А., Камбарова Ж.Т., Саулебекова Д.А.

«Сақина-ось» тоғыстау режимінде жұмыс істейтін квадрупольдік-цилиндрлік өріс негізіндегі зарядталған бөлшектердің электрстатикалық энергия талдағышы.

Квадрупольдік-цилиндрлік өріс негізіндегі бұрын ұсынылған электрстатикалық энергия талдағыш сұлбасының корпускулярно-оптикалық параметрлері зерттелген. Зарядталған бөлшектердің көзі ішкі цилиндрде, ал детектор симметрия осінде орналасқан («сақина-ось» тоғыстау режимі) жағдайы үшін энергия талдағыштың жұмыс істеу режимі қарастырылған. Квадрупольдік-цилиндрлік айнаның тоғыстаушы қасиеттері есептелген. Аппараттық функция алынған. Құрылғының салыстырмалы энергиялық ажыратуы мен жарық күші анықталған.

Саулебеков А.О., Трубицын А.А., Камбарова Ж.Т., Саулебекова Д.А.

Электростатический энергоанализатор заряженных частиц на основе квадрупольно-цилиндрического поля в режиме фокусировки «кольцо-ось».

Проведено исследование корпускулярно-оптических параметров схемы электростатического энергоанализатора на основе квадрупольно-цилиндрического поля, предложенной ранее. Рассмотрен режим работы энергоанализатора, при котором источник заряженных частиц расположен на внутреннем цилиндре, а детектор – на оси симметрии (фокусировка «кольцо-ось»). Рассчитаны фокусирующие свойства квадрупольно-цилиндрического зеркала. Построена аппаратная функция. Оценено относительное энергетическое разрешение и светосила устройства.

Дудин И.В., Нариманов Р.К., Нариманова Г.Н.

Тұтқырлы сұйықтағы эллипсоидтың айналуы кезіндегі кедергі моменті. Эллипсоид мысалында қатты дененің сұйық ішінде айналуы кезіндегі сұйық тарапынан кедергі күші әрекет ететіндігі көрсетілген. Берілген күш үйкеліс күштерімен де, қысым күштерімен де құрылады. Олар қосылған массаның әрекет ету эффектісінің байқалу нәтижесінде пайда болады. Кез келген дене үшін кедергіні есептеу әдістемесі өңдеп шығарылған. Тұтқырлы сұйықтағы айналатын эллипсоидтың кедергі күштері үшін аналитикалық формулалар орнатылған. Алынған нәтижелерді техникалық құрылғыларда екіфазалы ағыстарды есептеу үшін қолдануға болады.

Дудин И.В., Нариманов Р.К., Нариманова Г.Н.

Момент сопротивления при вращении эллипсоида в вязкой жидкости.

На примере эллипсоида показано, что при вращении твердого тела в жидкости, на него со стороны последней действует сила сопротивления. Данная сила создается как силами трения, так и силами давления, которые возникают в результате проявления эффекта действия присоединенной массы. Разработана методика расчета сопротивления для произвольного тела. Установлены аналитические формулы для сил сопротивления вращающегося в вязкой жидкости эллипсоида. Полученные результаты применимы для расчета двухфазных течений в технических устройствах.

Кучеренко М.Г., Налбандян В.М.

Фонондар мен шекаралық беттердегі электрондардың шашырауы кезіндегі нанобөлшектердің плазмондық резонанстың спектрлік контурының енін құру.

Нанобөлшектердің плазмондық резонансты температураны төмендету есебінен тарыту әдісінің тиімдігіне бағалау жүргізілген. Радиусы 70 нм-ден кем бөлшектер үшін бөлшек бетіндегі электрондардың шашырауын ескеру қажеттілігі көрсетілген. Бұл шашыраудың температуралық реттеу мүмкіндігін айтарлықтай шектейді.

Сыртқы магниттік өрісте «кор-қабықша» құрылымына ие қабатты сфералық нанокомпозиттердің жұтылу спектрінің экситондық және плазмондық жолақтардың трансформациясын зерттеу бойынша мәліметтер келтірілген. Магниттік өрістегі плазмондық резонанс жолағының жіктелуі 10^{12} c^{-1} –тен төмен электрондардың шашырау жиілігі кезінде ғана бақылау мүмкіндігі көрсетілген.

Кучеренко М.Г., Налбандян В.М.

Формирование ширины спектрального контура плазмонного резонанса наночастиц при рассеянии электронов на фонах и граничной поверхности.

Произведена оценка эффективности метода сужения плазмонных резонансов наночастиц посредством снижения температуры. Показано, что для частиц радиусом менее 70 нм необходимо учитывать рассеяние электронов поверхностью частицы, которое существенно ограничивает возможности температурного регулирования рассеяния. Приведены данные по исследованию трансформации экситонных и плазмонных полос спектров поглощения сферических слоистых нанокомпозитов со структурой «кор-оболочка» во внешнем магнитном поле. Показано, что расщепление полосы плазмонного резонанса в магнитном поле можно наблюдать лишь при частотах рассеяния электронов ниже 10^{12} c^{-1} .

Гученко С.А., Коваль Н.Н., Юров В.М., Крысина О.В., Завацкая О.Н.

Көпқатпарлы Ti/Cu жабындарының қасиеттері.

Осы жұмыста Ti және Cu катодтары пайдаланылды. Жабындар жоғарыда аталған катодтарды вакуумды қондырғыларда бір уақытта тозаңдату (себу) кезінде ионды-плазмалы болат үлгілерге жағылған. Көп қатпарлы жабындар келесі түрде жасалған: 2 минут бойы Ti жағылды, содан кейін 2 минут Ti+Cu жағылады. Барлығы аргон мен азот атмосферасында 100 қабат жағылады. Электронды-микроскопиялық зерттеулер TESCAN фирмасының MIRA 3 растрлық электронды микроскоппен жүргізілген болатын. Зерттеулер 20 кВт үдетуші кернеу кезінде және 15 мм жуық жұмыс қашықтығында жасалды. Оптикалық микроқұрылым Эпиквант металграфикалық микроскопта зерттелді. Жабындардың микроқаттылығын зерттеу микроқатты HVS-1000 А жасалды. Азоттағы TiN+(Ti+Cu)N микроқаттылықты өлшеу нәтижелері TiN титан нитриды үшін жабынның қалыпты қаттылығының $H = 20$ -д ан $H = 30$ ГПа дейінгі мәнде артқанын көрсетті. Электронды-микроскоптық зерттеулер TiN+(Ti+Cu)N жабындары әдетте, өсіміне қарай созылған, диаметрі 2-5 нм жіпше түйірлері бар бағаналы құрылымды екенін көрсетті. Титан нитридының TiN қалыпты көміртекті болат бойынша және бөлме температурасында жылжу кезінде үйкеліс коэффициенті 0,9 құрайды, ал көп қатпарлы жабынның TiN+(Ti+Cu)N үйкеліс коэффициенті 3 есе кемиді және 0,3 артпайды. TiN+(Ti+Cu)N жабыны қаттылығының артуы мен үйкеліс коэффициентінің 3 есе артуы біріге отырып, тозуға төзімділігін айтарлықтай арттыруға алып келді. Бұл әсіресе, кескіш құралдар үшін өте маңызды. Алынған жабындардың барлық артықшылықтарын қосатын болсақ, оған қоса жоғары температурада тотығуға тұрақтылығы мен салыстырмалы түрде олардың құнының арзандығын қоса алғанда, көпқатпарлы TiN+(Ti+Cu)N жабын метал өңдеу өнеркәсібінде, машина жасауда, энергетикада және бірқатар басқа да бағыттарда кеңінен қолданылуы күтіледі.

Гученко С.А., Коваль Н.Н., Юров В.М., Крысина О.В., Завацкая О.Н.

Свойства многослойных покрытий Ti/Cu.

В настоящей работе использовались катоды Ti и Cu. Покрытия наносились на стальные образцы ионно-плазменным методом на вакуумной установке при одновременном распылении указанных выше катодов. Создавались многослойные покрытия следующим образом: в течение 2 минут наносился Ti, затем в течении 2 минут Ti+Cu. Всего наносилось 100 слоев в атмосфере аргона и азота. Электронно-микроскопическое исследование было проведено на растровом электронном микроскопе MIRA 3 фирмы TESCAN. Исследования проводились при ускоряющем напряжении 20 кВ и рабочем расстоянии около 15 мм. Оптическая микроструктура исследовалась на металлографическом микроскопе Эпиквант. Исследование микротвердости покрытий проводилось на микротвердомере HVS-1000 А. Результаты измерения микротвердости TiN+(Ti+Cu)N в азоте показывают увеличение твердости покрытия от стандартного для нитрида титана TiN значения $H = 20$ до $H = 30$ ГПа. Электронно-микроскопические исследования показали, что покрытия TiN+(Ti+Cu)N обычно обладают столбчатой структурой с нитевидными зернами диаметром 2–5 нм, вытянутыми в сторону роста. При скольжении нитрида титана TiN по обычной углеродистой стали и комнатной температуре коэффициент трения составляет 0,9, а коэффициент трения многослойного покрытия TiN+(Ti+Cu)N уменьшается в 3 раза и не превышает 0,3. Увеличение твердости покрытия TiN+(Ti+Cu)N и уменьшение коэффициента трения в 3 раза в совокупности приводит к существенному повышению износостойкости. Это особенно важно для режущего инструмента. Если сложить все преимущества полученных покрытий, включая стойкость к высокотемпературному окислению и сравнительно небольшую их стоимость, то можно ожидать, что многослойные покрытия TiN+(Ti+Cu)N найдут широкое применение в металлообрабатывающей промышленности, машиностроении, энергетике и ряде других направлениях.

Шайкенова А.А., Бейсенов Р.Е., Муратов Д.А.

WS₂ кристаллдарын химиялық буфазада тұндыру әдісімен өсіру.

Кварц төсенішінде жұқа вольфрам қабақтарын химиялық бу фазада (CVD) сульфуризация арқылы өсірілген WS₂ монокристаллдарының сипаттамалары зерттелінді. WS₂ 800-1000° С температурада CVD жүйесінде жүргізілді. Күкірт буы аргон газдарымен тасымалданды (500 sccm). Оптикалық микроскоп, Раман және фотолюминесценттік талдаулар арқылы сипатталған WS₂ монокристалдары алынды. Оптикалық микроскоп WS₂ үшбұрышты бір фазалы кристаллдық құрылымы бар домендердің түзілгендігін көрсетті. Фотолюминесценттік талдаулар нәтижелері тыйым салынған ауданы 1,96 эВ болатын, WS₂ монокабатты кристалдарына сәйкес келетіндей 600-660 нм шамаларының арасында күшті пиктерді көрсетті.

Шайкенова А.А., Бейсенов Р.Е., Муратов Д.А.

Рост кристаллов WS₂ методом химического парофазного осаждения.

Изучены синтез и характеристика монокристаллов WS₂, выращенных методом химического осаждения из паровой фазы (CVD), путем сульфуризации тонкого слоя оксида вольфрама на кварцевой подложке. Синтез WS₂ проводился при 800-1000°С в системе CVD. Пар серы транспортировался аргоновым газом (500 sccm). Получены монокристаллы WS₂, исследованы на оптическом микроскопе, проведен Рамановский анализ и фотолюминесценция. Оптический микроскоп показал образование треугольных однофазных кристаллических структур доменов WS₂. Толщина WS₂составляет 6 слоев, что определяется комбинационной спектроскопией. Анализ фотолюминесцентной спектроскопии показал сильный пик между 600-660 нм, как правило для монослойного кристалла WS₂, где ширина запрещенной зоны равна 1,96 эВ.

Шайкенова А.А., Бейсенов Р.Е., Муратов Д.А.

Химиялық бу фазалы қондыру синтезінде графеннің түзілу механизмін зерттеу.

2D материалдар өзінің ерекше қасиеттерінің арқасында әр түрлі салаларда қолданыс аясы өте кең. Графенді синтездеу кезінде химиялық буфазада тұндыру (CVD) әдісі кеңінен қолданылатыны айтылған. Осы мақалада мыс (Cu) фольгасында химиялық буфазасында тұндыру (CVD) әдісімен графен қабақтарын синтездеудің эксперименттері нәтижелері талқыланды. Алайда, қажетті сапалы графен қабақтарын алу әрқашан қол жетімді бола бермейді. Демек, кең ауқымды қосымшалар үшін өлшемі мен домендік морфологиясы бойынша басқарылатын синтез қажет. Поликристалды және бір кристалды графенді синтездеудің параметрлері келтірілген. Синтез процесінде графеннің қалыптасу механизмі зерттелінді. Үлгіні дайындау процестері, көп қабатты және бір қабатты графен CVD әдісімен өсу механизмдерінің негізгі талқыланды. CVD арқылы алынған графен қабақтары Раман, АСМ және СЭМ талдаулары арқылы сипатталынды.

Шайкенова А.А., Бейсенов Р.Е., Муратов Д.А.

Изучение механизма формирования графена при синтезе химического парофазного осаждения.

Благодаря своим уникальным свойствам 2D материалы имеют большой потенциал в различных областях применения. Утверждается, что метод химического осаждения из паровой фазы (CVD) широко используется в синтезе графена. В данной работе обсуждаются результаты экспериментов по синтезу графеновых слоев методом химического осаждения из паровой фазы (CVD) на медной (Cu) фольге. Однако желаемое качество графеновых слоев не всегда достижимо. Следовательно, для крупномасштабных приложений необходим управляемый синтез по размеру и морфологии домена. Приведены примеры параметров синтеза поликристаллического и монокристаллического графена. Механизм образования графена изучен в процессе синтеза. Процессы подготовки образца и основные механизмы роста многослойных и однослойных графена методом CVD обсуждалось. Полученные CVD графеновые слои характеризуются рамановским, АСМ и СЭМ анализом.

Ибраев Н.Х., Афанасьев Д.А.

Күміс нанобөлшектермен допирленген жартылай өткізгішті полимерлі қабықшалардың электрлік сипаттамаларының ерекшеліктері.

Ag бөлшектердің және Ag–TiO₂ нанокұрылымдардың қоспаларынан құралатын PEDOT:PSS полимер негізіндегі композитті қабықшалардың электрлік қасиеттері зерттелген. Полимерлі күн ұяшықтарының вольт-амперлік сипаттамаларының өлшеуі PEDOT:PSS полимерге Ag бөлшектерін және Ag–TiO₂ нанокұрылымдарын қосқан жағдайда қысқа тұйықталу тоғының артуын көрсетті. Күміс нанобөлшектерден құралатын ұяшықтарда рекомбинация жылдамдығының артуы байқалды. Полимерлі күн ұяшықтарының электрлік импедансын өлшеу кезінде күміс нанобөлшектерден құралатын PEDOT:PSS қабықшасының диэлектрлік өтімділігінің айтарлықтай артуы бақыланған.

Ибраев Н.Х., Афанасьев Д.А.

Особенности электрических характеристики полупроводниковых полимерных пленок, допированных наночастицами серебра.

Изучены электрические свойства композитных пленок на основе полимера PEDOT:PSS с добавками наночастиц Ag и наноструктур Ag-TiO₂. Измерения вольт-амперных характеристик полимерных солнечных ячеек показали рост тока короткого замыкания при добавлении наночастиц Ag и наноструктур Ag-TiO₂ в полимер PEDOT:PSS. Так-же наблюдается рост скорости рекомбинации в ячейках с наночастицами серебра. При измерениях электрического импеданса полимерных солнечных ячеек обнаружен значительный рост диэлектрической проницаемости пленки PEDOT:PSS, содержащей наночастицы серебра.

Безродный М.К., Сақыпов К.Е., Айтмагамбетова М.Б., Жакишев Б.А.

Өндірістік және тұрмыстық қалдықтарды кәдеге жарату үшін газдың жұқа тазалау жүйесін пайдалану.
Жұмыста газ қозғалыс бағытын өзгертуге негізделген шаң бөлшектерінің (немесе сұйық тамшылардың) шөгінділерінің инерциалды әдісінің мәселесі шешіледі. Шындығында, адамзат алдында тұрған ең маңызды экологиялық проблемалардың бірі - қоршаған ортаны тұрмыстық және өндірістік қалдықтармен ластануы. Бұл қалдықтар әдетте улылық, канцерогендік, мутагендік, коррозиялық, реактивтік қабілеттілікке және өрт қаупі сияқты зиянды қасиеттерге ие. Кез келген газды тазалау жүйесінің тиімділігі газ ағынынан ұсақ бөлшектерді жою мүмкіндігімен анықталады. Осы мәселені шешу үшін градиент сепараторына негізделген газдарды жұқа тазартуды дамыту арқылы гетерогенді газ қоспаларын бөлу мүмкіндігін қарастырдық. Градиент сепараторы негізінде ұсақ газды тазалау жүйесі бөлінген бөлшектерден, жеке аэрозольдерден, сублиматтардан және бөлек гетерогенді қоспалардан газ ағындарын тазалауға арналған.

Безродный М.К., Сакипов К.Е., Айтмагамбетова М.Б., Жакишев Б.А.

Использование системы тонкой очистки газов при утилизации промышленных и бытовых отходов.

Безродный М.К., Сакипов К.Е., Айтмагамбетова М.Б., Жакишев Б.А.

В работе решается задача о инерционном способе осаждения частиц пыли (или капель жидкости), который основан на изменении направления движения газа со взвешенными в нем частицами. Действительно одной из самых серьезных экологических проблем, стоящих перед человечеством, является загрязнение окружающей среды бытовыми и промышленными отходами. Эти отходы в основном обладают такими нежелательными свойствами, как токсичность, канцерогенность, мутагенность, коррозия, реакционная способность и пожароопасность. Известно, что эффективность любой системы газоочистки определяется ее способностью удалять мелкие частицы из газового потока. Чтобы получить решение данной задачи рассмотрели возможность разделения гетерогенных газовых смесей, разработкой тонкой очистки газов на базе градиентного сепаратора. Система тонкой очистки газов на базе градиентного сепаратора предназначена для очистки газовых потоков от диспергированных частиц, сепарации аэрозолей, возгонов, разделения гетерогенных газовых смесей на отдельные компоненты.

Сакипов К.Е., Абиров А.А., Шарифов Д.М., Махмудов Б.Н.

Құйынды гидравликалық көтергіштің тәжірибелік зерттеулердің нәтижелері.

Мақалада автономды су тазарту жүйесінің құйынды гидравликалық лифтінің оңтайлы жұмыс режимдерін бағалау үшін тәжірибелік зерттеулердің нәтижелері келтірілген. Тәжірибелік зерттеулерге сүйенсек, жұмыс және сору ағындарын бұру құйынды гидравликалық көтергіштердің эжекция қабілетін айтарлықтай арттырады. Алынған нәтижелерді талдау (эжекция коэффициентінің жұлын параметрлеріне тәуелділігінің қысқ сызығы) құйынды гидравликалық лифт пен гидро приваттың оңтайлысыни мәндері бар, бұл эжекция коэффициентінің ең үлкен мәніне қолжеткізілген қабылдау ортасының тангенстік қабылдауымен. Сондай-ақ, айналмалы белсенді және пассивті ағындар гидравликалық лифт араластыру камерасына сұйықты қалу үшін тетікке түбегейлі әсер етеді. Айналдыру қарқындылығының жоғарылауы ағынның араласуын арттырады, ал үлкен қысым градиенттері тек осьтік емес, сонымен бірге радиалды бағытта жүреді. Бұл эжекция коэффициентінің ұлғаюына әкеледі. Осылайша, өткізілген тәжірибелік зерттеулер мен алдын-ала техникалық-экономикалық есептер негізінде әр түрлі қоспаларды гидропрепарациялау үшін құйынды гидравликалық лифттерді пайдалану энергияны тұтынуды айтарлықтай азайтады және оларды қолдану тиімділігін арттырады деп қорытынды жасауға болады.

Сакипов К.Е., Абиров А.А., Шарифов Д.М., Махмудов Б.Н.

Результаты экспериментальных исследований вихревого гидроэлеватора

В статье приводятся результаты экспериментальных исследований для оценки оптимальных режимов работы вихревого гидроэлеватора системы автономной водоочистки. На основе экспериментальных исследований показано, что закрутка рабочего и всасываемого потоков значительно увеличивает эжекционную способность вихревых гидроэлеваторов. Проводимый анализ полученных результатов (кривых зависимостей коэффициента эжекции от параметров закрутки), позволяют сделать вывод, что существуют оптимальные критические значения для вихревого гидроэлеватора и гидроэлеватора с тангенциальным подводом всасываемой среды, при котором достигается наибольшее значение коэффициента эжекции. Также выявлены, что закрученные активный и пассивный потоки коренным образом влияют на механизм вовлечения всасываемой жидкости в

камеру смешения гидроэлеватора. Увеличение интенсивности закрутки увеличивает подмешивание потока, при этом возникают большие градиенты давления не только в осевом, но и в радиальном направлении, что приводит к увеличению коэффициента эжекции. Таким образом, на основе проводимые экспериментальные исследования и предварительных технико-экономических расчетов можно сделать вывод, что использование вихревых гидроэлеваторов при гидро-транспортировании различных смесей позволит значительно сократить энергозатраты и повысить эффективности их применения.

Перчаткина Е.В., Миньков Л.Л.

Осцилляциялайтын жоғары қабырғаға не жазық каналдағы дыбыстан асқан жылдамдыққа не газдың ағысы туралы есептің сандық шешімі.

Берілген жұмыста газ үшін гармоникалық заң бойынша тербелістерді жасайтын, жоғары шекарамен жылжымалы өткізбейтін жазық каналдағы газдың дыбыстан асқан жылдамдықты ағысы туралы есеп шешілген. Газ динамикасының теңдеулердің сандық шешімін алу үшін кеңістік пен уақыт бойынша аппроксимациясының бірінші ретті Ван Лир әдісі бойынша ағыстарды есептеулерін қолдануымен айырымдық сұлба іске асырылған. Ван Лир әдісін қолдануымен айырымдық тордың ұяшықтар қырларындағы ағындарды есептеуге мүмкіндік беретін газдық динамикасының теңдеулерінде ағындардың ерекше формасы берілген. Гармоникалық заң типі мен газ ағысының бастапқы шарттарынан тәуелді қисықсыздықты облыстарда қозғалатын бұрыштық соққы толқынның таралу ерекшеліктеі зерттелген. Кейбір нақты жиілігі кезінде қабырғаның тербелісі ағыс сипатына ешбір әсер етпейтіндігі анықталған. Нәтижелердің дұрыстығы AnsysFluent бағдарламасымен алынған сандық шешімінен салыстыру арқылы дәлелденді.

Перчаткина Е.В., Миньков Л.Л.

Численное решение задачи о сверхзвуковом течении газа в плоском канале с осциллирующей верхней стенкой.

В данной работе решается задача о сверхзвуковом течении газа в плоском канале с подвижной непроницаемой для газа верхней границей, совершающей колебания по гармоническому закону. Для получения численного решения уравнений газовой динамики реализована разностная схема с использованием расчета потоков по методу Ван Лира первого порядка аппроксимации по пространству и времени. Дана особая форма потоков в уравнениях газовой динамики, позволяющая рассчитывать потоки на гранях ячеек разностной сетки с использованием метода Ван Лира. В зависимости от типа гармонического закона и начальных условий притока газа исследованы особенности распространения угловой ударной волны в движущихся криволинейных областях. Установлено, что при определенной частоте колебаний наличие пристеночных колебаний практически не влияет на режим потока внутри домена. Сравнение численного решения, полученного с помощью разработанной программы, с решением по программе Ansys Fluent показывает корректность результатов.

Ершина А.К., Ыдырысова А.А.

Желкенді жел турбинасының аэродинамикалық характеристикаларын анықтау.

Барлық жел турбиналарын жұмыс істеу принциптеріне қарай 3 типке бөлуге болады: желкенді жел турбинасы (Савониус), пропеллерлік жел турбинасы және қалақшалы Дарье тәрізді жел турбиналары. Мақалада желкенді жел турбинасының құрылыс мен жұмыс істеу принциптері қарастырылған. Сонымен қатар жел турбинасының аэродинамикалық характеристикалары: қалақшаның көтеру күші мен маңдайлық кедергі күшінің коэффициенттері, турбинаның қуаты, жел энергиясын пайдалану коэффициенті мен жүрдектік дәрежесі және т.б. теориялық негізде анықталған. Нәтижесінде теориялық жолмен анықталған мәндер экспериментпен салыстырылған. Есептеу нәтижелерінің белгілі тәжірибелік мәліметтермен жақсы сәйкес келетіндігі көрсетілген.

Ершина А.К., Ыдырысова А.А.

Определение аэродинамических характеристик парусной ветротурбины.

Ветротурбины по принципу работы можно разделить на 3 типа: парусные (Савониус), пропеллерные и крыловые (типа Дарье) ветротурбины. В статье кратко изложены основы теории парусной ветротурбины. Определены аэродинамические характеристики: коэффициенты подъемной силы и лобового сопротивления, мощность турбины, коэффициент использования энергии ветра, степень быстроходности и др. Представлены результаты сравнения расчетных и экспериментальных данных. Показано удовлетворительное согласие результатов расчета с известными экспериментальными данными.

Саттинова З.К., Рамазанова Г.И., Жапбасбаев У.К., Асилбеков Б.К., Мусенова Э.К.

Бериллий тотығы термопласт шликерін құю процесіндегі жылулық режимін зерттеу.

Құю қондырғысының каналындағы термопласт шликерінің қозғалысы мен жылуалмасуының математикалық моделі бойынша сандық есептеулер нәтижесі мен эксперимент деректері келтірілген. Есептеу нәтижелері құю

жүйесіндегі шликердің салқындатылуы мен қатуын көрсететін температура өрісінің таралуы, шликерді формалау барысында ақаудың пайда болуы шартын болжауға және қату процесінде температура-фазалық өріс өзгерісін бақылауға мүмкіндік береді. Алынған деректер негізінде шликердің қату шекарасы аймағының құю режимдері параметрлеріне тәуелділігі орнатылды. Құю процесінің математикалық моделі бойынша сандық әдіспен жүргізілген есептеулер нәтижесі тәжірибе деректерімен сәйкес келетіндігі орнатылды.

Саттинова З.К., Рамазанова Г.И., Жапбасбаев У.К., Асилбеков Б.К., Мусенова Э.К.

Исследование тепловых режимов процесса формования термопластичного шликера оксида бериллия.

Приводятся результаты экспериментов и расчетов математической модели движения и теплообмена шликерной массы в кольцевой полости. Результаты экспериментов были анализированы и обобщены с использованием математической модели. Численные расчеты проводились при тех же режимных параметрах и условиях проведения экспериментов, которые позволяют прогнозировать условия появления дефектов при формовании изделий, получить распределения полей температуры, показывающие динамику охлаждения и отвердевания термопластичного шликера, отследить изменение температурно-фазовых полей в процессе отвердевания. Результаты расчетов находятся в согласии с данными экспериментов, и показывают физическую обоснованность предложенной математической модели процесса формования бериллиевой керамики.

Шрагер Э.Р., Сакипова С.Е., Танашева Н.К., Ахмерова К.Е., Ботпаев Н., Кусаинова А.К.

Желтурбиналарының электрфизикалық параметрлерін зерттеу.

Мақалада кіші және орташа қуатты жел электрлік қондырғылардың тиімділігін зерттеу нәтижелері келтірілген. Арнайы жасалған кіші айналмалы электр генераторымен екі түрлі жел турбиналарының үлгісіндегі табиғи желдің жағдайында сынақтар нәтижелері талқыланды. Желтурбиналардың қондырғы сипаттамасы және техникалық параметрлері келтірілген. Ұзақ уақыт аралығында табиғи желдің жылдамдығынан электрфизикалық сипаттамаларының тәуелділіктері алынды. Желкенді типті жел диірменге қарағанда цилиндрлік қалақтары бар жел диірменмен қосылған электр генераторының өндіретін қуаты үлкен екені көрсетілді.

Шрагер Э.Р., Сақыпова С.Е., Танашева Н.К., Ахмерова К.Е., Ботпаев Н., Кусаинова А.К.

Исследование электро-физических параметров ветротурбин.

В статье рассматриваются результаты изучения эффективности ветроэнергетических установок малой и средней мощности. Обсуждаются результаты испытаний в условиях естественного ветра двух различных макетов ветротурбин комбинированных со специально разработанным малооборотистым электрогенератором. Приведено описание устройства и технических параметров ветротурбин. Получены зависимости электро-физических характеристик от скорости естественного ветра в течение длительного времени. Показано, что вырабатываемая мощность электрогенератора, соединенного с ветроколесом в цилиндрическими лопастями, больше мощности генератора с ветроколесом парусного типа.

Шаймерденова К.М., Стоев М., Тусыпбаева А.С., Рахманқызы А., Секербаева Г.

Анализ влияния электро-разрядной обработки воды на степень ее очистки.

В данной статье рассматривается исследование анализа влияния электроимпульсных разрядов на степень очистки воды. Приведено описание техники измерения удельной электрической проводимости с помощью кондуктомера. Показан технический регламент получения очищенной и обеззараженной воды при электро-разрядной обработке. В ходе исследований было изучено изменение солесодержания и удельной электропроводности водопроводной и природной образцов воды после обработки электроимпульсным методом. В экспериментах учитывалось время обработки и количество электро-импульсных разрядов.

Шаймерденова К.М., Стоев М., Тусыпбаева А.С., Рахманқызы А., Секербаева Г.

Суды электр-разрядымен өңдеуде оның тазарту дәрежесіне әсерін талдау.

Берілген мақалада соққы толқыны разрядтарының саны мен эксперимент жүргізілген уақыттың суды тазарту дәрежесіне әсерін талдау жұмыстарына зерттеулер жүргізілді. Кондуктометр арқылы меншікті электр өткізгіштігі анықталды. Зерттеу барысында электр импульс әдісімен өңделген табиғи және құбыр суының тұз мөлшері және меншікті электр өткізгіштігі зерттелді. Электрлік разрядтар саны мен уақытын ескере отырып, эксперимент тәжірибелік үлгідегі электр гидроимпульстік қондырғысында жүргізілді.

Файзуллаев А.Р., Астанов С.Х., Эргашева Н.М.

Пияз қабығынан алынған бояғыштарды алу процесінде спектроскопияның қолданылуы.

Мақалада пияз қабығы формасындағы қалдықтардан бояғышты алу технологиясы қарастырылған. Спектроскопиялық әдістермен пигменттер режимінде экстракция температурасы анықталды. Пияз қабығынан алынған биофлавоноидтар мен экстракттар металл иондарымен кешендерді түзу тенденциясына ие екендігі

көрсетілген. Кверцетиннің металл иондарымен кешенді түзу реакциясы металдың d-орбиталінен кверцетиннің π *-орбиталіне электронды тасымалдау кезінде металмен байланыс түзуімен сипатталады. Пияз қабығы мен Руян өсімдігінің қабығының табиғи бояғыштарын зерттеу нәтижелері тоқыма өнеркәсібінде қолданылуы мүмкін. Бояғыштардың негізгі бояу пигменттері анықталған және бояғыштарды тұрақтандыру әдістері ұсынылған.

Файзуллаев А.Р., Астанов С.Х., Эргашева Н.М

Применение спектроскопии в процессе получения красителей из луковой шелухи.

В статье рассматривается технология получения красителя из отходов в форме шелухи лука. Спектроскопическими методами определена температура экстракции в режиме пигментов. Показано, что биофлавоны и экстракты из шелухи лука имеют тенденцию образовывать комплексы с ионами металлов. Установлено, что реакции комплексообразования с ионом металла кверцетина характеризуются образованием связи с металлом при переносе электрона с d-орбиталей металла на π *-орбитали кверцетина. Результаты изучения естественных красителей шелухи лука и коры растений Руян применимы в текстильной промышленности. Определены основные красящие пигменты красителей и предложены методы стабилизации красителей.

Жунусов Е.Т., Жумадилов К.Ш., Чайжунусова Н.Ж., Саякенов Н.Б., Шабдарбаева Д.М., Гныря В.С., Азимханов А.С., Степаненко В.Ф., Фуджимото Н., Шичиджо К., Хоши М.

Дозиметриялық әдістердің мүшелерді ішкі сәулелендіруде және алыстатылған эффектілерге мүмкін болатын әсер етуінде қолданылуы.

«Байкал-1» Курчатов реакторлық комплексінде (Курчатов к., Шығыс Қазақстан облысы) әсер ету эффектісін зерттеу бойынша эксперимент кезінде ^{56}Mn ұнтағы шаңының егеуқұйрықтарға әсері бойынша ішкі дозиметриялық зерттеу жүргізілді. Берілген зерттеу Жапония, Қазақстан және Ресей Федерациясының ғалымдары тобымен жүзеге асырылды. Адамға мүмкін әсері эффектісімен және Семей ядролық сынақ полигонына жақын орналасуы әсерінен мүмкін ішкі сәулелену эффектісімен, сондай-ақ Хиросима мен Нагасакидегі атом бомбасының жарылысы, Чернобыль АЭС-дағы апат, т.б. әсерінен сәулелену постэффектісімен шартталған радиация әсерін зерттеу маңызды болды. Егеуқұйрықтарды сәулелендірудің екі сценарийінің мәліметтерін салыстыру жүргізілді: а) эксперименттік бокс тек қана ауа фильтрімен жабдықталды (жануарлардың тыныс алуына арналған); б) эксперименттік бокс мәжбүрлі вентиляция жүйесімен жабдықталды. ^{56}Mn радиоактивті ұнтағымен сәулелендіруден кейін егеуқұйрықтардың мүшелері мен ұлпаларындағы радиоактивтілік өлшенді. Эксперименттік жануарларға тозандатылған ұнтақтағы нейтронмен белсендірілген ^{56}Mn сәулеленуінің ішкі дозаларын бағалау нәтижелерін салыстыру жүргізілді.

Жунусов Е.Т., Жумадилов К.Ш., Чайжунусова Н.Ж., Саякенов Н.Б., Шабдарбаева Д.М., Гныря В.С., Азимханов А.С., Степаненко В.Ф., Фуджимото Н., Шичиджо К., Хоши М.

Применение дозиметрических методов при внутреннем облучении органов и возможном влиянии на отдаленные эффекты.

Было проведено внутреннее дозиметрическое исследование по воздействию пыли порошка ^{56}Mn на крыс во время эксперимента по изучению эффекта воздействия на реакторном комплексе Байкал-1 (г. Курчатов, Восточно-Казахстанская область). Данное исследование проводилось группой ученых из Японии, Казахстана и Российской Федерации. Было важно изучение влияния радиации, обусловленное эффектом возможного воздействия на человека, и эффектом возможного внутреннего облучения из-за близкого расположения к Семипалатинскому испытательному ядерному полигону и постэффектам облучения вследствие атомной бомбардировки в Хиросиме и Нагасаки, аварии на Чернобыльской АЭС и других. Проведено сравнение данных двух сценариев облучения крыс: а) экспериментальный бокс снабжался только воздушным фильтром (предназначенным для дыхания животных); б) экспериментальный бокс снабжался системой принудительной вентиляции. После облучения радиоактивным порошком ^{56}Mn измерялась активность в органах и тканях крыс. Проведено сравнение результатов оценки внутренних доз облучения нейтронно-активированным ^{56}Mn в порошке, распыленном в боксах на экспериментальных животных.

**INFORMATION ABOUT
AUTHORS**

**АВТОРЛАР ТУРАЛЫ
МӘЛІМЕТТЕР**

**СВЕДЕНИЯ
ОБ АВТОРАХ**

Abirov, A.A. - Candidate of Technical Sciences, Associate Professor, Eurasian National University. L.N. Gumilyov, Astana, Kazakhstan

Afanasyev, D.A. - PhD, Senior lecturer, Department of Physics and Nanotechnology; Executive Director of the Institute of Applied Mathematics, Ministry of Education and Science of Republic Kazakhstan, Karaganda, Kazakhstan

Akhmerova, K.E. - Master, Researcher, Physical-Technical Faculty, Ye.A. Buketov Karaganda State University, Karaganda, Kazakhstan

Assilbekov, B.K. – PhD, Satbayev Kazakh National Technical University, Almaty, Kazakhstan

Astanov, S.X. – Doctor of phys.-math. sciences, Professor, Department of "Physics, Bukhara Engineering-Technologies Institute, Bukhara, Uzbekistan

Aytmagambetova, M.B. – Senior Lecturer, «Heat Power Engineering» Department, L.N. Gumilyov Eurasian National University, Astana, Kazakhstan

Azimkhanov, A.S. - Deputy head of the CIR "Baikal-1"; National Nuclear Center of the Republic of Kazakhstan, Kurchatov, Kazakhstan

Beisenov, R.E. - PhD, Associated Professor, Satbayev University; Head of the EPR Spectroscopy Laboratory named after Gorelinsky, Institute of Physics and Technology, Almaty, Kazakhstan

Bezrodny, M. K. - Doctor of Technical Sciences, Professor, Deputy Head of the Theoretical and Industrial Heat Engineering Department, National Technical University of Ukraine “Igor Sikorsky Kiev Polytechnic Institute”, Kiev, Ukraine

Botpayev, N. – Researcher, Institute of Applied Mathematics, Ministry of Education and Science of Republic Kazakhstan, Karaganda, Kazakhstan

Chaizhunosova, N.Zh. - Doctor of medical sciences, professor, Semey State Medical University, Semey, Kazakhstan

Dudin, I.V. - Candidate of phys.-math. sciences, Assoc. Professor, Tomsk State University, Tomsk, Russia

Ergasheva, N. M. - Junior research, Department of "Physics, Bukhara Engineering-Technologies Institute, Bukhara, Uzbekistan

Fayzullaev, A.R. - Junior research, Department of "Physics, Bukhara Engineering-Technologies Institute, Bukhara, Uzbekistan

Fujimoto, N. - PhD, professor, Hiroshima University, 734-8553, Japan

Gnyrya, V.S. - Head of the CIR "Baikal-1"; National Nuclear Center of the Republic of Kazakhstan, Kurchatov, Kazakhstan

Guchenko, S.A. - PhD, Faculty of Physics and Technology, Ye.A. Buketov Karaganda State University, Karaganda, Kazakhstan

Hoshi, M. - PhD, professor, Hiroshima University, 734-8553, Japan

Ibrayev, N.Kh. - Doctor of phys.-math. sciences, Professor, Director of the Institute of Molecular Nanophotonics, Ye.A. Buketov Karaganda State University, Karaganda, Kazakhstan

Kambarova, Zh.T. – PhD, Docent, Physical-Technical faculty, Ye.A. Buketov Karaganda State University, Karaganda, Kazakhstan

Kazhikenova, S.Sh. - Doctor of Technical sciences, Associated Professor, Head of the Higher Mathematics Department, Karaganda State Technical University, Karaganda, Kazakhstan

Koval, N. - Doctor of Technical Sciences, Professor, Head of the Laboratory of Plasma Emission Electronics, Institute of High Current Electronics, Siberian Branch RAS, Russia

Krygina, O. - Candidate of phys.-math.science, Researcher, Laboratory of Plasma Emission Electronics, Institute of High Current Electronics, Siberian Branch RAS, Russia

Kucherenko, M.G. - Doctor of phys.-math. sciences, Professor, Director of the Centre of Laser and Information Biophysics, Orenburg State University, Orenburg, Russia

Kussaiynova, A.K. - Master, Junior Researcher, Institute of Applied Mathematics, Ministry of Education and Science of Republic Kazakhstan, Karaganda, Kazakhstan

Makhmudov, B.N. – Postgraduate student, S.U. Umarov Physical-Technical Institute, Academy of Sciences of the Republic of Tajikistan, Dushanbe, Tajikistan

Minkov, L.L. - Doctor of phys.-math. sciences, Professor, National Research Tomsk State University, Tomsk, Russia

Muratov, D.A. - PhD student, Satbayev University; Junior Researcher, EPR Spectroscopy Laboratory named after Gorelinsky, Institute of Physics and Technology, Almaty, Kazakhstan

Mussenova, E.K. - Candidate of phys.-math. sciences, Assoc. Professor, Ye.A. Buketov Karaganda State University, Karaganda, Kazakhstan

Nalbandyan, V. M. - Candidate of phys.-math.science, Research scientist, Centre of Laser and Information Biophysics, Orenburg State University, Orenburg, Russia

Narimanov, R.K. - Candidate of phys.-math. sciences, Assoc. Professor, Tomsk State University, Tomsk, Russia

Narimanova, G.N. - Candidate of phys.-math. sciences, Assoc. Professor, Dean of the Faculty of Innovative Technologies, Tomsk State University of Control Systems and Radioelectronics, Tomsk, Russia

Perchatkina, E.V. – Master student, National Research Tomsk State University, Tomsk, Russia

Potapov, A.A. - Doctor of phys.-math. sciences, Professor, Academician, Head of the Chinese-Russian laboratory of informational technologies and signals fractal processing of JNU-IREE RAS, JiNan University (JNU), Guangzhou, China, V.A. Kotelnikov Institute of Radio Engineering and Electronics, RAS, Moscow, Russia.

Rakhmankyzy, A. – 1st year postgraduate student, Physical-Technical Faculty, Ye.A. Buketov Karaganda State University, Karaganda, Kazakhstan

Ramazanova, G.I. – Candidate of phys.-math. sciences, Assoc. Professor, Satbayev Kazakh National Technical University, Almaty, Kazakhstan

Sakipov, K.E. - Candidate of Technical Sciences, Assoc. Professor, Head of the «Heat Power Engineering» Department, L.N. Gumilyov Eurasian National University, Astana, Kazakhstan

Sakipova, S.E. - Candidate of phys.-math. sciences, Professor, Physical-Technical Faculty Ye.A. Buketov Karaganda State University, Karaganda, Kazakhstan

Sattinova, Z.K. – Candidate of phys.-math. sciences, Assoc. Professor, Department Thermal Engineering, L.N. Gumilyov Eurasian National University, Astana, Kazakhstan

Saulebekov, A.O. - Doctor of phys.-math. sciences, Professor, M.V. Lomonosov Moscow State University, Kazakhstan branch, Astana, Kazakhstan

Saulebekova, D.A. - master student, M.V. Lomonosov Moscow State University, Kazakhstan branch, Astana, Kazakhstan

Sayakenov, N.B. - Candidate of medical sciences, associate professor, Semey State Medical University, Semey, Kazakhstan

Sekerbaeva, G. - 4th year student, Physical-Technical Faculty, Ye.A. Buketov Karaganda State University, Karaganda, Kazakhstan

Shabdarbaeva, D.M. - Doctor of medical sciences, professor, Head of Department, Semey State Medical University, Semey, Kazakhstan

Shaikenova, A.A. – PhD student, Satbayev University; Junior Researcher, EPR Spectroscopy Laboratory named after Gorelkin, Institute of Physics and Technology, Almaty, Kazakhstan

Shaimerdenova, K.M. – Candidate of technical sciences, Assoc. Professor, Head of the Engineering Thermophysics Department, Ye.A. Buketov Karaganda State University, Karaganda, Kazakhstan

Sharifov, D.M. – Candidate of phys.-math.sciences, Associate Professor, Eurasian National University. L.N. Gumilyov, Astana, Kazakhstan

Shichijo, K. - PhD, professor, Nagasaki University, 1-12-4, Sakamoto, Nagasaki 852-8523, Japan

Shrager, E.R. - Doctor of phys.-math. sciences, Professor, Dean, National Research Tomsk State University, Tomsk, Russia

Stepanenko, V.F. - Doctor of biological sciences, professor, Head of Department, A.F. Tsyb Medical Radiological Research Center, Obninsk, Russia

Stoev, M. - Doctor of Technical Sciences, Associate Professor, Neofit Rilа University, South-West, Blagoevgrad, Bulgaria

Tanasheva, N.K. - Ph.D, Senior Researcher, Institute of Applied Mathematics, Ministry of Education and Science of Republic Kazakhstan, Karaganda, Kazakhstan

Trubitsyn, A.A. - Doctor of phys.-math. sciences, Professor, Ryazan State Radio Engineering University, Ryazan, Russia

Tussybaeva, A.S. – Master, Lecturer, Physical-Technical Faculty, Ye.A. Buketov Karaganda State University, Karaganda, Kazakhstan

Ydyryssova, A.A. - Master student, Kazakh State Women's Teacher Training University, Almaty, Kazakhstan

Yershina, A.K. - Doctor of phys.-math. sciences, Professor, Kazakh State Women's Teacher Training University, Almaty, Kazakhstan

Yurov, V.M. - Candidate of phys.-math.sciences, Professor, Director of the Scientific Research Center, Ye.A. Buketov Karaganda State University, Karaganda, Kazakhstan

Zavatskaya, O.N. - Master of Physics, Junior Researcher, Ye.A. Buketov Karaganda State University, Karaganda, Kazakhstan

Zhakishev, B.A. - Ph.D., Assoc. Professor, «Heat Power Engineering» Department, L.N. Gumilyov Eurasian National University, Astana, Kazakhstan

Zhapbasbayev, U.K. - Doctor of Technical Sciences, Professor, Satbayev Kazakh National Technical University, Almaty, Kazakhstan

Zhumadilov, K.Sh. - PhD, Assoc. professor, Head of the International Department of Nuclear Physics, New Materials and Technologies, L.N. Gumilyov Eurasian National University; Department of Theoretical Physics of Reactor, National Research Nuclear University "MEPhI", Moscow, Russian Federation.

Zhunosov, Y.T. – Doctor of medical sciences, professor, Semey State Medical University, Semey, Kazakhstan

About «Eurasian Physical Technical Journal»

ISSN 1811-1165 Key title: Eurasian physical technical journal (Print)

Abbreviated key title: Eurasian phys. tech. j. (Print)

ISSN 2413-2179 Key title: Eurasian physical technical journal (Online)

Abbreviated key title: Eurasian phys. tech. j. (Online)

“Eurasian Physical Technical Journal” (Eurasian phys. tech. j.) is a peer-reviewed open access international scientific journal publishing original research results on actual problems of Physics, Technology and Engineering.

Since 2004 “Eurasian phys. tech. j.” is publishing in English. Periodicity is 2 issues per year.

The E.A. Buketov Karaganda State University is the main organizer and financial sponsor of EAPhTJ. The efforts of the international highly qualified Editorial Board consisting prominent physicists from 12 countries allow provide EAPhTJ international level.

Since 2004 more than 200 scientific papers written by physicists representing 23 countries were published. Among the authors there are full members and corresponding members of National Academies of Sciences of several countries and scientists with high H-index.

Since 2008 EAPhTJ has been included in the list of publications recommended by the Ministry of Science Education and Science of the Republic of Kazakhstan for the publication of the main results of the master's and PhD doctoral dissertations on the physical and mathematical sciences.

Publication Ethics and Malpractice Statement

Submission of an article to the Eurasian phys. tech. j. implies that the paper described has not been published previously, that it is not under consideration for publication elsewhere, that its publication is approved by all authors and tacitly or explicitly by the responsible authorities where the paper was carried out, and that, if accepted, it will not be published elsewhere in the same form, in English or in any other language, including electronically without the written consent of the copyright holder. In particular, translations into English of papers already published in another language are not accepted.

For information on Ethics in publishing and Ethical guidelines for journal publication see <http://www.elsevier.com/publishingethics> and <http://www.elsevier.com/journal-authors/ethics>.

The Eurasian phys. tech. j. follows the Code of Conduct of the Committee on Publication Ethics (COPE), and follows the COPE Flowcharts for Resolving Cases of Suspected Misconduct (http://publicationethics.org/files/u2/New_Code.pdf).

To verify originality, your article may be checked by the originality detection service Cross Check <http://www.elsevier.com/editors/plagdetect>.

Authors are responsible for the content of their publications. No other forms of scientific misconduct are allowed, such as plagiarism, falsification, fraudulently data, incorrect interpretation of other works, incorrect citations, etc. Authors are obliged to participate in peer review process and be ready to provide corrections, clarifications, retractions and apologies when needed. All authors of a paper should have significantly contributed to the research.

Reviewers should provide objective judgments and should point out relevant published works which are not yet cited. Reviewed articles should be treated confidentially. The reviewers will be chosen in such a way that there is no conflict of interests with respect to the research, the authors and/or the research funders.

Editors have complete responsibility and authority to reject or accept a paper, and they will only accept a paper when reasonably certain. They will preserve anonymity of reviewers and promote publication of corrections, clarifications, retractions and apologies when needed.

The acceptance of a paper automatically implies the copyright transfer to the Eurasian phys. tech. j. All submitted papers will be sent for reviewing to leading experts in the given area. The Editorial Board of the Eurasian phys. tech. j. will monitor and safeguard publishing ethics. The editors reserve the right to accept or reject manuscripts.

GUIDELINES FOR AUTHORS

Research articles, survey papers and short notes are accepted for exclusive publication in the «**Eurasian phys. tech. j.** » in English

The manuscripts and short notes must contain original results of investigation in the following scientific areas of Physics:

Non-linear Physics.

Modeling of the nonlinear physical - technical processes.

Energetics. Thermophysics. Hydrodynamics.

Material Sciences. Technologies for creating new materials.

Ecological Aspects of New Technologies.

Engineering. Devices and methods of experiment.

All publishing manuscripts and short notes must have been recommended by a member of the editor board or by the organization (University), where the work was performed. The author who submitted an article for publication will be considered as a corresponding author.

The paper, short note or review paper shall include an abstract of the contents, not exceeding 200 words and keywords (no more than 10). The abstract must not coincide with the introduction or conclusive part of the work and must not contain references, abbreviations and other unknown words.

All articles should have list of keywords or terms (3 to 10) for indexing purposes.

The text of a paper must not exceed 8-12 pages including tables, figures (no more than 6) and references. A short note must not exceed 4-5 pages including no more than 2 figures. A review paper must not be more than 20 pages (including no more than 10 figures).

The text should be divided on structural parts: **Introduction, Theoretical part, Experimental technique, Results and Discussion, Conclusion**, etc.

Printed copies shall be on good quality paper of International size A4. All texts must be printed in Microsoft Word. It is preferable to use the Times fonts. The text must be printed in 12 point letters, 1.5 intervals. There shall be a margin of 30 mm at the left-hand edge, of 15 mm at the fore edge, of 30 mm at the head of the page and of 30 mm at the tail. All pages must be numbered.

Acknowledgments may be shown at the end of the article text, before **REFERENCES**.

All references must be numbered in the text (for example, [1], [2-4]) and listed in numerical order.

Equations in your paper have to be written using the Microsoft Equation Editor or the MathType (<http://www.mathtype.com>) for (Insert | Object | Create New | Microsoft Equation or MathType Equation).

Tables must be inserted into the text.

Figures should be prepared in a digital form suitable for direct reproduction. Figures shall be submitted on the separate sheets and not included into the text.

The following files must be submitted via e-mail:

- Article text (*.doc);
- Figures (fig1.jpg, fig2.pcx);
- Figure captions (*.txt, *.doc).

